

# **Stratigraphy, Structure and Geochronology of Archean Lode Gold Deposits in the Southeastern Rice Lake Greenstone Belt, Southeast Manitoba**

by

Xiaohui Zhou

A thesis  
presented to the University of Waterloo  
in fulfillment of the  
thesis requirement for the degree of  
Doctor of Philosophy  
in  
Earth Sciences

Waterloo, Ontario, Canada, 2017

© Xiaohui Zhou 2017

## **Examining Committee Membership**

The following served on the Examining Committee for this thesis. The decision of the Examining Committee is by majority vote.

External Examiner

Dr. Bruno Lafrance

Professor, Laurentian University

Supervisor

Dr. Shoufa Lin

Professor, University of Waterloo

Internal Member 1

Dr. Brian Kendall

Assistant Professor, University of Waterloo

Internal Member 2

Dr. Chris Yakymchuk

Assistant Professor, University of Waterloo

Internal-external Member

Dr. William K. Annable

Associate Professor, University of Waterloo

### **Author's Declaration**

This thesis consists of material all of which I authored or co-authored: see Statement of Contributions included in the thesis. This is a true copy of the thesis, including any required final revisions, as accepted by my examiners.

I understand that my thesis may be made electronically available to the public.

## **Statement of Contributions**

I would like to express my sincere gratitude to the following co-authors that I have worked with:

Dr. Shoufa Lin, primary supervisor, University of Waterloo

Dr. Scott D. Anderson, co-supervisor, Manitoba Geological Survey

Dr. Brian Kendall, internal committee member, University of Waterloo

Dr. Donald W. Davis, external collaborator, University of Toronto

Dr. Holly J. Stein, external collaborator, Colorado State University

I carried out geological mapping with field assistants and collected all field data in the summer seasons of 2012, 2013 and 2014. I wrote the entire manuscript of this thesis and incorporated comments from the above co-authors and suggestions from the committee (see Examining Committee Membership). Drs. Shoufa Lin and Scott D. Anderson supervised the entire mapping project and provided inspiring discussions and thorough editorial advice on this thesis. Dr. Brian Kendall also made editorial corrections on the thesis and helped interpret all geochronological data in Chapter 4 and Appendix. The U-Pb geochronological work in Chapter 4 was conducted by Dr. Donald W. Davis at the Jack Satterly Geochronology Laboratory at the University of Toronto. I assisted in picking up zircon/monazite grains and measuring isotope composition. Dr. Donald W. Davis also provided zircon/monazite morphology images (Fig. 4.14), analytical methods (Section 4.4.1.1), results (Table 4.1.1, 4.1.2, 4.1.3, 4.1.4, 4.2), diagrams (Fig. 4.15, 4.16) and associated interpretations (Section 4.4.1.2). The Re-Os geochronological work was carried out by the staff through the AIRIE program at the Colorado State University. Dr. Holly J. Stein provided molybdenite images (Fig. 4.17b, c), Re-Os results (Table 3, A1) and helped interpret all Re-Os data in Chapter 4 and Appendix. Drs. Chris Yakymchuk, Bruno Lafrance and William K. Annable from the examining committee also provided detailed advice on this thesis.

## Abstract

The Central Manitoba mine trend is one of the most important lode gold camps in the Rice Lake greenstone-granitoid belt of the western Uchi Subprovince within the western Superior Province, Manitoba, Canada. Neoarchean host rocks consist of a south-facing volcano-sedimentary succession (2.75–2.73 Ga) intruded by voluminous gabbroic sills and tonalitic-granodioritic plutons (2.73–2.72 Ga), as well as late aplite dikes (2.73–2.72 Ga) and quartz-feldspar porphyry dikes (2.73–2.71 Ga). Five generations of deformation structures have been recognized through detailed geological mapping. The entire succession was folded during early deformation prior to rare late aplite dike emplacement. All fault-fill veins and extension veins cut all lithologic units, and are structurally governed by late conjugate shear zones. Main gold mineralization occurs within fault-fill veins hosted by west-trending steeply-dipping dextral brittle-ductile and ductile shear zones, which occur along or across contacts of metabasalt, metagreywacke and metagabbro or entirely within metagabbro. Microstructural and paragenetic analyses on main gold-bearing veins have revealed that gold is intimately associated with quartz, pyrrhotite and tellurobismuthite. Main gold introduction is interpreted to have taken place contemporaneously with pyrrhotite and tellurobismuthite deposition early during dextral shearing.

The Ogama-Rockland gold deposit consists of shear zone-associated quartz veins hosted by the Ross River pluton, a ca. 2728–2724 Ma tonalitic-granodioritic intrusion in supracrustal rocks (< ca. 2745–2731 Ma) of the Bidou assemblage within the Rice Lake greenstone belt. The plutonic host rocks contain NE-to-ENE-trending, steep, early foliation that is overprinted by late conjugate sets of W-to-NW-trending dextral and N-to-NE-trending sinistral shear zones. Early gold introduction associated with folded veins and low grade planar extension veins occurred before shearing. Main gold mineralization and remobilization are associated with highly auriferous NW-trending steep shear veins. They were likely emplaced late during dextral shearing. Most of the native gold occurs in fractures and grain boundaries of quartz, pyrite and chalcopyrite-bornite in shear veins, which reflects a strong structural and mechanical control on the microscopic scale.

Early gold mineralization associated with low grade planar veins at the Ogama-Rockland deposit is constrained at ca. 2728 Ma, based on U-Pb zircon ages from two phases of host tonalite ( $2728.7 \pm 0.7$  Ma;  $2728.2 \pm 0.6$  Ma) and one aplite dike ( $2727.9 \pm 1.6$  Ma) that cuts the

early low grade veins. A Re-Os molybdenite age of  $2727.4 \pm 4.8$  Ma was obtained from one vein that cuts aplite dikes and sheeted veins, which agrees well with the U-Pb zircon ages of the dated tonalite phases and the aplite dike. The dated tonalite phases, aplite dike and the dated vein are all cut by late ductile or brittle-ductile shear zones, indicating their emplacement, and possibly early gold mineralization, occurred before dextral shearing. The close time association and high Re concentration in the dated molybdenite suggest that granitoid magmas were the source of mineralizing fluids for early gold mineralization. High grade gold mineralization in dextral shear-zone-hosted veins represents a later gold introduction and/or remobilization during dextral shearing.

## Acknowledgements

Life is full of surprises and doing a Ph.D. is definitely one of them. I can't imagine coming to Waterloo across half the earth for graduate studies without an inadvertent suggestion from my close friend Peng Jiang. I would like to thank my supervisor Dr. Shoufa Lin for his prominent mentoring and unceasing guidance since I started from scratch. His open mind and academic excellence have inspired me over the years that passed. Geological mapping constitutes a significant portion of my study and I am so grateful that I have carried it out with the prestigious Manitoba Geological Survey (MGS). I sincerely thank my co-supervisor Dr. Scott D. Anderson for accompanying me every field season and discussing my discoveries throughout the project. His invaluable knowledge of the Rice Lake greenstone belt and extensive comments on my field reports and journal articles keep me thinking critically about my field observations. I also appreciate other geologists from MGS, namely Dr. Xueming Yang, Tim Corkery, Paul Kremer, and director Dr. Christian Böhm for their helpful discussions on my project. Summer students Skye Kushner, Paul Belanger, Mark Hamilton, Justin Calkin and Shaun Kirchmann are gratefully acknowledged for their enthusiastic field assistance and for filling every field season with joy. Field geologists from the Bison Gold Resource Inc., namely Scott Snider, David Benson, Dorian Chamale, Stephanie Bell, Erin Neufeld, Mat Porter are much appreciated for their kind help in the 2012 field season. I am very grateful to Dr. Don W. Davis for detailed instructions and insightful discussions on U-Pb geochronology during my visit at the Jack Satterly Geochronology Laboratory at the University of Toronto. Particular thanks go to Dr. Brian Kendall for introducing me to the world of Re-Os geochronology, and to Dr. Holly Stein for inspiring discussions and precise Re-Os data through her AIRIE program at the Colorado State University. Drs. Carl Guilmette and Chris Yakymchuk are greatly acknowledged for sharing their knowledge on petrology and ore deposits. I want to extend my deep gratitude to Dr. Bruno Lafrance from Laurentian University for excellent teaching in his structural mapping course and perceptive comments on my journal article during the publication process. I would like to thank Drs. Jen Parks and Changcheng Li for their kind help over the years. Many thanks also go to graduate students from Shoufa's squad and beyond, particularly Nathan Cleven and Ryan Martin; it has always been a lovely and dynamic atmosphere in the office room. Finally, I am greatly indebted to my family for their patience, support and understanding, especially during the past few work-intensive months.

# Table of Contents

Examining Committee Membership .....	ii
Author's Declaration.....	iii
Statement of Contributions .....	iv
Abstract .....	v
Acknowledgements.....	vii
Chapter 1 Introduction .....	1
1.1 The Superior Province in southeastern Manitoba.....	2
1.2 The Rice Lake greenstone belt.....	3
1.3 Brief deposit history and previous work.....	3
1.3.1 The Central Manitoba mine trend .....	3
1.3.2 The Ogama-Rockland gold deposit .....	4
1.4 Thesis objectives .....	4
1.5 Organization of thesis .....	5
Chapter 2 Stratigraphy, structure and lode gold system at the Central Manitoba mine trend, Rice Lake greenstone belt, Archean Superior Province, Manitoba, Canada .....	9
2.1 Introduction.....	10
2.2 Geological Setting.....	11
2.3 Supracrustal rocks and stratigraphy .....	12
2.3.1 Bidou assemblage .....	12
2.3.2 Mafic intrusions .....	13
2.3.3 Quartz-feldspar porphyry dikes .....	13
2.4 Structural geology.....	13
2.4.1 First generation ( $G_1$ ) structures .....	14

2.4.2 Second generation ( $G_2$ ) structures .....	15
2.4.3 Third generation ( $G_3$ ) structures .....	16
2.4.4 Fourth generation ( $G_4$ ) structures with rare $F_5$ fold .....	18
2.5 Vein system.....	20
2.5.1 Vein type and field relations .....	20
2.5.2 Vein mineralogy, microstructure and paragenesis.....	23
2.6 Discussion .....	28
2.6.1 Stratigraphic setting of gold mineralization.....	28
2.6.2 Structural control of ore shoots.....	29
2.6.3 Gold precipitation and modification at microscopic level .....	30
2.7 Conclusions.....	31
Chapter 3 Structural setting and lithologic control of the Ogama-Rockland lode gold deposit, southeastern Ross River pluton, Rice Lake greenstone belt, Superior Province, Manitoba, Canada .....	59
3.1 Introduction.....	60
3.2 Regional Geologic Setting .....	61
3.3 Local lithology .....	61
3.3.1 Tonalite .....	62
3.3.2 Quartz feldspar porphyry dikes.....	63
3.3.3 Aplite dikes .....	64
3.4 Structural geology .....	64
3.4.1 First generation ( $G_1'$ ) structures.....	65
3.4.2 Second generation ( $G_2'$ ) structures .....	66
3.5 Vein system.....	70
3.5.1 $V_1'$ veins.....	70
3.5.2 $V_2'$ veins.....	70

3.5.3 V <sub>3</sub> ' veins.....	72
3.5.4 V <sub>4</sub> ' veins.....	73
3.5.5 V <sub>5</sub> ' veins.....	73
3.6 Gold distribution and its structural control .....	75
3.6.1 Gold distribution and related structures on an ore-body scale.....	75
3.6.2 Structural control on gold mineralization on a microscopic scale .....	76
3.7 Discussions .....	78
3.7.1 Localization and origin of shear zones .....	78
3.7.2 Genesis of Ogama-Rockland gold deposit.....	79
3.7.3 Regional correlations of structure and metallogeny in the Rice Lake belt .....	79
3.8 Summaries and Conclusions .....	80
Chapter 4 Timing of gold mineralization at the Ogama-Rockland lode gold deposit in the Neoarchean Rice Lake greenstone belt, southeastern Manitoba, Canada: new constraints from ore texture, U-Pb zircon/monazite and Re-Os molybdenite geochronology .....	120
4.1 Introduction.....	121
4.2 Geological background .....	122
4.3 Hydrothermal alteration, vein mineralogy and paragenesis .....	124
4.3.1 Hydrothermal alteration.....	124
4.3.2 Vein mineralogy.....	124
4.3.3 Paragenesis.....	129
4.4 Geochronological methods and results .....	131
4.4.1 U-Pb zircon/monazite chronometer .....	131
4.4.2 Re-Os molybdenite chronometer .....	135
4.5 Discussions .....	137
4.5.1 Relative timing of alteration and vein infill .....	137
4.5.2 Age constraints on magmatism, vein formation, deformation and gold mineralization	

.....	139
4.5.3 Implications of ore texture and geochronology for the origin and setting of the Ogama-Rockland area.....	141
4.6 Conclusions.....	142
Chapter 5 Summary of conclusions .....	170
5.1 Summary of the thesis.....	171
5.2 Main conclusions .....	171
5.2.1 Stratigraphy, structure and vein system at the Central Manitoba mine trend.....	171
5.2.2 Structural setting and vein system at the Ogama-Rockland deposit.....	171
5.2.3 Timing of gold mineralization at the Ogama-Rockland deposit.....	172
6.3 Future work .....	172
Letter of Copyright Permission.....	174
References .....	175
Appendix Enigmatic Re-Os molybdenite dates from a V <sub>5</sub> ' fault-fill vein at the Ogama-Rockland deposit .....	184

# **Chapter 1**

## **Introduction**

This thesis is focused on the structural and lithostratigraphic setting and timing of gold mineralization at two Archean lode gold deposits in the southeastern Rice Lake greenstone belt of the western Superior Province. One case study deals with stratigraphic succession, structural setting and lode system at the greenstone-hosted Central Manitoba mine trend. The other case study examines the structural setting, veining sequence and paragenesis, and absolute timing of the tonalite-hosted Ogama-Rockland deposit. In this chapter, the author introduces basic geological background and overall objectives and organization of the thesis. Geology of the Superior Province and Rice Lake greenstone belt is summarized first. This is followed by a very brief review of exploration history and previous literature at these two gold deposits. The objectives and organization of this thesis are documented in detail. Lastly, publication of chapters is briefly described.

## **1.1 The Superior Province in southeastern Manitoba**

The western Superior Province in southeastern Manitoba is subdivided into three east-trending lithotectonic units based on rock type, absolute ages, metamorphic grades and geophysical signatures: the North Caribou terrane, the Uchi Subprovince and the English River Subprovince (Fig. 1.1; Poulsen et al., 1996; Bailes et al., 2003; Anderson, 2008, 2013a, b). The North Caribou terrane consists of the 2.99–2.92 Ga Mesoarchean Wallace assemblage (Davis, 1994; Percival et al., 2006a, b; Sasseville et al., 2006), the 2.87–2.85 Ga Mesoarchean Garner assemblage (Davis, 1994; Anderson, 2013a, b), and the 3.01–2.99 Ga English Lake, 2.94–2.90 Ga East shore and the 2.75–2.69 Ga Wanipigow River plutonic complexes (Corfu and Stone, 1998; Whalen et al., 2003; Percival et al., 2006a, b). The boundary between the North Caribou terrane and the Uchi Subprovince is defined by the Wanipigow fault, which is a crustal-scale, subvertical shear zone with a multiphase deformation history (Anderson, 2008). The Uchi Subprovince is constituted of the 2.75–2.73 Ga Neoarchean Bidou assemblage (Turek et al., 1989; Bailes et al., 2003; Percival et al., 2006a; Anderson, 2008); the 2.73–2.72 Ga Ross River plutonic suite (Turek et al., 1989; Anderson, 2008; Chapter 4); the 2.73–2.72 Ga Gem assemblage (Davis, 1994; Anderson, 2013b); the 2.71–2.69 Ga Edmunds assemblage (Davis, 1996; Lemkow et al., 2006; Anderson, 2013a, b); and < 2.705 Ga San Antonio assemblage (Percival et al., 2006a). The Rice Lake greenstone belt defines the western-most exposed portion of the Uchi Subprovince to the west of the southern border between Manitoba and Ontario. The

interface between the Uchi and English River Subprovinces is marked by the curvilinear, crustal-scale, subvertical Manigotagan fault (Poulsen et al., 1996; Anderson, 2008). The English River Subprovince is equivalent to the English River basin in Ontario, using the nomenclature of Stott et al. (2010). The English River Subprovince includes 2.72–2.70 Ga amphibolite to granulite facies metasedimentary rocks (Corfu et al., 1995; Davis, 1996; Anderson, 2013a) and the 2.7 Ga voluminous diorite–tonalite–granodiorite plutonic rocks (Corfu et al., 1995).

## 1.2 The Rice Lake greenstone belt

Neoarchean metavolcanic rocks in the Rice Lake greenstone belt mostly range from 2.75 to 2.72 Ga, and are overlain by metasedimentary rocks deposited after 2.71 Ga (Krogh et al., 1974; Ermanovics and Wanless, 1983; Turek et al., 1989; Turek and Weber, 1991; Davis, 1994, 1996; Percival et al., 2006; Sasseville et al., 2006; Anderson, 2008, 2013a, b) (Fig. 1.2). All the supracrustal rocks are metamorphosed to greenschist facies, although amphibolite facies conditions were reached around the margins of plutons (Poulsen et al., 1996). We omit the prefix “meta” in the following descriptions for brevity, since primary sedimentary and volcanic structures are well preserved.

The greenstone belt is intruded by voluminous gabbroic intrusions and by the ca. 2.73–2.72 Ga tonalitic-granodioritic Ross River pluton (Turek et al., 1989; Anderson, 2008, 2013b). All of these rocks are intruded by ca. 2.73–2.71 Ga quartz feldspar porphyry and aplite dikes (Turek et al., 1989; Anderson, 2008, 2013a, b; Chapter 4).

All the supracrustal rocks of the Bidou assemblage to the east of the Ross River pluton are folded by the regional-scale Beresford Anticlinorium. Supracrustal units strike west-to-northwest and are steeply-dipping (Fig. 1.1b, 1.2). Discrete, narrow and widely-spaced brittle-ductile shear zones are well developed in the supracrustal and plutonic rocks. Some ductile shear zones are concordant or slightly discordant with lithologic trends (e.g., the North Carbonate Shear Zone), whereas others crosscut lithologic contacts (e.g., the South Carbonate Shear Zone).

## 1.3 Brief deposit history and previous work

### 1.3.1 The Central Manitoba mine trend

The Central Manitoba mine trend (Fig. 1.1, 1.2) produced ~160,000 ounces of gold between 1927 and 1937 from four main shafts: the Growler, Kitchener, Tene and Hope (Stockwell and

Lord, 1939; Poulsen et al., 1996). Here, gold is associated with quartz veins in shear zones along or across the contacts among gabbro, basalt and greywacke. The deposit appears to be a typical orogenic gold deposit, providing an ideal opportunity to further our understanding of this type of deposit. Although pioneering regional-scale to camp-scale surface mapping and underground mapping were conducted in the 1930s and 1990s (Stockwell and Lord, 1939; Brommecker, 1991), little detailed research has been published, nor has the genesis of the deposits been addressed.

### ***1.3.2 The Ogama-Rockland gold deposit***

The Ogama-Rockland gold deposit is situated within the southeast margin of the Ross River pluton (Fig. 1.1, 1.2). It produced ~ 50,000 ounces of gold in the 1940s (Poulsen et al., 1996), and has recently been estimated to contain an inferred mineral resource of 337,000 ounces at an average grade of 8.17 g/t based on results of new drilling programs (Chater et al., 2013). Gold mineralization mainly occurs in quartz-(carbonate) veins spatially associated with discrete ductile shear zones in altered host felsic plutonic rocks. Previous work at this deposit includes several thesis studies by Troop (1949), Keith (1988) and briefly by Brommecker (1991), which are mainly concerned with shear zone kinematics and its relation to ore shoot.

### **1.4 Thesis objectives**

The main objectives of the thesis are to establish the lithostratigraphic and structural setting of the Central Manitoba mine trend and the Ogama-Rockland deposit through detailed geological mapping, and to constrain relative and absolute timing of gold mineralization at the Ogama-Rockland deposit via field relations, ore textures, and U-Pb and Re-Os geochronology. The specific and critical objectives of this thesis are to investigate:

1. Sequential, contact and crosscutting relationships of the host stratigraphic succession at the Central Manitoba mine trend;
2. Various intrusive phases of the host Ross River pluton and their crosscutting relations at the Ogama-Rockland gold deposit;
3. Multiple generations of deformation structures and their structural development, with emphasis on shear zone geometry and kinematics and their spatial and temporal relationships with host vein emplacement for both deposits;
4. Veining sequence at both deposits; and its spatial, temporal, and possibly genetic

relationships with host plutonic rocks and associated aplite dikes, particularly at the Ogama-Rockland gold deposit;

5. Paragenetic sequence of vein minerals for both deposits and their relative timing with alteration minerals during progressive development of zoned alteration envelopes at the Ogama-Rockland gold deposit;

6. Nature and different stages of primary gold deposition and secondary gold remobilization associated with deformation processes at the Ogama-Rockland gold deposit; and structural control on ore shoots at all scales for both deposits;

7. Absolute age constraints on gold mineralization at the Ogama-Rockland gold deposit.

In order to solve these outstanding issues and uncover fundamental geologic processes that were related to gold mineralization, detailed camp-scale (1:1000; 1:5000) and outcrop-scale (1:50) geological mapping have been carried out in the vicinity of both deposits for three summers, with emphasis on key crosscutting relationships and structural analysis. This is followed by careful hand specimen and thin section examinations on petrography, ore texture and microstructure, to constrain paragenesis and related deformation structures. Absolute age constraints have been obtained via the U-Pb zircon/monazite isotope dilution – thermal ionization mass spectrometry (ID-TIMS) and Re-Os molybdenite isotope dilution – negative thermal ionization mass spectrometry (ID-NTIMS) methods, using samples with well-established structural and paragenetic contexts.

## **1.5 Organization of thesis**

The thesis is constituted of three main chapters (2-4). Each chapter is concerned with several key issues around a certain topic at one single deposit and is written as a stand-alone journal manuscript. For the latter reason, some repetition among the chapters, e.g., in description of regional geological setting, is unavoidable. Evidence in individual chapters is generally organized from field to laboratory with progressively increasing observation scale, and comparisons with earlier chapters are common. References for all chapters are compiled at the end of the thesis.

For the convenience of structural description and correlation, a certain deformation generation, and associated fold, foliation as well as lineation are termed  $G_n$ ,  $F_n$ ,  $S_n$ , and  $L_n$  at the Central Manitoba mine trend; whereas for the Ogama-Rockland deposit they are termed  $G_n'$ ,  $F_n'$ ,

$S_n'$  and  $L_n'$ , respectively. Five generations of deformation structures have been recognized at the Central Manitoba mine trend and two of them have been identified at the Ogama-Rockland deposit. The relationships between structures at two deposits are  $G_2=G_1'$ ;  $G_2=G_4'$ . A specific veining stage is termed  $V_n$  at the Central Manitoba mine trend and  $V_n'$  at the Ogama-Rockland gold deposit.

The second chapter deals with the stratigraphic and structural settings of the lode gold system at the Central Manitoba mine trend. Five generations of deformation structures ( $G_1 - G_5$ ) and three stages of veining ( $V_1-V_3$ ) have been identified in the supracrustal rocks of the Bidou assemblage. Main gold mineralization is structurally controlled by west-trending, steeply-dipping  $V_2$  fault-fill veins hosted by dextral  $G_4$  shear zones.

The third chapter is mainly concerned with the lithological and structural settings of the granitoid-hosted Ogama-Rockland gold deposit. Early gold mineralization associated with low grade  $V_2'$  sheeted extension veins might have occurred before or early during ductile shearing, whereas late gold mineralization and/or remobilization associated with  $V_5'$  veins might have occurred late during  $G_2'$  dextral shearing.

The fourth chapter establishes the relative timing of gold mineralization through recognizing vein paragenetic sequences and the progressive development of zoned alteration halos, and further constrains the absolute age of gold mineralization via U-Pb and Re-Os geochronology. Primary gold deposition was contemporaneous with pyrite, chalcopyrite-bornite, and possibly bismuth-bearing minerals. Secondary gold remobilization is structurally controlled by late fractures within quartz and pyrite crystals. U-Pb zircon/monazite geochronology on host tonalite phases and one aplite dike that cuts the auriferous  $V_2'$  veins reveals that early gold mineralization mostly likely occurred at ca. 2728 Ma. This age is in good agreement with a Re-Os molybdenite age of ca. 2727 Ma from one  $V_4'$  vein.

The fifth chapter summarizes the entire thesis and the main conclusions. The appendix reports two Re-Os molybdenite ages from one  $V_5'$  vein, with an average age of ca. 2782 Ma. This age appears to older than the dated tonalite phases, aplite dike and  $V_4'$  vein. The significance of the age is open to discussion and requires further detailed analysis on molybdenite and future geochronological work on the immediate adjacent tonalite wall rocks.

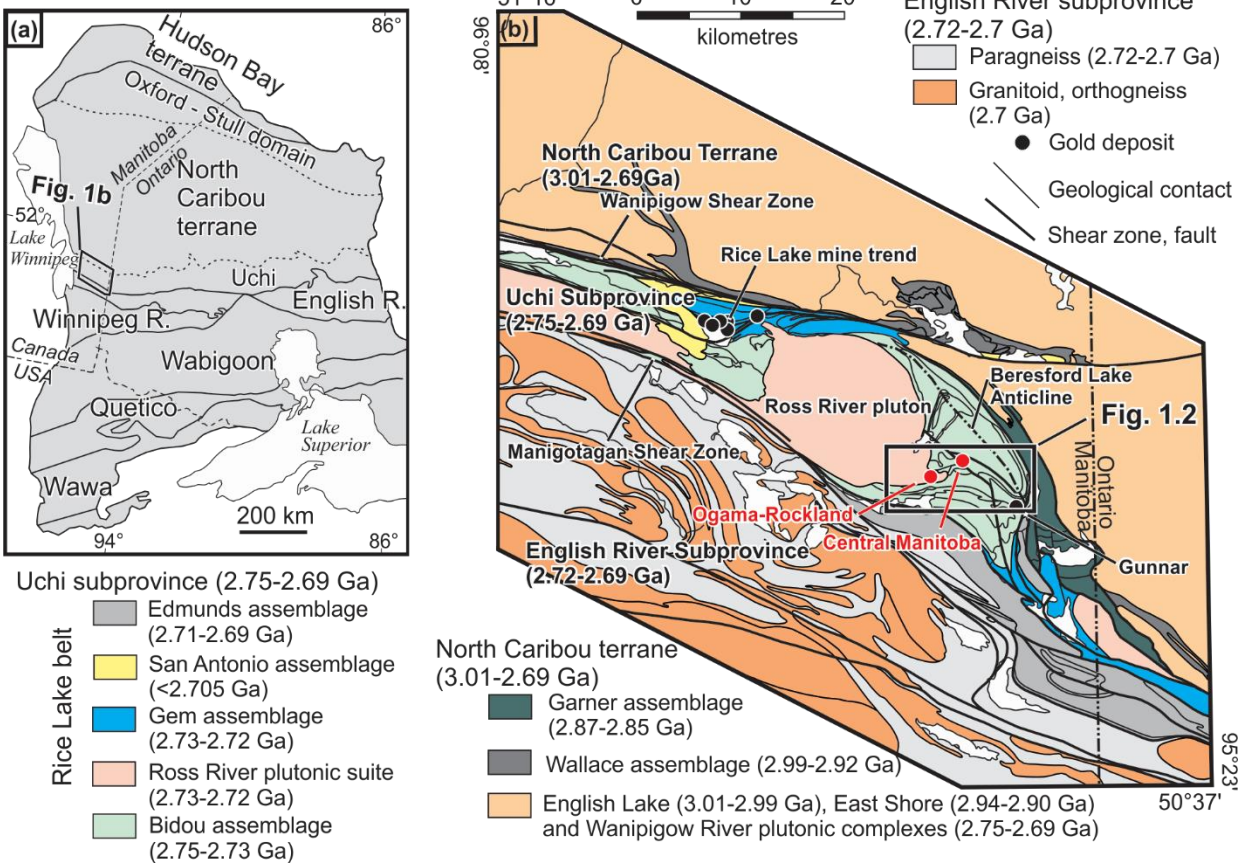


Figure 1.1 a) Tectonic framework of the western Superior Province, showing major Subprovinces, domains and terranes; modified from Lin and Beakhouse (2013); b) Regional geologic map of the western Superior Province in southeastern Manitoba, illustrating two major Subprovinces and one terrane, terrane boundaries, significant gold deposits and U-Pb zircon age constraints; modified from Anderson (2013a). See text for age data source. Locations of the Central Manitoba mine trend and the Ogama-Rockland gold deposit are indicated in red.

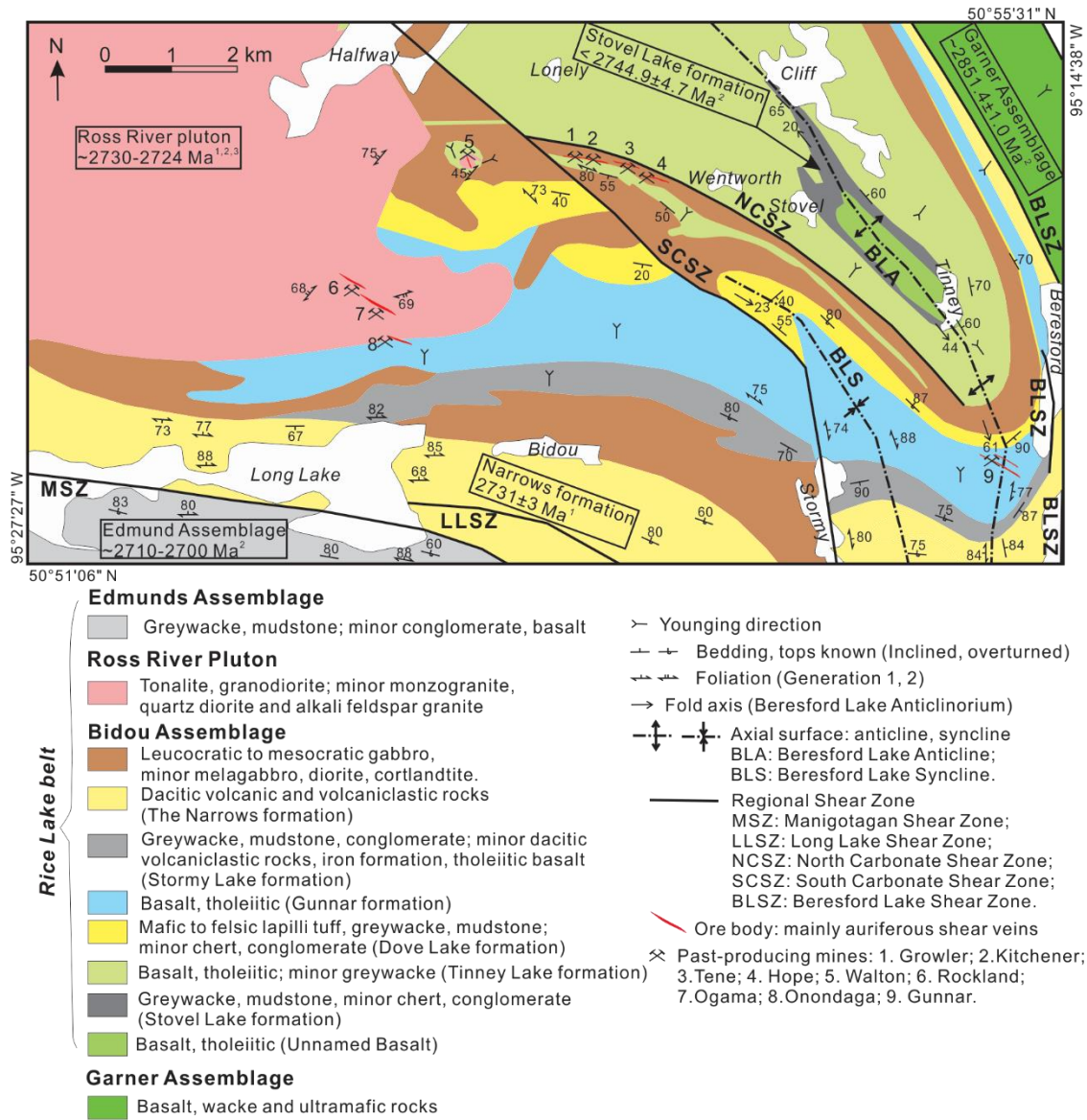


Figure 1.2 Generalized regional geologic map of the Bidou assemblage and Ross River pluton in the southeastern Rice Lake greenstone belt in southeastern Manitoba, showing principal formations, lithologic units, deformation structures, U-Pb zircon ages and gold deposits; modified from Stockwell and Lord (1939), Stockwell (1945), Zwanzig (1971), Brommecker (1996), Anderson (2013b) and Zhou (2014). Age source: <sup>1</sup> Turek et al. (1989), <sup>2</sup> Anderson (2013b), <sup>3</sup> Chapter 4.

## **Chapter 2**

**Stratigraphy, structure and lode gold system at the  
Central Manitoba mine trend, Rice Lake greenstone  
belt, Archean Superior Province, Manitoba, Canada**

## 2.1 Introduction

The Superior Province hosts numerous world class gold deposits (>8, 500 t) in Archean greenstone–granitoid belts (Goldfarb et al., 2001). Four main types of gold deposits have been documented in the Province (e.g., Robert et al., 2005, 2007): orogenic gold deposits (e.g., Kirkland Lake, Rice Lake), gold-rich volcanogenic massive sulfide (VMS) deposits (e.g., Doyon-LeRonde-Bousquet, Horne), intrusion-related (reduced or oxidized) deposits (e.g., Beattie, Young-Davidson), and other atypical gold deposits (e.g., Hemlo). For orogenic gold deposits, it is widely debated whether gold deposits adjacent to major crustal-scale shear zones formed during an early extensional phase and are associated with alkaline and/or calc-alkaline magmatism, or formed during a late compressional phase and the closure of extensional basins along the shear zone (e.g., Mercier-Langevin et al., 2012b).

The Neoarchean Rice Lake belt in southeastern Manitoba contains several gold deposits (Fig. 2.1) situated on either side of a tonalite-granodiorite pluton (Rice Lake and Central Manitoba mine trends) and within its margin (Ogama-Rockland mine trend) (Fig. 2.2). The Central Manitoba mine trend (Fig. 2.2) produced ~160, 000 ounces of gold between 1927 and 1937 from four main shafts: the Growler, Kitchener, Tene and Hope (Stockwell and Lord, 1939; Poulsen et al., 1996). Here, gold is associated with quartz veins in shear zones and the deposit appears to be a typical orogenic gold deposit, providing an ideal opportunity to further our understanding of this type of deposit. Although regional-scale to camp-scale surface mapping and underground mapping were conducted in the 1930s (Stockwell and Lord, 1939), little detailed research has been published, nor has the genesis of the deposits been addressed. In particular, detailed structural analysis in this area is lacking and structural timing of auriferous quartz veins has not been fully determined.

In order to improve understanding of the geological processes that led to the formation of the deposits, the Central Manitoba mine trend was mapped at a scale of 1:5000 (Zhou et al., 2013, 2014). Several key outcrops were mapped in detail (1:50) to document field relationships between various rock types, deformation structures and auriferous quartz veins. This work combines results from extensive surface mapping and key information from underground workings, considers structures from microscopic to camp scales, integrates structural development with vein emplacement, and examines the paragenetic sequence of vein minerals associated with gold. These results have led to a better understanding of structural setting and the

paragenesis of the Central Manitoba mine trend, which provides new constraints for structural evolution and gold mineralization of the Rice Lake belt.

In this paper, bedrock lithology and stratigraphic succession of the deposit area are described first. Then a detailed description of five generations of deformation structures is provided, with emphasis on brittle-ductile shear zones that are spatially associated with auriferous quartz veins. Three stages of vein emplacement are documented based on specific generation of associated brittle-ductile shear zones. This is followed by mineralogical and textural analyses of infill and alteration minerals of gold-bearing veins, with a focus on gold introduction and related sulfide deposition.

## 2.2 Geological Setting

The Central Manitoba mine trend is situated in the southeastern Rice Lake greenstone belt of the western Uchi Subprovince, western Superior Province, Manitoba (Fig. 2.2). Neoarchean metavolcanic rocks in the Rice Lake greenstone belt mostly range from 2.75 to 2.72 Ga, and are overlain by metasedimentary rocks deposited after 2.71 Ga (Krogh et al., 1974; Ermanovics and Wanless, 1983; Turek et al., 1989; Turek and Weber, 1991; Davis, 1994, 1996; Percival et al., 2006; Sasseville et al., 2006; Anderson, 2008, 2013a, b) (Fig. 2.2). All the supracrustal rocks are metamorphosed to greenschist facies, although some amphibolite facies assemblages are present around the margins of plutons (Poulsen et al., 1996). Since primary sedimentary and volcanic structures are well preserved in this belt, we omit the prefix “meta” in the following descriptions in the interest of brevity.

The greenstone belt is intruded by voluminous gabbroic sills and dikes and by the ca. 2.73–2.72 Ga (Turek et al., 1989; Anderson, 2008, 2013b) tonalitic-granodioritic Ross River pluton and related satellite intrusions. All of these rocks are intruded by ca. 2.73–2.71 Ga (Turek et al., 1989; Anderson, 2008, 2013b) quartz feldspar porphyry and aplite dikes (Anderson, 2013a; Zhou et al., 2014).

In the district around the Central Manitoba mine trend (Figs. 2.2 and 2.3), supracrustal rocks belonging to the Bidou assemblage include several conformable formations of mafic and felsic volcanic/volcaniclastic rocks and sedimentary rocks, all of which were deposited within a relatively brief time span of < 2745 Ma to ~2731 Ma (Fig. 2.4a) (Turek et al., 1989; Anderson, 2013b). A biotite granodiorite phase in the central portion of the Ross River pluton yielded a U-

Pb zircon age of ~2724 Ma (Anderson, 2008), whereas a biotite tonalite phase at the Ogama mine in the southeastern margin of the pluton yielded a U-Pb zircon age of ~2728–2729 Ma (Turek et al., 1989; Zhou, unpublished data), which represents the minimum age of the host rocks to the Central Manitoba mine trend. Quartz feldspar porphyry dikes dated at several locations yield U-Pb zircon ages identical to hosting or adjacent plutonic rocks (see age data from Anderson, 2013a). Preliminary U-Pb zircon data of aplite dikes near the Rockland and Ogama mines suggest a similar igneous age at ~2728 Ma (Zhou, unpublished data).

Rocks in the study area are variably deformed. Deformation is most intense in numerous discrete, narrow, widely-spaced brittle-ductile shear zones, within both the greenstone belt and the plutonic rocks. High-strain zones also occur along lithologic contacts.

## 2.3 Supracrustal rocks and stratigraphy

The study area is underlain by volcanic and sedimentary supracrustal rocks of the Bidou assemblage, which are intruded by several different intrusive phases, including the Ross River pluton (Fig. 2.3; Zhou, 2014). The Bidou assemblage is subdivided into several formations, interpreted to represent a conformable stratigraphic succession (Stockwell and Lord, 1939; Campbell, 1971), although the contacts are locally reactivated by ductile shear zones (Fig. 2.4a; Brommecker, 1991, 1996; Anderson, 2013a). The map units identified as part of this study are largely consistent with previous subdivisions of the Bidou assemblage. Following the stratigraphic terminology of Campbell (1971), three formations are exposed within the map area: Tinney Lake, Dove Lake and Gunnar formations (Fig. 4b).

### 2.3.1 Bidou assemblage

#### 2.3.1.1 Tinney Lake formation

This formation is extensively exposed north of the North Carbonate shear zone (NCSZ) and east of the South Carbonate shear zone (SCSZ). It consists mainly of two units of mafic volcanic rocks (units 1 and 3) and two layers of sedimentary rocks (units 2 and 4). Pillows in mafic flows contain variable amounts of amygdales and exhibit variable degrees of flattening. Pillow cusps suggest younging to the south. The sedimentary rocks include feldspathic greywacke, locally interlayered with mudstone and pebbly conglomerate at the bottom. Normal tabular graded beds, crossbeds, scour surfaces and flame structures in this unit indicate younging to the south (Fig. 2.5a).

### *2.3.1.2 Dove Lake formation*

Rocks of the Dove Lake formation consist of mafic to intermediate crystal-lithic lapilli tuff with local interbeds of felsic tuff and lapilli tuff (unit 5; Fig. 2.5b). Campbell (1971) described primary structures, such as scour structures, load structures, flame structures, graded bedding and crossbedding, all indicating that the younging direction is towards the south.

### *2.3.1.3 Gunnar formation*

Pillowed basalt of the Gunnar formation (unit 6) is abundant and well exposed in the southern part of the map area. Pillows vary in size and strain, but commonly contain rounded to elongate carbonate-quartz amygdules, representing radial pipe vesicles. Pillow cusps and a higher concentration of amygdules in the upper portions of individual pillows indicate this unit youngs to the south (Fig. 2.5c).

## **2.3.2 Mafic intrusions**

Leucocratic and mesocratic gabbros (unit 7) typically have a spotted appearance and are medium-grained. Some leucocratic gabbro includes irregular-shaped pegmatitic pods with euhedral hornblende crystals up to 1 cm in size (Fig. 2.5d). Most of these intrusions occur as concordant sills; minor intrusions form discordant dikes. Amphibolite, peridotite and melanocratic gabbro of unit 8 typically consist of discordant dikes, some of which are localized along northwest-trending ductile shear zones near the Walton pluton, or along the South Carbonate Shear Zone south of Dove Lake (for the peridotite variety, see Scoates, 1971).

### **2.3.3 Quartz-feldspar porphyry dikes**

A few thin quartz-feldspar porphyry dikes strike westerly to northwesterly and dip very steeply. They contain saussuritized plagioclase, hornblende and minor quartz phenocrysts with fine-grained groundmass of plagioclase, hornblende and quartz.

## **2.4 Structural geology**

Five generations of ductile deformation structures as well as brittle faults have been recognized on the basis of overprinting relationships and fold styles at the outcrop scale in the vicinity of the Central Manitoba mine trend. Despite contrasting rock types, overprinting relations among the various deformation structures in the Bidou assemblage are consistent with those in the Ross River pluton. However, this paper is mostly concerned with deformation within the supracrustal rocks and associated gabbroic and feldspar ± quartz porphyry intrusions, which

are spatially associated with and structurally control gold mineralization in the Central Manitoba mine trend. The different generations of ductile deformation structures are termed  $G_1$  to  $G_5$ , and associated folds, foliations and lineations are termed  $F_1$  to  $F_5$ ,  $S_1$  to  $S_5$ , and  $L_1$  to  $L_5$ , respectively.  $F_5$  folds are rare and overprint  $F_4$  in a single shear zone so they are described with  $G_4$  structures. In addition, intersection lineations between bedding ( $S_0$ ) and  $S_1$  are termed  $L_{0-1}$ .

#### **2.4.1 First generation ( $G_1$ ) structures**

##### **2.4.1.1 Mesoscopic (outcrop-scale) structures**

Evidence for  $G_1$  deformation is well preserved in supracrustal rocks of the Bidou assemblage.

The  $S_1$  foliation is defined by a preferred orientation of quartz, feldspar and felsic clasts in felsic lapilli tuff (Fig. 2.5b), by flattened pillows and varioles in basalt (Figs. 2.7a and b), and by a continuous to closely-spaced slaty cleavage in feldspathic greywacke and mudstone (Fig. 2.7c).  $S_1$  foliation strikes westerly to northwesterly and dips steeply (mostly  $> 75^\circ$ ), or is vertical.  $S_1$  foliation dips more shallowly than bedding (Fig. 2.7c), and is usually at small angle ( $\sim 20^\circ$ ) clockwise to bedding ( $S_0$ ) on the horizontal surface through most of the study area. To the southeast of the Ross River pluton, finite strain increases toward high strain zones based on the aspect ratios of deformed basaltic pillows; the X/Z ratios range from 1:1 to 7:1 in the north (Fig. 2.7a), which is similar to the aspect ratios of the fragmented clasts in the Long Lake shear zone (Zwanzig, 1971).

The  $L_1$  lineation, developed on the  $S_1$  foliation, is defined by a preferred orientation of feldspar, quartz and elongate felsic clasts in lapilli tuff (Fig. 2.5b), and elongate varioles in basalt (Fig. 2.7b). The  $L_1$  lineation is best developed south of the Kitchener mine, and in small outcrops along the northern section of the South Carbonate Shear Zone. It plunges steeply (mostly  $> 80^\circ$ ) to the north or south (Fig. 2.6).

$F_1$  folds are rarely preserved. Isoclinal  $F_1$  folds with amplitude of approximately 10 cm occur within turbiditic feldspathic wacke beds southeast of the Walton mine. Their associated axial planar cleavage ( $S_1$ ) is continuous to very closely spaced (less than 1 mm), and typically dips steeply to the north. The  $F_1$  fold axes plunge moderately to the west, based on the orientation of the  $L_{0-1}$  intersection lineation (Fig. 2.6); however, some of the fold axes at hinge zones are doubly plunging (moderately west and east), indicative of a sheath fold geometry (Fig. 2.6c). In this outcrop, west-trending, greyish-white aplite dikes with heterogeneous

discontinuous smoky quartz segregations crosscut  $F_1$  folds indicating that the folds predate the emplacement of dikes (Figs. 2.6a and b).

#### *2.4.1.2 Macroscopic (district-scale to regional scale) $F_1$ folds*

The dominant structure in the southeastern Rice Lake greenstone belt is the northwest-trending, upright, doubly-plunging Beresford Lake anticlinorium (Figs. 2.1b and 2.2), which is defined by younging reversals and regional-scale map patterns of the Bidou, Gem and Edmunds assemblages (Stockwell and Lord, 1939; Brommecker, 1991, 1996; Anderson, 2013b). It has well-developed northwest-striking, very steeply dipping axial plane cleavage ( $S_1$ ), and plunges moderately to steeply to the southeast near Beresford Lake and shallowly to the northwest near Cliff Lake (Fig. 2.2) (Brommecker, 1996). The anticlinorium includes several district-scale, isoclinal to tight, parasitic synclines (Beresford Lake syncline; BLS in Fig. 2.2) and anticlines (Beresford Lake anticline; BLA in Figs. 1b and 2.2) (Stockwell and Lord, 1939; Brommecker, 1991, 1996). Similarities in deformation style and orientations of fabric elements suggest regional-scale BLA and associated district-scale folds are  $F_1$  folds. Regional studies reveal that the development of the BLA occurred concurrently with crustal thickening and sinistral transpression during collisional processes at ca. 2690 – 2680 Ma (Anderson, 2008, 2013a).

### **2.4.2 Second generation ( $G_2$ ) structures**

#### *2.4.2.1 Mesoscopic (outcrop-scale) structures*

Second generation ( $G_2$ ) structures are pervasive in sedimentary rocks around the Walton pluton and in plutonic rocks within the southeastern tongue of the Ross River pluton (RRP).  $S_2$  foliation and  $F_2$  folds were produced during the  $G_2$  ductile deformation process.

The  $S_2$  foliation is defined by closely spaced penetrative cleavage in mudstone, greywacke and pebbly conglomerate west of the SCSZ, and by aligned tabular plagioclase, elongate biotite/hornblende and ellipsoid quartz aggregates in porphyritic intrusive phases of the RRP.  $S_2$  foliation dips steeply to moderately to the southeast or northwest (Fig. 2.8).  $S_2$  foliation is at a moderate to high angle to  $S_1$  foliation in sedimentary rocks west of SCSZ.

The  $F_2$  folds are rarely preserved. One example is a close to open symmetric fold, with a well-developed axial plane cleavage ( $S_2$ ). The  $F_2$  fold axis plunges moderately ( $\sim 45^\circ$ ) to the southeast (Fig. 2.8). As shown in Figure 6a, an aplite dike cuts across the  $F_2$  fold without discernible deformation, which indicates this aplite dike postdates  $F_2$  folding in this location.

We've separated  $G_1$  and  $G_2$  structures on the mesoscopic scale exclusively based on local

overprinting fold style (Fig. 2.6a) and change of orientation. It is also possible that  $S_2$  foliation described above could be re-oriented  $S_1$  foliation that was caused by a later folding event associated with shear zone development. This alternative interpretation is less likely when two cleavages  $S_1$  and  $S_2$  are planar and through-going on an outcrop of greywacke, and no discernible shear zone is close to the outcrop. Shear zones we've recognized are typically less than 1 m thick and their influence on early fabric typically does not extend far from the margin of the shear zone.

#### *2.4.2.2 Macroscopic $F_2$ fold*

The map pattern and younging directions of the sedimentary unit around the Walton stock define a macroscopic  $F_2$  fold, here referred to as the Walton fold (Fig. 2.3). It has been mapped by previous workers (Stockwell and Lord, 1939) and supported by this study. It is open, symmetric, with well-developed axial plane cleavage ( $S_2$ ) that strikes northeast. Its fold axis plunges moderately to the southwest as indicated by outcrop-scale parasitic folds.

### **2.4.3 Third generation ( $G_3$ ) structures**

#### *2.4.3.1 Mesoscopic structures*

$G_3$  structures comprise steeply-dipping discrete brittle-ductile shear zones. They can be divided into two groups on the basis of orientation and kinematics: southwest to west-northwest-trending sinistral ( $G_{3a}$ ), and northwest to north-trending dextral ( $G_{3b}$ ) (Figs. 2.9, 2.10, 2.11, 2.12). These shear zones are mainly observed in gabbro, and locally in massive basalt, greywacke and quartz feldspar porphyry dikes. The wide range of the orientations of  $G_{3a}$  shear zones is due to refraction or competency contrast of these rock units. Within  $G_3$  brittle-ductile shear zones, modal proportion of zoisite (plagioclase alteration product) and carbonate increases significantly whereas modal proportion of actinolite and chlorite decreases dramatically. S-C fabric, shear bands, asymmetric folds are well developed and are used to determine bulk shear zone kinematics. The two groups of  $G_3$  shear zones are interpreted as conjugate sets on the basis of similar mineralogy and kinematics, as well as close spatial relations. Direct outcrop evidence was also observed to support that they were kinematically-related conjugate sets (Fig. 2.11).

Southwest to west-striking, steeply dipping, discrete  $G_{3a}$  brittle-ductile shear zones range from several centimetres to two metres in thickness; they extend several or tens of metres along strike (Fig. 2.9). The shear zones are defined by well-foliated fine-grained mylonites. Two distinct types of secondary foliation are well developed: mylonitic foliation (“S surfaces”; Berthé

et al., 1979) and shear foliation (“C surfaces”; Berthé et al., 1979). The mylonitic foliation ( $S_3$  foliation) is defined by continuous compositional layers of actinolite alternating with those of plagioclase and carbonate. The shear foliation ( $C_3$  foliation) is defined by spaced shear fractures, or second-order shear zones that constitute smaller-scale shear fractures that contain alternating compositional layers. Outside the shear zones, rocks are significantly less deformed (Fig. 2.9b). The transition from shear zones to less deformed country rocks is typically gradational. The mylonitic foliation is defined by parallelism of coarse-grained ellipsoidal aggregates of actinolite and/or chlorite, elongate plagioclase and carbonate aggregates, and gradually transitions into continuous thin compositional layering within shear zones, indicating strain increases gradationally from country rock to shear zone (Fig. 2.9c). Mylonitic foliation along the margins of the shear zones is typically oriented at a moderate to high angle to shear zone boundaries, and curves smoothly into shear foliation in the core. The angular relationship between S/C foliation and deflected S foliation indicate a sinistral component of shear displacement on horizontal surfaces (Fig. 2.9d).

Chevron folds and drag folds (Fig. 2.9e) are also present within  $G_{3a}$  high-strain zones. Their axial plane cleavage is typically west-trending, steeply dipping, and the amplitude of these folds is typically tens of centimetres. Clearly the folding postdates the formation of the mylonitic foliation. The S-shaped fold asymmetry suggest a sinistral sense of shear.

$G_{3b}$  structures comprise northwest-to-north-trending dextral brittle-ductile shear zones in gabbroic intrusions (Fig. 2.10) and basalt. They are usually approximately half a metre thick in gabbroic intrusion and several centimetres thick in basalt. Steeply dipping mylonitic and shear foliations define these shear zones (Figs. 2.10a, b, c and d). Narrow synthetic shear bands ( $C'$ -type foliation, Berthé et al., 1979; or extensional crenulation cleavage, Platt and Vissers, 1980) and sigmoidal shear-bounded lozenges (Bell and Rubenach, 1980; Bell, 1981; Ponce et al., 2013) are also present (Figs. 2.10a, c). The deflection of the foliation at the confluence or intersection between mylonitic and shear foliations, shear bands or sigmoidal lozenges consistently indicate dextral shear.

The southwest to west-northwest-trending sinistral discrete ( $G_{3a}$ ) ductile shear zones and northwest-to-west-trending ( $G_{3b}$ ) dextral ones are truly conjugate sets, as evidenced at one outcrop of intrusion breccia (Figs. 2.11a, b, c and d). The host quartz feldspar porphyry contains several angular to subangular mafic xenoliths (Fig. 2.11b). Narrow subvertical shear zones are

typically one to three centimetres thick, and extend along strike up to 1.5 metres. They are developed only locally along the margins of the xenoliths. Mylonitic foliation is defined by elongate chlorite and/or actinolite lamination within shear zones, and is at  $\sim 30^\circ$  to the shear zone boundaries (Fig. 2.11c). Kinematic interpretation of individual shear zones is made on the basis of mylonitic foliation deflection and angular relationship between foliation and shear zone boundary (Fig. 2.11c). Since these shear zones are localized at sparsely spaced incompetent mafic xenolith margins, they cannot be as continuous and merge together as classic conjugate ductile shear zones within homogeneous isotropic host rocks.

#### *2.4.3.2 Macroscopic structures*

Based on the similar deformation style, orientation and kinematics, the G<sub>3</sub> shear zones are correlated with the regional-scale Wanipigow shear zone to the north and the South Garner shear zone to the south (Fig. 2.1b). They are interpreted to have developed during continued belt-scale sinistral transpressional collisional processes (Anderson, 2008, 2013b).

### **2.4.4 Fourth generation (G<sub>4</sub>) structures with rare F<sub>5</sub> fold**

#### *2.4.4.1 Mesoscopic structures*

G<sub>4</sub> structures are defined by northwest-to-southwest-trending, steeply-dipping to subvertical, dextral brittle-ductile and ductile shear zones that are localized within and slightly discordant to lithologic boundaries of the lower feldspathic wacke layer (unit 2), pillowed and massive basalt (unit 3) and the lower gabbroic sill (unit 5), or occur entirely within gabbroic intrusions (Fig. 2.13). The wide orientation range of G<sub>4</sub> shear zones is due to refraction or competency contrast of various host rocks. They are typically half a metre to two metres thick, and extend up to approximately two kilometres along strike. G<sub>4</sub> brittle-ductile and ductile shear zones host the major auriferous quartz veins in the mine trend. Compared to G<sub>3</sub> shear zones, the G<sub>4</sub> shear zones are rich in chlorite (Fig. 2.9b). G<sub>4</sub> shear zones are kinematically different from G<sub>3</sub> shear zones, even though they share identical orientations in some cases.

The structures within G<sub>4</sub> brittle-ductile shear zones are complex and record multiphase deformation. One example of this is illustrated in Fig. 2.13a. Mylonitic foliation is well developed and defined by compositional layers of actinolite and/or chlorite alternating with layers of plagioclase and carbonate. Two generations of folds (F<sub>4</sub> and F<sub>5</sub>) with short wavelengths were recognized. F<sub>4</sub> folds are isoclinal upright folds that fold the mylonitic foliation, and F<sub>4</sub> folds are clearly overprinted by F<sub>5</sub> tight or gentle upright folds (Fig. 2.13b). C'-type shear band

cleavage and  $\sigma$ -porphyroclasts indicate dextral sense of shear on horizontal observation planes (Fig. 2.13c).

Southwest-to-west-trending G<sub>4</sub> dextral shear zones locally have close spatial relationships to southwest-to-west-trending G<sub>3</sub> sinistral ones. The outcrop in Fig. 2.9a illustrates G<sub>3</sub> and G<sub>4</sub> shear zones are in contact with each other, but distinctly different in composition, structure and kinematics. G<sub>4</sub> shear zones are relatively rich in actinolite and chlorite. S/C fabric and shear out porphyry dike boudins in G<sub>4</sub> shear zones indicate a dextral sense of shear on the subhorizontal surface (Fig. 14a). Ridge-in-groove slickenside L<sub>4</sub> striation (Means, 1987; Will and Wilson, 1989; Lin and Williams, 1992) on the curviplanar shear foliation (C foliation) plunges moderately ( $\sim 45^\circ$ ) to the east (Fig. 2.14b). It is interpreted that the shear direction is along the ductile slickenside striation developed on the C foliation (e.g., Lin et al., 2007). Therefore, the kinematics of this G<sub>4</sub> ductile shear zone includes components of south-side-up dip-slip and dextral strike-slip movement.

A feldspar ( $\pm$ quartz) porphyry dike with two branches is boudinaged in the G<sub>4</sub> shear zone and the adjacent less-deformed leucocratic gabbroic intrusion (Fig. 2.9a), indicating the felsic dike was more competent than the altered and foliated mafic intrusion during deformation. A weak to moderate penetrative continuous foliation within this feldspar ( $\pm$  quartz) porphyry is defined by a preferred orientation of elongate hornblende and tabular plagioclase. Since this foliation is subparallel to the mylonitic foliation in adjacent G<sub>4</sub> shear zones with slight refraction, it is interpreted to be S<sub>4</sub> foliation (Fig. 2.9a). The bulk extension direction of feldspar ( $\pm$  quartz) porphyry boudins is subparallel to the S<sub>4</sub> foliation, which indicates that the formation of the boudins was probably before or during the early G<sub>4</sub> ductile dextral shearing process. The bulk shortening direction is interpreted to be north-northwest-trending, perpendicular to the S<sub>4</sub> foliation and the bulk extension direction of boudinaged feldspar ( $\pm$  quartz) porphyry.

Auriferous fault-fill veins at the Kitchener mine were previously described as being hosted in a west-trending sinistral ductile shear zone, whereas gold-bearing veins at the Hope mine were described as being hosted in a west-trending dextral shear zone (Brommecker, 1991, 1996; Poulsen et al., 1996). Kinematic interpretation was based on S-shaped folds in the shear zone (Brommecker, 1991, 1996; Poulsen et al., 1996). Drag-folds or rolls were described by Stockwell and Lord (1939). They documented kinematically contradictory drag-folds in the western and eastern portions of this shear zone. These seemingly contradictory explanations probably result

from the fact that west-trending sinistral and dextral ductile shear zones are locally in contact with each other, and they share identical orientations but dextral ones postdate sinistral ones (e.g., Figs. 2.9a and b).

#### *2.4.4.2 Macroscopic structures*

The G<sub>4</sub> dextral shear zones are the latest ductile deformation structures, which are also commonly present in the other areas in the Rice Lake greenstone belt. The North Carbonate and South Carbonate shear zones (Fig. 2.2) are also interpreted as G<sub>4</sub> structures, since they share similar deformation style and kinematics. Other type examples are the regional-scale dextral Manigotagan shear zone, Beresford Lake shear zone and Long Lake shear zone (Fig. 2.2). These macroscopic structures are interpreted to have formed during belt-scale terminal dextral transpressional collision (Anderson, 2013b).

## **2.5 Vein system**

Veins of different types and orientations are distributed heterogeneously throughout the Central Manitoba mine trend. They often exhibit intimate spatial relationships with G<sub>3</sub> and G<sub>4</sub> brittle-ductile shear zones. Ore bodies were associated with quartz veins and highly altered and strongly deformed supracrustal and mafic intrusive rocks near the quartz veins (Figs. 2.4b and 2.15). To elucidate the sequence of vein growth and deformation, we investigated field relations and internal textures of differing veins, with emphasis on spatial and temporal relations with associated brittle-ductile shear zones. We also conducted detailed work on the ore texture of various vein-forming minerals at scales of hand specimen and polished thin sections to establish mineral depositional sequence associated with gold mineralization.

### ***2.5.1 Vein type and field relations***

Based on geometry, internal textures, and geometric relationship to associated shear zones, veins can be classified into three main types: fault-fill, extension (oblique-extension) and breccia veins (Hodgson, 1989; Robert et al., 1994; Robert and Poulsen, 2001). In the study area, all three types of veins have been recognized, and are intimately spatially associated with G<sub>3</sub> and G<sub>4</sub> brittle-ductile shear zones. En echelon veins are the most common vein arrays in the study area. No stockwork veins or sheeted veins have been recognized. All vein types and vein arrays are described firstly in the sense of “structural timing” (Robert and Poulsen, 2001), i.e., temporal relationships with associated shear zones. Relative timing of veins within one single generation

deformation structure is further established in terms of crosscutting relationship.

#### 2.5.1.1 $G_3$ -related veins

$G_3$ -related veins, termed  $V_1$  veins, are mostly lenticular massive or laminated fault-fill veins and planar to sigmoidal en echelon extension veins. They are spatially associated with steeply-dipping  $G_3$  brittle-ductile shear fractures or dextral ductile shear zones. The former are termed  $V_{1a}$  and the latter  $V_{1b}$ . Relative timing of  $V_{1a}$  and  $V_{1b}$  sets has not been directly established because no crosscutting relationship between these two vein sets has been observed. They were most likely penecontemporaneously emplaced during  $G_3$  shearing. These veins are seldom reported in previous studies, probably due to their relatively low gold grades (e.g., 85–96 ppb).

Figs. 2.16a and b illustrate an example of  $V_{1a}$  association of a central fault-fill vein and en echelon arrays of extension veins in mafic intrusions. Host rocks are mainly coarse-grained equigranular leucocratic to mesocratic gabbroic rocks with sparse pegmatitic dioritic pods, appearing little deformed at the outcrop scale. Both the central fault-fill vein and tension gashes consist primarily of milky white blocky quartz, locally euhedral tourmaline, with fine-grained chlorite-rich slivers or pods. Minor portions of the vein exhibit a spotted smoky grey appearance. The vertical central fault-fill vein strikes north, and tension gashes strike north-northeast ( $\sim 20\text{--}45^\circ$ ), and merge with the central vein. Tension gashes on the eastern side of the central vein are curviplanar and long, oriented at a moderate angle ( $\sim 40\text{--}50^\circ$ ) to the central vein; whereas on the western side they are sigmoidal, shorter, and the lateral tips are oriented at a small angle ( $\sim 10\text{--}15^\circ$ ) to the central vein. Several models have been proposed for strain analysis on geometrical evolution of en echelon vein arrays (e.g., Beach, 1975; Ramsay and Huber, 1983; Olson and Pollard, 1991; Lisle, 2013). Recent two-dimensional modelling (e.g., Lisle, 2013) indicates that curved sigmoidal tension gashes accommodate more shear strain and volume increase compared to planar ones. Altered leucogabbro west of the central vein accommodates more strain, probably because it is less competent due to heterogeneous composition or alteration intensity compared to wallrock east of the central vein. However, since sigmoidal and planar tension gashes merge with the central fault-fill vein, they must have formed synchronously.

$V_{1b}$  sets are hosted by north-northwest-to-north-trending subvertical  $G_3$  dextral ductile shear zones (Fig. 2.16c). They are commonly grey blocky massive quartz lenses with a width up to 10 cm and a length of tens of centimetres. They are seldom continuous, and commonly pinch and swell along shear foliation within ductile shear zones (Fig. 2.10a). They were probably emplaced

before or during early G<sub>3</sub> shearing. Minor white blocky extension veinlets are also commonly present in shear-bounded lozenges within ductile shear zones, and cut the mylonitic foliation at moderate angles (Fig. 2.16c), suggesting they postdate some G<sub>3</sub> deformation increments. However, these extension veinlets are still compatible with bulk shear zone kinematics, indicating they were formed during late G<sub>3</sub> progressive deformation.

A few V<sub>1b</sub> extension veins are situated in competent quartz feldspar porphyry, and also crosscut one of the xenoliths (Fig. 2.11a). Vein filling minerals are predominantly quartz with subordinate tourmaline and chlorite. Quartz typically exhibits a comb texture within veins. The preferred orientation of euhedral quartz crystals is at a very high angle or orthogonal to the wall rock boundaries (Fig. 2.11d). Euhedral quartz terminations in these veins and absence of crack-seal texture (Ramsay, 1980) indicate the opening direction of the tensile fractures is almost perpendicular to the wallrock, and the tensile fractures remained open under effective stress (Hubbert and Rubey, 1959) with the aid of hydrothermal fluid pressure. Therefore, these veins are interpreted as extension veins with a dominant boundary-normal opening component and negligible shear (Poulsen and Robert, 1989; Lafrance, 2004). These extension veins indicate the maximum principal stress was north– to north-northeast–trending at the time of vein emplacement, which is kinematically compatible with relative movement of G<sub>3a</sub> (①②③⑥⑦ in Fig. 2.11a) and G<sub>3b</sub> shear zone (④⑤⑧⑨ in Fig. 2.11a) conjugate sets. Therefore, these extension veins are interpreted to have emplaced during G<sub>3</sub> shearing.

#### 2.5.1.2 G<sub>4</sub>-related veins

G<sub>4</sub>-related veins are mostly west-trending curviplanar through-going fault-fill veins, termed V<sub>2</sub> with local breccia veins or isolated vein lenses, hosted in G<sub>4</sub> dextral ductile shear zones in the vicinity of the contacts between the lower greywacke, basalt and gabbroic sills of the Tinney Lake formation. Auriferous V<sub>2</sub> quartz veins typically extend ~ 500–800 metres along strike and are up to 0.5 metres in thickness. Ore bodies hosted by these veins extended as deep as ~140 metres at the Kitchener mine based on descriptions of underground workings by Stockwell and Lord (1939) (Fig. 2.15b). Outside the G<sub>4</sub> shear zones, the host rocks are commonly less altered, and contain primary structures (i.e., bedding). Wallrock blocks within veins in shear zones are typically ductilely deformed and sericite-altered greywacke (Fig. 2.17a). A few of these greywacke inclusions in veins contain a wavy cleavage (Fig. 2.17a, b). Quartz boudins and S-C fabric in altered greywacke at vein margins indicate a sense of dextral shearing (Fig. 2.17b).

Since some altered greywacke inclusions in the quartz veins have undergone various degrees of ductile deformation, it is interpreted that V<sub>2</sub> vein emplacement at least postdated some increments of shearing; otherwise, all altered greywacke inclusions would have experienced less pervasive strain because surrounding vein material would have protected them from post-veining shearing. Combined with evidence for post-veining shearing in altered wallrocks and the presence of ridge-in-groove slickenside striations overprinted on vein margins, it is interpreted that V<sub>2</sub> veins were likely emplaced during G<sub>4</sub> shearing.

Hydrothermal alteration halos are typically asymmetric adjacent to V<sub>2</sub> veins: basalt contains much thicker halos than greywacke (Fig. 2.18a and b). In altered basalt, mafic minerals are mostly altered to chlorite and plagioclase phenocrysts are saussuritized, whereas in altered greywacke primary sedimentary structures and textures are completely destroyed, replaced by pervasive alteration minerals and penetrative foliation defined by sericite and minor chlorite (Fig. 2.21a).

V<sub>3</sub> veinlets are typically milky white, thin (< 10 cm thick) and barren. They often display euhedral quartz crystals and internal comb structure, and are thus interpreted as extension veins (Fig. 2.19a).

Crosscutting relationships among V<sub>1</sub>, V<sub>2</sub> and V<sub>3</sub> sets are evident in the field. One north-trending V<sub>1a</sub> vein can be traced along strike for approximately 50 metres and curves into a west-trending vertically-dipping G<sub>4</sub> ductile shear zone, and is cut by a V<sub>2</sub> fault-fill vein. This V<sub>2</sub> vein is cut by north-trending V<sub>3</sub> extension veinlets with comb structures (Fig. 2.19a). V<sub>1</sub> veins are short-wavelength folded within west-trending G<sub>4</sub> ductile shear zones (Fig. 2.19b). Early V<sub>2</sub> fault-fill veins are locally boudinaged, subparallel to S<sub>4</sub> foliation in G<sub>4</sub> ductile shear zones (Fig. 2.19b). It is interpreted that both V<sub>2</sub> and V<sub>3</sub> sets formed during G<sub>4</sub> dextral transpressional shearing: V<sub>2</sub> were emplaced during early dextral boundary-parallel shearing, whereas V<sub>3</sub> extension veinlets were emplaced relatively late during shearing with a dominant boundary-normal component. It is also interpreted that V<sub>1</sub> veins were folded and V<sub>2</sub> veins were boudinaged during late G<sub>4</sub> shearing as well. Another possible explanation is that both V<sub>1</sub> and early V<sub>2</sub> veins were emplaced during G<sub>3</sub>, then deformed during G<sub>4</sub>; gold mineralization could have been decoupled with host vein emplacement (e.g., Lin and Corfu, 2002).

### **2.5.2 Vein mineralogy, microstructure and paragenesis**

Textures and relative temporal relationships of vein and alteration minerals were examined

in over 150 hand specimens, 70 cut slabs, and 40 polished thin sections. Mineral identification was mainly carried out through conventional transmitted and reflected light microscopy, and aided by scanning electron microscope (SEM) analysis. Most of the polished thin sections were cut perpendicular to the mylonitic foliation and parallel to the ridge-in-groove slickenlines of shear zones for the purpose of kinematic analysis. A few sections were cut orthogonal to both foliation and lineation, or parallel to both foliation and lineation, in order to facilitate three-dimensional structural analysis.

High grade gold-bearing quartz veins in the Central Manitoba mine trend are mainly west-trending subvertical V<sub>2</sub> veins hosted by G<sub>4</sub> ductile shear zones, either in contact zones of basalt, lower greywacke and gabbro (Figs. 2.15a, 2.20a), or in gabbro closely north of contact zones (Fig. 2.15a, 2.20b). A few V<sub>1a</sub> veins, e.g. the central fault-fill vein and en echelon vein arrays in Fig. 2.16a, yield low, but anomalous, gold grades (85–96 ppb). Even within V<sub>2</sub> veins, gold is heterogeneously distributed, as indicated by gold assay results (Fig. 2.20) and underground milled bodies (Fig. 2.15b). Textural relationships among different vein-filling minerals are examined in detail to establish spatial and temporal relationships among quartz, alteration minerals, sulfide minerals and gold. Deformation at the microscopic scale is also considered to help constrain structural timing of gold mineralization compared to mesoscopic structures described above. Since V<sub>1</sub> and V<sub>3</sub> sets are barren or of very low grade, we focus on auriferous V<sub>2</sub> sets.

#### 2.5.2.1 V<sub>2</sub> mineralogy and microstructure

V<sub>2</sub> veins are homogeneous in mineral assemblage, habit and internal texture, but variable in mineral composition and modal proportion. They typically consist of over 85% grey or clear quartz, ~ 5% metallic sulfides and associated oxides, and ~ 10% micaceous minerals such as chlorite and sericite. They are commonly homogeneous and mesoscopically massive without ribbon or fibrous texture. Sulfides are attached to chlorite and large quartz-vein boudins, defining the foliation in ductile shear zones (Fig. 2.21a). We describe V<sub>2</sub> mineralogy in a chronologic order of mineral deposition.

*Quartz:* These mineral grains can be classified into three main types on basis of crystal shape, grain size and optical axis orientation. Type-I quartz grains are typically one to three millimetres in diameter, and have tabular to trapezoid euhedral crystal shapes (Figs. 2.22a, b and c). They account for an insignificant modal proportion in veins, compared to dominant type-II

and type-III recrystallized grains. Type-I quartz grains exhibit a shape preferred orientation at a moderate angle ( $\sim 30^\circ$ – $60^\circ$ ) to vein margins. The euhedral crystal habit indicates that the hydrothermal fluids crystallized slowly. Grain boundaries are sharp and clear; overall polygonal, but locally lobate with smaller-sized ( $< 30 \mu\text{m}$ ) new grains, which are characteristic of bulging recrystallization (Stipp et al., 2002; Passchier and Trouw, 2005). Most grains display patchy undulose extinction, indicating existence of elongate sub-grains. Boundaries between sub-grains are curvilinear, gradational or vague. Most large quartz grains are rich in fluid inclusions as well. Chlorite, pyrite and chalcopyrite commonly infill quartz grain boundaries or fractures.

Type-II quartz grains are commonly one to two millimetres in diameter and typically display sweeping chessboard undulose extinction (Fig. 2.22d and e). They are commonly completely surrounded by new dynamically recrystallized ( $< 100 \mu\text{m}$ ) grains. Transitions from old to new grains is gradual and less abrupt, which is typical of sub-grain rotation recrystallization (Passchier and Trouw, 2005). Sub-grains are typically flattened, and their aggregates exhibit a domain shape preferred orientation that defines a continuous foliation in a few samples. This foliation is almost orthogonal to the adjacent healed fracture with pyrite-chalcopyrite aggregates (Fig. 2.22d).

Type-III quartz grains are mostly elongate or equant grains that predominantly range from  $20 \mu\text{m}$  to  $50 \mu\text{m}$ , but can be up to  $100 \mu\text{m}$ . Undulose extinction is common, but for a few grains extinction is homogeneous. They usually have clear lobate irregular grain boundaries, but are also surrounded or encompassed by old large grains. In a few samples, quartz (and sericite) is finer grained ( $< 20 \mu\text{m}$ ) in healed fractures (Fig. 2.22d). Elongate quartz and sericite grains define a continuous foliation at an acute angle to zone boundaries, indicating a sinistral sense of shear, as in the north-trending healed fracture shown in Fig. 2.22d. It is interpreted that formation of this sub-grain aggregate foliation in type-II quartz aggregates was probably concurrent with the dilation of the adjacent fracture zone, and this filled fracture zone was dynamically recrystallized in sinistral shearing to form type-III quartz grains. This micro-scale north-trending sinistral shear zone locally postdates V<sub>2</sub> quartz veinlet formation and G<sub>4</sub> dextral shearing along east-west strike, but might be a conjugate branch to west-striking G<sub>4</sub> dextral shear zones.

*Chlorite:* These mineral grains are euhedral to subhedral or acicular, typically less than 2 mm in diameter. Most occur in small patches (hundreds of microns in diameter) sparsely distributed in alteration envelopes and quartz veins. They are typically interstitial to sericite,

zoisite, quartz, pyrite and chalcopyrite (Fig. 2.21b and c). A few chlorite grains occur as elongate grain aggregates attached to or surrounding lens-shaped aggregates of pyrite-chalcopyrite-quartz in strongly deformed alteration envelopes, defining a prominent continuous foliation (Fig. 2.21a). Some chlorite grains enclose anhedral chalcopyrite and subhedral pyrite inclusions (< 50 µm). A few acicular chlorite grains form inclusions in chalcopyrite. And some chlorite aggregates are enclosed by large euhedral quartz grains or small dynamically recrystallised quartz grains. Chlorite grains in-fill fractures together with sericite, pyrite, chalcopyrite and goethite.

*Sericite*: Flakes of this mineral are pervasive throughout altered wallrock greywacke and are also common, but to a much lesser extent, in quartz veins. Sericite either forms aggregates that define a continuous foliation in altered greywacke, or occurs as small discontinuous patches associated with chlorite, pyrite and chalcopyrite aggregates, commonly concentrated on the margins of quartz veins (Fig. 2.22b and d).

*Pyrite*: This mineral can be grouped into three main types in terms of habit, occurrence and spatial relationship with other minerals. Type-I pyrite occurs in altered greywacke immediately adjacent to quartz veins. It is typically ~ 0.5 mm in diameter, characterized by colloform texture (Fig. 2.23a). Each band within pyrite is ~ 1–5 µm thick, bounded by rusty dark wavy material. This colloform texture is interpreted as direct crystallization from ore-forming fluids during periodic change of physico-chemical conditions (Barrie et al., 2009). Type-I pyrite is mostly irregular-shaped, and has clean non-banded pyrite rims, which are interpreted to result from partial replacement of colloform pyrite. It is usually attached to and surrounded by irregular chalcopyrite, clean pyrite, acicular radiating chlorite and sericite aggregates, and quartz. Minor chalcopyrite-pyrite aggregates enclosed by colloform pyrite are interpreted as a cut effect in the polished thin section.

Type-II pyrite typically occurs as euhedral to subhedral individual grains or grain aggregates and is characterized by numerous randomly-oriented chalcopyrite, chlorite and quartz inclusions (Fig. 2.23b). Grain size ranges from tens of microns to two millimetres. They are closely spatially associated with quartz boudins in altered greywacke, and have a shape preferred orientation parallel to the external chlorite-sericite foliation.

Type-III pyrite commonly occurs as irregular patches that are intimately associated with irregular chalcopyrite. Mineral grains are subhedral to anhedral, and can be up to several

millimetres in diameter. They define a continuous foliation together with chalcopyrite, ellipsoid quartz aggregates and stretched chlorite (Figs. 2.21a, 2.23c and d) in altered greywacke. They also occur in veins as irregular-shaped aggregates attached to chalcopyrite, chlorite, quartz, bismuthinite and bismite (Fig. 2.23e). Some grains contain randomly-oriented inclusions of chlorite, quartz, chalcopyrite, pyrrhotite, bismuthinite and bismite (Fig. 2.23f).

*Chalcopyrite*: This mineral is the predominant sulfide mineral within alteration zones and quartz veins. It is often anhedral, and interstitial to chlorite and quartz. It is also in contact with type-III pyrite, pyrrhotite, bismuthinite, bismite, sericite and quartz. It is present as inclusions within type-II and type-III poikiloblastic pyrite grains, and also contains minor chlorite, quartz, bismuthinite and bismite inclusions within quartz veins (Fig. 2.23e). It also fills in fractures with pyrite, sericite and dynamically recrystallised quartz (Q III) (Fig. 2.22e).

*Pyrrhotite*: This mineral commonly occurs as irregular patches together with chalcopyrite. It is often subhedral to anhedral, and tens of microns to several millimetres in diameter. It is interstitial to quartz, chlorite and sericite in quartz veins. Minor pyrrhotite also occurs as inclusions in pyrite (Xue, 2011). Pyrrhotite is intimately associated with chalcopyrite, tellurobismuthite and gold in high grade auriferous quartz veins hosted by gabbro (Xue, 2011).

*Bismuth-bearing minerals*: Bismuth-bearing minerals typically occur as small tabular or irregular grains interstitial to quartz in veins. They are commonly attached to chalcopyrite, pyrite and quartz. They are also present as subhedral grains encompassed by pyrite (Fig. 2.23f), or as sub-rounded to irregular inclusions in chalcopyrite (Fig. 2.23e). Bismuthinite is partially or completely replaced by bismite, which is typical of secondary oxidation of bismuth minerals (Fig. 2.23f). Native bismuth is also present in high grade auriferous quartz veins (Fig. 2.23f; Xue, 2011). Tellurobismuthite typically occurs as small grains in contact with quartz and pyrrhotite, and is spatially associated with gold (Xue, 2011).

*Gold*: Native gold typically forms gold-silver alloy (electrum) with an Au-Ag ratio that averages 11, but ranges from 23 to 0.44 (Xue, 2011). Gold occurs as free grains (10–300 µm) interstitial to quartz and pyrrhotite, or in contact with pyrrhotite (Xue, 2011). Gold is also closely spatially associated with chalcopyrite and tellurobismuthite (Xue, 2011).

*Goethite*: This mineral is the secondary oxidation product of iron-bearing sulfides, especially pyrite. It partially or completely replaces pyrite along cleavages or fractures within individual pyrite grains, or as rims along pyrite grain boundaries.

### 2.5.2.2 $V_2$ paragenesis

Although mineral assemblages and their proportions are variable, textural and chronologic relationships between vein minerals are consistent throughout the Central Manitoba mine trend. The depositional sequence of various minerals can be divided into two stages: a primary infill stage during which mineral deposition took place during one or several episodes of open-space filling, and a post-filling stage of deformation and quartz recrystallization, followed by fracturing and deposition of late chalcopyrite. Oxidation of bismuth-bearing and iron-bearing sulfides took place latest.

During the initial open-space filling stage, euhedral type-I quartz was deposited together with chlorite and sericite along vein margins. Colloform type-I pyrite in greywacke was also enclosed during this stage. Poikilitic pyrite of type-II grew after with randomly-oriented chalcopyrite, quartz and chlorite inclusions. Colloform type-I pyrite was also replaced by type-II pyrite and chalcopyrite during this stage. Irregular patches of chalcopyrite and pyrrhotite were deposited afterwards. Gold, tellurobismuthite, bismuthinite and other bismuth-bearing minerals were introduced with pyrrhotite during this stage. Type-III pyrite and chalcopyrite were deposited after surrounding chlorite and sericite, since type-III pyrite and chalcopyrite enclose chlorite and sericite. Type-III pyrite and chalcopyrite were crystallised after some pyrrhotite and bismuth-bearing minerals were deposited because they also enclose some pyrrhotite and bismuthinite.

At the post-filling stage, quartz vein and associated minerals underwent intense  $G_4$  ductile deformation, causing undulose extinction in euhedral quartz grains. Some equant to elongate sub-grains grade laterally into recrystallised grains. Quartz-pyrite-chalcopyrite veinlets in altered greywacke were boudinaged during  $G_4$  dextral shear, parallel to the continuous foliation defined by sericite and chlorite.

## 2.6 Discussion

### 2.6.1 Stratigraphic setting of gold mineralization

There are only a few examples of Archean lode gold deposits that are entirely hosted or intimately associated with clastic metasedimentary rocks (Colvine et al., 1988), as at Hemlo (Muir, 1983; Burk et al., 1986; Lin, 2001), Geraldton (Macdonald, 1983), Timmins (Walsh et al., 1986), and Contwoyto Lake (Kerswill, 1986), etc. Some lithologic associations, such as iron-rich

metasedimentary rafts within differentiated gabbroic sills, are especially favorable hosts for gold mineralization due to their combined iron-rich and competent nature (Robert et al., 2005). This is similar to the case in the Central Manitoba mine trend in terms of the lithologic association of diagenetic pyrite-rich greywacke and adjacent gabbro.

## **2.6.2 Structural control of ore shoots**

### *2.6.2.1 Lithology competency and deformation manner*

As discussed in the section dealing with the stratigraphic setting of gold mineralization, vein emplacement may favor structurally more competent rocks where a strong competency contrast exists between adjacent lithologies (e.g., Colvine et al., 1988). This competency contrast may result from primary compositional differences (e.g., syenite more competent than sedimentary rocks, Young Davidson mine; Zhang et al., 2014), or may result from secondary alteration processes (e.g., metasomatic ankerite-rich units more competent than surrounding rocks, Cochenour-Willans mine; Sanborn-Barrie, 1987). However, for the Central Manitoba mine trend, auriferous quartz veins are predominantly hosted by ductile shear zones, which occur at or near altered contacts of basalt, greywacke and gabbro, as well as within the gabbro, suggesting anisotropy reactivation on contact zones of primary competency contrast was a significant control on shear zone development and vein emplacement. Strain was partitioned along primary planes of weakness (i.e., contact zones) during later deformation within an optimally-oriented kinematic frame. Brittle shears or brittle-ductile shear zones do host minor extension veins in the more competent gabbro, but these are mostly barren. Considering the extensive and pronounced sericite and chlorite alteration zones along high grade mineralized veins, we believe that textural destruction and compositional change due to phyllosilicate alteration along precursor faults, dramatically weakened the more competent gabbro allowing for the development of ductile shear zones.

### *2.6.2.2 Local structural control*

As shown in Figs. 15 and 24, auriferous quartz veins mainly occur within sheared and altered contacts between greywacke, basalt and gabbro intrusions, or entirely within gabbro. Based on longitudinal sections of underground workings (Fig. 2.15b), the major ore bodies were shallowly plunging and did not have much depth extent, although quartz veins do continue to greater depths (Stockwell and Lord, 1939).

The shallowly plunging ore shoots (Fig. 2.15b) are subparallel to shallowly to moderately

plunging slickenlines on the vein margins and ridge-in-groove slickenside striations in host shear zones. This is unlike most other lode gold deposits in the southern Archean Superior Province, where ore shoots are typically aligned at a high angle or perpendicular to the movement direction of host shear zones (e.g., Poulsen and Robert, 1989). However, it is concurrent with quite a few greenstone gold deposits in southern Africa and Western Australia, where ore shoots are typically parallel to mineral elongation lineation and slip direction of host shear zones (e.g. Vearncombe et al., 1989). The shallow plunge of ore zones could be explained by vertical extension and the associated boudinage of the veins and gold remobilization into low strain domains along the veins, and/or gold remobilization into grain-scale dilational sites by hydrothermal fluids that flowed along the shear zones during shearing and recrystallization of the veins.

As pointed out by Stockwell and Lord (1939), North Carbonate Shear Zone and South Carbonate Shear Zone may play an important role in the fact that ore bodies do not extend to greater depths. Sheared quartz veins are widest at surface where the distance between these two shears is greatest and narrow at depth where the two shears intersect; and ore bodies under Growler shaft narrowed and terminated close to the South Carbonate Shear Zone (Fig. 2.15b; Stockwell and Lord, 1939).

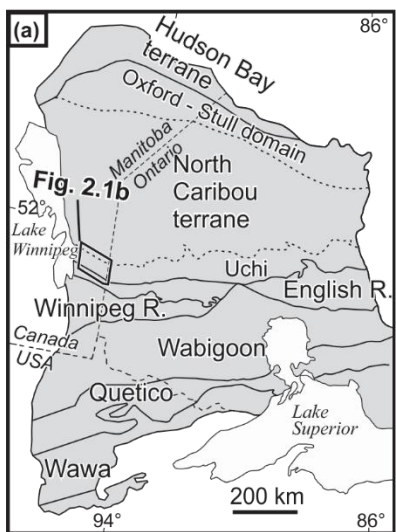
### ***2.6.3 Gold precipitation and modification at microscopic level***

Textural relationships between gold, sulfides and alteration minerals in quartz veins reveal that free gold is spatially and temporally associated with pyrrhotite and Bi minerals at the Central Manitoba gold deposit, as revealed by Xue (2011) and this study. Gold precipitation may have occurred contemporaneously with deposition of pyrrhotite and Bi minerals. This close association between gold and Bi minerals has been recently documented in several other gold deposits (e.g., Törmänen and Koski, 2005; Ciobanu et al., 2010; Acosta-Góngora et al., 2015). Some researchers proposed that "invisible" gold particles within Bi minerals could have been remobilized to form visible free gold (e.g., Acosta-Góngora et al., 2015). This mechanism might readily explain free gold association with Bi minerals at the microscopic scale in the Central Manitoba mine trend. More microprobe work on associated Bi minerals and mass-balance calculations on chemical change might help solve this problem.

## **2.7 Conclusions**

In this paper, the stratigraphic and structural setting of the Central Manitoba lode gold deposit were established based on new results of detailed geological mapping. Moreover, auriferous quartz veins and associated alteration envelopes were documented through microstructural and paragenetic analyses. The current study of stratigraphic succession, deformation structure and vein mineralization has revealed the following major points:

1. Auriferous quartz veins are concentrated at, and slightly discordant to, sheared contacts between greywacke, basalt and gabbro intrusions, or are entirely hosted by gabbro intrusions adjacent to contacts.
2. Five generations of ductile deformation structures as well as brittle faults were recognized in the field. Quartz veins are structurally controlled by G<sub>3</sub> and G<sub>4</sub> conjugate sets of brittle-ductile shear zones. West-trending auriferous quartz veins were emplaced before or during G<sub>4</sub> dextral shearing, and then overprinted by late G<sub>4</sub> deformation. Veins, either hosted by greywacke, basalt or gabbro, are extensive but not necessarily well-mineralized throughout their strike and dip directions. Ore bodies plunge shallowly along quartz veins, which are subparallel to vein margin slickenline and ridge-in-groove slickenside striation of G<sub>4</sub> ductile shear zones.
3. Free gold (electrum) is intimately associated with quartz, pyrrhotite, chalcopyrite and bismuth-bearing minerals in high grade veins. Gold was introduced contemporaneously with pyrrhotite and tellurobismuthite relatively early in the paragenetic sequence.



**Rice Lake belt**

- Uchi subprovince (2.75-2.69 Ga)
  - Edmunds assemblage (2.71-2.69 Ga)
  - San Antonio assemblage (<2.705 Ga)
  - Gem assemblage (2.73-2.72 Ga)
  - Ross River plutonic suite (2.73-2.72 Ga)
  - Bidou assemblage (2.75-2.73 Ga)

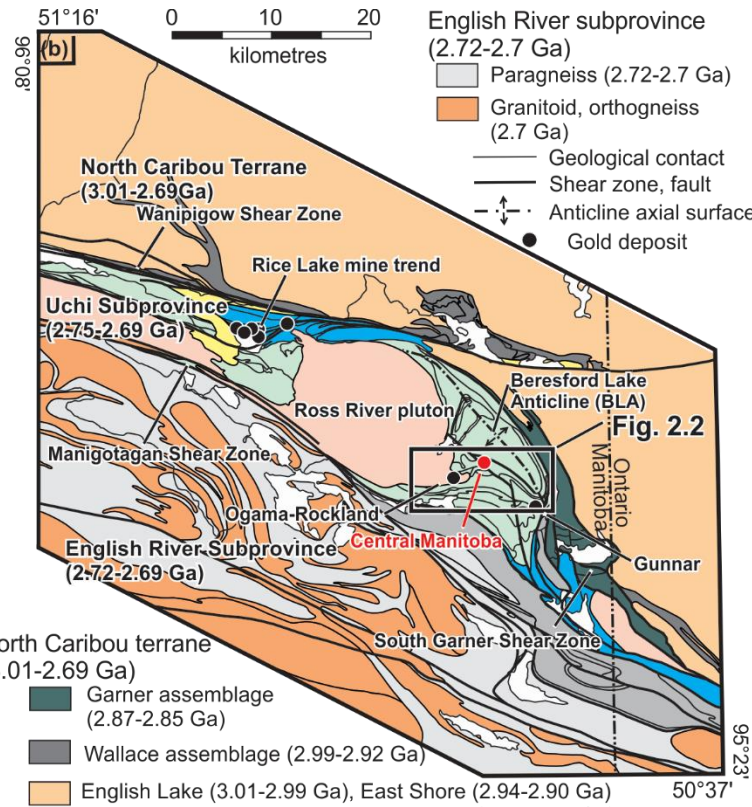


Fig. 2.1 a) Tectonic framework of the western Superior Province, showing major tectonic domains, terranes, or Subprovinces; modified from Lin and Beakhouse (2013); b) Regional tectonic map of the western Superior Province in southeastern Manitoba, exhibiting major Subprovinces, lithostratigraphic assemblages, crustal-scale shear zones, and significant gold deposits; modified from Anderson (2013b).

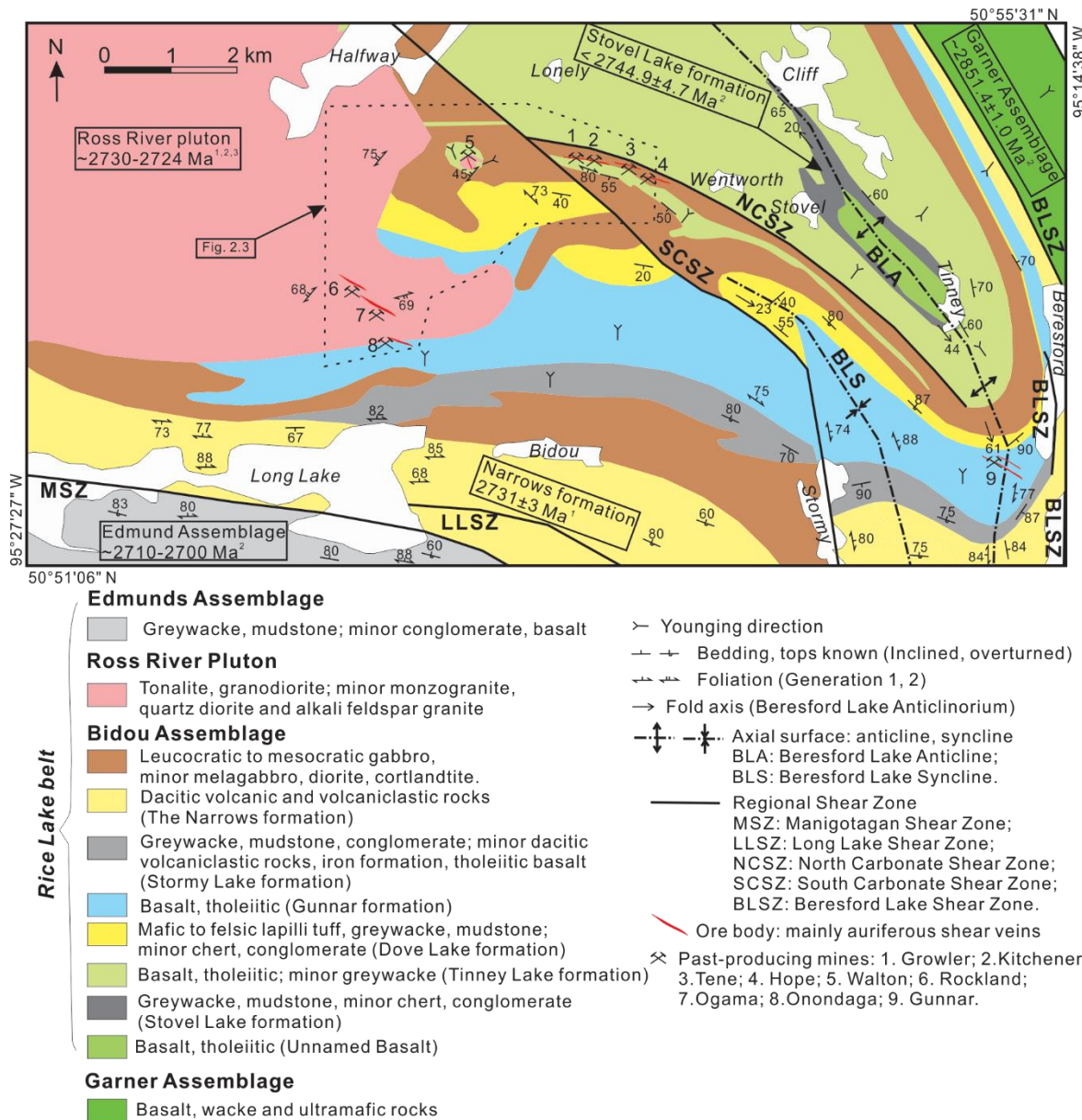


Fig. 2.2 Generalized regional geological map of the southeastern Rice Lake greenstone belt, displaying major formations within the Bidou assemblage and gold deposits in this area; modified from Stockwell (1945), Zwanzig (1971), Brommecker (1996), Anderson (2013b) and Zhou (2014). Location of Fig. 2.3 is indicated. Age source: <sup>1</sup> Turek et al. (1989), <sup>2</sup> Anderson (2013b), <sup>3</sup> Chapter 4.

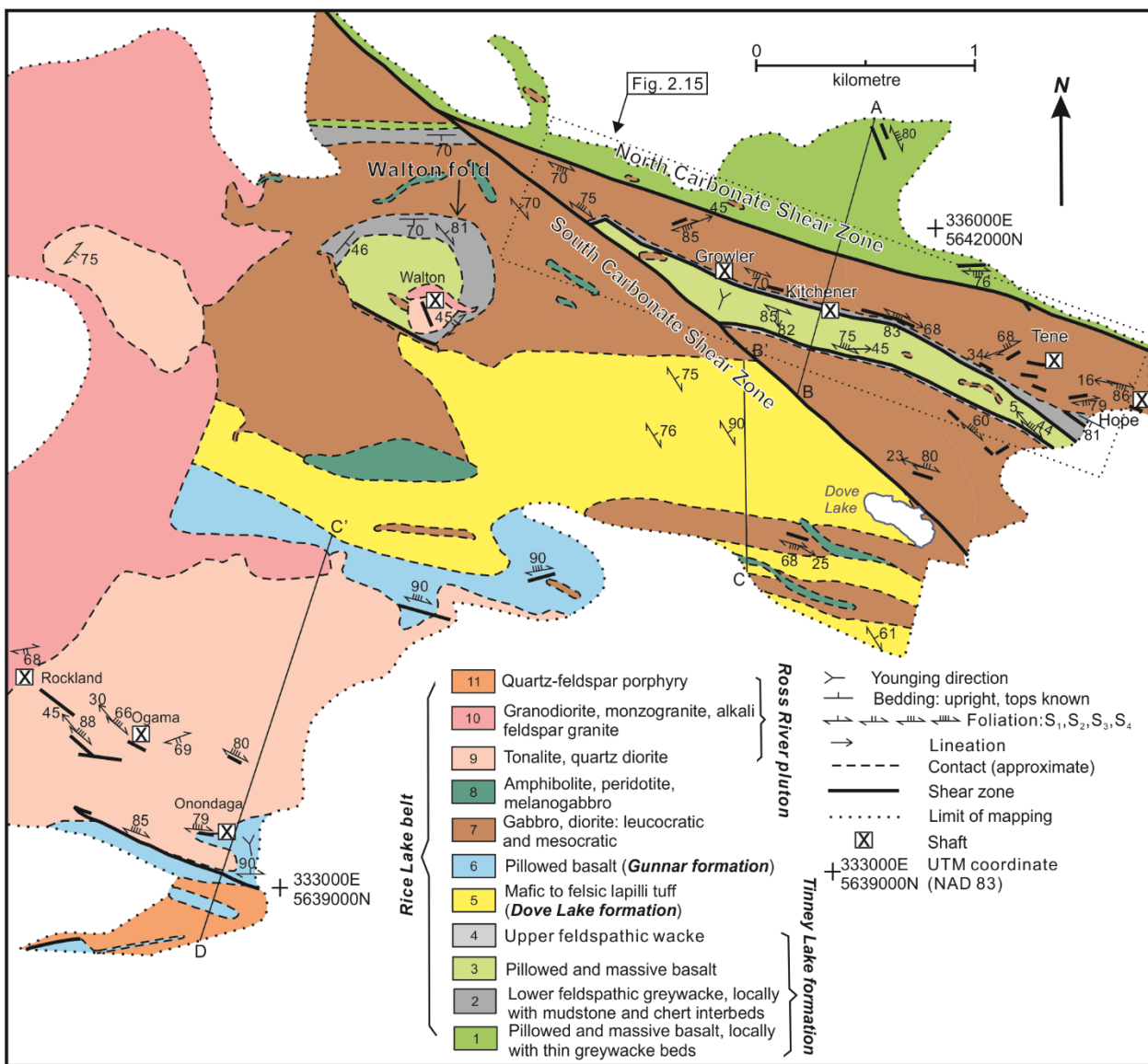


Fig. 2.3 Simplified local geological map in the vicinity of the Central Manitoba mine trend, illustrating major lithostratigraphic units, structures and past-producing shafts; modified from Zhou et al. (2014). Location of Fig. 2.15 is indicated.

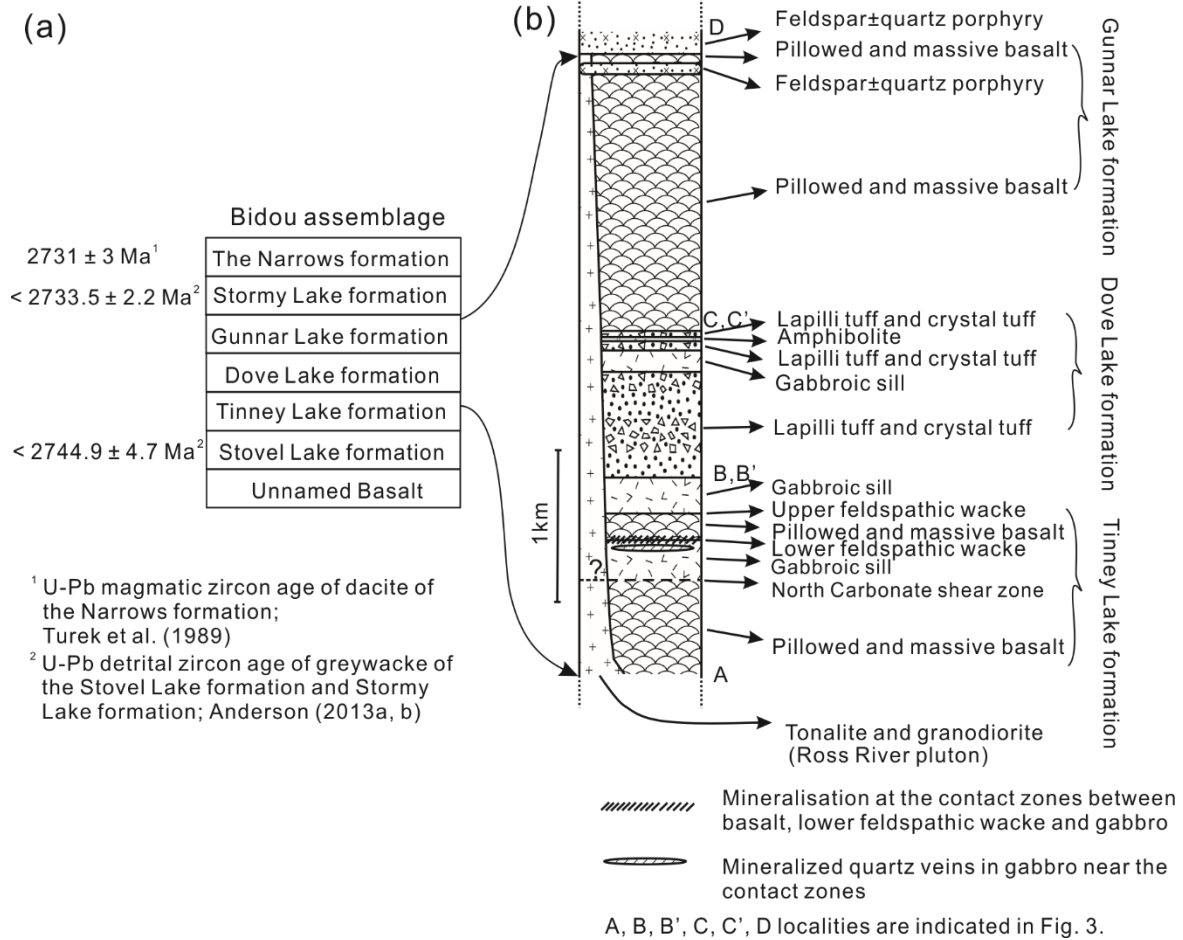


Fig. 2.4 a) A diagram showing seven conformable formations within the Bidou assemblage (Campbell, 1971) and available U-Pb zircon age constraints (Turek et al., 1989; Anderson, 2013a, b); b) local lithologic column constructed from Fig. 2.3; ore bodies are indicated.

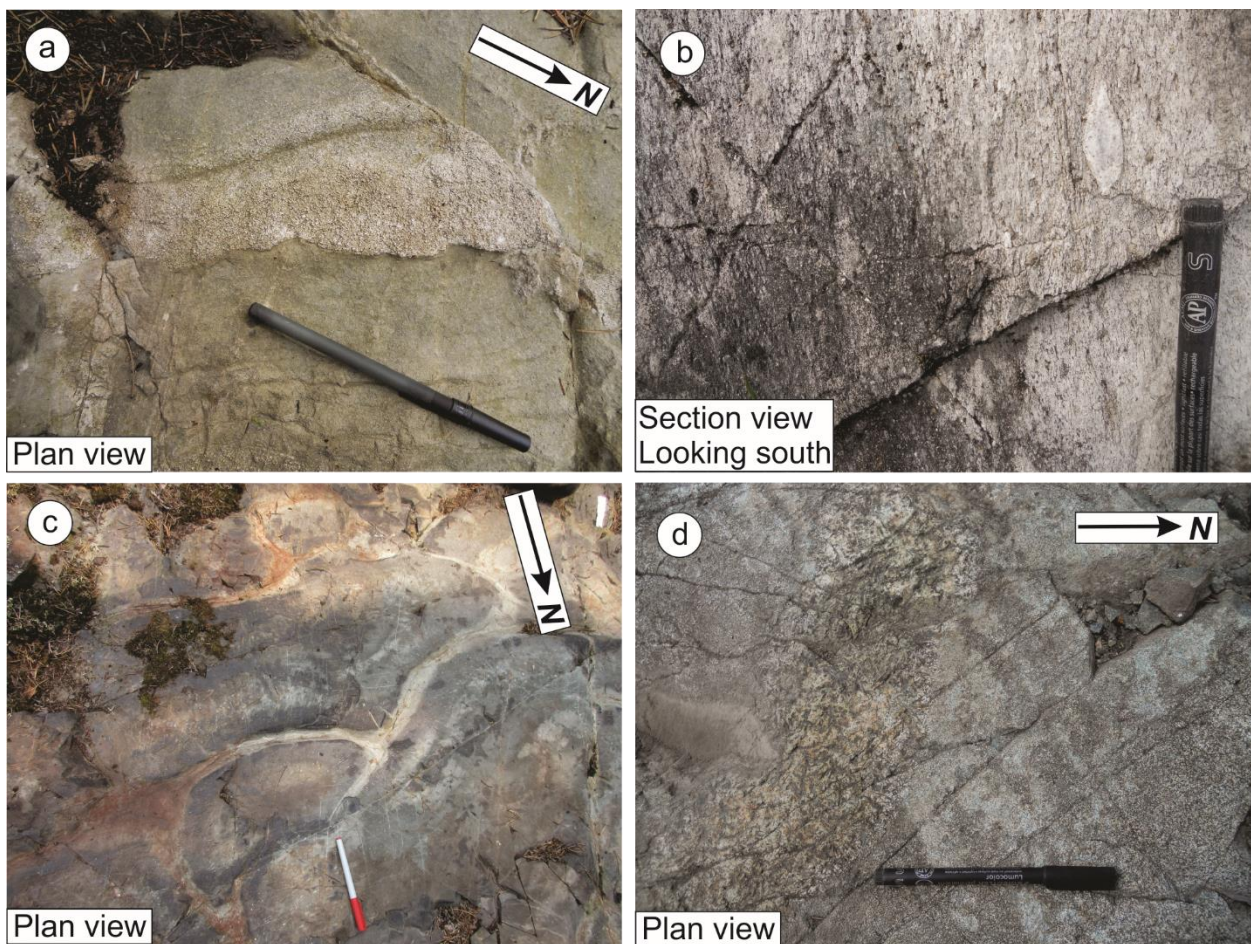


Fig. 2.5 Outcrop photographs of bedrock lithology: a) greywacke showing spectacular normal graded bedding and scour surface at one bed's bottom, younging toward southwest; southeast of Walton shaft; b) felsic lapilli tuff with a prominent subvertical foliation; c) pillow-shaped basalt south of the Ross River pluton, younging to the south; d) irregular-shaped pegmatitic segregations within leucocratic gabbro.

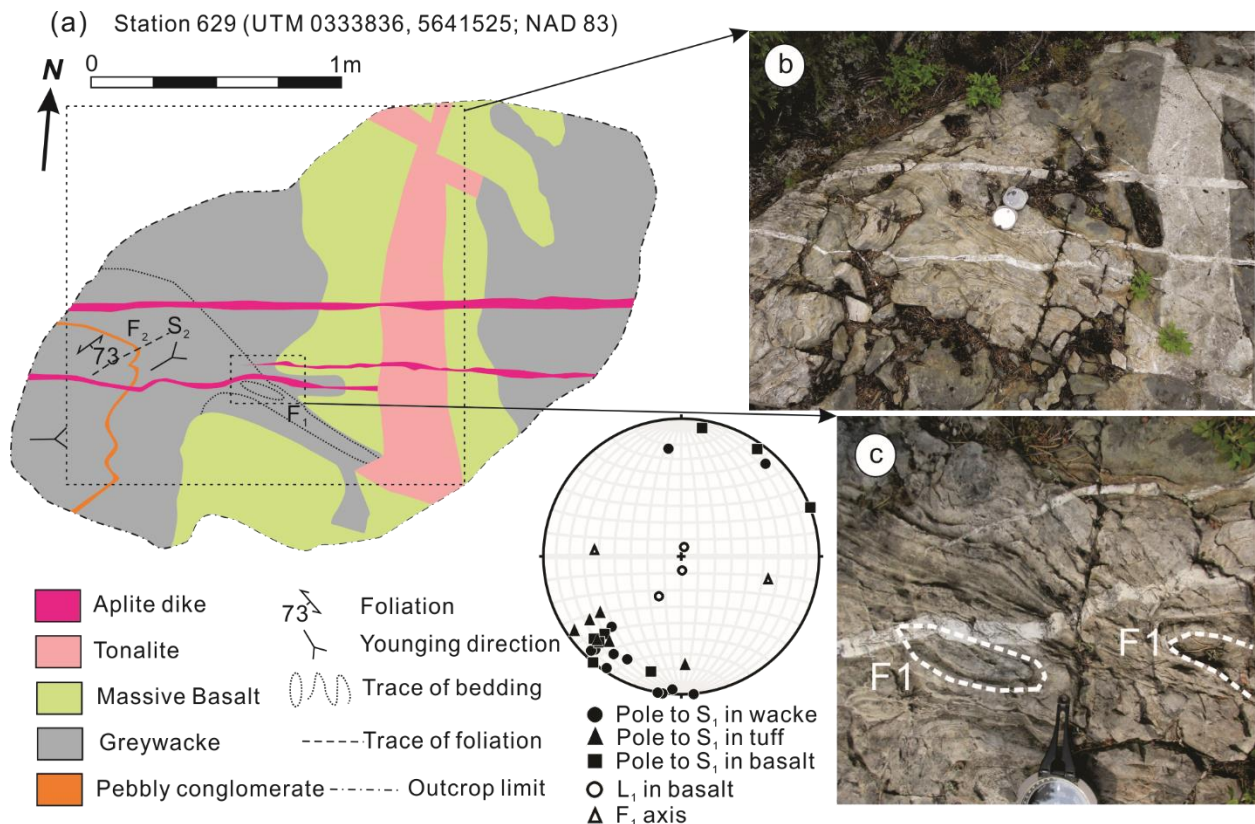
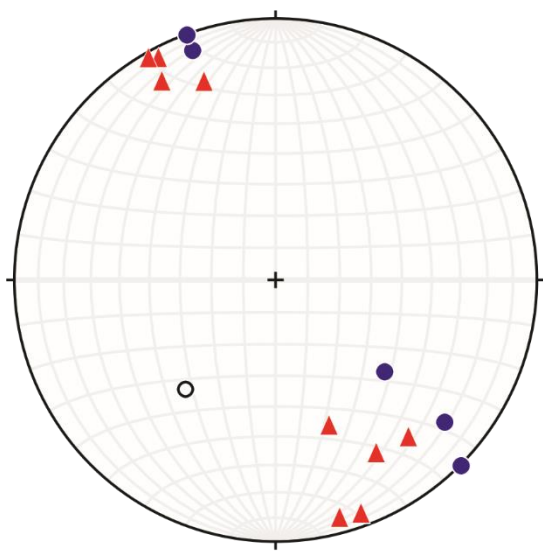


Fig. 2.6 a) Outcrop sketch illustrating main lithologic units and F<sub>1</sub>, F<sub>2</sub>, and S<sub>2</sub> structures; b, c) Outcrop photographs showing crosscutting relationships between lithologic units and doubly-plunging isoclinal F<sub>1</sub> folds. G<sub>1</sub> structural data are equal-area lower hemisphere stereonet projections. All stereonet data presentations in this thesis were produced through the software "Stereonet 8" by Allmendinger et al. (2012) and Cardozo and Allmendinger (2013).



Fig. 2.7 Outcrop photographs displaying  $G_1$  structures: a) flattened pillowd basalt defining west-striking  $S_1$  foliation; b) flattened and elongate basalt varioles defining a west-striking subvertical  $S_1$  foliation and subvertically plunging  $L_1$  lineation; finite strain axes are indicated; c) west-striking vertical bedding and steeply south-dipping, closely-spaced cleavage in greywacke.



- Pole to  $S_2$  in the Bidou assemblage
- ▲ Pole to  $S_2$  in the Ross River pluton
- $F_2$  axis

Fig. 2.8 Equal-area lower hemisphere stereonet projection of G<sub>2</sub> structural data.

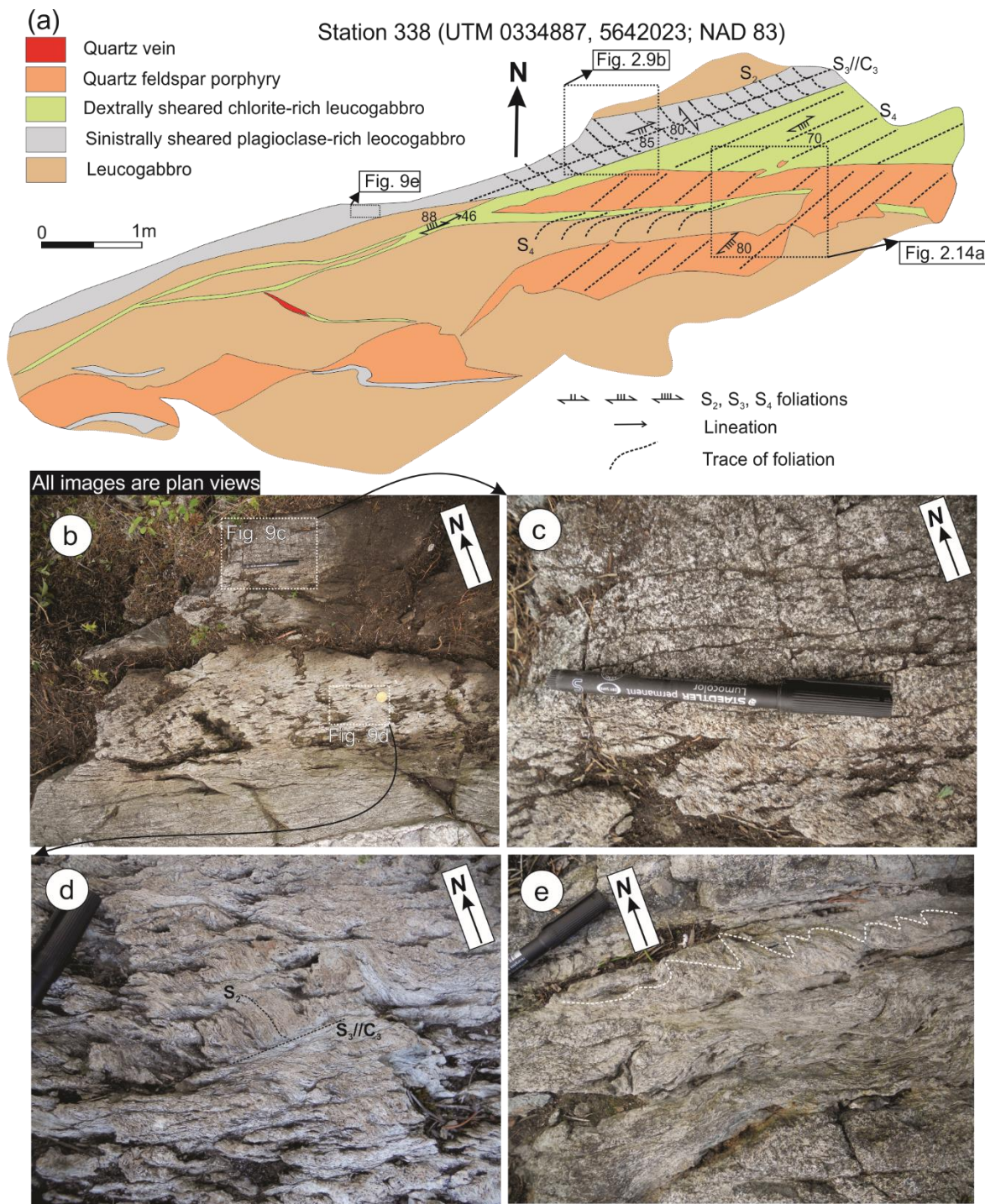


Fig. 9. a) Outcrop sketch of west-southwest-striking G<sub>3a</sub> sinistral and G<sub>4</sub> dextral gabbroic ductile shear zones, and associated quartz-feldspar porphyry boudins; b) outcrop photograph showing from top to bottom three subparallel gabbroic domains: undeformed leucogabbro, greyish white G<sub>3a</sub> ductile shear zone and greenish grey G<sub>4</sub> ductile shear zone; c) close-up of the contact between undeformed leucogabbro and G<sub>3a</sub> sinistral ductile shear zone; d) spectacular S/C

mylonitic rocks within the G<sub>3a</sub> ductile shear zone indicating a sinistral sense of shear; note that S<sub>2</sub> foliation is crenulated and overprinted by S<sub>3</sub> (subparallel to C<sub>3</sub>) foliation; e) short-wavelength chevron folds in G<sub>3a</sub> shear zone indicating a sinistral sense of shear.

All images are plan views

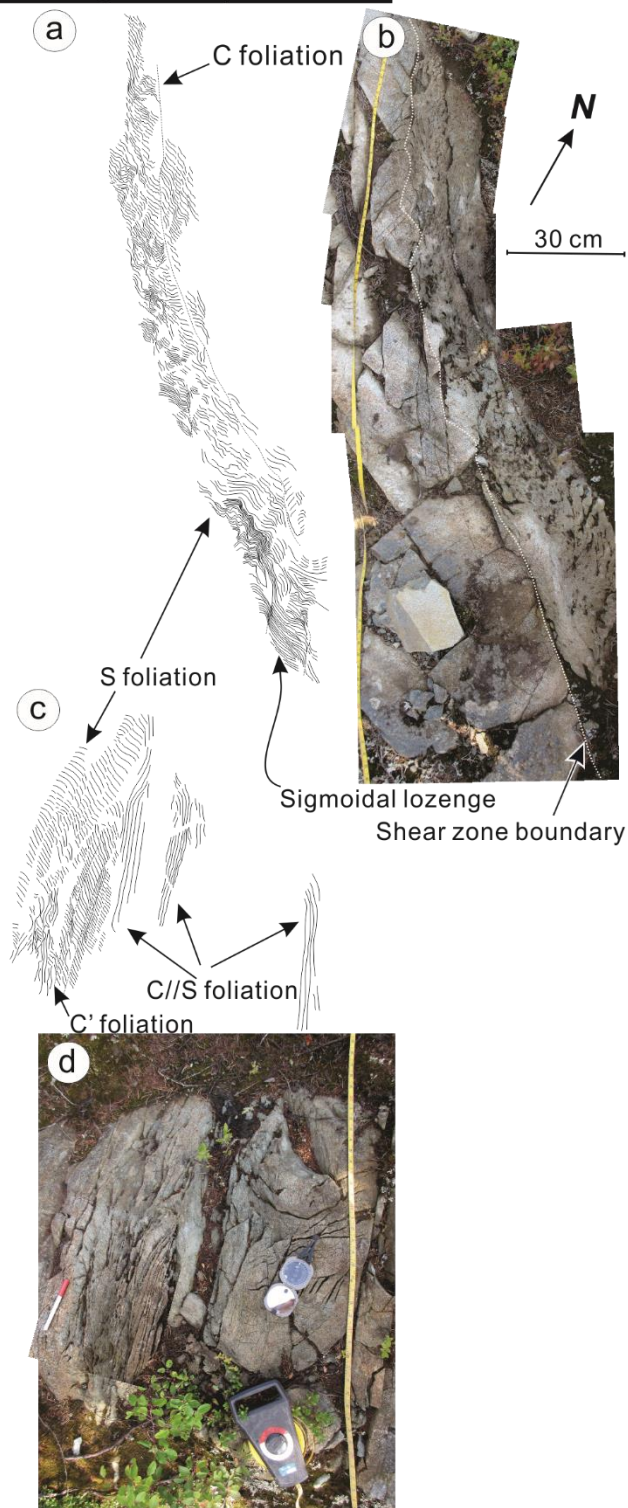


Fig. 2.10 Outcrop photographs and line drawings of north-northwest-striking  $G_{3b}$  dextral subvertical gabbroic shear zones: a, b) west-southwest-striking curviplanar to short-wavelength-folded S foliation and north-northwest-striking C foliation as well as the sigmoidal lozenge indicating dextral shearing; C foliation is defined by physical breaks of weathered out low grounds that are partially filled by quartz veinlet lenses; c, d) west-trending curviplanar S foliation and north-trending C foliation suggesting dextral shearing.

Station 506 (UTM 0336549, 5641179; NAD 83)

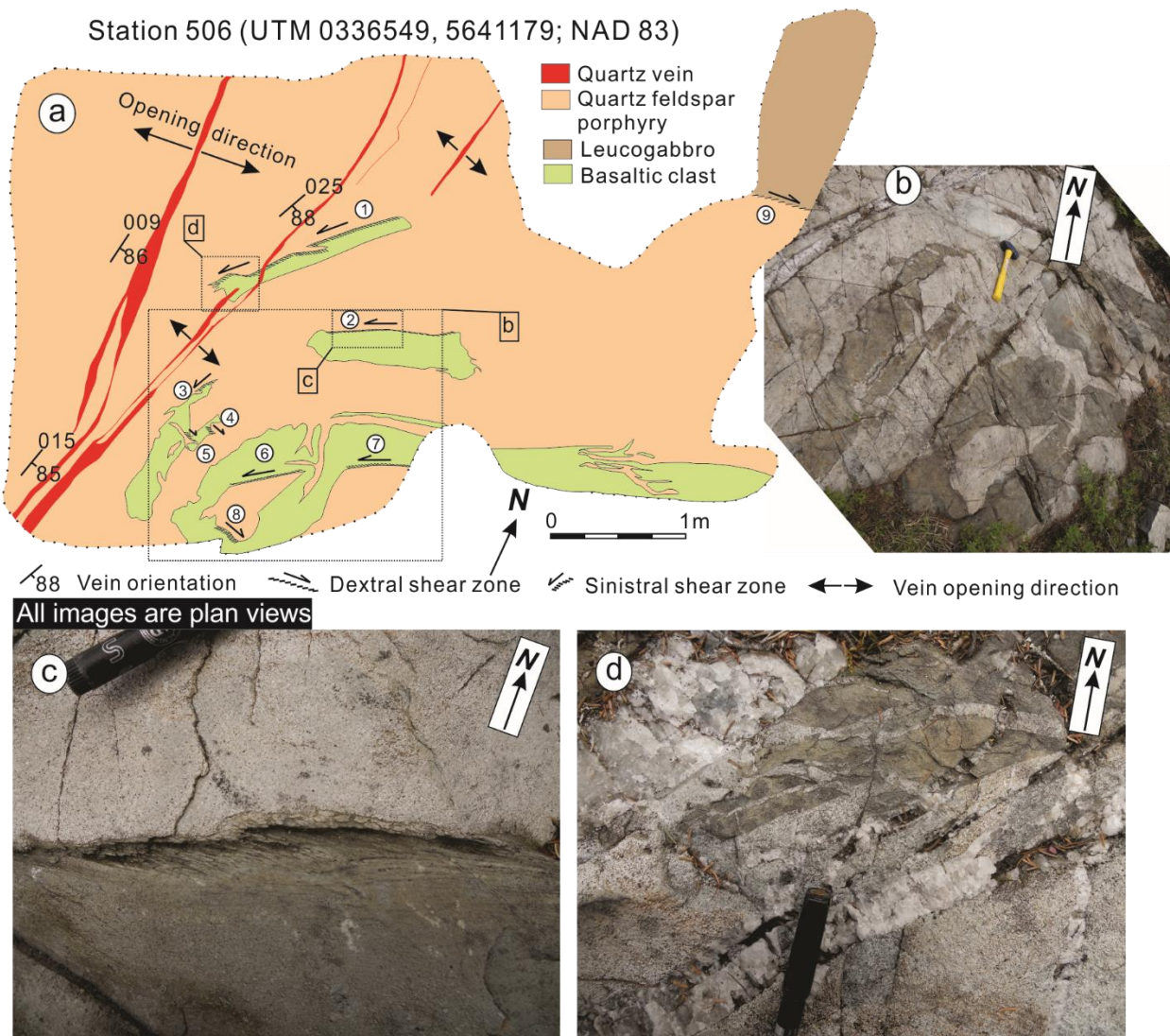
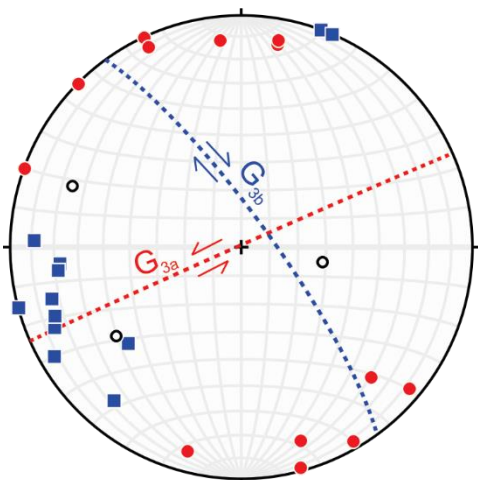


Fig. 2.11 a) Outcrop sketch of intrusion breccia, extension quartz veins and associated shear basaltic clast margins; b) close-up outcrop photograph illustrating basaltic clasts and feldspar porphyry; c) outcrop photograph exhibiting sinistral sheared margin of a basaltic clast; d) outcrop photograph showing numerous basaltic clasts and extension quartz veins with comb structure.



- Pole to  $G_{3a}$  sinistral shear zone
- Pole to  $G_{3b}$  dextral shear zone
- $L_3$  lineation

Fig. 2.12  $G_{3a}$  and  $G_{3b}$  shear zones are plotted on the equal-area lower hemisphere stereonet.

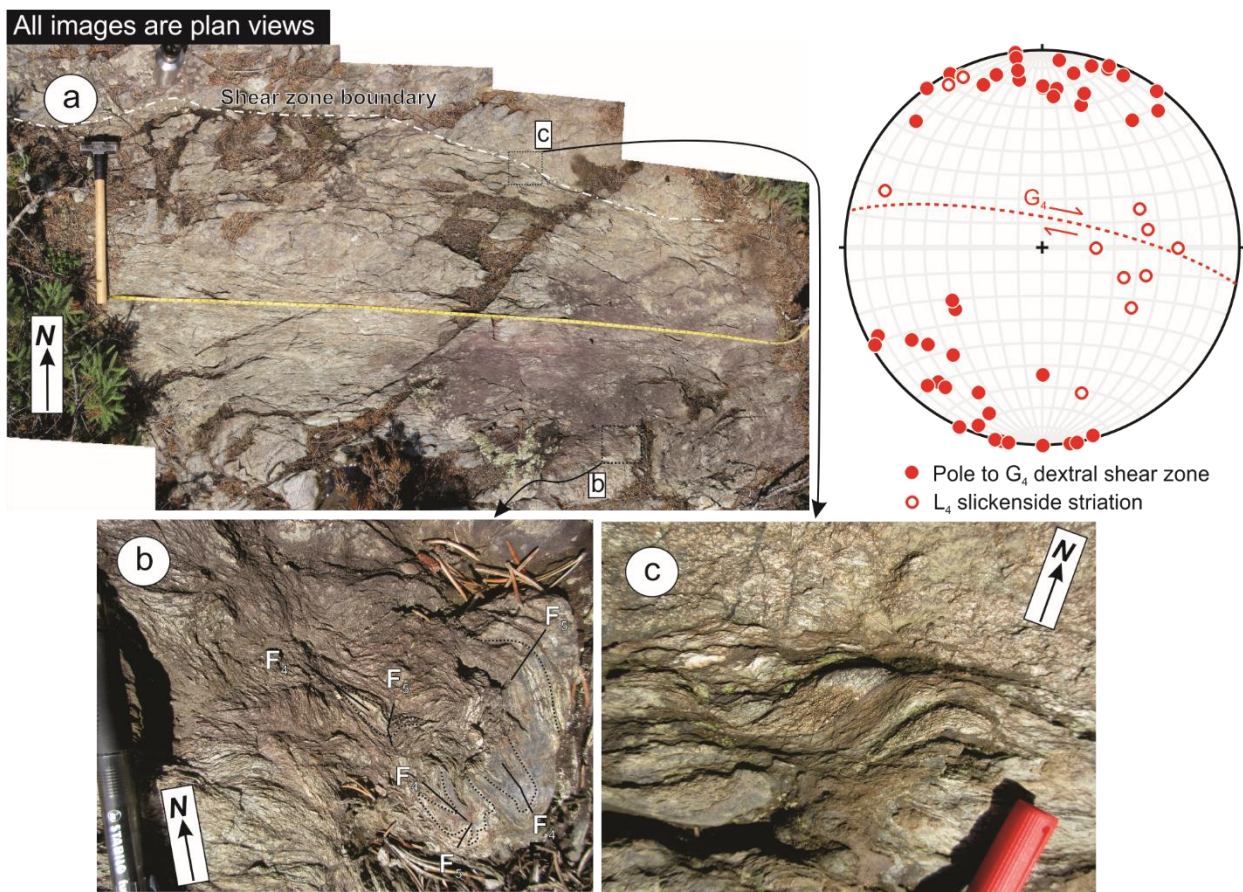


Fig. 2.13 Outcrop photographs showing  $G_4$  and  $G_5$  structures: a) west-trending subvertical  $G_4$  ductile shear zone; b) isoclinal  $F_4$  folds are overprinted by open  $F_5$  folds in  $G_4$  ductile shear zone; c) spectacular  $\sigma$ -type porphyroblast at the  $G_4$  ductile shear zone boundary indicating dextral shearing. The equal-area lower hemisphere projection shows  $G_4$  structural data.

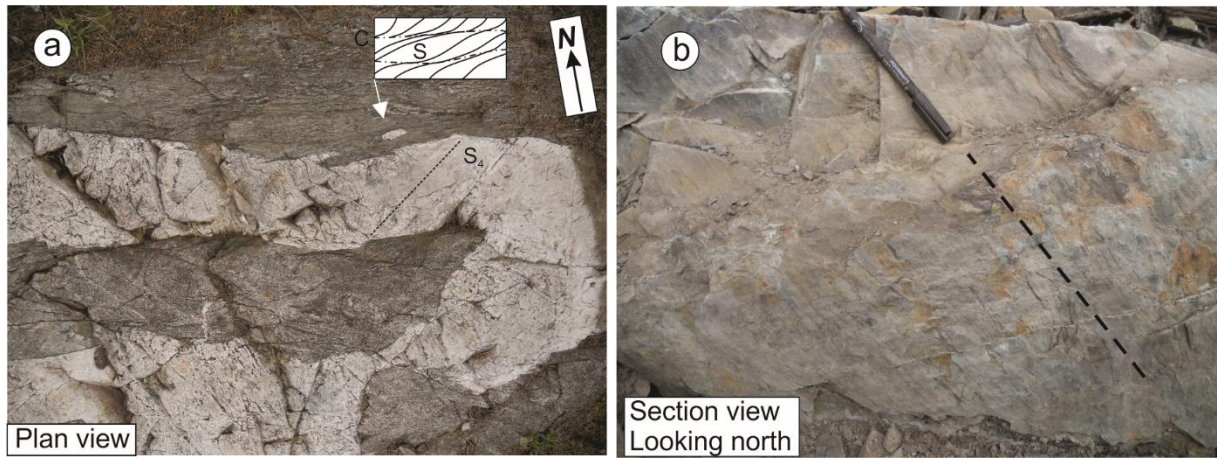


Fig. 2.14 a) Outcrop photograph of a G<sub>4</sub> ductile shear zone adjacent to boudinaged porphyry dikes, and line drawing of S/C fabric indicating dextral shearing; see photo location indicated in Fig. 2.9a; b) moderately east-plunging L<sub>4</sub> slickenside striation.

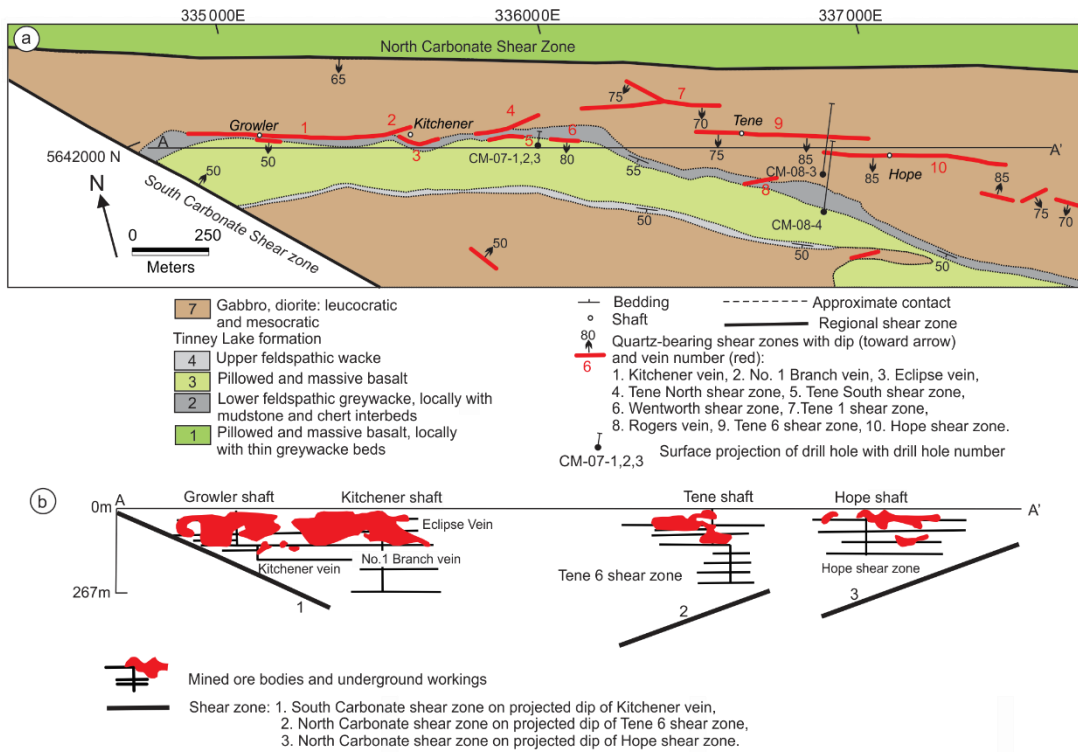
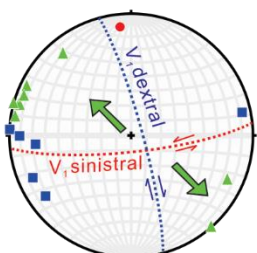
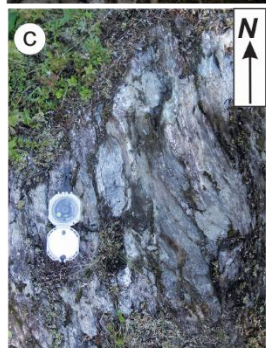
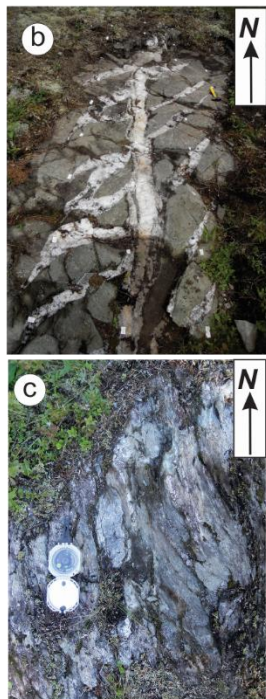
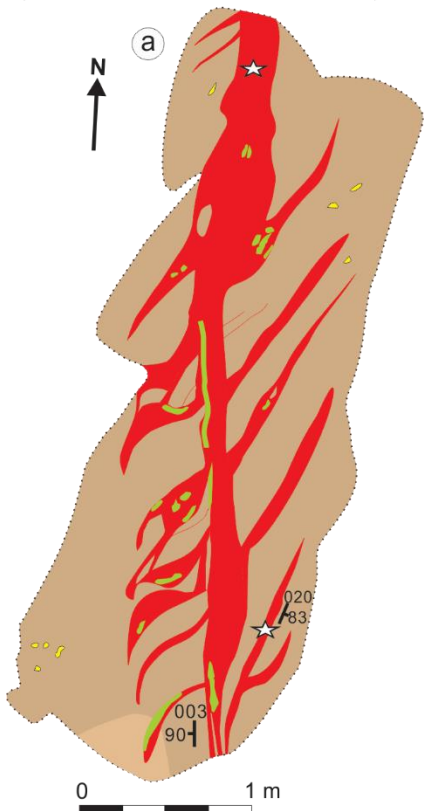


Fig. 2.15 a) Geological map showing vein systems at the Central Manitoba mine trend; b) longitudinal sectional projection along line A–A' in Fig. 2.15a, showing milled ore bodies and underground workings. Modified from Stockwell and Lord (1939).

All images are plan views

Station 548/612  
(UTM 0336416, 5641246; NAD 83)



- Quartz vein
  - Vein orientation
  - Chlorite alteration and tourmaline infill
  - Pegmatitic dioritic pods
  - Leucocratic gabbro
  - Quartz-bearing leuco-mesocratic gabbro
  - ☆ Gold assay locality
- Pole to V<sub>1</sub> sinistral shear vein
  - Pole to V<sub>1</sub> dextral shear vein
  - ▲ Pole to V<sub>1</sub> extension vein
  - ← Opening vector

Fig. 2.16 a, b) Sketch and outcrop photograph showing V<sub>1a</sub> association in undeformed leucogabbro: a north-trending central fault-fill vein and northeast-trending extension vein arrays in en echelon fashion, which indicate dextral shearing of a G<sub>3b</sub> brittle shear fracture; c) G<sub>3b</sub> dextral ductile shear zone and associated V<sub>1b</sub> lenses. V<sub>1</sub> possible conjugate shear veins and extension veins are plotted on the equal-area lower hemisphere stereonet.

All images are plan views

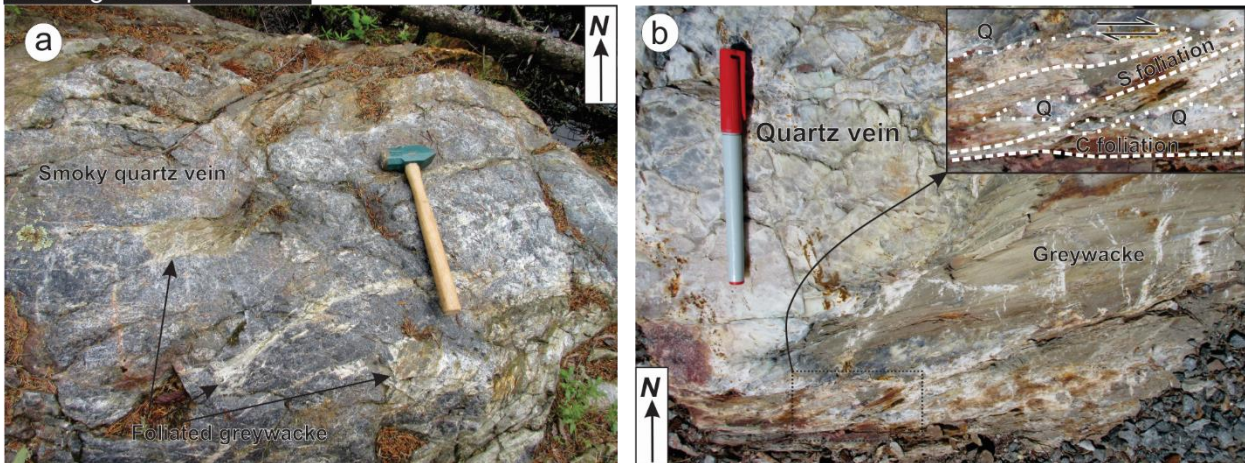


Fig. 2.17 Outcrop and hand specimen photographs showing west-trending subvertical G<sub>4</sub>-related V<sub>2</sub> association: a) smoky quartz veins with enclosed elongate irregular-shaped foliated and altered greywacke blocks; b) quartz vein and encompassed foliated and altered greywacke; in the upper right corner, close-up photograph of altered greywacke with S-C fabric indicating dextral shearing. Q = Quartz.

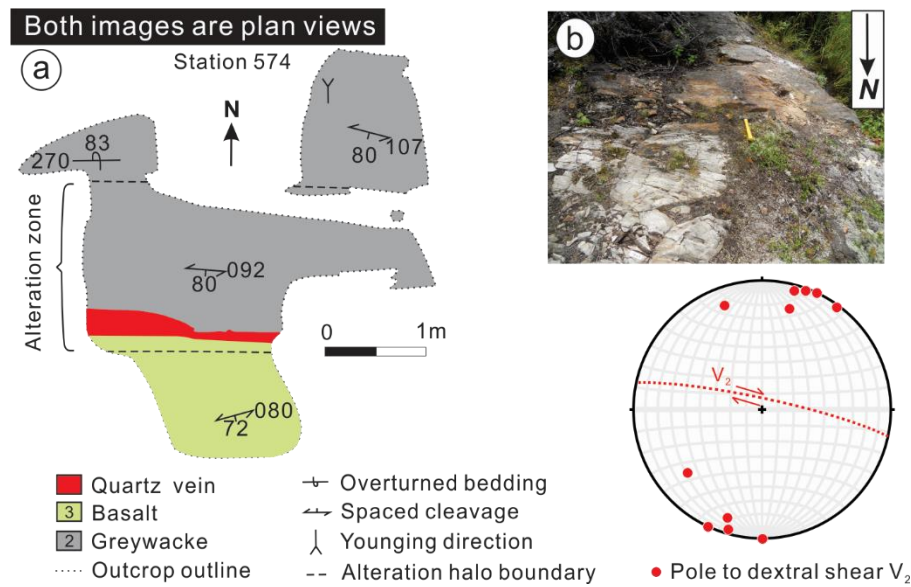


Fig. 2.18 a, b) Sketch and outcrop photographs showing  $V_2$  veins at the contact between basalt and greywacke; asymmetrical alteration halos are indicated in the sketch. Poles to  $V_2$  veins are plotted in the lower-hemisphere equal-area stereonet.

Both images are plan views

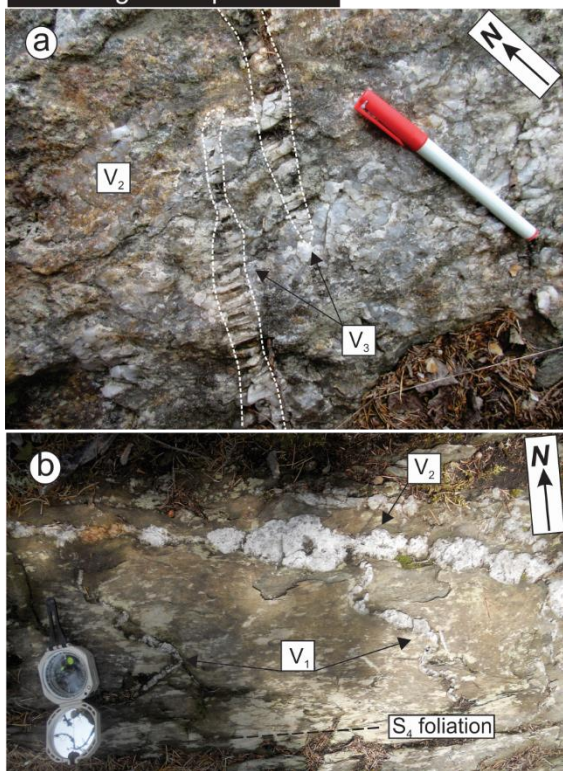


Fig. 2.19 a) Outcrop photograph showing crosscutting relationships between  $V_2$  and  $V_3$  sets; b) Outcrop photograph showing north-trending  $V_1$  veins are folded and a west-trending  $V_2$  vein is boudinaged subparallel to mylonitic foliation in a  $G_4$  ductile shear zone.

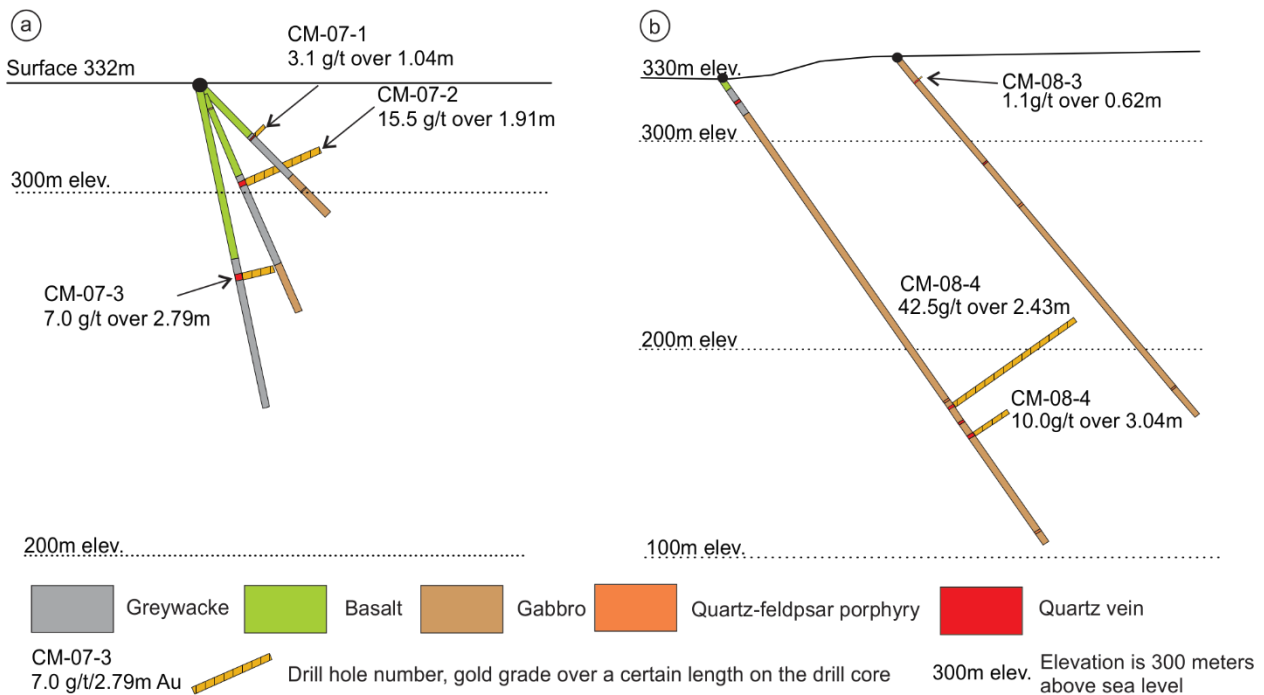


Fig. 2.20 Representative cross sections of drill holes at the Central Manitoba mine trend showing high grade auriferous quartz veins are located at or close to the contact of basalt and lower greywacke in a), or entirely hosted by gabbro north of lower greywacke. Drill hole locations are indicated in Fig. 16a. Modified from Hood and Chater (2009).

All images are plan views; north is to the top

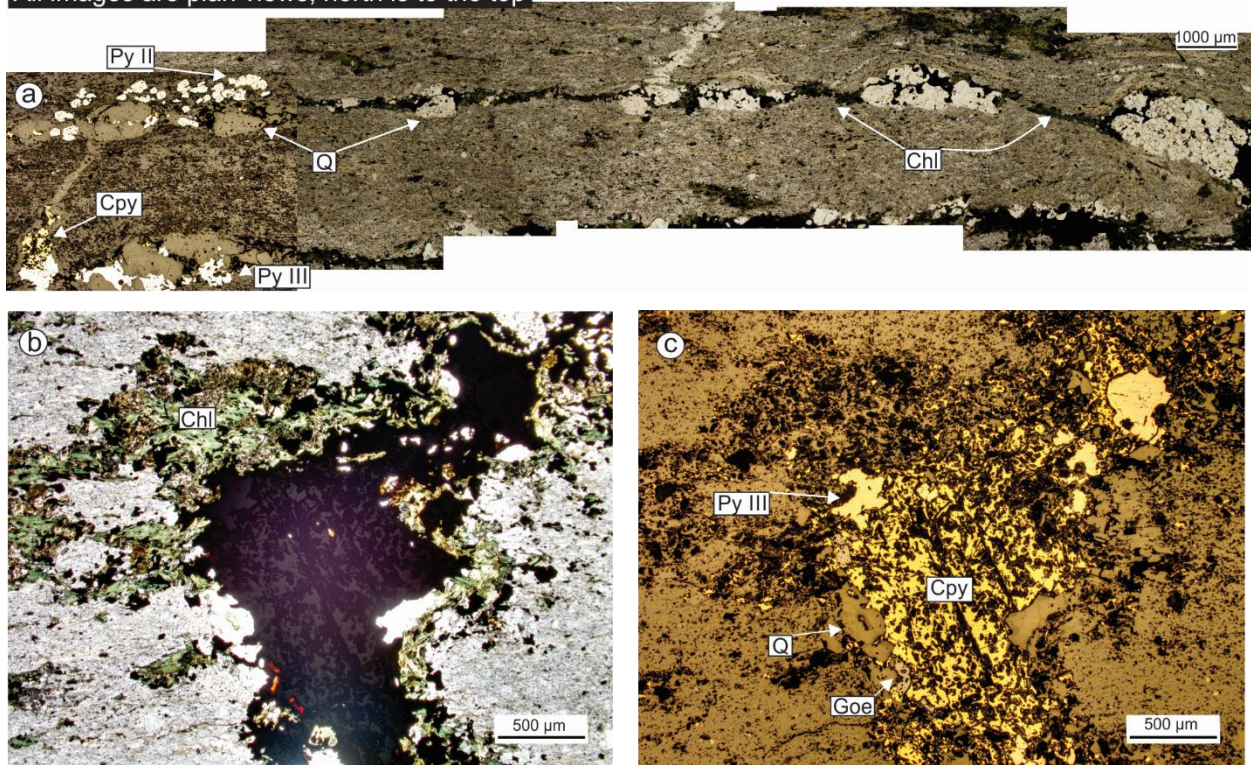


Fig. 2.21 Thin section photomicrographs illustrating V2 mineralogy and microstructure: a) merged photomicrographs showing west-trending quartz vein boudins in altered and foliated greywacke; the left photomicrograph viewed under plane polarized reflected light, all the rest under plane polarized transmitted light; b, c) close spatial association of chlorite, pyrite type-III and chalcopyrite; photomicrograph (b) viewed under plane polarized transmitted light, and (c) under plane polarized reflected light; Py II=pyrite type-II, Py III=pyrite type-III, Cpy=chalcopyrite, Chl=chlorite, Q=quartz, Goe=goethite.

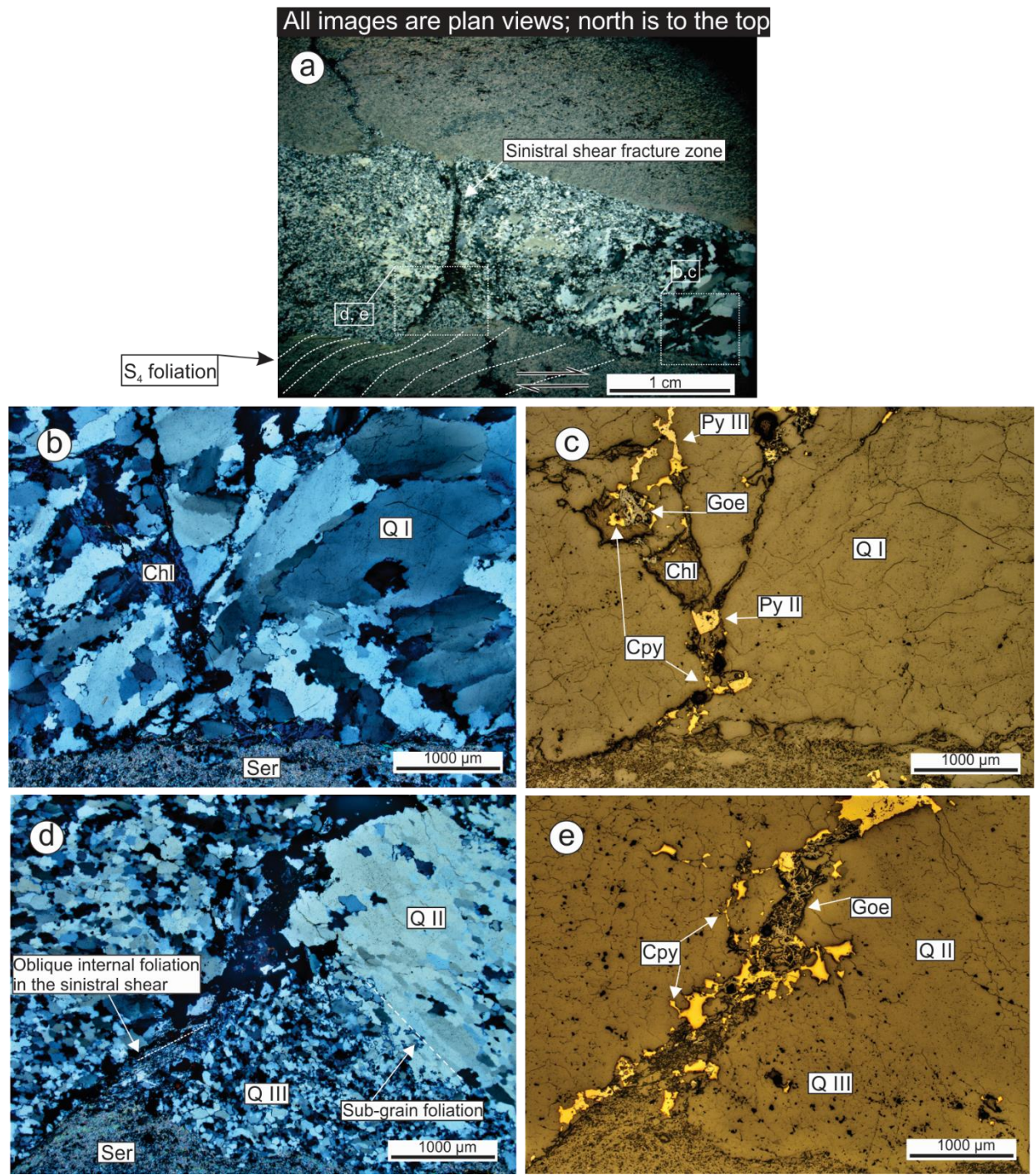


Fig. 2.22 Thin section photomicrographs showing west-striking V<sub>2</sub> mineralogy and microstructure: a) one V<sub>2</sub> veinlet in altered and foliated greywacke; under cross polarized transmitted light; b) euhedral type-I quartz grains exhibiting sweeping elongate undulose extinction, with enclosed equant chlorite grains and sericite adjacent to vein margins; under cross polarized transmitted light; c) pyrite type-II, pyrite type-III and associated chalcopyrite are

interstitial to quartz, also close to chlorite or enclosed by chlorite; same location as photomicrograph (b) but under plane polarized reflected light; d) type-II quartz grains with chessboard undulose extinction and type-III newly-recrystallised quartz grains; note a narrow sinistral shear zone (going from lower left to top right) offsets the quartz vein margin; under cross polarized transmitted light; e) chalcopyrite and goethite filled in the narrow sinistral shear zone or interstitial to adjacent quartz grains; under plane polarized reflected light, same location as photomicrograph (d); Py II=pyrite type-II, Py III=pyrite type-III, Cpy=chalcopyrite, Chl=chlorite, Q I=quartz type-I, Q II=quartz type-II, Q III=quartz type-III, Goe=goethite, Ser=sericite.

All images are plan views; north is to the top

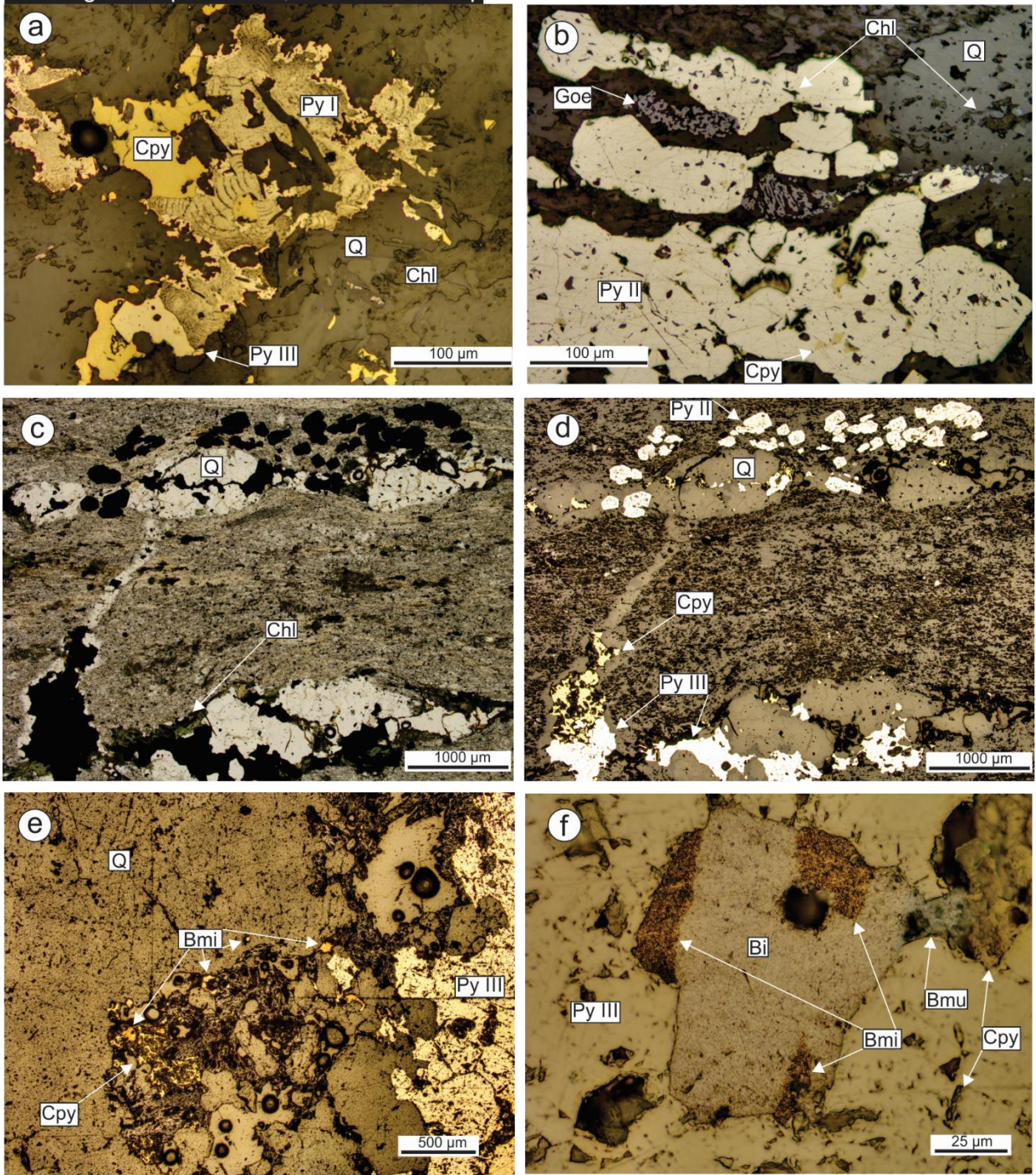


Fig. 2.23 Thin section photomicrographs showing west-striking V<sub>2</sub> mineralogy and microstructure, and sulfide associations in altered greywacke adjacent to V<sub>2</sub>: a) colloform pyrite type-I is replaced by clean irregular pyrite type-III and chalcopyrite; under plane polarized reflected light; b) euhedral to subhedral pyrite type-II grain aggregates with numerous randomly-oriented chlorite and chalcopyrite inclusions; under plane polarized reflected light; c) boudins of

quartz grain aggregates and closely spatially associated sulfide aggregates in foliated and altered greywacke; note chlorite is attached to sulfide minerals and quartz vein boudins; under plane polarized transmitted light; d) euhedral to subhedral pyrite type-II grain aggregates develop a weak preferred orientation parallel to the continuous foliation in altered greywacke in photomicrograph (c); pyrite type-III and associated chalcopyrite aggregates are interstitial to quartz vein boudins; under plane polarized reflected light, same location as photomicrograph (c); e) bismite occurs as free grains interstitial to quartz, attached to pyrite type-III and chalcopyrite, or encompassed by chalcopyrite; under plane polarized reflected light; f) bismuthinite, bismuth, and chalcopyrite are in contact, and they are all encompassed by pyrite type-III; bismite replaced part of bismuth; under plane polarized reflected light; Py III=pyrite type-III, Cpy=chalcopyrite, Q=quartz, Bi=bismuth, Bmi=bismite, Bmu=bismuthinite.

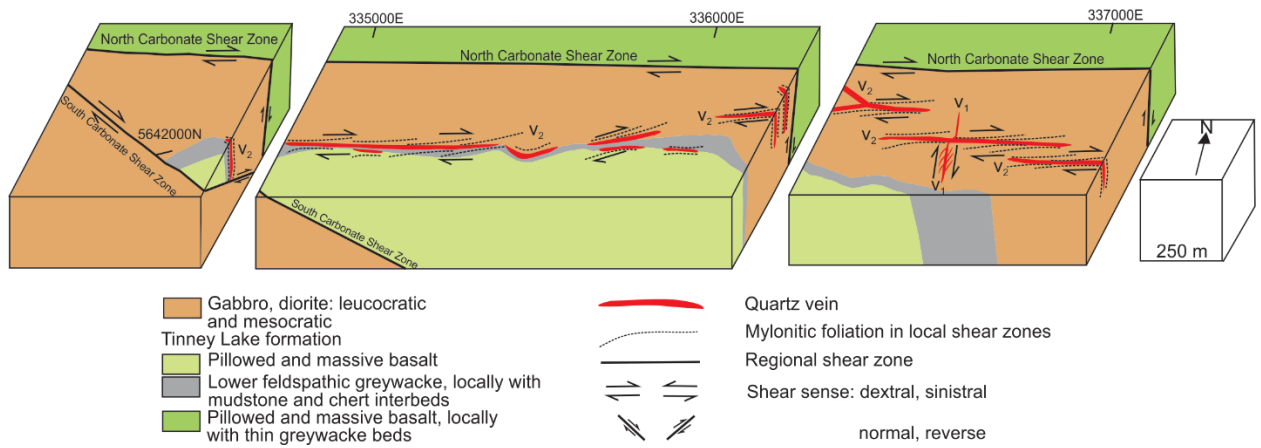


Fig. 2.24 Geometric and kinematic model for the Central Manitoba mine trend. See text for details.

## **Chapter 3**

**Structural setting and lithologic control of the  
Ogama-Rockland lode gold deposit, southeastern  
Ross River pluton, Rice Lake greenstone belt,  
Superior Province, Manitoba, Canada**

### 3.1 Introduction

The Superior Province hosts numerous significant gold deposits (> 8500 metric tons of gold production) in Mesoarchean to Neoarchean greenstone-granitoid belts associated with crustal scale high-strain zones that have undergone amphibolite to greenschist facies metamorphism (Goldfarb et al., 2001; Robert et al., 2005). Different classifications and corresponding empirical models have been proposed for gold deposits in various lithologic, structural and tectonic settings (Groves et al., 2003; Poulsen et al., 2000; Robert et al., 2007), of which orogenic gold deposits (Groves et al., 1998) and intrusion-related gold deposits (Sillitoe and Thompson, 1998) are two principal clans (Hagemann and Brown, 2000; Robert et al., 2007). Although our understanding on ore genesis continues to improve with new field and laboratory data, some Archean gold deposits, especially those hosted by intrusions, remain the subject of heated debate in terms of the source of ore-forming fluids, structural timing of ore bodies, pattern of alteration zoning, and absolute age of gold mineralization (e.g., Sillitoe and Thompson, 1998; Groves et al., 2003; Robert et al., 2005). The close spatial relationship between major gold deposits and host or adjacent felsic intrusions has been interpreted to indicate a genetic link between felsic magmatism and gold introduction (e.g., Cameron and Hattori, 1987; Robert, 2001; Xue et al., 2013), or is attributed to strain partitioning and competency contrast (e.g., Colvine et al., 1989; Zhang et al., 2014). Alternative models include multiple stages of mineralization, such as early pre-tectonic mineralization associated with felsic magmatism and late syn-tectonic remobilization associated with shear zone-related systems (e.g., Mercier-Langevin et al., 2012).

Here, we examine a tonalite-hosted, shear zone controlled, vein-type gold deposit (Ogama-Rockland) within the Rice Lake greenstone belt as a comprehensive case study, using extensive camp-scale and outcrop-scale geologic mapping to illustrate the complicated interplay of late Archean magmatism, ductile deformation processes and ore-forming hydrothermal systems. Field relations reveal fundamental geologic processes that were responsible for gold mineralization and therefore are a major focus of this study. In particular, we focus on various intrusive phases of the host Ross River pluton, intricate crosscutting relationships between aplite dikes and mineralized quartz veins, and spatial and temporal relations between different generations of ductile shear zones and associated quartz veins. We use these critical geologic features to constrain the fundamental geologic processes that may have induced gold endowment, and to provide an empirical model for ongoing exploration.

### **3.2 Regional Geologic Setting**

The western Superior Province in the region is subdivided into three east-trending lithotectonic units based on rock type, absolute ages, metamorphic grades and geophysical signatures: the North Caribou terrane, Uchi Subprovince and English River Subprovince (Fig. 3.1; Poulsen et al., 1996; Bailes et al., 2003; Anderson, 2008, 2013a, b). The North Caribou terrane is composed of the Mesoarchean Wallace assemblage, Mesoarchean Garner assemblage, and English Lake, East shore and Wanipigow River plutonic complexes. The interface between the North Caribou terrane and Uchi Subprovince is manifest by the Wanipigow fault, which is a curvilinear, crustal-scale, subvertical shear zone with a multiphase deformation history (Anderson, 2008). The Rice Lake greenstone belt defines the western-most exposed portion of the Uchi Subprovince. The terrane boundary between the Uchi and English River Subprovinces is defined by the curvilinear, crustal-scale, subvertical Manigotagan fault (Poulsen et al., 1996; Anderson, 2008). The English River Subprovince is equivalent to the English River basin in Ontario, using the nomenclature of Stott et al. (2010). Its constituents include medium- to high-grade metasedimentary rocks and voluminous diorite–tonalite–granodiorite plutonic rocks, emplaced prior to the regional deformation and high-T–low-P metamorphism at 2.69 Ga (Corfu et al., 1995), which is attributed to terminal collision of the North Caribou and Winnipeg River terranes (Percival et al., 2006a, b).

All the supracrustal rocks of the Bidou assemblage to the east of the Ross River pluton are folded by the regional-scale isoclinal to tight upright Beresford Anticlinorium. Supracrustal units strike west-to-northwest and are steeply-dipping (Fig. 3.1b, 3.2). Discrete, narrow and widely-spaced brittle-ductile shear zones are well developed in the supracrustal and plutonic rocks. Most supracrustal rocks have been subject to greenschist facies metamorphism, with narrow zones of amphibolite facies assemblages developed along the margins of the Ross River pluton (Poulsen et al., 1996). Because primary textures are often preserved, we omit the prefix ‘meta’ in the interest of brevity.

### **3.3 Local lithology**

The following description is based on detailed geologic mapping of supracrustal and intrusive rocks hosting the Central Manitoba (scale 1:5000) and Ogama-Rockland gold deposit (scale 1:1000) (Zhou et al., 2012, 2013, 2014), as well as previously published descriptions.

More detailed studies on field relations were carried out on numerous stripped outcrops in the study area. Stratigraphic and structural aspects of supracrustal rocks in the vicinity of the Central Manitoba gold deposit have been extensively documented by previous workers (Fig. 3.3) (Stockwell and Lord, 1939; Brommecker et al., 1991, 1996; Poulsen et al., 1996; Anderson, 2013a, b; Zhou et al., 2013, 2014, 2016). The Ross River pluton, host of the Ogama-Rockland gold deposit, intruded volcanic, sedimentary and associated gabbroic rocks of the Bidou assemblage (Zhou et al., 2012, 2014). It mostly consists of plagioclase-quartz-biotite-hornblende-porphyritic (locally equigranular) tonalite and granodiorite, with minor quartz diorite, monzogranite and alkali feldspar granite (Fig. 3.4) (Anderson, 2008; Zhou et al., 2012, 2014). The contacts among these intrusive phases are often unexposed, but locally sharp contacts exist between tonalite and granodiorite. The magmatic interaction and evolution among differing intrusive phases are beyond the scope of this paper. We mainly focus on the tonalite phase since it is the direct host rock for the Ogama-Rockland gold deposit. Quartz feldspar porphyry dikes and aplite dikes are intimately associated with auriferous quartz-(carbonate) veins; therefore, their relative ages with respect to shear zones, quartz veins and gold mineralization is documented in detail.

### **3.3.1 Tonalite**

Tonalite of the Ross River pluton around the Ogama-Rockland gold deposit is subdivided into three types on the basis of mineralogy and igneous texture. Sharp irregular contacts between type-I and type-II tonalite are evident in the field (Fig. 3.5a). Type-I tonalite typically displays sparsely porphyritic texture. Phenocrysts mainly include euhedral plagioclase (2–5 mm), subhedral to anhedral quartz (~ 2 mm), locally elongate biotite (2–4 mm), and rarely K-feldspar (2–4 mm). The crystalline groundmass includes fine to medium grained (typically < 0.1 mm) plagioclase, quartz, biotite and minor K-feldspar. Alteration is evidenced by weak to intense saussuritization of zoned plagioclase (Fig. 3.6a, b) and various degrees of marginal replacement of biotite by chlorite (Fig. 3.6d). There is a weak planar feather defined by parallel or subparallel alignment of phenocrysts of euhedral plagioclase, elongate biotite and anhedral quartz (Fig. 3.6a, d). These phenocrysts are typically internally deformed when viewed under the microscope. Biotite and quartz grains typically exhibit undulose extinction (Fig. 3.6d). Plagioclase phenocrysts often show polysynthetic deformation twinning, whose twinning lamella are wedge-shaped and taper away toward undeformed domains (Fig. 3.6b). Primary polysynthetic twinning

with extremely straight lamellar form does occasionally occur within a few plagioclase crystals.

Type-I and type-II tonalites are identical in terms of mineral assemblage and modal proportion of both phenocrysts and fine-grained crystalline groundmass. However, type-II is different from type-I in terms of grain size: the groundmass of type-II is distinguishably coarser than that of type-I (Fig. 3.6c). Type-II tonalite has also undergone ductile deformation mesoscopically as evidenced by alignment of plagioclase, quartz and biotite phenocrysts (Fig. 3.5a). Constitute minerals are also deformed microscopically as revealed by quartz grains with undulose extinction (Fig. 3.6c).

Type-III tonalite is relatively undeformed (no discernible deformation) mesoscopically compared to the two types mentioned above, probably because it is more competent due to coarser-grained igneous texture. Local planar contacts between type-III and type-I tonalites were observed in the field (Fig. 3.5b).

Geochemically these three types of tonalite share similar trace element and rare earth element signatures, which are also similar to felsic volcanic rocks and some dikes around the area (Fig. 3.7a, b; Table 3.1). These geochemical characteristics are also similar to granodiorite in the northwestern portion of the Ross River pluton near the Rice Lake mine trend.

### ***3.3.2 Quartz feldspar porphyry dikes***

Quartz feldspar porphyry dikes are abundant in the study area. They intrude both supracrustal rocks of the Bidou assemblage and plutonic rocks of the Ross River pluton. Two varieties of quartz feldspar porphyry dikes are identified: one with larger euhedral plagioclase and rare rounded quartz phenocrysts (~ 2–5 mm) (QFP 1 in Fig. 3.5c), and one with smaller plagioclase and quartz phenocrysts (~ 1–2 mm) (QPF 2 in Fig. 3.5c). All quartz feldspar porphyry dikes are identical in modal proportion of phenocrysts and groundmass, and in the composition and texture of the aphanitic to very fine-grained groundmass. Primary contacts between these two dike varieties are locally obscured by intense ductile deformation (Fig. 3.5c). Most quartz feldspar porphyry intrusions display sharp planar contacts with wallrock tonalite or basalt. They are typically less than 1 m thick; mostly strike northwesterly to northeasterly and are steeply dipping (mostly > 70°) (Fig. 3.8a). A few quartz feldspar porphyry intrusions form irregular-shaped patches within tonalite, which can sometimes be traced to connected dikes. Least altered and least deformed quartz feldspar porphyry dike is identical to tonalite in trace element and rare earth element signatures (OG-11-07A, see Fig. 3.7a, b; Table 3.1), whereas an

altered quartz feldspar porphyry dike with numerous thin quartz veinlets is more depleted in light rare earth elements and shows an extreme negative Eu anomaly (102-13-228B1, see Fig. 3.7b; Table 3.1).

### 3.3.3 Aplite dikes

Aplite dikes intrude supracrustal rocks and plutonic rocks in the study area, but are only abundant close to or within the Ross River pluton. They are typically ~ 10–30 cm thick, with a maximum thickness of ~ 50 cm. They always display sharp curviplanar contacts with wallrock tonalite. They often show fine-grained sugary texture, which locally grades into porphyritic texture with pink alkali feldspar phenocrysts, or quartz, plagioclase and biotite phenocrysts. Biotite modal proportions increase (from 5–10 % to 15–20 %) toward the contacts. The aplite dikes typically contain a central zone, less than 0.5 cm thick and extending tens of centimeters along strike, composed of quartz, microcline and albite (aplite dike 2 in Fig. 3.5d; Fig. 3.5e). A few aplite dikes contain continuous vein-like bodies of reddish or smoky quartz along the dike centres; these are < 1 cm thick and pinch out along strike with the aplite dikes (aplite dike 4 in Fig. 3.5d; Fig. 3.5f); or they are continuous into quartz veins without bounding dike material. Some aplite dikes lack quartz segregations or quartz veins.

Aplite dikes are mostly steeply dipping and their strikes span a wide range from outcrop to outcrop (Fig. 3.8b). Their emplacement may have taken place over several stages, based on complex crosscutting relationships among aplite dikes of diverse orientations. Some of these crosscutting relations include apparent offsets with differing relative movement along specific directions, suggesting planar fractures must have controlled the emplacement of a few aplite dikes, and were reactivated by later deformation (Fig. 3.5d).

## 3.4 Structural geology

Four main generations of ductile and brittle-ductile deformation structures have been identified in supracrustal rocks adjacent to the Ross River pluton (Zhou et al., 2016). However, only two generations of ductile deformation structures, as well as brittle faults, have been recognized on the basis of overprinting relationships within the Ross River pluton in the area of the Ogama-Rockland gold deposit (Fig. 3.4). First and second generation structures are termed  $G_1'$  and  $G_2'$  structures. Associated foliation, lineation and folds are termed  $S_1'$ ,  $L_1'$ ,  $F_1'$ , and  $S_2'$ ,  $L_2'$ ,  $F_2'$ , respectively.

### **3.4.1 First generation ( $G_1'$ ) structures**

First generation structures comprise a pervasive foliation ( $S_1'$ ) and a locally developed lineation ( $L_1'$ ) in most intrusive phases of the southeastern Ross River pluton. Associated  $F_1'$  folds are locally developed. The  $S_1'$  foliation,  $L_1'$  lineation and  $F_1'$  folds were produced during  $G_1'$  ductile shearing.

The  $S_1'$  foliation is predominantly defined by a preferred orientation of euhedral plagioclase, ellipsoid quartz and stretched biotite/hornblende (Fig. 3.9a). In some locations where mafic minerals are rare,  $S_1'$  foliation is purely defined by ellipsoid smoky quartz, which is parallel to a few smoky quartz veinlets (Fig. 3.9b). The deformed magmatic minerals are still individually distinct and do not conjoin to form continuous folia. The foliation is commonly homogeneous at the outcrop scale. The  $S_1'$  foliation dips moderately to steeply to the northwest or southeast (Fig. 3.10a). However, in most outcrops, only strikes of  $S_1'$  foliation can be determined due to the lack of vertical surfaces. The strike of  $S_1'$  foliation varies from northeast to east (typically  $060^\circ - 070^\circ$ ; Fig. 3.10b). This variation in orientation results from the influence of late ductile shear zones or from foliation refraction, in locations where two lithologies of contrasting competency exist. The  $S_1'$  foliation curves smoothly into late west-to-northwest-trending ductile shear zones and grades into a continuous foliation. Foliation refraction between two types of tonalite is often visible (Fig. 3.5a): the angle between foliation and the contact is larger in type-II tonalite than that in type-I tonalite, suggesting competency of type-II tonalite is greater than that of type-I tonalite. Similar foliation refraction also exists between quartz feldspar porphyry dikes and tonalite, indicating that the quartz feldspar porphyry dike is less competent than tonalite (Fig. 3.7c). These examples of foliation refraction presented here illuminate that grain size is an important mechanical factor that results in competency contrast when two lithologies of similar mineralogy coexist.

The  $L_1'$  lineation is defined by a preferred orientation of quartz, biotite/hornblende and/or feldspar in felsic intrusive rocks. It plunges shallowly to the southwest east of the Ogama shaft, and plunges shallowly to the east or northeast close to the Rockland shaft (Fig. 3.10a).

$F_1'$  folds mainly comprise tight-to-open upright folded fractures partially filled with quartz veins.  $F_1'$  folds are typically associated with a well-developed axial plane  $S_1'$  foliation (Fig. 3.9d). The hinges of  $F_1'$  folds are rarely measurable.  $F_1'$  folds are symmetrical or asymmetrical, with an amplitude of 1 – 2 m and wavelength of less than 10 m. The symmetry can be disturbed

by heterogeneous lithologies or late shear zones (Fig. 3.9d).

### **3.4.2 Second generation ( $G_2'$ ) structures**

Second generation ( $G_2'$ ) structures comprise various shear zones of differing orientations and kinematics, interpreted to represent a conjugate set. Based on deformation behavior of crosscut markers, shear zones vary from brittle to brittle-ductile or ductile (Ramsay, 1980). Brittle faults are defined by a clear discontinuity that is less than half a centimeter thick or with negligible thickness. Wallrock on the sides of brittle faults are typically unstrained or occasionally brecciated. Crosscut aplite dikes are displaced with minor offsets by brittle faults (Fig. 3.11a, b). Aplite dikes and brittle faults are very steeply dipping (Fig. 3.8b, 3.13a). Two main sets of brittle faults were identified in terms of kinematics and orientation: north-northeast to northeast striking sinistral; west-southwest to north-northwest striking dextral, with two examples that strike north-northeast (Fig. 3.13a). Based on local crosscutting relations, which show that dextral faults displace sinistral faults, dextral faulting was, at least locally, younger (Fig. 3.11b). This relative timing relationship is also in agreement with crosscutting fracture-controlled aplite dikes (Fig. 3.5d).

Second generation ( $G_2'$ ) structures also comprise two sets of ductile or brittle-ductile shear zones (Fig. 3.11c): west-southwest to north-northwest-trending dextral and north to northeast-trending sinistral, although two examples of northwest-trending sinistral shear zones were also mapped (Fig. 3.13b). All shear zones are steeply dipping (mostly  $> 75^\circ$ ) (Fig. 3.13b). The sinistral shear zones are typically less than five centimeters thick. They can be brittle-ductile, with the bulk ( $S_1'$ ) foliation in wallrock tonalite and distorted aplite dikes dragged into the discontinuity (Fig. 3.11d). They can also be ductile shear zones, within which deformation and differential displacement of wallrock tonalite were entirely accommodated by ductile flow; no discontinuities can be seen at the outcrop scale.

The dextral ductile and brittle-ductile shear zones are dominant around the Ogama-Rockland gold deposit. They can be several or tens of centimeters thick, or up to one meter thick and are typically filled with foliated and lineated fine-grained protomylonite, mylonite or ultramylonite. Aplite dikes oriented at high angles to these shear zones are often thinned, sometimes broken apart and dragged into these shear zones (Fig. 3.11f). The S, C, and C' foliations (Berthé et al., 1979) are well developed within ductile shear zones. The curviplanar S foliation (mylonitic foliation) is typically outlined by: (i) aligned  $\sigma$ -type mantled plagioclase or rarely K-feldspar

porphyroclasts (Fig. 3.11f); (ii) ribbons or elongate aggregates of slightly elongate quartz that were derived from dynamic recrystallization of magmatic quartz crystals (Fig. 3.14a, b, c); (iii) aligned recrystallized biotite/muscovite grains (around ten to thirty microns in width) derived from magmatic biotite grains (Fig. 3.14a, b); (iv) aligned sericite and clay mineral aggregates, which are alteration products of precursor plagioclase (Fig. 3.14d). C foliation (shear foliation) is often apparent as curviplanar or planar discontinuities in the field. It parallels the bulk shear zone boundary. C foliation is typically defined by: (i) thin layers of dynamically recrystallized, very fine-grained quartzofeldspathic and carbonate grains (Fig. 3.14a, d), or tourmaline aggregates (Fig. 3.12b); (ii) folia of recrystallized mica or clay grains, which is formed by corresponding S foliation wrapping around feldspar augens or ellipsoid aggregates of recrystallized quartz grains and curving smoothly into C foliation (Fig. 3.14b, c). C foliation is at an acute angle ( $< 45^\circ$ , usually  $\sim 30^\circ$ ) or subparallel to S foliation (Fig. 3.11f, g, h; 3.14). C' foliation (Berthé et al., 1979), or shear band cleavage (Roper, 1972; White, 1979; Gapais and White 1982), or extensional crenulation cleavage (Platt and Vissers, 1980), is typically also defined by thin layers of very fine-grained recrystallized quartzofeldspathic grains or folia of recrystallized mica or clay grains. It is also defined by penetrative parallel planar discontinuities in the field. C' foliation is at a small angle to the shear zone boundary, typically around  $30^\circ$ . It is also oblique to S foliation ( $< 45^\circ$ ). C' foliation always crosscuts S and C foliations, which means it formed late during shearing with respect to S and C foliation (Fig. 14c). The deflection of S foliation at the intersection to C' foliation always agrees with the deflection of S foliation at the intersection to C foliation within one ductile shear zone, and is consistent with the curvature of S foliation or aplite dike markers approaching the shear zone. Therefore, S-C' fabric is always synthetic to S-C fabric and bulk shear zone kinematics.

Two types of L<sub>2'</sub> lineations, typically well developed on C foliation, were distinguished in the field: tourmaline slickenline lineation and ridge-in-groove striation. Tourmaline slickenline lineation is mostly defined by a shape preferred orientation of moderately elongate tourmaline grains or aggregates (Fig. 3.12a), or sometimes by alignment of continuous extremely elongate tourmaline crystals (Fig. 3.12b). It often plunges shallowly or moderately on the slip surface of north-to-northeast-striking sinistral brittle faults (Fig. 3.12a, 3.13a, c) or associated vein margins. It also plunges subhorizontally to shallowly on C foliation or associated vein margins of west-to-northwest-striking dextral ductile or brittle-ductile shear zones (Fig. 3.12b, 3.13b, d).

Ridge-in-groove striation (Means, 1987; Lin and Williams, 1992), mostly plunges shallowly or subhorizontally, on C foliation or associated vein margins in dextral (Fig. 3.12c, d) and sinistral ductile or brittle-ductile shear zones, or rarely in northwest-striking dextral brittle faults (Figs. 3.13c, d). Steps, which are also well developed on the C foliation, are typically orthogonal to the ridge-in-groove striation (Fig. 3.12c, d). Although steps can be incongruous (along micro-scale S foliation) or congruous (which truncate micro-scale S foliation) with respect to bulk shear zone kinematics (Lin and Williams, 1992; Doblas, 1998), our field observations suggest these steps are predominantly congruous in northwest-striking steeply-dipping dextral ductile shear zones (Fig. 3.13c, d) and in northeast-striking steeply-dipping sinistral brittle faults (Fig. 3.13a). Ridge-in-groove striation on well-developed curviplanar C foliation, is interpreted to parallel the shear direction because insignificant rotation has occurred on the C foliation, and therefore is a reliable shear sense indicator (Lin et al., 2007). The tourmaline lineation typically parallels the ridge-in-groove striation (Fig. 3.13a), which is interpreted to indicate that hydrothermal fluid precipitation was post-dated by at least some shearing increments. Both lineations mostly plunge shallowly or horizontally, which indicates that the along-strike, boundary-parallel shearing component was dominant during deformation.

The dextral and sinistral shear zones are interpreted as a conjugate set on the basis of mutual overprinting relationships observed in continuous outcrop exposures (Fig. 3.11c, 3.15a). However, the conjugate set is not equally developed: north-northwest dextral ductile shear zones are mostly thicker and more continuous (Fig. 3.11c, 3.15a). Shear zone thickness is considered roughly proportional to its relative age when rocks are rheologically homogeneous (Mitra, 1979), although strain softening or strain hardening can influence this relationship (Hull, 1988; Means, 1995). Crosscutting relationships at the intersections between shear zone sets is direct unambiguous evidence of their relative timing (Schwarz and Kilfitt, 2008; Carreras et al., 2010). The thicker west-to-northwest-trending dextral shear zones typically crosscut and displace thinner north-to-northeast-trending sinistral shear zones (Fig. 3.15a), which indicates the former succeeded the latter. More often, north-trending sinistral shear zones are dragged continuously into northwest-trending ductile shear zones in a dextral manner on the basis of mylonitic foliation deflection; and S-C' fabric at the intersection between those two conjugate sets also indicates the northwest-trending dextral ductile shear zones succeeded the north-trending sinistral ones (Fig. 3.16c, d).

As pointed out by Carreras et al. (2010), the geometric configuration and kinematic framework of an anastomosing network of natural ductile shear zones can vary considerably. Similar to their brittle counterparts (Anderson, 1951), conjugate sets of ductile shear zones intersect at an acute angle (e.g., Lamouroux, 1991). The principal direction of finite shortening deduced from the kinematics bisects the acute angle of the conjugate set (Fig. 3.17a; Lamouroux, 1991). The angle facing the maximum bulk shortening direction can also be almost perpendicular (Fig. 3.17b; Carreras, 2010), or obtuse for most ductile shear zones (Fig. 3.17c; Ramsay, 1980; Gapais et al., 1987; Marquer et al., 1996). Some sets might have an octahedral configuration (Mitra, 1979), or more complex and less regular arrangement (Bhattacharyya and Hudleston, 2001). Based on our field observations, the angle facing the maximum bulk shortening direction of the conjugate set varies from outcrop to outcrop. It can be acute (Fig. 3.11c, 3.19a), or obtuse (Fig. 3.18, 3.19) or nearly orthogonal (Fig. 3.19). There are dextral brittle shear fractures and dextral ductile shear zones along the same strike; and one brittle shear fracture gradually changes into one brittle-ductile shear fracture with decreasing apparent horizontal displacement northwestward (Fig. 3.16e, f). Several meters northwestward along strike, this fracture becomes a ductile shear zone with classical S-C fabric. It is possible that these ductile shear zones nucleated and were localized along precursor joints or brittle shear fractures (e.g., Mancktelow and Pennacchioni, 2005; Pennacchioni, 2005), as illustrated by Fig. 3.15e and f. This may explain the maximum finite strain direction facing the acute angle of ductile conjugate sets, which is identical to brittle conjugate faults. However, final orientations of ductile conjugate sets may reflect rotation and displacement during progressive deformation, which is described from natural examples (e.g., Carreras et al., 2010), numeral modeling (Mancktelow, 2002) and analogue experiments (Schwarz and Kilfitt, 2008). This may explain why the direction of bulk shortening mostly bisects the obtuse angle of ductile conjugate sets after a certain amount of rotation, whereas the original angle can be acute (Schwarz and Kilfitt, 2008) or almost perpendicular (Mancktelow, 2002; Carreras et al., 2010).

West-trending subvertical brittle fractures are locally dragged into northwest-trending ductile shear zones, indicating that ductile shearing at least locally postdates some increments of brittle deformation (Fig. 3.19e). However, most brittle deformation postdates ductile shearing at some places. Brittle fractures locally show the classic “Riedel shears” pattern (R-, R'-, P-, Y-shears, and extensional T-fractures), each with a characteristic orientation and shear sense (Fig.

3.16a, b; Riedel, 1929). Shear sense is mostly determined by deflection of the foliation, since suitable displaced markers are not available. As illustrated in Fig. 3.16a and b, the mylonitic foliation ( $S_M$ ) is deflected by R- and P-shears in a dextral manner, indicating dextral brittle faulting postdates ductile shearing. These brittle fractures typically crosscut veins (Fig. 3.16), indicating some brittle deformation occurred after vein formation.

We have described brittle faults together with ductile shear zones due to inevitable spatial relations, but this does not imply all brittle faults were formed penecontemporaneously with their ductile counterparts.

### 3.5 Vein system

Veins crosscut tonalite, granodiorite and other intrusive phases of the Ross River pluton throughout the Ogama-Rockland gold deposit area. Veins are intimately spatially associated with aplite dikes and deformation structures in the study area. To reveal lithologic and structural control of vein formation and deformation, we have conducted detailed mapping on several continuous stripped outcrops. We document the sequential development of veining with respect to their associated structures.

#### 3.5.1 $V_1'$ veins

$V_1'$  veins typically fill in fractures that were folded by  $F_1'$  folds (Fig. 3.9d, 3.20), or locally fill in fold axial plane  $S_1'$  cleavage (Fig. 3.20). Vein thickness varies from 1 to 50 cm, and generally increases in fold hinges and decreases on fold limbs, or where veins approach shear zones. These veins are massive and smoky. They often show reddish brown color pervasively on weathered surface, probably due to weathering of metal sulfides.  $V_1'$  veins consist of over 90 % quartz, 5% phyllosilicate (sericite, chlorite) and carbonate minerals, with less than 5 % sulfides (chalcopyrite, pyrite, molybdenite) and their oxidation or weathering products (malachite, goethite), and gold. The origin of initial cracks is indeterminable, which might be joints or shear fractures. Most  $V_1'$  veins are interpreted to be emplaced before  $F_1'$  folding with possibly minor ones early during  $G_1$ . These veins are locally dragged and displaced by northwest-trending  $G_2'$  dextral ductile shear zones (Fig. 3.20).

#### 3.5.2 $V_2'$ veins

$V_2'$  veins are sheeted, spaced tens of centimeters to one meter apart, strike northwesterly to north-northwesterly and dip very steeply (Fig. 3.21a). They are mostly smoky, massive and from

1 to 20 cm thick.  $V_2'$  veins consist of over 95 % blocky or massive quartz ( $\pm$  carbonate), with less than 5 % sulfides (predominantly pyrite, chalcopyrite and molybdenite) and traces of phyllosilicate minerals (sericite, chlorite), and gold.

$V_2'$  veins display complex crosscutting relationships with pinkish aplite (locally K-feldspar-phyric) dikes. As shown in Fig. 3.21a, b and c, there are two main sets of steeply dipping aplite dikes: northeast-striking planar and west-northwest-striking curviplanar. The west-northwest-striking dikes also contain aggregates of molybdenite and traces of chalcopyrite and pyrite. Northeast-striking aplite dikes are cut and displaced by west-northwest-trending aplite dikes for an apparent horizontal offset of  $\sim$  6–15 cm along strike in a dextral shear sense (Fig. 3.21b). Northwest-striking  $V_2'$  veins offset northeast-striking aplite dikes with a horizontal displacement of  $\sim$  5 cm (Fig. 3.21b), and are cut by west-northwest-trending aplite dikes with no discernible displacement (Fig. 3.21b, c). Therefore, chronologic order of emplacement of  $V_2'$  veins and aplite dikes at this location is: northeast-trending aplite dikes, followed by northwest-trending  $V_2'$  veins, and west-northwest-trending aplite dikes.

$V_2'$  veins and the two aplite dike sets shown in Fig. 3.21 are not hosted by ductile shear zones. Thus, associated offsets were probably accomplished by precursor brittle shears before dike or vein fillings, or by open-space filling during oblique dilation of pre-existing brittle fractures (joints). A west-northwest-trending shear fracture that parallels aplite dikes also cuts northeast-trending aplite dikes and some northwest-trending veins in a dextral brittle manner, or slightly deflects one northwest-trending vein in a brittle-ductile manner (Fig. 3.21b). A west-southwest-trending vertical sinistral brittle-ductile shear zone cuts aplite dikes and  $V_2'$  veins with a horizontal offset of  $\sim$  25 cm (Fig. 3.11d). There are also parallel arrays of west-southwest-trending brittle shear fractures that offset  $V_2'$  veins by little (< 1 cm) sinistral horizontal displacement (Fig. 3.21c), which are presumably kinematically related to the adjacent subparallel sinistral brittle-ductile shear zone. The west-northwest-trending dextral and west-southwest-trending sinistral brittle-ductile shear zone are interpreted as conjugate sets, with the maximum finite strain axis (approximately north-trending) bisecting the obtuse angle of conjugate sets. This estimated maximum finite strain direction is at a high angle ( $\sim$  70°) to the bulk foliation ( $S_1'$ ) in tonalite, and at a small angle to north-northwest-trending  $V_2'$  veins. Therefore, the  $V_2'$  veins and associated deformation structures can be interpreted to have formed during progressive deformation with compatible kinematics and geometry: northwesterly to

north-northwesterly striking  $V_2'$  veins filled in synthetic dextral R-shears during oblique-extensional opening, and were cut by later synthetic dextral P-shears and antithetic sinistral R'-shears. Alternatively, the  $V_2'$  veins were emplaced before or early during  $G_1'$  shearing and later displaced by  $G_2'$  shear zones.

### 3.5.3 $V_3'$ veins

$V_3'$  veins are sheeted, spaced 5–10 cm apart and form subparallel arrays or stockworks that contain two sets of near-orthogonal veins (Fig. 3.22a).  $V_3'$  veins contain predominantly quartz ( $\pm$  carbonate, sericite) with traces of chalcopyrite, pyrite and molybdenite. These veins are all steeply dipping. West-trending veins are typically less spaced than the north-trending ones. They merge with each other at the intersection, indicating these two sets were emplaced contemporaneously. They often show apparent displacement along their orientations: west-trending vein sets dextrally offset a few north-trending veins by 1 – 3 cm, whereas north-trending veins sinistrally offset a few west-trending ones by 3 – 5 cm (Fig. 3.22a). Individual veins (0.5 – 5 cm thick) are typically smoky, laminated or locally brecciated. The laminae are defined by white tonalite or yellowish aplite slivers that appear to be the same as wallrock tonalite or aplite dikes that host veins (Fig. 3.22b).  $V_3'$  veins locally contain elongate tonalite or aplite fragments (microlithons) (Fig. 3.22b). No ductile shear zones are discernible bounding  $V_3'$  veins. Based on the above observations, it is interpreted that  $V_3'$  veins were emplaced during the multiple opening/shearing of precursor brittle orthogonal conjugate faults, which enclose several tonalite or aplite slivers or fragments from adjacent host rocks. Pre-existing north-trending brittle faults were sinistral and west-trending ones were dextral, which are consistent with kinematic interpretations of brittle faults mentioned in the structural geology section (Fig. 3.13a). Moreover, it is possible that north-trending and west-trending brittle conjugate faults were penecontemporaneously developed in a pulsing manner, with mutual crosscutting relationships between two conjugate sets (Fig. 3.22a), whereas mostly west-trending dextral brittle faults postdate north-trending sinistral ones (Figs. 3.11b, 3.5d). An alternative explanation is that  $V_3'$  veins were emplaced before significant  $G_2'$  shearing and displaced by  $G_2'$  conjugate shear zones.

$V_3'$  veins postdate  $V_2'$  veins based on crosscutting relationships between west-northwest-trending aplite dikes and these two veins. As illustrated in Fig. 3.21, northwest-trending  $V_2'$  veins postdate two west-northwest-trending aplite dikes since  $V_2'$  veins are cut by west-northwest-trending aplite dikes. On another outcrop (Fig. 3.22) just approximately 50 meters

northeast of the one in Fig. 3.21, a few west-trending  $V_3'$  veins occur in the center of west-northwest-trending aplite dikes and enclose some aplite fragments or slivers, indicating  $V_3'$  veins postdate west-northwest-trending aplite dikes. Thus,  $V_3'$  veins postdate west-northwest-trending aplite dikes.

### **3.5.4 $V_4'$ veins**

$V_4'$  veins are north-to-northeast-striking, steeply dipping,  $\sim 30 - 50$  cm thick and composed of massive quartz. These veins are not homogeneous in terms of white and smoky quartz color (Fig. 3.23a). The smoky portion is rich in crenulated or blade-shaped molybdenite, irregular-shaped chalcopyrite and euhedral or subhedral pyrite. Most west-trending aplite dikes are cut by  $V_4'$  veins with a discernible displacement of several centimeters, indicating  $V_4'$  veins were formed during oblique dilation with both boundary-normal and boundary-parallel components (Fig. 3.23b). One  $V_4'$  vein cuts across west-striking sheeted  $V_3'$  veins and associated aplite dikes in one outcrop, indicating  $V_4'$  veins at least locally postdate  $V_3'$  veins and associated aplite dikes (Fig. 3.23a). Locally slightly deflected  $V_3'$  veins on both sides of this  $V_4'$  vein suggest minor sinistral shearing along  $V_4'$  vein margins, which might result from sinistral reactivation during  $G_2'$  shearing. This  $V_4'$  vein has been displaced by a northwest-striking steeply-dipping  $G_2'$  dextral ductile shear zone, indicating  $V_4'$  veins at least locally predate  $G_2'$  shearing.

### **3.5.5 $V_5'$ veins**

$V_5'$  veins are dominant around the Ogama-Rockland gold deposit. They contain high grade gold. They can either be smoky or milky white. They can be continuous curviplanar bodies or discontinuous lenses that extend hundreds of meters along strike. They are mostly tens of centimeters thick, and up to 1 m thick. Most of them strike westerly to north-northwesterly, and dip steeply (mostly  $> 65^\circ$ ) to the north or south; a few of them strike northerly to northeasterly and dip steeply or subvertically (Fig. 3.24). These two vein sets are hosted by  $G_2'$  conjugate sets of west-to-northwest-striking dextral ductile shear zones and north-to-northeast-striking sinistral ones. A few vein sets dip steeply to vertically and strike northwesterly to northerly, which are inclined to associated shear zones; they are not hosted by  $G_2'$  ductile shear zones but are possibly kinematically and genetically related to  $G_2'$  shearing. Most auriferous veins are west-to-northwest-striking shear-hosted veins, or fault-fill veins. It is often seen that  $G_2'$  shear zone-hosted  $V_5'$  veins cut across earlier  $V_4'$  veins at a high angle (Fig. 3.19d).

$V_5'$  veins typically consist of over 85% quartz, ~ 10% alteration minerals (in order of decreasing content: carbonate, sericite, chlorite, ± apatite), and ~ 5% sulfide minerals (mainly pyrite, chalcopyrite, bornite, ± molybdenite), goethite, malachite and free gold (mostly electrum). Most auriferous veins are bounded by ankerite-sericite-chlorite (Fig. 3.19b) or sericite alteration halos (Fig. 3.19c); a few are bounded by altered aplite dikes (Fig. 3.11f, 3.25f).  $V_5$  veins are rich in molybdenite at outcrops close to the Rockland mine, whereas at outcrops close to the Ogama mine  $V_5'$  veins with visible gold seldom contain any molybdenite.

$V_5'$  fault-fill veins occur in the centres of  $G_2'$  ductile shear zones or along the margins. There is a variety of internal structures associated with  $V_5'$  fault-fill veins. They can be massive (Fig. 3.25a), laminated (Fig. 3.16c, 3.25b), brecciated (Fig. 3.25c), or show complicated internal structure identical to S-C fabric (Fig. 3.25d). The lamination within fault-fill veins is defined by compositional layering of parallel wallrock slivers and veinlets. These internal structures are interpreted to have developed during  $G_2'$  shearing: fault-fill veins enclose sheared tonalite or aplite dike wallrock slivers or fragments (microlithons) (Fig. 3.25a, b, d), indicating fault-fill veins postdate some shearing increments; these fault-fill veins are superimposed by late  $G_2'$  shearing, as evidenced by ridge-in-groove striations on vein margins. Brecciated veins were probably formed during shearing at low ductility, since they contain minor foliated wallrock microlithons. Veins might have filled in micro-dilational jogs along the S and C foliations within ductile shear zones to form S-C-fabric-like structure. The opening mechanism for most fault-fill massive veins is dilation of C foliation in  $G_2'$  ductile shear zones. A few laminated fault-fill veins contain less deformed or apparently undeformed tonalite microlithons, and the lamination is subparallel to brittle-ductile shear zone boundaries (Fig. 3.15b, c). These observations indicate some laminated veins might have formed during oblique dilation of initial brittle P shears of a brittle shear zone (Riedel, 1929; Tchalenko, 1968; Hodgson, 1989), and later reactivated by ductile shearing with the same shear sense (Fig. 3.15e).

$V_5'$  extension veins are typically oriented at a moderate to high angle to ductile shear zones. They are often displaced by  $G_2$  ductile shear zones but merge with  $V_5'$  hosted fault-fill veins (Fig. 3.18a); therefore, these extension veins were crystallized synchronously with  $V_5'$  fault-fill veins and predate some  $G_2'$  shearing increments. The dilation of extension veins is compatible with the kinematics of associated ductile shear zones. Hence, these extension veins are interpreted to have filled in extensional fractures early during  $G_2'$  shearing, and were later

dragged by continued  $G_2'$  shearing.

$V_5'$  fault-fill and extension veins display intimate spatial relationships with aplite dikes. As shown in Fig. 3.18a, north-northwest-trending and northeast-trending aplite dikes with discontinuous quartz segregations (or continuous quartz veins) are truncated and displaced by west-northwest-trending  $V_5'$  fault-fill veins or folded by associated dextral  $G_2'$  ductile shear zones (Fig. 3.11f, 18b). These aplite dikes are therefore older than  $V_5'$  fault-fill veins but must have emplaced before or early during  $G_2'$  shearing. Quite a few laminated  $V_5$  fault-fill veins are bounded by white aplite (locally porphyritic) dikes with a well-developed S-C ( $G_2'$ ) structure (Fig. 3.18c, 3.25d), indicating aplite dikes were probably emplaced before or during  $G_2'$  shearing.  $V_5'$  fault-fill veins definitely postdate bounded aplite dikes since they encompass white aplite slivers. Northwest-trending aplite dikes that bound  $V_5'$  veins postdate north-trending aplite dikes based on local crosscutting relationships (Fig. 3.25f). A few aplite dikes die out gradually along strike on  $V_5'$  vein margins. Some vein-centered aplite dikes are cut by S-C structured  $V_5'$  fault-fill veins (Fig. 3.25d) and the vein in the center of aplite dikes merge with S-foliation-parallel veinlets of  $V_5'$  fault-fill veins (Fig. 3.25e). Therefore, the continuous planar vein in the center of aplite dikes was synchronously emplaced with  $V_5'$  fault-fill veins.

### 3.6 Gold distribution and its structural control

#### 3.6.1 Gold distribution and related structures on an ore-body scale

Gold is heterogeneously distributed among auriferous veins, as revealed by grade distribution within a  $V_5'$  vein from the perspective of a vertical block model longitudinal section (Fig. 3.26). Higher-grade shoots plunge steeply towards the northwest in the northwest-striking subvertical veins (Fig. 3.26). This steep plunge of ore shoots is compatible with the intersection lineation between the average orientations of the shear zone conjugate set (Fig. 3.27). It is also parallel to the intersection lineation between the average orientation of the northwest-striking auriferous shear zones and that of the  $S_1'$  foliation (Fig. 3.27). The plunge of ore shoots is at a high angle or almost perpendicular to the slip direction along northwest-striking gold-bearing shear veins, as defined by the shallowly-plunging mineral lineation or ridge-in-groove slickenside striation on vein margins (Fig. 3.27). These angular relationships between the plunge of ore shoots and the structural elements of host shear zones, combined with syn-deformational internal vein structures, suggest that gold mineralization is controlled by the progressive

development of active shear zones and vein formation.

### ***3.6.2 Structural control on gold mineralization on a microscopic scale***

In thin sections, gold and related sulfide minerals are hosted either by altered and deformed tonalite wallrock attached to vein margins (Fig. 3.28a) or mostly by fault-fill veins (Fig. 3.28b, c, d, e and f). They are intimately spatially associated with northwest-trending steeply-dipping G<sub>2'</sub> dextral ductile shear zones.

#### ***3.6.2.1 Microstructures in shear zones and auriferous veins***

In tonalitic shear zones attached to vein margins, sulfides are attached to quartz, plagioclase and secondary chlorite, and typically occur on mylonitic foliation wrapping around plagioclase porphyroclasts (Fig. 3.28a). Plagioclase grains usually display Carlsbad twinning and bent wedge-shaped polysynthetic twinning, and exhibit almost orthogonal cleavage sets (Fig. 3.28a). Elongate quartz phenocrysts typically show undulose extinction, and aligned quartz phenocrysts constitute the S<sub>1'</sub> foliation in tonalite (Fig. 3.28a). The S<sub>1'</sub> foliation is rotated clockwise by ~30° and curved into mylonitic (S<sub>2'</sub>) foliation in a micro-shear zone (Fig. 28a). Dextral shear sense is established by the S-C fabric and σ-type plagioclase porphyroclasts (Fig. 28a).

A prominent microstructural feature associated with auriferous shear veins is the extensive development of completely penetrative, 20–50 µm spaced, cubic-octahedral, transgranular fracture sets (England, 1979; Craig et al., 1998) on competent minerals like quartz and pyrite (Fig. 3.28b, c, d, e, f). The fracture sets are continuous within pyrite and quartz grains, may show refraction across pyrite-quartz or quartz-quartz grain boundaries. This brittle fracturing also occurs in dynamically recrystallized quartz phenocrysts (Q<sub>F</sub> in Fig. 3.28a) within or immediately close to tonalitic S-C mylonites in a micro-shear zone attached to shear veins, but appears not to have developed in dynamically recrystallized quartz phenocrysts (Q<sub>I</sub> in Fig. 3.28a) away from the micro-shear zone. This spatial relationship leads to the interpretation that the brittle fracturing might have been generated during ductile shearing: competent pyrite, less altered plagioclase and some quartz phenocrysts respond to stress in a brittle behavior, whereas incompetent minerals like chlorite, sericite and other clay minerals respond in a ductile way. This brittle fracturing seems to have occurred rather late during shearing, since fractures are through-going across quartz sub-grain boundaries defined by patchy undulose extinction (Fig. 3.28b).

#### ***3.6.2.2 Gold occurrences on a microscopic scale***

Most gold grains are electrum in composition, with gold to silver weight fraction ratios

ranging from 23:1 to 0.44:1 (Xue, 2011). The size of individual grains of gold ranges from 0.5 mm to 10 µm. Most of the gold occurs in fractures of quartz, pyrite or interstices of recrystallized quartz (Fig. 3.28b, c, e). In quartz veins, gold is commonly accompanied by pyrite, chalcopyrite and bornite (Fig. 3.28b, c, d, f).

Gold is commonly intimately associated with pyrite in the shear veins. In this case, gold occurs chiefly in the cubic fractures of the pyrite with relatively straight and sharp contacts to the pyrite (Fig. 3.28c), or occurs along pyrite grain boundaries forming discontinuous coatings on the surface of the pyrite grains (Fig. 3.28c, d). This occurrence of gold locally grades into gold in fractures and in interstices of pyrite and recrystallized quartz (Fig. 3.28c), indicating synchronicity of gold that fills fractures in pyrite and gold that coats pyrite.

In another setting, gold occurs as tiny globular inclusions (< 30 µm) in pyrite (Fig. 3.28c, d). These droplet inclusions are randomly oriented and heterogeneously distributed within the fractured pyrite (Fig. 3.28c, d).

In a few cases, gold forms irregular patches interstitial to recrystallized quartz (Fig. 3.28c, d, e), or linear fillings along the fractures of quartz (Fig. 3.28d). As irregular gold patches are observed to grade locally into linear fracture fillings (Fig. 3.28e), both occurrences of gold might have formed contemporaneously.

In some instances, gold occurs as irregular patches in contact with chalcopyrite (partially replaced by bornite along grain boundaries) and fractured quartz grains (Fig. 3.28f). This form of gold locally grades into gold that fills interstices of recrystallized quartz and gold that occupies fractures of quartz, indicating contemporaneity of these three gold occurrences (Fig. 3.28f).

### *3.6.2.3 Microstructural control on gold mineralization*

Visible native gold as micron-sized inclusions or fracture fillings spatially associated with sulfides is a common occurrence in Archean lode gold deposits (e.g., Gorman et al., 1981). The former occurrence is thought to be either a primary feature or due to remobilization of “invisible gold” (solid solution or submicroscopic particles; Cabri et al., 1989; Cook and Chryssoulis, 1990) in sulfides, whereas fracture-filling gold is generally considered as an outcome of subsequent remobilization of invisible gold (Mumin et al., 1994; Oberthür et al., 1997; Velásquez et al., 2014, and references therein). As described above, both forms of gold are present on the microscopic scale in shear veins at the Ogama-Rockland deposit. The micron-sized gold inclusions in pyrite do not appear to have a preferred orientation and are randomly-

distributed (Fig. 3.28c, d); therefore, this form of gold does not seem to be related to secondary deformation and could well be an independent depositional event separated from fracture fillings of gold.

Native gold along grain boundaries and fractures in shear veins represents most of the economic mineralization (Fig. 3.28c, d, e, f). Since gold occurs as irregular patches in grain boundaries interstitial to quartz, pyrite, chalcopyrite or bornite, this form of gold must have precipitated relatively late with respect to quartz and associated sulfides during the veining stage. In contrast, gold must have deposited along fractures during the opening of brittle fractures in pyrite and quartz. Local gradational relationships between gold in grain boundaries and gold in fractures indicate that fracture-filling gold could be a result of remobilization and reprecipitation of gold in mineral boundaries due to micro-fracturing of quartz and pyrite. It is uncertain whether gold along grain boundaries or in fractures was remobilized from invisible gold in pyrite, or it was simply a separate late gold introduction. Nevertheless, mineralization was enhanced by fracturing of pyrite and quartz and the main gold deposition and/or remobilization was structurally induced.

### 3.7 Discussions

#### 3.7.1 Localization and origin of shear zones

Brittle-ductile and ductile shear zones are nucleated and localized along primary lithologic heterogeneities, such as lithologic contacts (Fig. 3.5c), dikes (Fig. 3.18c), or veins (Fig. 3.25d). Primary lithologic heterogeneity leads to competency contrast such that the contact becomes a plane of weakness that can easily be activated or reactivated as brittle-ductile or ductile shear zones. Other recent studies have also suggested that compositional heterogeneity plays a major role in controlling the localization and nucleation of shear strain on the mesoscopic scale (e.g., Pennacchioni and Mancktelow, 2007; Pennacchioni and Zucchi, 2013). Competency contrast also results from secondary alteration processes. Altered tonalite is less competent than quartz veins due to enrichment of rheologically weak phyllosilicate minerals such as sericite and chlorite. Hence, ductile shear zones also favor alteration halos along veins (Fig. 3.19b). Some brittle-ductile or ductile shear zones simply reactivated joints or early brittle faults (Figs. 3.15a, 3.16c).

### **3.7.2 Genesis of Ogama-Rockland gold deposit**

Geometrical relationships of structures, veins and aplite dikes are summarized in Fig. 3.29. As described in the vein system (Section 3.5), V<sub>1</sub>' veins were mostly emplaced before G<sub>1</sub>' bulk shortening, with minor ones emplaced early during G<sub>1</sub>'. V<sub>2</sub>' veins were emplaced before main G<sub>2</sub>' shearing, but could be kinematically related to an early stage of progressive ductile shearing. Therefore, early gold mineralization associated with V<sub>1</sub>' and V<sub>2</sub>' veins might have occurred before main ductile shearing.

More significant gold mineralization associated with V<sub>5</sub>' veins at the Ogama-Rockland deposit seem to be controlled predominantly by secondary deformation structures. On a deposit scale, northwest-trending steep veins and host shear zones dominate the structural pattern and mine trend (Fig. 3.4, 3.29). On an outcrop scale, host shear zone conjugate sets control vein formation and deformation (Fig. 3.15, 3.19, 3.29). Most of the economic gold in V<sub>5</sub>' fault-fill veins was structurally induced on a microscopic scale as well (see Section 3.6.2). The spatial relationship of their structural elements to the plunge of ore shoots from a longitudinal section view also indicates an active development of shear zone and V<sub>5</sub>' vein formation and thus a structural control on gold mineralization.

### **3.7.3 Regional correlations of structure and metallogeny in the Rice Lake belt**

Although when modern-style plate tectonics operated is still controversial (Smart et al., 2016; Tang et al., 2016), there must have been plate-tectonics-like processes operating (“horizontal tectonism”; Lin, 2005) in the late Archean, considering progressive younging of supracrustal rocks from north to south across the western Superior Province in Manitoba and crustal Subprovince-scale strike-slip shear zones along lithotectonic terrane boundaries. Therefore, each gold deposit has been interpreted in the context of multiphase deformation events linked to Neoarchean accretionary and collisional orogenic processes under a contractional regime (Table 1). It is of vital importance to correlate auriferous host structures from different deposits to reveal regional structural evolution and its control on gold genesis. Based on our field observations and interpretations from recent literature, regional structural correlation has been performed and the relative timing of gold mineralization has been inferred. Each deposit in the Rice Lake belt (Table 3.2) has multiple stages of gold mineralization associated with specific generations of structure during orogenesis. Early tectonic events that were deemed to be associated with arc extension or initial back-arc spreading seldom triggered

gold deposition, but may have been important in creating a gold-enriched reservoir for later mineralizing events (e.g., Hronsky et al., 2012). Gold mineralization in the Rice Lake belt seems to have taken place during early sinistral-oblique collisional and crust thickening processes, and continued into late dextral transpressional and main terminal collisional processes. Therefore, from a structural perspective, most deposits within the Rice Lake greenstone belt fit in a classic orogenic gold system (Groves et al., 1998), including the late phase of gold mineralization at the Ogama-Rockland deposit.

The Ogama-Rockland gold deposit is interpreted to have experienced two generations of deformation under a relatively uniform strain field of north-northwest–south-southeast oriented shortening, while other deposits in the Rice Lake belt show evidence of early sinistral-oblique shearing under a strain field of northeast–southwest shortening followed by dextral transpression with northwest–southeast shortening. Direct evidence for early sinistral-oblique shearing appears to be missing in the Ross River pluton, which is probably due to complete overprint by late dextral shearing. The present northwest-trending subvertical dextral shear zones could originally have been northwest-trending subvertical fractures or cleavages that were associated with regional folding (Beresford Lake Anticlinorium) during early sinistral-oblique shearing. Another alternative explanation is the Ross River pluton was emplaced after the early sinistral-oblique shearing but before the late dextral transpression. This interpretation is unlikely according to regional correlations in the Rice Lake mine area northwest of the Ross River pluton: The Timiskaming-type conglomerate (San Antonio assemblage) contains tonalite clasts that were derived from the Ross River pluton, have experienced regional folding that is deemed to be associated with early sinistral-oblique shearing (Anderson, 2008). Therefore, the Ross River pluton, which is older than the San Antonio assemblage, must have emplaced before sinistral-oblique shearing.

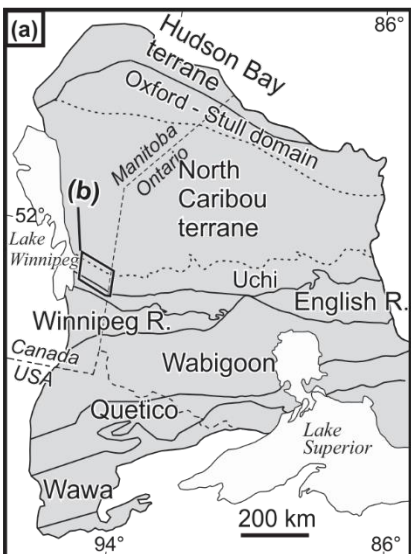
### 3.8 Summaries and Conclusions

The Ogama-Rockland deposit is an intrusion-hosted, shear-related and vein-type mesozonal gold deposit. Host plutonic rocks experienced  $G_1'$  bulk shortening and formed east-northeast–trending  $S_1'$  foliation and steep  $L_1'$  stretching lineation in various intrusive phases. The  $G_1'$  fabrics were clockwise rotated and overprinted by  $G_2'$  structures during regional dextral transpressional shearing.  $G_2'$  structures are manifest by steep mylonitic foliations and shallow

$L_2'$  tourmaline lineations and ridge-in-groove striations, within unequally developed conjugate sets of thick west-to northwest-trending dextral shear zones and thin north-to-northeast-trending sinistral shear zones. Deformation behavior of  $G_2'$  shear zones varied from brittle to brittle-ductile and ductile. It is interpreted that brittle-ductile and ductile shear zones were reactivated along precursor brittle faults, or developed along primary lithologic heterogeneities such as dikes or veins or secondary alteration halos.

Early gold introduction associated with folded  $V_1'$  veins and low grade planar extension  $V_2'$  veins occurred before  $G_2'$  deformation, and possibly before  $G_1'$  as well. Main gold mineralization/remobilization associated with auriferous northwest-trending steep  $V_5'$  shear veins occurred late during  $G_2'$  shearing. Most of the native gold occurs in fractures and grain boundaries of quartz, pyrite and chalcopyrite in shear veins, which reflects a strong structural and mechanical control on the microscopic scale. The steep plunge of ore shoots indicates that interactive development of shear zones and veins played a dominant role in localizing gold mineralization.

Our study unravels a fundamental structural control at all scales on gold mineralization, and an intimate interplay among shear zone development, vein emplacement and main gold mineralization during Neoarchean accretionary and collisional processes. A similar exploration model can be applied to other Archean lode gold deposits, especially those hosted in the felsic plutonic rocks near the greenstone-pluton contact.



**Rice Lake belt**

- Uchi subprovince (2.75–2.69 Ga)
  - Edmunds assemblage (2.71–2.69 Ga)
  - San Antonio assemblage (<2.705 Ga)
  - Gem assemblage (2.73–2.72 Ga)
  - Ross River plutonic suite (2.73–2.72 Ga)
  - Bidou assemblage (2.75–2.73 Ga)

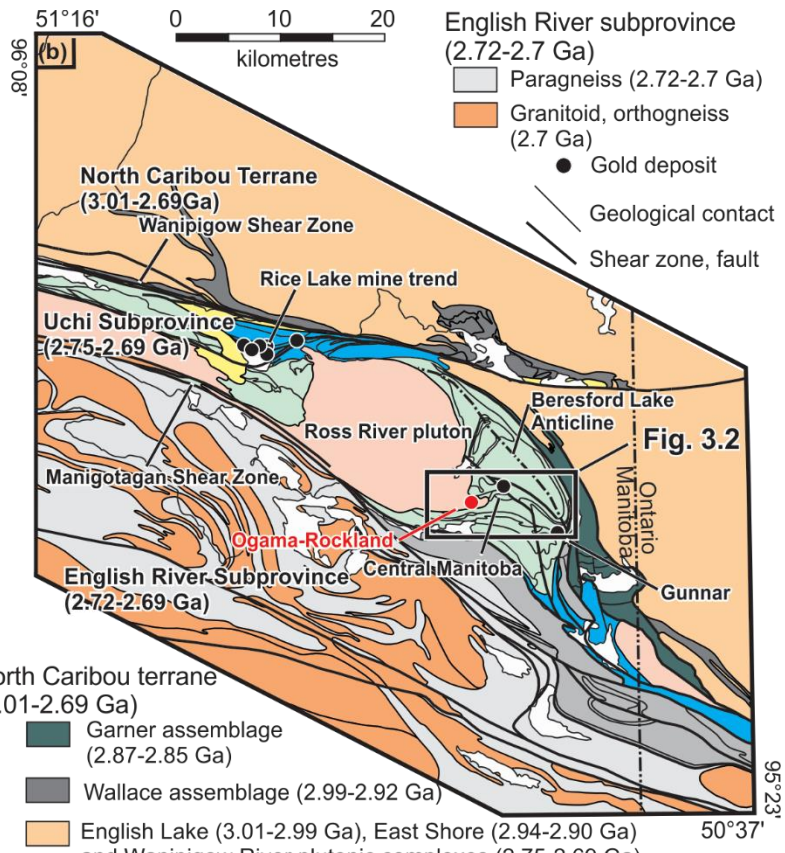


Figure 3.1 a) Tectonic framework of the western Superior Province, showing major Subprovinces, domains and terranes; modified from Lin and Beakhouse (2013); b) Regional geologic map of the western Superior Province in southeastern Manitoba, illustrating two major Subprovinces and one terrane, terrane boundaries, significant gold deposits and U-Pb zircon age constraints; modified from Anderson (2013a). See text for age data sources.

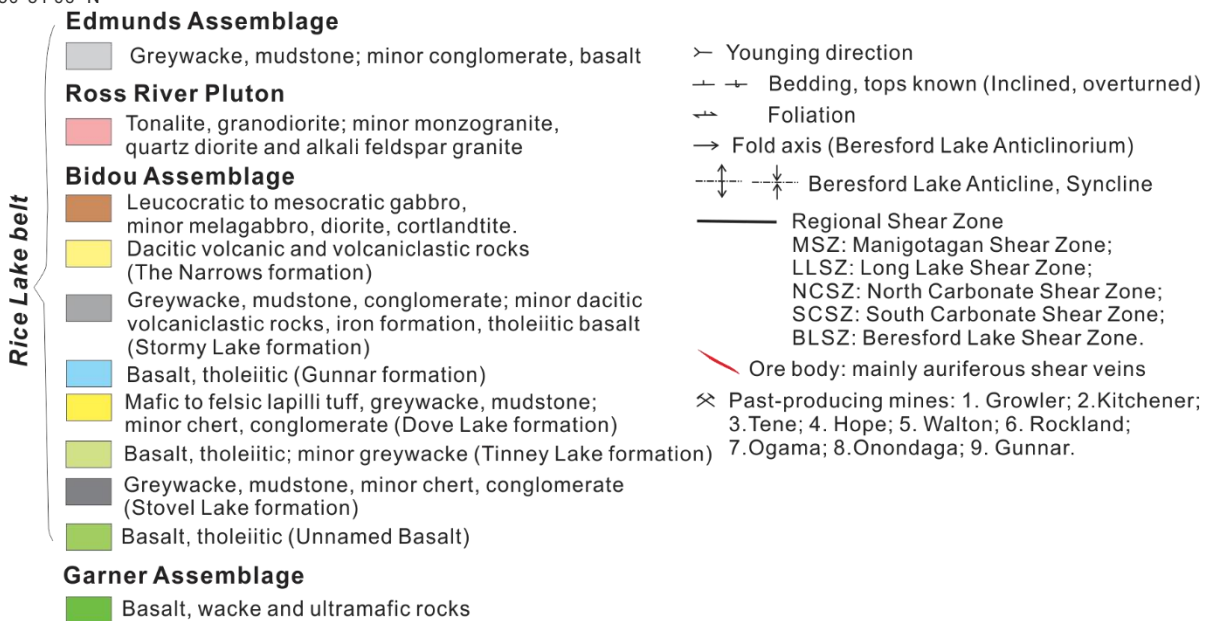
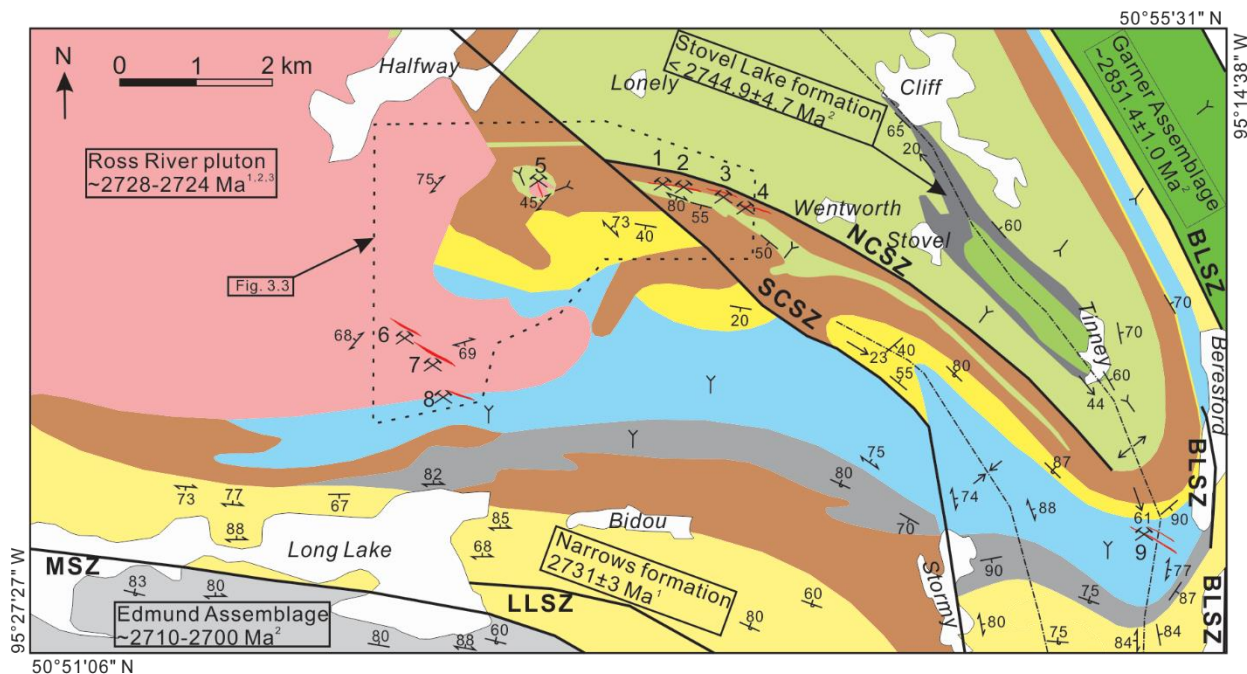


Figure 3.2 Generalized regional geologic map of the Bidou assemblage and Ross River pluton in the southeastern Rice Lake greenstone belt in southeastern Manitoba, showing principal formations, lithologic units, deformation structures, U-Pb zircon ages and gold deposits; modified from Stockwell and Lord (1939), Stockwell (1945), Zwanzig (1971), Brommecker (1996), Anderson (2013b) and Zhou (2014). Age source: <sup>1</sup> Turek et al. (1989), <sup>2</sup> Anderson (2013b), <sup>3</sup> Zhou, Chapter 4.

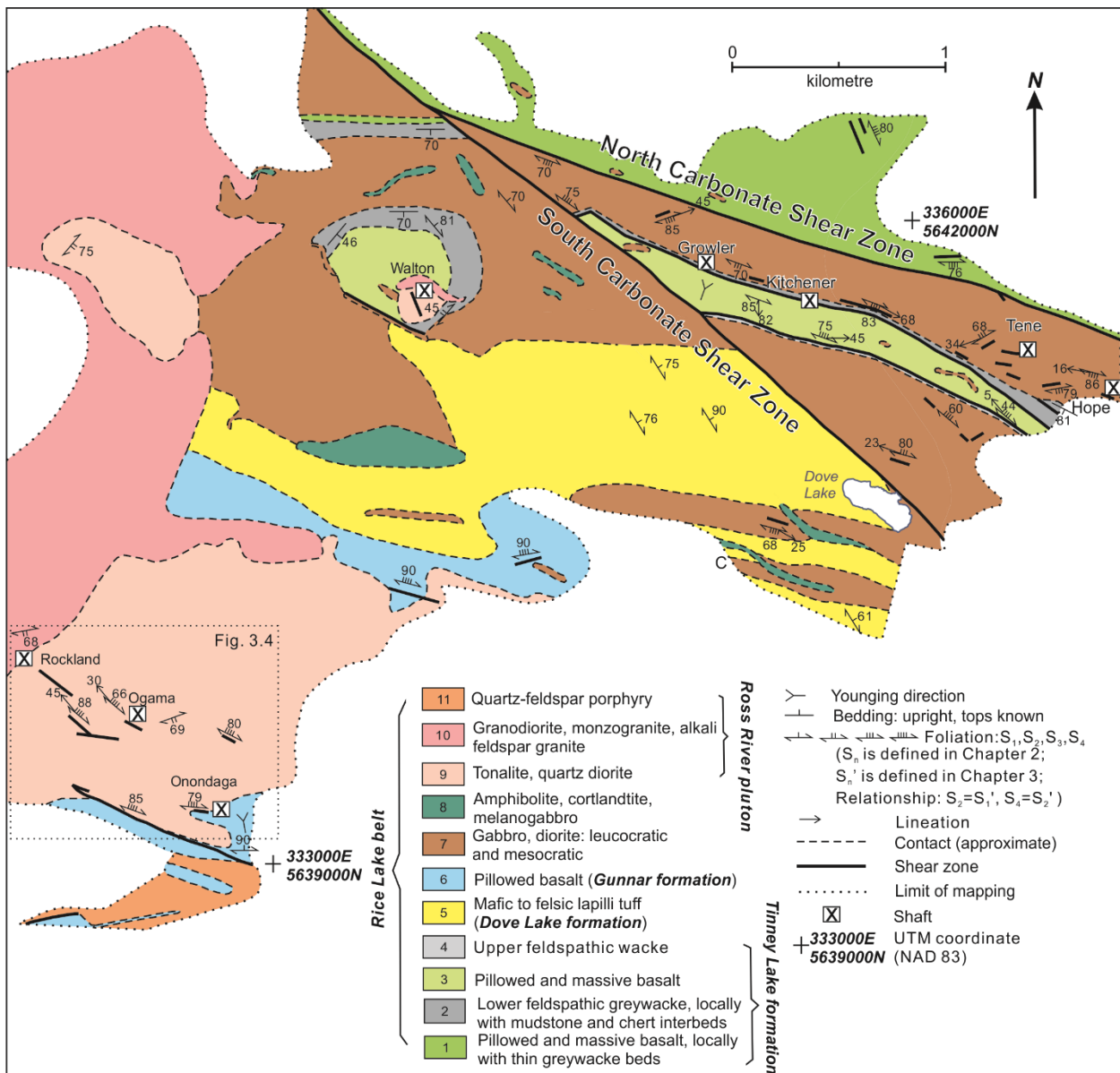


Figure 3.3 Simplified geologic map around the Central Manitoba gold deposit and the Ogama-Rockland gold deposit, illustrating major lithostratigraphic units, deformation structures and past-producing shafts; modified from Zhou (2014). Location of Fig. 3.4 is indicated.

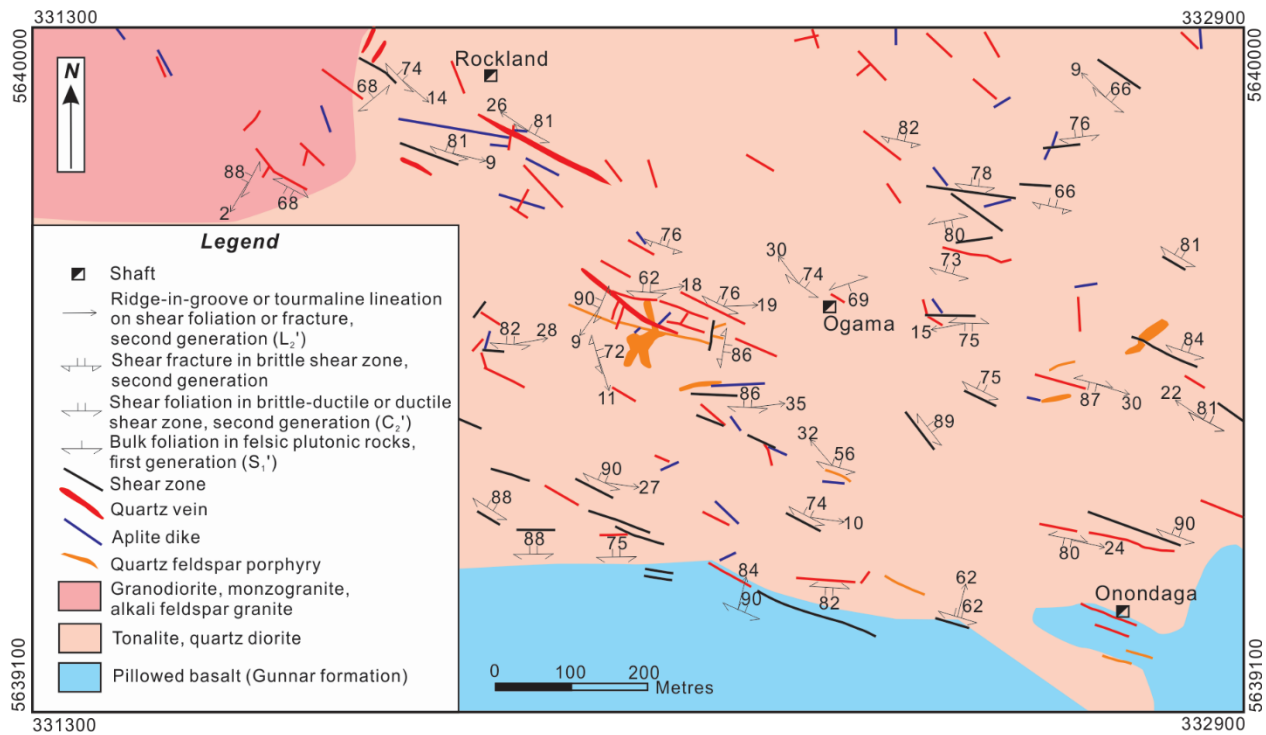


Figure 3.4 Simplified local geologic map around the Ogama-Rockland gold deposit, displaying main lithologic units, deformation structures and past-producing shafts. Modified from Zhou et al. (2012) and Zhou (2014).

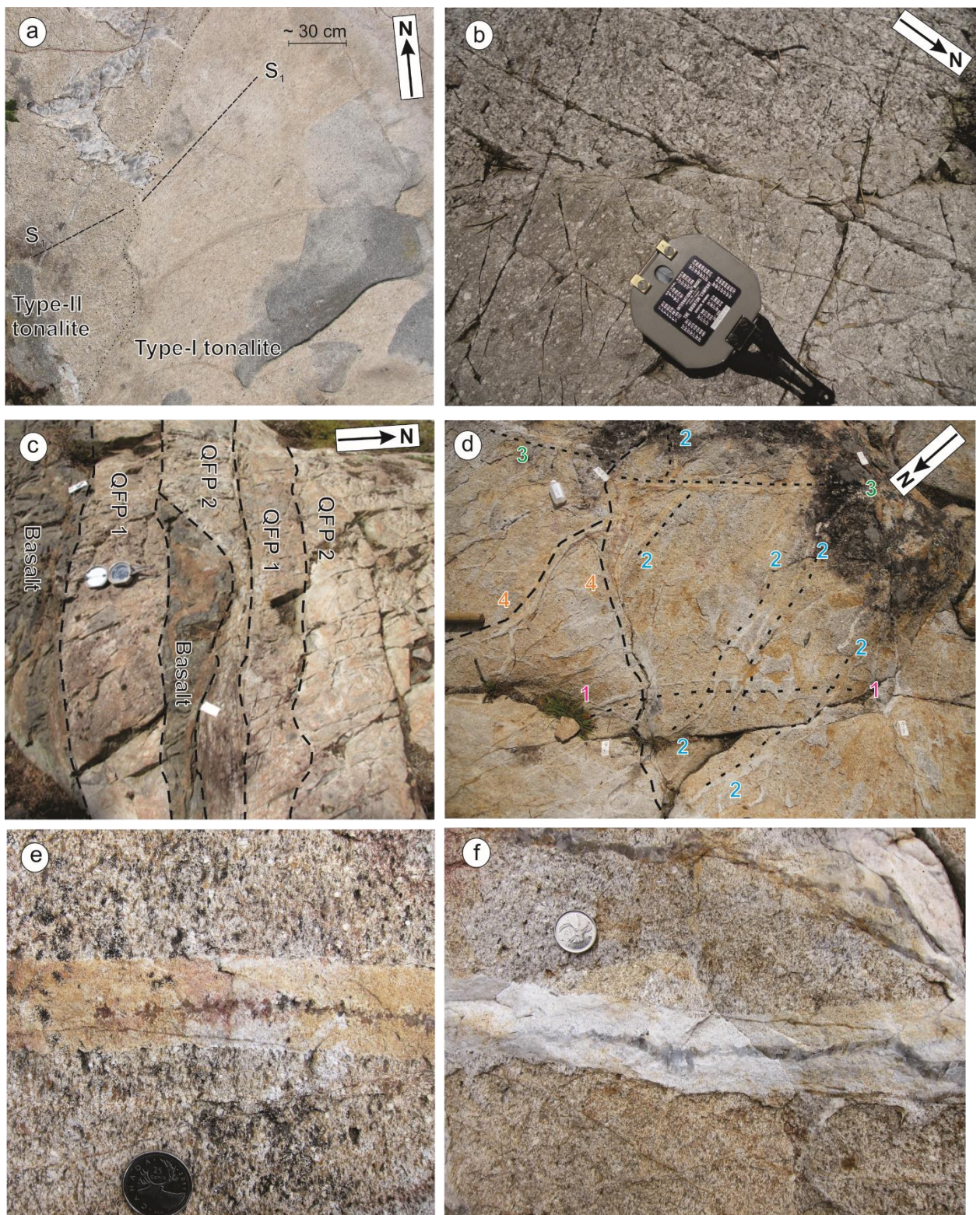


Figure 3.5 Outcrop photographs of major lithologic units at the Ogama-Rockland gold deposit (all plan views): a) two subphases of tonalite; note foliation refraction between two tonalite subphases; see location in Fig. 3.15a; b) sharp contact between coarse grained apparently

undeformed tonalite on the top and weakly deformed plagioclase-phyric tonalite at the bottom; c) two subparallel deformed quartz-feldspar porphyry dikes in sharp deformed contact with basalt; note the basalt xenolith in quartz feldspar porphyry dikes in the centre; d) various stages (1–4 from oldest to youngest) of aplite dike emplacement revealed by crosscutting relationships; e) discontinuous quartz segregations (at the centre left) grade into continuous segregations (at the centre right) in one aplite dike; f) continuous quartz vein dies out to the left in one whitish aplite dike.

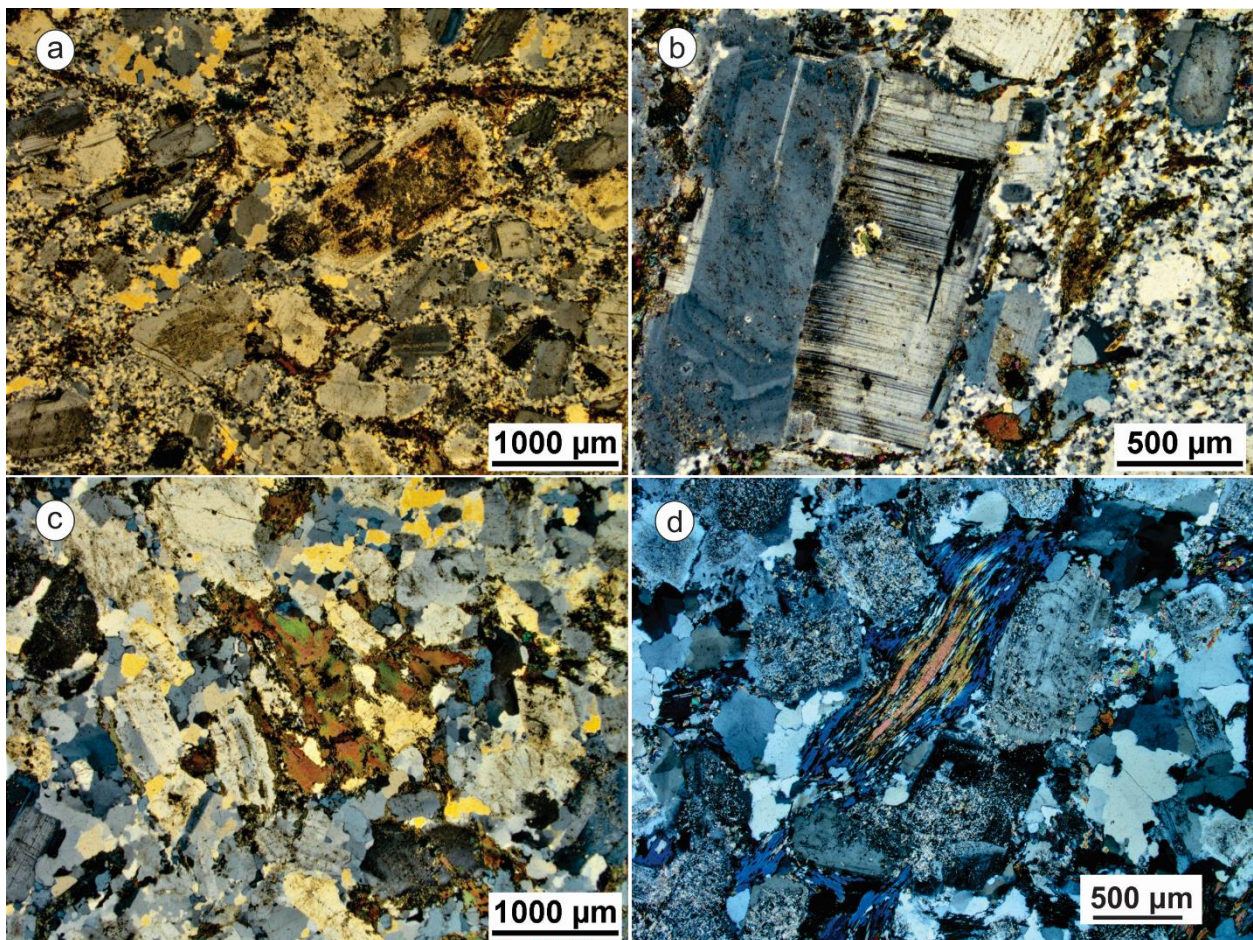


Figure 3.6 Photomicrographs of tonalite at the Ogama-Rockland gold deposit: a) aligned saussuritized plagioclase phenocrysts defining a preferred orientation from lower left to upper right; b) Carlsbad twinning and deformation twinning of weakly saussuritized plagioclase phenocrysts; c) undulose extinction on quartz grains; d) Marginal replacement of biotite to chlorite and intensely saussuritized plagioclase phenocrysts. All under cross polarized transmitted light.

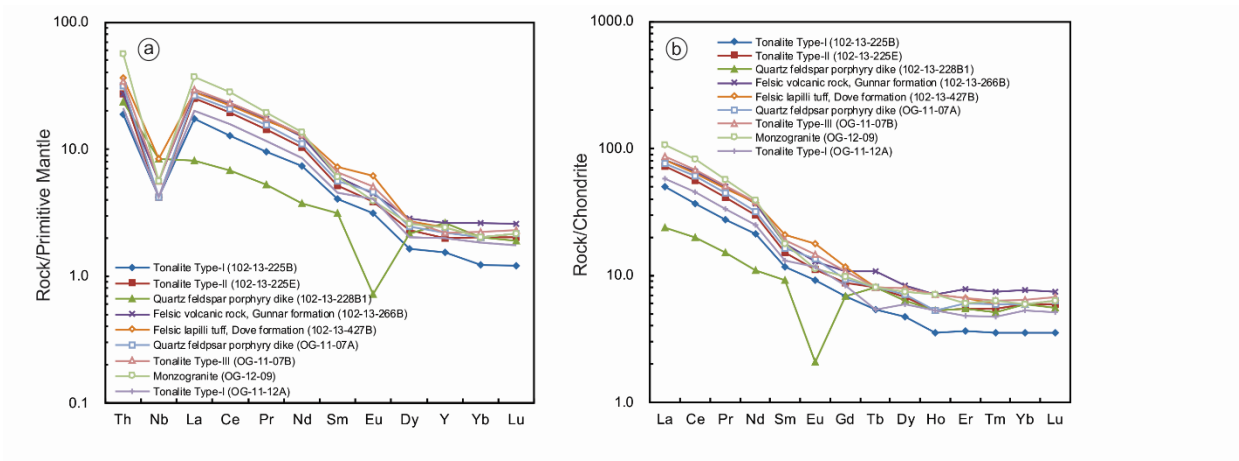


Figure 3.7 a) Primitive-mantle-normalized and b) chondrite-normalized extended-element plots for felsic and volcanic rocks from the Ogama-Rockland deposit area. Normalizing values are from Sun and McDonough (1989).

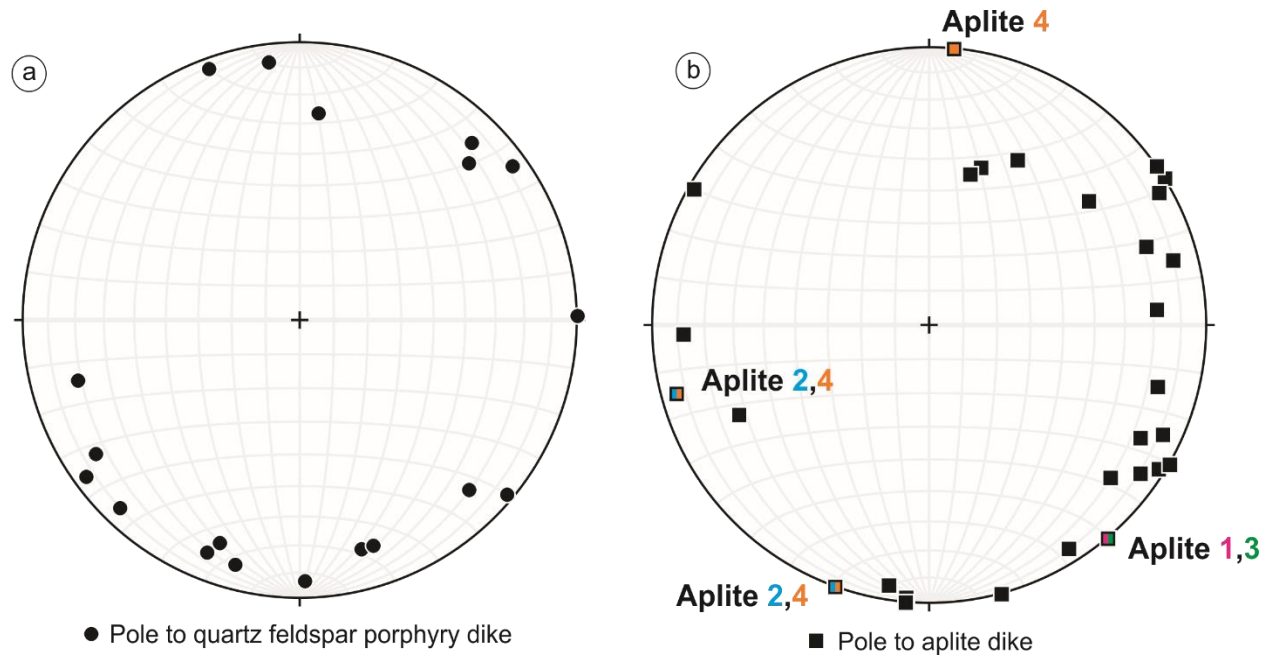


Figure 3.8 Lower hemispheric equal area stereonet projections of a) quartz feldspar porphyry dikes and b) aplite dikes; note that different stages of aplite dikes corresponding to Fig. 3.5d are indicated. All stereonet data presentations in this chapter were produced through the software “Stereonet 8” by Allmendinger et al. (2012) and Cardozo and Allmendinger (2013).

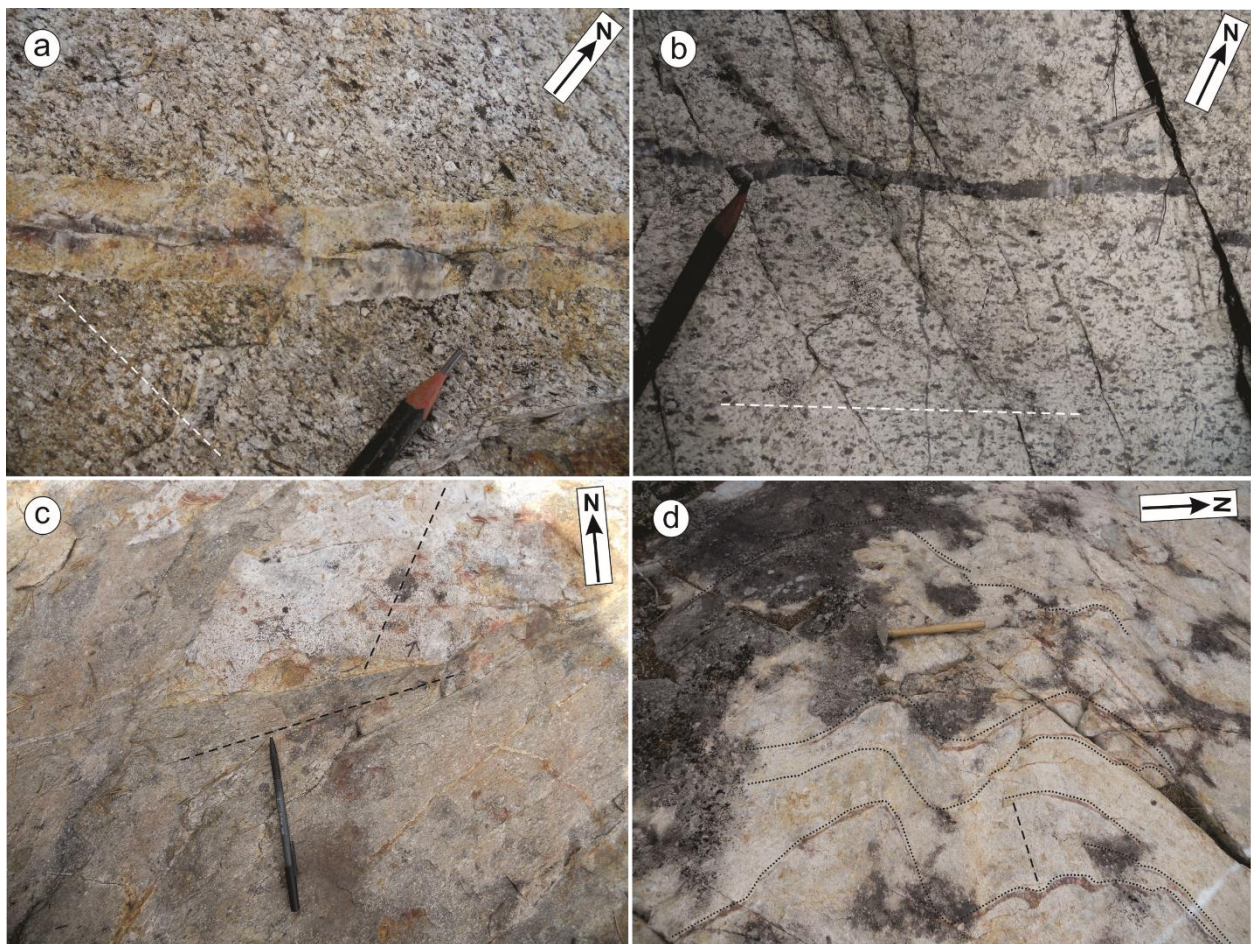


Figure 3.9 Outcrop photographs of  $G_1'$  structures at the Ogama-Rockland gold deposit (all plan views): a) east-striking  $S_1'$  foliation defined by a preferred orientation of plagioclase, biotite and quartz, indicated by a dash line; b) east-northeast-striking  $S_1'$  foliation defined by aligned elongated smoky quartz phenocrysts, which is parallel to an adjacent smoky veinlet; c) Shape contact and  $S_1'$  foliation (dash lines) refraction between medium to coarse grained porphyritic tonalite and fine grained quartz feldspar porphyry dikes; d)  $F_1'$  folded veins (dotted lines) and associated  $S_1'$  axial plane foliation (dash line).

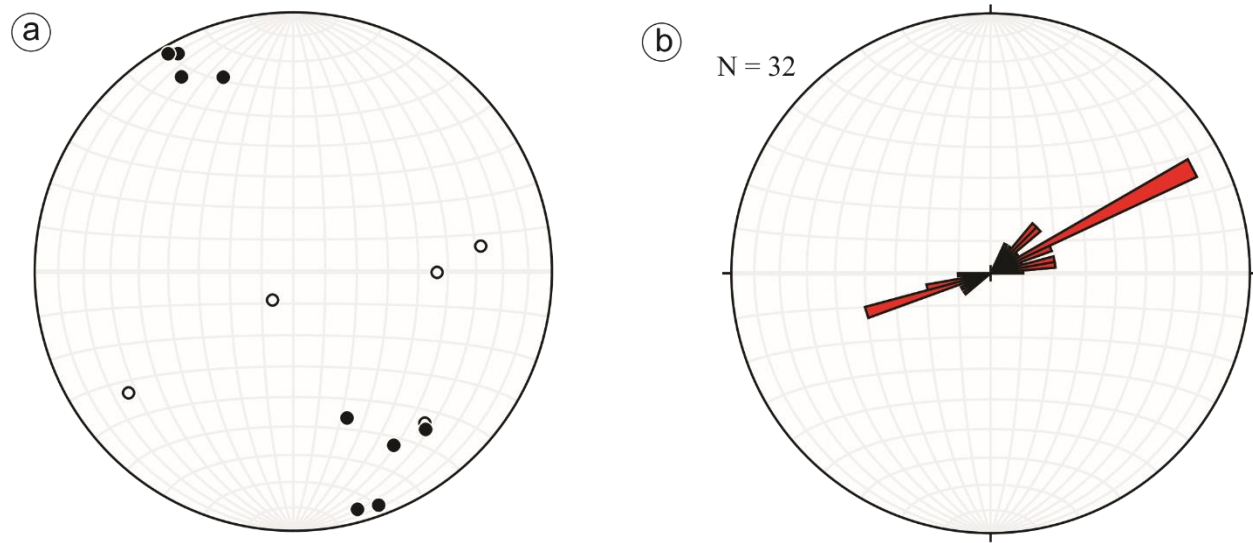


Figure 3.10 a) Lower hemispheric equal area stereonet projection of  $S_1'$  foliation with dip and  $L_1'$  lineation; b) rose diagram of  $S_1'$  foliation without dip.

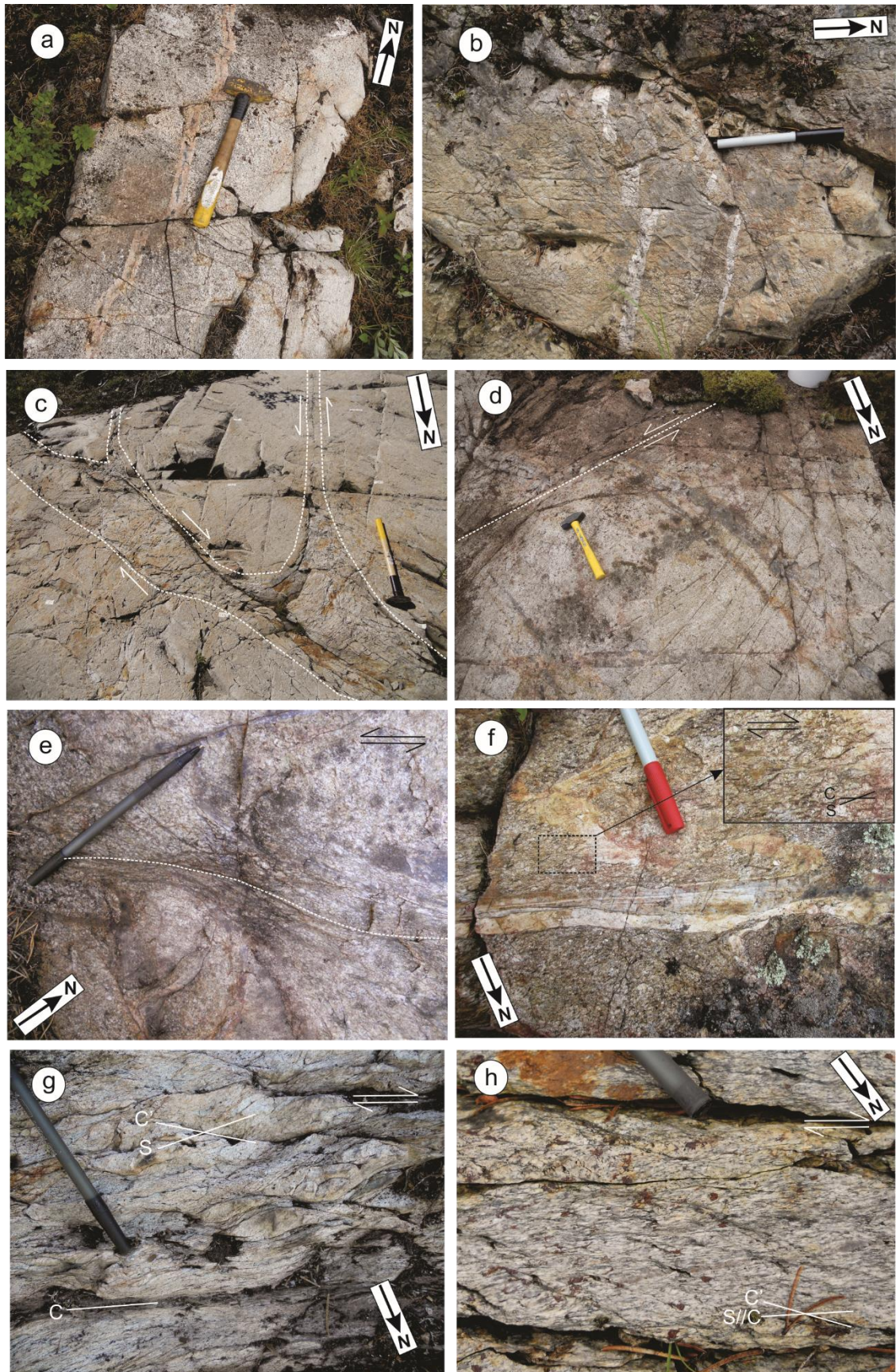


Figure 3.11 Outcrop photographs of  $G_2'$  structures around the Ogama-Rockland gold deposit (all plan views): a) west-southwest-trending subvertical brittle faults offset pinkish aplite dikes with centred quartz segregations in a dextral manner on a horizontal surface; b) north-trending subvertical brittle faults offset whitish aplite dikes in a sinistral fashion, and are displaced by a west-southwest-trending subvertical brittle fault in a dextral fashion on a horizontal surface; c) conjugate sets of two thin north-trending steep sinistral ductile shear zones and one thick northwest-trending steep dextral ductile shear zone; see location in Fig. 3.15a; d) a west-trending brittle-ductile shear zone offsets smoky quartz veins in a sinistral way; note the pinkish dike crosscuts smoky quartz veins in the lower right corner; e) a northeast-trending steep ductile sinistral shear zone; shear sense is indicated by deflected mylonitic foliation; f) a west-northwest-trending steep dextral ductile shear zone-bounded laminated quartz vein and aplite dike (in the centre) truncate, displace and fold another aplite dike (upper portion) in a dextral fashion; shear sense is indicated by S-C fabric in the close-up photograph in the top right corner; g) spectacular S-C-C' fabric in a west-northwest-trending dextral ductile shear zone; h) S foliation is subparallel to C foliation, and at a small angle to C' foliation in a northwest-striking steep dextral ductile shear zone.



Figure 3.12 Outcrop photographs of  $L_2'$  mineral lineation/striation and steps on C foliation or vein margins in  $G_2'$  shear zones (all section views): a) shallowly southwest-plunging discontinuous tourmaline lineation and congruous steps in a northeast-striking steep sinistral brittle fault; b) subhorizontal continuous tourmaline lineation on C foliation in a northwest-striking steep dextral ductile shear zone; c) shallowly northwest-plunging ridge-in-groove type striation and congruous steps on vein margins in a northwest-striking steep dextral ductile shear zone; d) shallowly southeast-plunging ridge-in-groove type striation and congruous steps on vein margins in a northwest-trending steep dextral ductile shear zone.

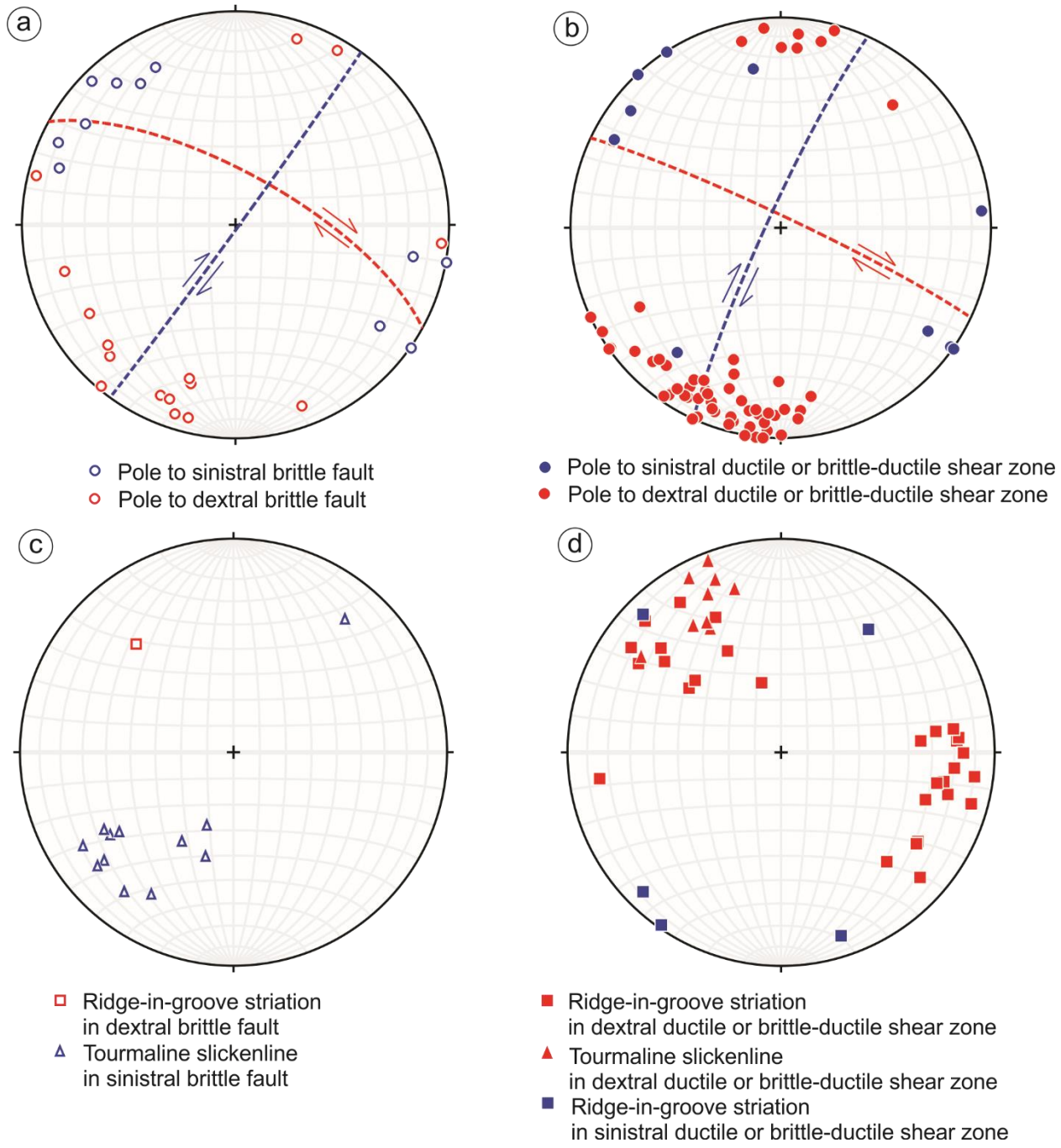


Figure 3.13 Lower hemispheric equal area stereonet projections of structural elements in G<sub>2</sub>' shear zones and statistically “best fit” great circles with determined shear sense.

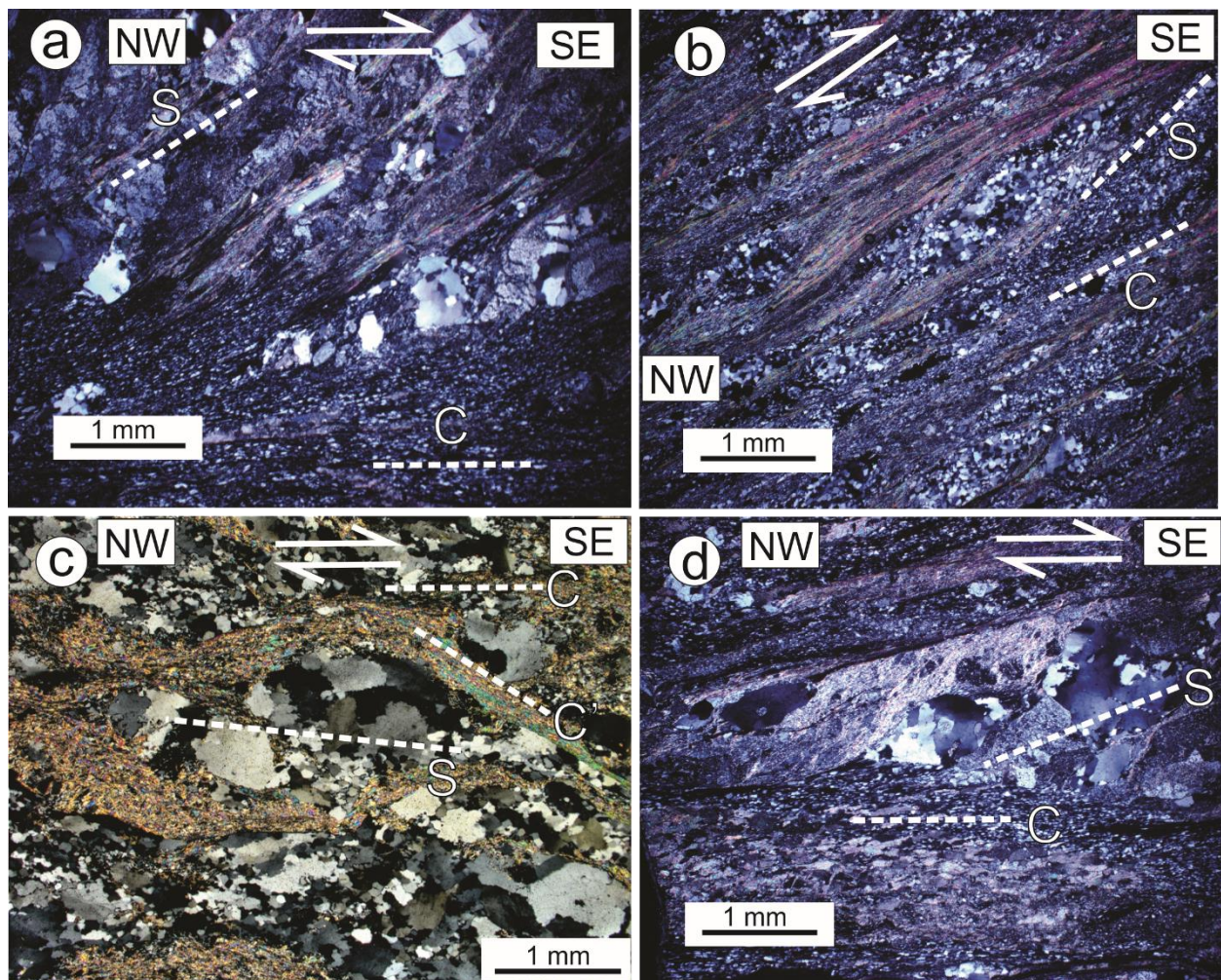
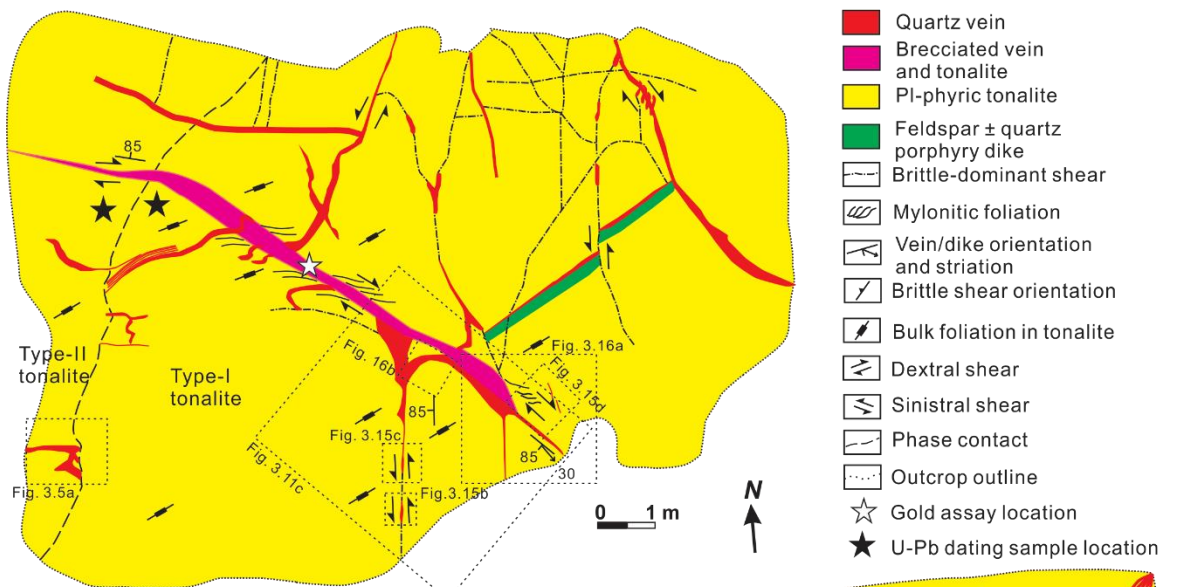


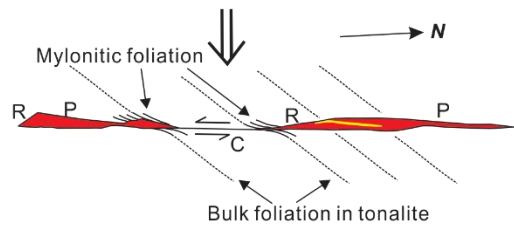
Figure 3.14 Photomicrographs of tonalitic S-C-(C') mylonites and quartz veins in northeast-striking subvertical dextral ductile shear zones; all oriented thin sections were made perpendicular to subvertical mylonitic foliation and parallel to subhorizontal ridge-in-groove striation; all under cross polarized transmitted light. See text for detailed descriptions.

**(a) Station 197/596 (UTM 0332074E, 5639632N; NAD 83) Outcrop mapping**



**e) Initial fracture**

R P R P C R P



**f) Initial fracture**

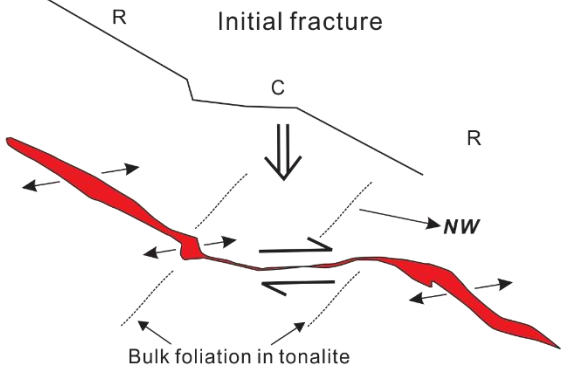


Figure 3.15 a) an outcrop sketch showing spatial relations among bulk foliation, conjugate shear zones and associated quartz veins, ~ 200 m west of the Ogama mine; b) a laminated greyish vein hosted in a north-striking steep sinistral ductile shear zone; see location in Fig. 3.15a; c) a laminated smoky vein with tonalite microlithons hosted in a north-striking steep sinistral brittle shear zone; see location in Fig. 3.15a; d) a west-northwest-trending steep dextral ductile shear zone and associated north-northwest-trending steep oblique-extension veins; shear sense is indicated by S-C fabric in the close-up photograph in the upper right corner; see location in Fig. 3.15a; e) an explanation for the development of laminated shear veins in Fig. 3.15b, c; initial fractures could have been in a Riedel shear pattern; laminated veins formed due to dilation of P shear during  $G_2'$  dextral shearing; P=pressure shear, R=Riedel shear, C=displacement shear, or C foliation in shear zone; long dash lines represent  $S_1'$  foliation and short solid lines are  $S_2'$  mylonitic foliation; f) an explanation for the formation of the west-northwest-trending dextral ductile shear zone and associated oblique-extension veins in Fig. 3.15d; oblique-extension veins formed due to dilation of Riedel shears during  $G_2'$  dextral shearing; R=Riedel shear, C=displacement shear, or C foliation in shear zone; long dash lines represent  $S_1$  foliation and short solid lines are  $S_2'$  mylonitic foliation.

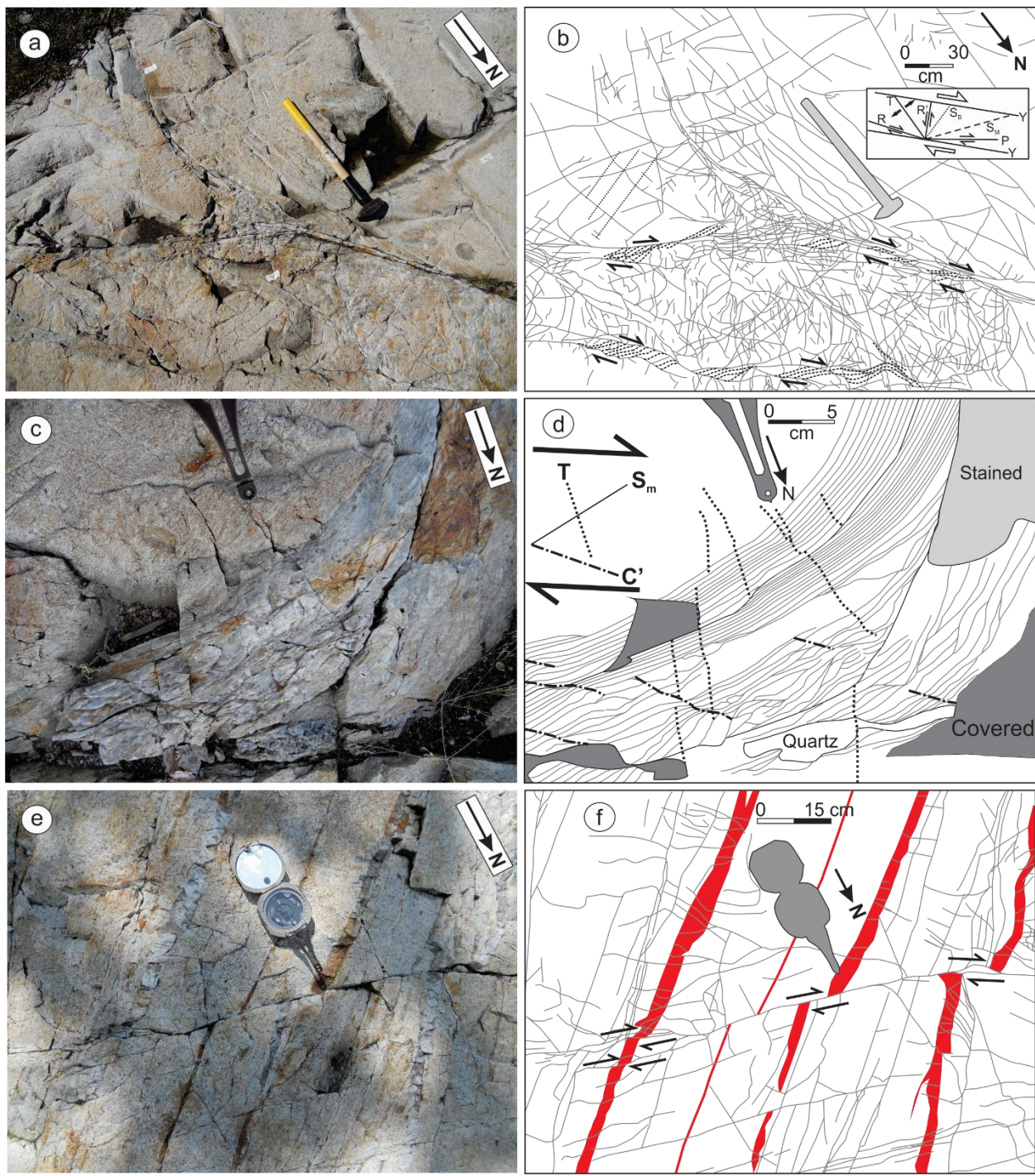


Figure 3.16 Outcrop photographs and corresponding sketches of  $G_2'$  shear zones (see Fig. 3.15a for location; all plan views): a, b) conjugate sets of a thin north-trending subvertical sinistral ductile shear zone and a thick northwest-trending subvertical dextral shear zone, hosting brecciated and shear veins; note the fracture sets are in agreement with the “Riedel shears” pattern; R=low angle synthetic Riedel shear, R’=high angle antithetic Riedel shear, P=pressure

shear, Y=boundary shear, T=extensional fracture; SB (in dotted line) represents bulk foliation in tonalite, SM (in dash line) represents mylonitic foliation; shear sense is established from deflection of mylonitic foliation; c, d) north-trending laminated and brecciated veins curve clockwise into a north-trending steep dextral ductile shear zone; shear sense is established from S-C' fabric; SM=mylonitic foliation, C'=extensional crenulation cleavage, T=extensional fracture; e, f) a west-northwest-trending brittle to brittle-ductile shear zone crosscuts sheeted veins at a high angle in a dextral sense; note displacement in the western portion is sharp and larger than that in the eastern portion, indicating a deformation behavior change from brittle to brittle-ductile; several meters west of this outcrop is a dextral ductile shear zone along strike in Fig. 3.15d.

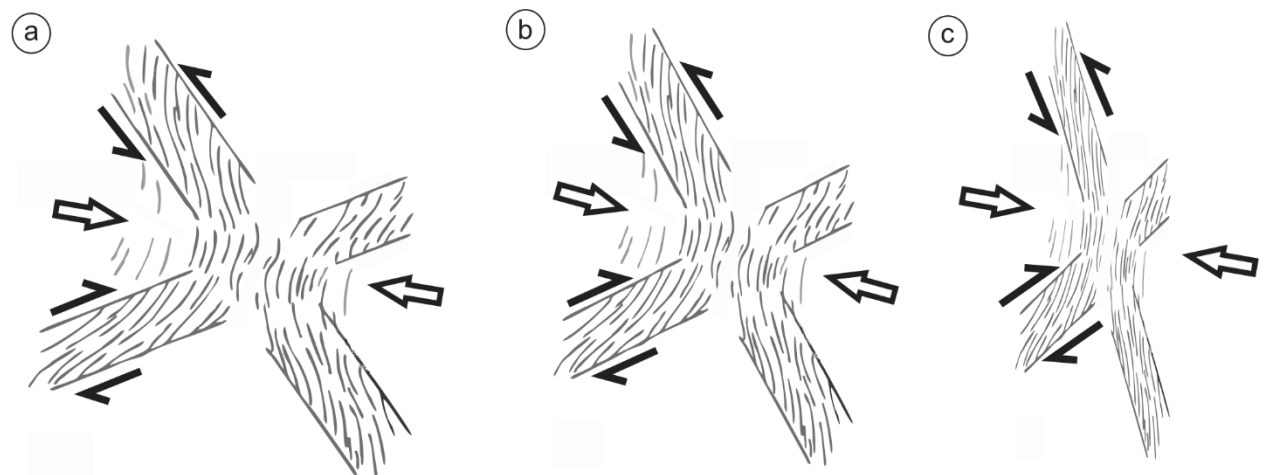


Figure 3.17 Sketches of conjugate shear zones; the maximum finite strain axis bisects the a) acute angle, b) right angle, or c) obtuse angle of the conjugate sets. Sketches are modified from Lamouroux et al. (1991).

Station 196 Outcrop-scale mapping (UTM 0332117E, 5639615N; NAD 83)

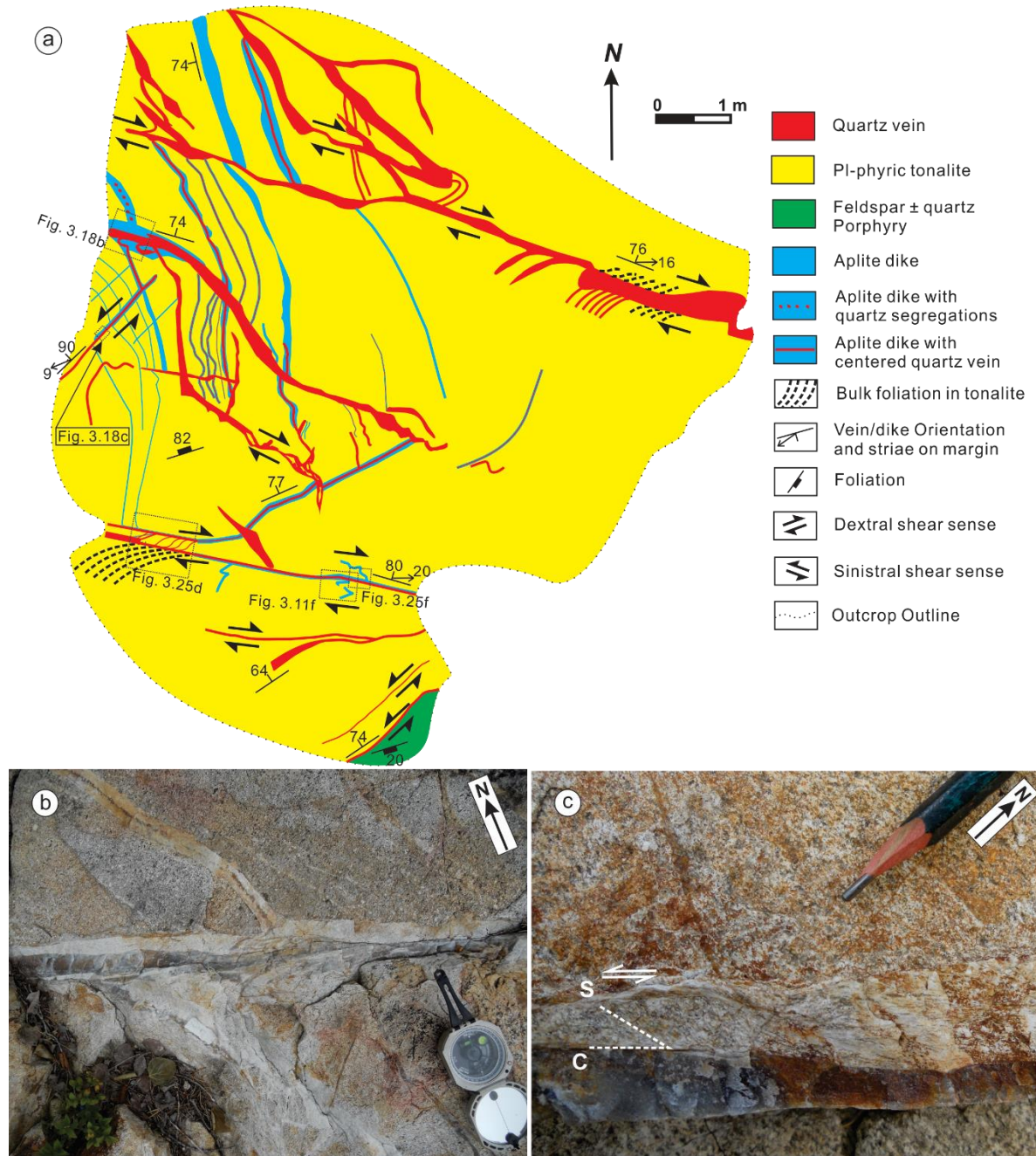


Figure 3.18 a) an outcrop sketch exhibiting intimate spatial relationships among aplite dikes, quartz veins and conjugate sets of ductile shear zones, ~ 150 m west of the Ogama mine; b) a north-northwest-striking steep aplite dike with quartz segregations is cut by a west-northwest-striking, ductile shear zone-hosted, aplite-bounded, laminated, smoky quartz vein; c) a northeast-striking, steep, narrow, sinistral ductile shear zone-hosted, smoky vein; shear sense is determined by S-C fabric. All plan views.

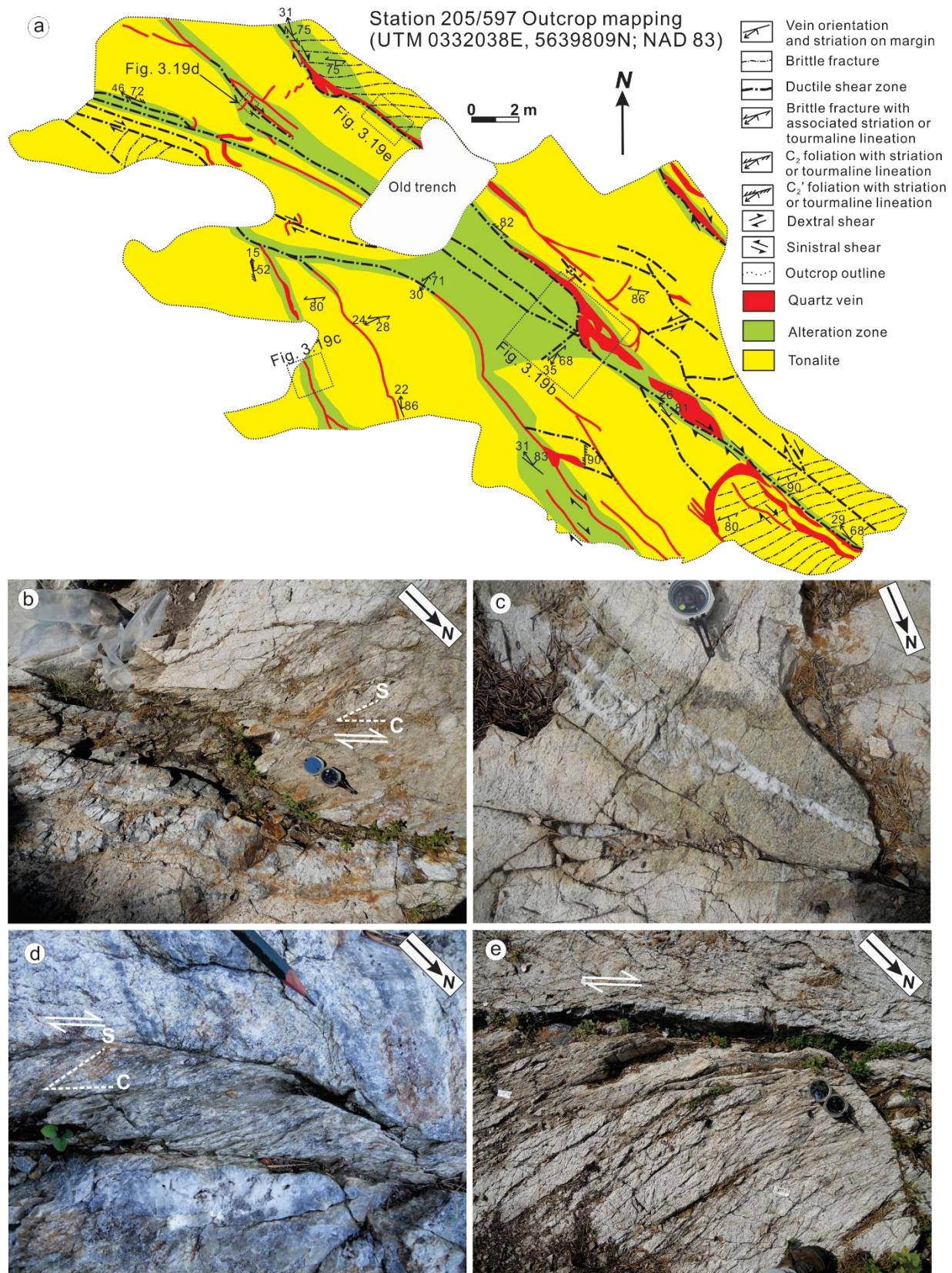


Figure 3.19 a) an outcrop sketch illustrating spatial relationships among quartz veins, alteration

zones, brittle or ductile shear zones; b) wavy smoky-white quartz lenses with intensely foliated sericite-chlorite-ankerite alteration halos; see a) for location; c) planar white quartz veins with sericite alteration halos; see a) for location; d) a northwest-trending subvertical dextral ductile shear zone (in the central part), in concordant contact with a northwest-trending smoky-white quartz vein (in the lower portion), cuts across north-northeast-trending smoky quartz veins (in the upper right and upper left portions); see a) for location; e) subparallel west-trending subvertical brittle fractures are dragged into a northwest-trending subvertical ductile shear zone with a planar smoky-white quartz vein; see a) for location.



Figure 3.20 An outcrop photograph showing that  $F_1'$ -folded and  $S_1'$  foliation-filling  $V_1'$  veins were dragged into a west-trending steep dextral shear zone. Plan view.

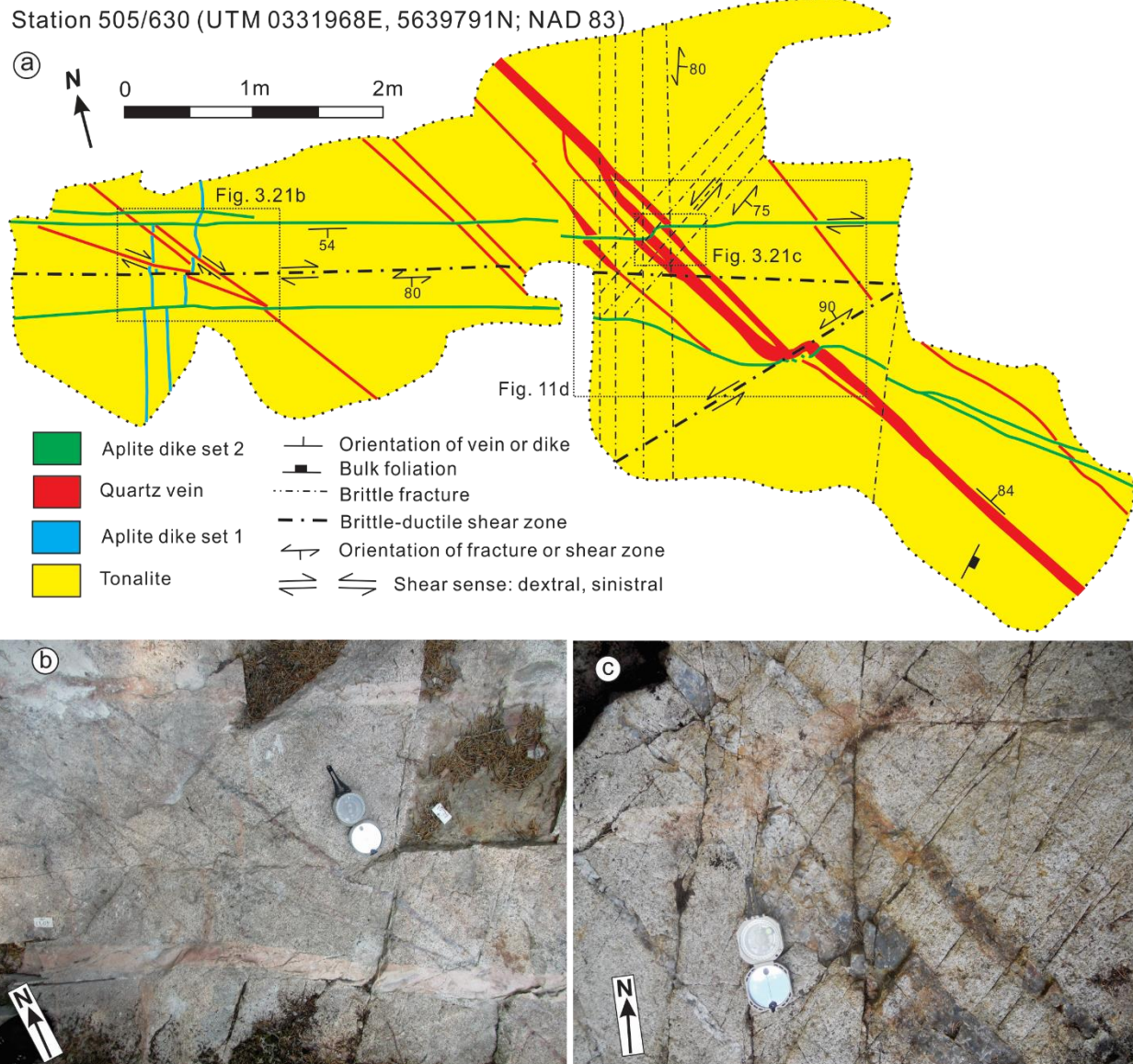


Figure 3.21 a) An outcrop sketch displaying subparallel steep  $V_2'$  veins and mutually crosscutting aplite dikes and shear zones; b) a narrow north-northwest-trending veinlet crosscuts a thin pinkish aplite dike (in the upper central portion) and is cut by west-northwest-trending steep aplite dikes (upper left and lower right corners); c) a wavy aplite dike crosscuts northwest-trending subvertical subparallel smoky quartz veins. All plan views.



Figure 3.22 Outcrop photographs of  $V_3'$  veins (all plan views): a) west-trending steep subparallel laminated smoky  $V_3'$  veins and less developed subparallel north-trending steep laminated smoky veins are mutually crosscut; b) west-trending steep subparallel laminated smoky  $V_3'$  veins are locally bounded by pinkish aplite dikes (in the central part), and contain pinkish aplite microlithons (lower right corner).

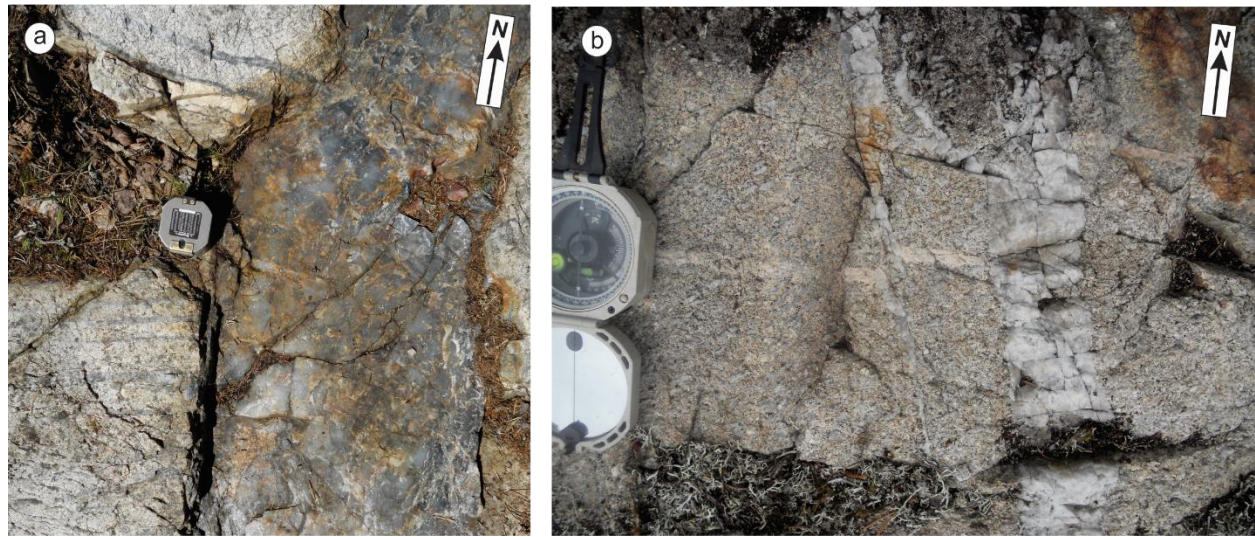


Figure 3.23 Outcrop photographs of V<sub>4</sub>' veins (all plan views): a) a north-trending subvertical smoky-white V<sub>4</sub>' vein cuts across sheeted laminated smoky V<sub>3</sub>' veins and minor greyish aplite dikes (upper left corner); b) north-trending steep V<sub>4</sub>' veins crosscut and displace a west-trending subvertical pinkish aplite dike.

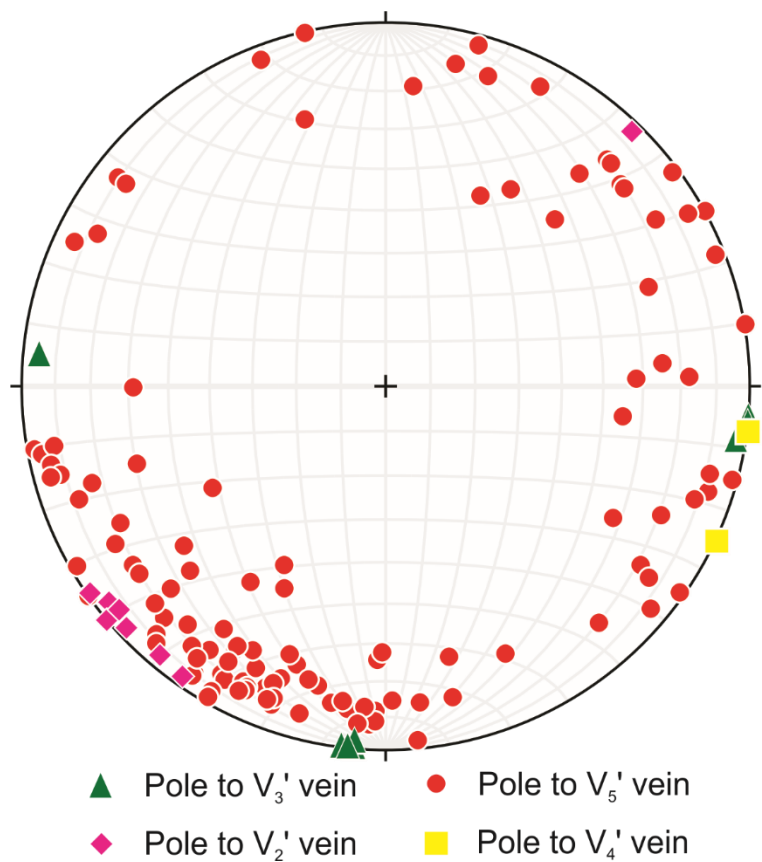


Figure 3.24 Lower hemispheric equal area stereonet projection of  $V_2'$ ,  $V_3'$ ,  $V_4'$  and  $V_5'$  veins.

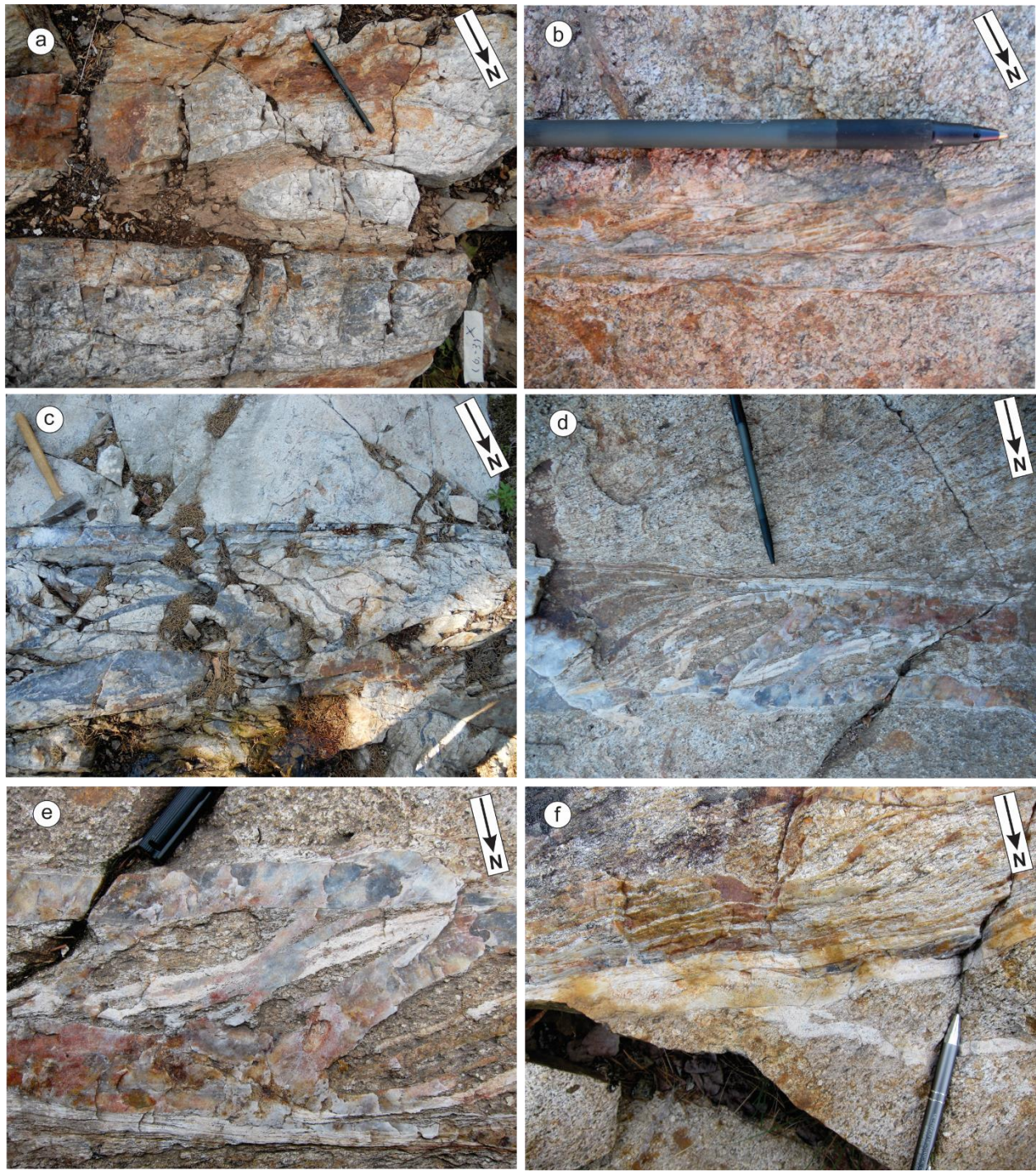


Figure 3.25 Outcrop photographs of west-to-northwest-trending subvertical V<sub>5'</sub> fault-fill veins (all plan views): a) laminated fault-fill veins with strongly foliated and ankerite-sericite altered microlithons in the centre; note the gossan staining on the vein to the top; b) a narrow laminated V<sub>5'</sub> vein; the inclined lamination and weakly developed bulk foliation deflection (upper right corner) indicate dextral shearing; c) brecciated smoky veins; d) S-C fabric-like internal structure

of a  $V_5'$  vein; S-C fabric-like structure and deflected  $S_1$  foliation (in the upper portion) indicate dextral shearing; note inclined veins (filling S foliation) within the central shear zone and boundary veins (filling C foliation) crosscut narrow planar and curved aplite dike fragments; see Fig. 3.18a for location; e) close up of Fig. 3.25d showing one inclined vein (filling S foliation; in the central part) with gossan staining actually merging with the continuous veinlet material bounded by the narrow aplite dike (in the central part); note the mylonitic aplite dike in concordant contact with the boundary vein (in the bottom part); f) sheeted wavy gossan staining  $V_5'$  veinlets in concordant contact with one whitish aplite dike, which crosscuts a folded thin whitish aplite dike; see Fig. 3.18a for location.

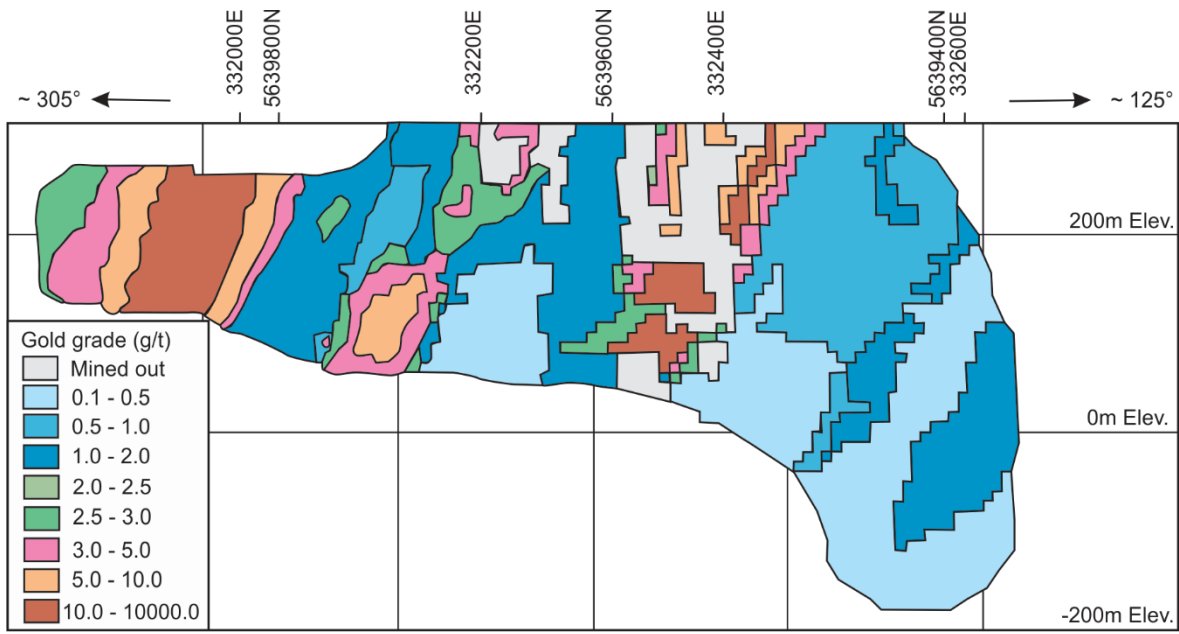


Figure 3.26 Block model longitudinal section of 400 domains (northwest-trending, vertical) at the Ogama mine; note the steep plunge of ore shoots defined by range of gold grade; modified from Chater et al. (2013).

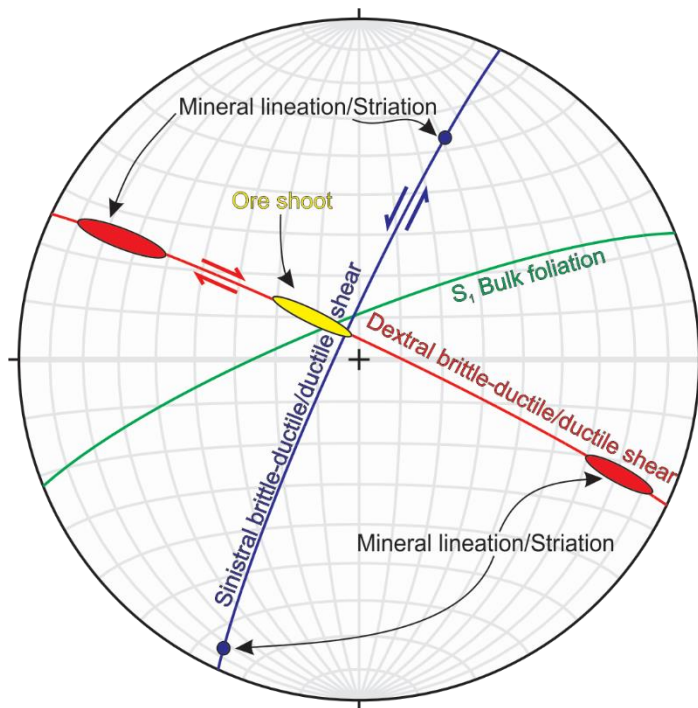


Figure 3.27 Lower hemispheric equal area stereonet projections of structural elements and the plunge of ore shoots.

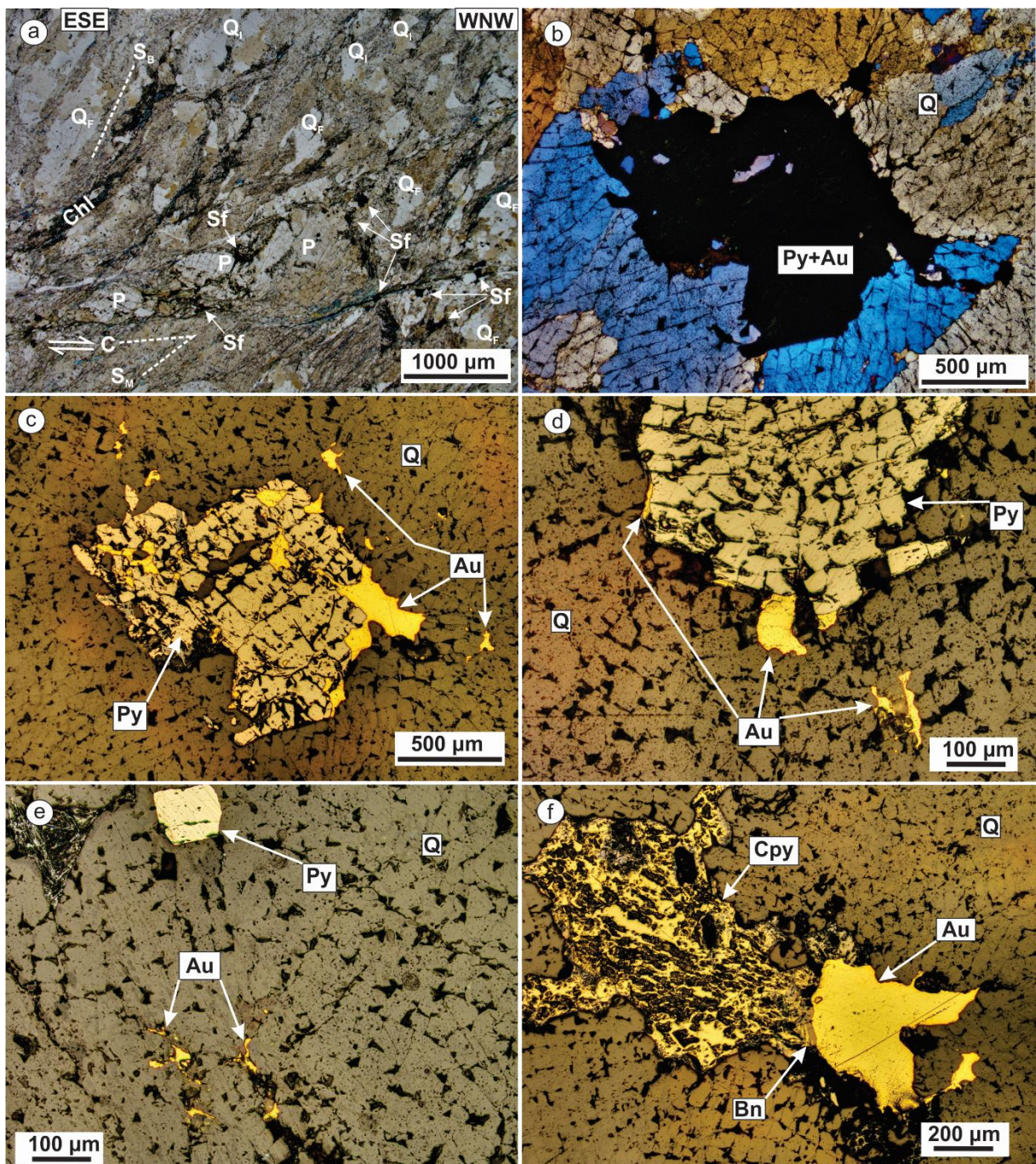


Figure 3.28 Photomicrographs of gold occurrences in quartz veins and associated shear zones: a, b) under cross polarized transmitted light; c, d, e, f) under plane polarized reflected light. See text for detailed descriptions. SB=bulk foliation in tonalite, SM=mylonitic foliation, C=shear foliation, Q=quartz, Q<sub>F</sub>=fractured quartz phenocrysts, Q<sub>I</sub>=intact quartz phenocrysts without fractures, P=plagioclase, Chl=chlorite, Sf=sulfides, Py=pyrite, Au=gold (electrum), Cpy=chalcopyrite, Bn=bornite.

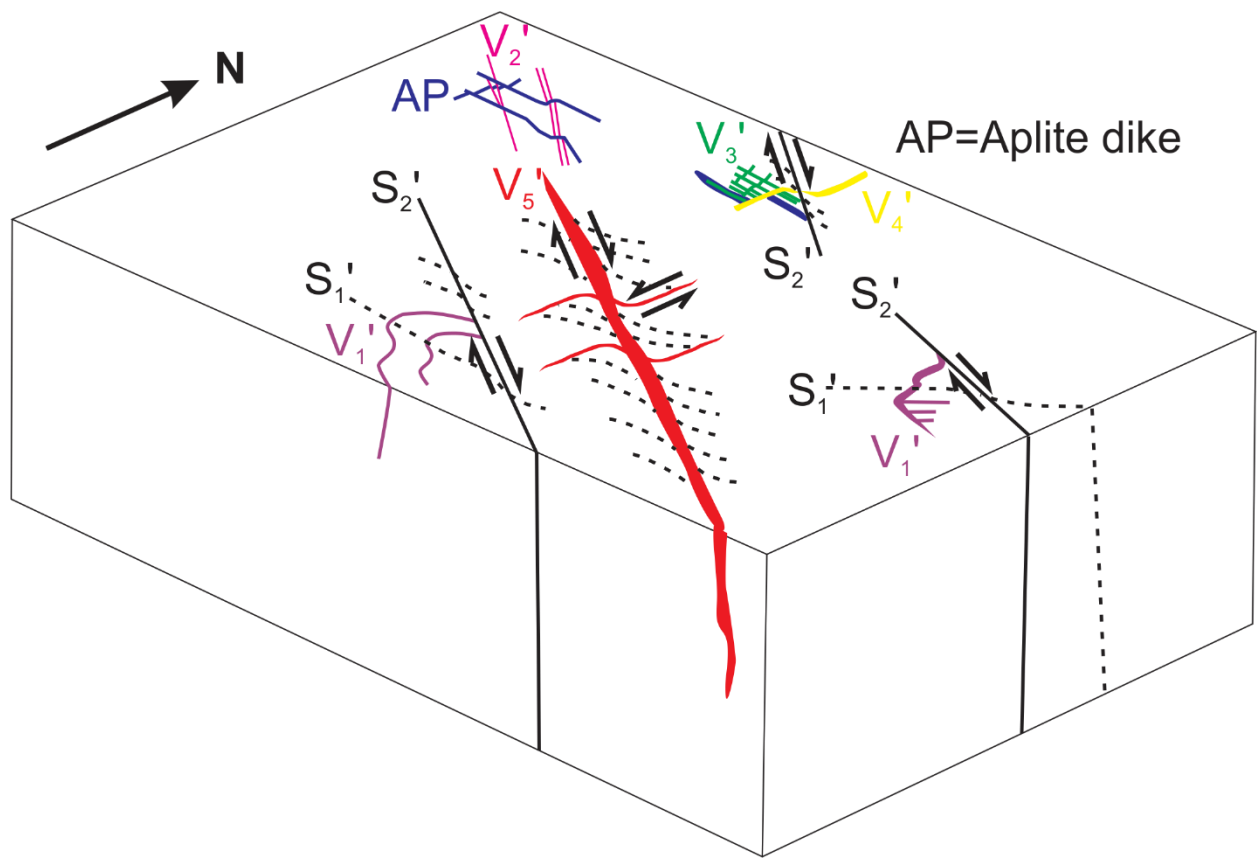


Figure 3.29 Schematic block diagram showing geometry and kinematics of the Ogama-Rockland gold deposit.

Table 3.1 Lithogeochemical data for representative samples from felsic rock units in the Ogama-Rockland area.

Sample ID	102-13-225B	102-13-225E	102-13-228B1	102-13-266B	102-13-427B	OG-11-07A	OG-11-07B	OG-12-09	OG-11-12A
Descriptions	Tn type-I	Tn type-II	QFP dike 1	FVR, GF	FLT, DLF	QFP dike 2	Tn type-III	Mzg	Tn type-I
SiO <sub>2</sub>	70.07	68.73	76.02	70.97	65.38	68.59	66.12	70.82	68.03
Al <sub>2</sub> O <sub>3</sub>	15.7	15.22	13.59	12.37	14.72	14.87	15.67	13.82	15.43
Fe <sub>2</sub> O <sub>3</sub> (T)	3.85	4.34	1.15	4.31	6.49	4.88	5.29	4.47	4.49
MnO	0.055	0.051	0.026	0.058	0.123	0.066	0.074	0.062	0.05
MgO	0.91	1.04	0.11	1.19	3.08	1.42	1.41	1.11	1.23
CaO	3.61	3.68	0.66	4.61	4.95	4.01	4.31	2.65	3.71
Na <sub>2</sub> O	4.53	4.28	4.19	3.3	1.54	3.92	4.02	4.52	4.1
K <sub>2</sub> O	1.29	1.22	4.7	0.33	0.94	1.21	1.22	0.72	1.33
TiO <sub>2</sub>	0.332	0.363	0.022	0.388	0.589	0.424	0.469	0.392	0.373
P <sub>2</sub> O <sub>5</sub>	0.09	0.12	0.06	0.12	0.15	0.12	0.14	0.1	0.11
LOI	0.47	0.72	0.42	1.89	2.77	1.3	0.99	1.56	1.29
Total	100.9	99.78	100.9	99.53	100.7	100.8	99.71	100.2	100.1
Sc	5	6	2	6	11	7	8	7	6
Be	< 1	1	1	< 1	1	1	1	< 1	< 1
V	43	52	8	61	92	68	70	57	53
Cr	< 20	< 20	< 20	< 20	60	< 20	< 20	< 20	< 20
Co	6	6	< 1	11	14	9	10	8	8
Ni	< 20	< 20	< 20	< 20	40	< 20	< 20	< 20	< 20
Cu	40	140	< 10	90	< 10	70	80	150	120
Zn	60	30	< 30	< 30	110	60	50	30	< 30
Ga	19	19	18	14	19	18	19	17	19
Ge	1	1	2	2	1	1	2	2	2
As	< 5	< 5	< 5	< 5	< 5	< 5	< 5	6	< 5
Rb	31	32	79	8	20	29	30	21	36
Sr	392	419	52	287	139	389	409	258	413
Y	7	9	12	12	11	10	10	11	9
Zr	111	106	45	109	127	110	108	105	111
Nb	3	3	6	4	6	3	4	4	3
Mo	< 2	12	35	2	< 2	3	3	3	4
Ag	0.7	0.6	< 0.5	0.6	0.7	0.5	0.6	0.6	< 0.5
In	< 0.2	< 0.2	< 0.2	< 0.2	< 0.2	< 0.2	< 0.2	< 0.2	< 0.2
Sn	< 1	< 1	1	1	1	< 1	1	1	1
Sb	< 0.5	< 0.5	< 0.5	< 0.5	< 0.5	< 0.5	< 0.5	< 0.5	< 0.5
Cs	< 0.5	0.7	0.5	< 0.5	< 0.5	1.3	0.9	< 0.5	1.3
Ba	353	280	564	132	170	281	292	152	236
La	11.9	17.3	5.6	19.2	19.2	18	20.4	25.5	13.7
Ce	22.6	34.2	12.1	40.5	39	36.9	41.5	50.2	27.9
Pr	2.62	3.94	1.44	4.78	4.6	4.25	4.86	5.37	3.18
Nd	9.9	14	5.1	17.1	17.5	14.9	17.7	18.4	11.6
Sm	1.8	2.3	1.4	2.7	3.2	2.5	2.9	2.7	2

Sample ID	102-13-225B	102-13-225E	102-13-228B1	102-13-266B	102-13-427B	OG-11-07A	OG-11-07B	OG-12-09	OG-11-12A
Descriptions	Tn type-I	Tn type-II	QFP dike 1	FVR, GF	FLT, DLF	QFP dike 2	Tn type-III	Mzg	Tn type-I
Eu	0.53	0.65	0.12	0.75	1.03	0.78	0.85	0.66	0.68
Gd	1.4	1.8	1.4	2.2	2.4	1.9	2.2	2	1.7
Tb	0.2	0.3	0.3	0.4	0.3	0.3	0.3	0.3	0.2
Dy	1.2	1.7	1.6	2.1	2	1.8	2	1.9	1.5
Ho	0.2	0.3	0.3	0.4	0.4	0.3	0.4	0.4	0.3
Er	0.6	0.9	0.9	1.3	1.1	1	1.1	1	0.8
Tm	0.09	0.14	0.13	0.19	0.15	0.15	0.16	0.16	0.12
Yb	0.6	1	1	1.3	1	1	1.1	1	0.9
Lu	0.09	0.15	0.14	0.19	0.16	0.16	0.17	0.16	0.13
Hf	2.6	2.5	1.5	2.5	3	2.5	2.4	2.6	2.6
Ta	0.3	0.3	1.1	0.3	0.5	0.3	0.5	0.5	0.3
W	< 1	< 1	5	< 1	< 1	< 1	2	< 1	2
Tl	< 0.1	< 0.1	0.2	< 0.1	< 0.1	< 0.1	< 0.1	< 0.1	< 0.1
Pb	< 5	< 5	9	< 5	< 5	< 5	< 5	< 5	< 5
Bi	< 0.4	< 0.4	< 0.4	< 0.4	< 0.4	< 0.4	< 0.4	< 0.4	< 0.4
Th	1.6	2.3	2	2.3	3.1	2.7	2.9	4.8	1.8
U	0.5	0.7	2.9	0.6	0.9	0.8	0.7	1	0.5

Abbreviations: Tn=Tonalite, QFP=Quartz feldspar porphyry, FVR=Felsic volcanic rock, GF=Gunnar formation, FLT=Felsic lapilli tuff, DLF=Dove Lake formation, Mzg=Monzogranite;

Full descriptions of analytical methods are given in Anderson (2013b). The whole-rock powders were submitted to Activation Laboratories Ltd. (Ancaster, Ontario) and analyzed using the ‘4Litho’ analytical package, which employs a lithium metaborate-tetraborate fusion technique, followed by nitric-acid digestion and analysis by inductively coupled plasma–emission spectrometry (ICP-ES) for the major elements and selected trace elements (Ba, Sc, Sr, V, Y, Zr), and by inductively coupled plasma–mass spectrometry (ICP-MS) for trace and rare-earth elements. Each sample batch included a minimum of one internal standard and one blind duplicate for analytical quality control. Totals for the major-element oxides range from 99.53 to 100.9 wt. %.

Table 3.2: Regional correlations of structures and gold mineralization (indicated by red bar; dash line represents uncertainties) in the Rice Lake greenstone belt

Researcher	Chapter 3	Chapter 2	Brommecker, 1996	Anderson, 2008	Anderson, 2013b
Deposit Tectonic significance	Ogama-Rockland gold deposit	Central Manitoba mine trend	Gunnar mine	Rice Lake mine trend	Gold occurrences around Garner Lake, Gem Lake, and Lily Lake
Arc extension; initial back-arc spreading?	Not found	Not found	Not reported	G <sub>1</sub> : finely spaced S <sub>1</sub> foliation in phyllite fragments in clastic dikes;	Not reported
Basin inversion; initial crustal thickening?		?	D <sub>1</sub> : Bedding-parallel S <sub>1</sub> foliation	G <sub>2</sub> : local, weak, layer-parallel S <sub>2</sub> foliation	G <sub>1</sub> : local layer-parallel S <sub>1</sub> foliation
Collisional (sinistral-oblique) tectonics; crustal thickening?	Not found	G <sub>1</sub> : NE-SW shortening; regional NW-trending steep S <sub>1</sub> foliation; steep L <sub>1</sub> stretching lineation; rare isoclinal, doubly-plunging F <sub>1</sub> folds	D <sub>2</sub> : NE-SW Shortening; regional NW-trending, steeply SE-dipping S <sub>2</sub> foliation; close to tight, lobate-cuspate, chevron, steeply SE-plunging F <sub>2</sub> folds	G <sub>3</sub> : NNE-SSW shortening; regional WNW-trending S <sub>3</sub> ; steep L <sub>3</sub> stretching lineation; upright F <sub>3</sub> folds	G <sub>2</sub> : NE-SW shortening; regional NW-trending S <sub>2</sub> foliation and flattening fabric; steep L <sub>2</sub> stretching lineation; tight to isoclinal, doubly-plunging, similar-style F <sub>2</sub> folds
Continued (bulk shortening) collisional tectonics?	G <sub>1</sub> : NNW-SSE shortening; regional NNW-trending steep S <sub>2</sub> foliation in the Ross River pluton; tight to close, symmetric, upright F <sub>1</sub> folds	G <sub>2</sub> : NW-SE shortening; close, moderately SE-plunging F <sub>2</sub> folds with axial plane SW-trending regional S <sub>2</sub> cleavage	Not reported	Not reported	Not reported
Continued collisional (sinistral-oblique) tectonics and crustal thickening?	Not found	G <sub>1</sub> : NNE-SSW Shortening; WSW-trending S <sub>3</sub> crenulation cleavage; mylonitic S <sub>3</sub> foliation in NE-to-E-trending sinistral and NW-to-N-trending dextral shear zone conjugate sets; tight chevron and drag F <sub>3</sub> folds			
Onset of (oblique terminal collision; dextral transpression)	Not found	Not found	D <sub>3</sub> : NNW-SSE shortening; ESE-trending, steeply S-dipping S <sub>3</sub> crenulation cleavages, kink bands; NW-trending dextral and N-trending sinistral shear zone conjugate sets	G <sub>4</sub> : NW-SE shortening; regional, WSW-trending, S <sub>4</sub> crenulation cleavage; F <sub>4</sub> Z-folds	G <sub>3</sub> : NNW-SSE shortening; S <sub>3</sub> crenulation cleavage; minor F <sub>3</sub> Z-folds
Main terminal (dextral-oblique) collision; transcurrent shear deformation with progressive folding	G <sub>2</sub> : NNW-SSE shortening; Mylonitic S <sub>2</sub> foliation in WSW-trending dextral and SSW-trending sinistral subvertical shear zone conjugate sets; shallow L <sub>2</sub> tourmaline lineation or striation	G <sub>4</sub> : NW-SE shortening; Mylonitic S <sub>4</sub> foliation in SW-to-NW-trending subvertical dextral shear zones; shallow to moderate L <sub>4</sub> striation; isoclinal upright F <sub>4</sub> folds		G <sub>5</sub> : NNW-SSE shortening; regional S <sub>5</sub> shear-band cleavage; mylonitic S <sub>5</sub> in NW-trending high-strain zones; shallow L <sub>5</sub> lineation; F <sub>5</sub> Z-folds	G <sub>4</sub> : NW-SE shortening; S <sub>4</sub> shear-band cleavage; mylonitic S <sub>4</sub> in NW-trending high-strain zones; shallow L <sub>4</sub> lineation; open to tight parallel-style F <sub>4</sub> Z-folds with axial plane cleavage
Buttress effect on Ross River pluton; dextral transpression	Not found	Not found	Not reported	G <sub>6</sub> : E-W shortening; open, north-trending F <sub>6</sub> crenulations	
Late block faulting	Not found	Not found	Not reported	Not reported	G <sub>5</sub> : N-S shortening; discrete brittle-ductile faults

## **Chapter 4**

**Timing of gold mineralization at the Ogama-Rockland lode gold deposit in the Neoarchean Rice Lake greenstone belt, southeastern Manitoba, Canada: new constraints from ore texture, U-Pb zircon/monazite and Re-Os molybdenite geochronology**

## 4.1 Introduction

Felsic intrusions host several Archean lode gold deposits in the Superior Province, but the role of felsic magmas in the development of gold mineralization is controversial (Colvine et al., 1988). Two different genetic models have been proposed for intrusion-hosted gold deposits in Archean terranes. A genetic link may exist between host felsic plutonic rocks and gold precipitation (“intrusion-related origin”; Sillitoe and Thompson, 1998), or alternatively felsic intrusions are simply competent host rocks and effective structural traps (“orogenic model”; Groves et al., 1998). A few deposits show evidence for both processes at different stages of gold mineralization (e.g., Mercier-Langevin et al., 2012a).

One critical but challenging avenue for distinguishing different genetic models is to precisely and accurately determine the absolute timing of gold mineralization, relative to deformation, felsic magmatism and hydrothermal activity. Reliable maximum age constraints for Archean intrusion-hosted gold deposits are relatively easy to establish through dating of the host rocks, especially using U-Pb zircon crystallization ages for felsic plutonic rocks. However, gold mineralization in most Archean lode gold deposits is typically localized in auriferous quartz-(carbonate) veins associated with brittle-ductile or ductile shear zones, which appear to have formed relatively late in the history of granitoid-greenstone belts and are rarely cut by igneous rocks. Therefore, minimum age constraints have often been acquired via dating secondary hydrothermal minerals (e.g., Corfu and Muir, 1989b; Jemielita et al., 1990), but their geological significance has been debated, because these minerals may significantly postdate gold mineralization and some may not even be truly hydrothermal (e.g., Corfu and Davis, 1991).

The Ogama-Rockland deposit is an intrusion-hosted, shear-related lode gold deposit in the Neoarchean Rice Lake greenstone belt of the Uchi Subprovince within the western Superior Province. Compared to other Archean gold deposits, the Ogama-Rockland deposit is unique in that an early phase of gold mineralization seems to have occurred broadly synchronously with the emplacement of aplite dikes before or early during the development of G<sub>2'</sub> conjugate shear zones. Its vein system is entirely hosted in tonalite and part of the auriferous system is cut by aplite dikes (Chapter 3). Therefore, U-Pb dating of felsic igneous rocks can be used to precisely constrain the early phase of gold mineralization at this deposit.

A more direct approach for dating gold mineralization is by Re-Os sulfide geochronology because gold is typically, if not always, intimately spatially associated with sulfide minerals in

Archean lode gold deposits. The Re-Os chronometer in molybdenite seems to be robust under intense deformation and granulite metamorphism, whereas  $^{40}\text{Ar}/^{39}\text{Ar}$ , K-Ar, and Rb-Sr chronometers (on secondary alteration minerals) are susceptible to chemical and thermal disturbance by subsequent hydrothermal/magmatic activities (Stein et al., 2001; Stein, 2014). However, a Re-Os age obtained from sulfide minerals can only be directly linked to gold mineralization if the relative timing of deposition is clearly established. Hence, Re-Os geochronology combined with a well-established structural context and ore paragenesis of auriferous veins is necessary to constrain the absolute timing of sulfide precipitation and gold mineralization (e.g., Selby et al., 2002).

This chapter presents microstructural and paragenetic analyses of the Ogama-Rockland gold deposit, which provide key textural and temporal relationships among molybdenite, gold and other alteration and vein minerals. Four U-Pb geochronological results are reported from two major phases of tonalite (zircon) and one aplite dike (zircon and monazite), which represent the major lithologies in the district of the deposit. A Re-Os age was obtained from a molybdenite-rich vein, and represents the first published Re-Os age constraint for the Rice Lake greenstone belt. Combined with field-based lithologic and structural investigations (Chapter 3), the results tightly constrain the timing of gold mineralization and associated magmatism and deformation.

## 4.2 Geological background

The Rice Lake greenstone belt trends east-west between two Archean terranes, the North Caribou terrane to the north and the English River Subprovince to the south (Fig. 4.1). Terrane boundaries are defined by two crustal scale shear zones, the Wanipigow fault to the north and the Manigotangan fault to the south. The greenstone belt is dominated by metavolcanic and metasedimentary rocks of four lithostratigraphic assemblages, and is intruded by the Ross River granitoid pluton (Fig. 4.1b). Most supracrustal rocks are metamorphosed to greenschist facies, although amphibolite facies conditions were reached around the pluton (Poulsen et al., 1996).

The Ogama-Rockland deposit area has been mapped in detail by Stockwell and Lord (1939) and Zhou et al. (2012, 2014; Chapter 3). The area includes several south-facing formations of basaltic flows, mafic to felsic volcaniclastic rocks, greywacke and voluminous gabbroic sills (Fig. 4.2). These supracrustal rocks are intruded by the Ross River pluton, which includes various phases at its southeastern margin. The deposit is hosted by three phases of tonalite and

associated felsic dikes. Five generations of deformation structures are recognized in the supracrustal rocks near the deposit (Zhou et al., 2016), two of which ( $G_1'$  and  $G_2'$ ) are present in the plutonic rocks at the deposit (Fig. 4.3; Chapter 3). The entire stratigraphic succession was folded during early deformation prior to emplacement of some aplite dikes. All lithological units are crosscut by  $G_2'$  conjugate sets of ductile shear zones, which are spatially associated with several lode gold deposits in the area (Fig. 4.2).

Geochronological data from within the southern margin of the North Caribou Terrane, the Uchi Subprovince and the adjacent English River Subprovince are summarized in Anderson (2013a). Maximum ages of the supracrustal rocks in the southeastern Rice Lake belt are constrained by the youngest detrital zircon age of  $< 2745 \pm 5$  Ma (Anderson, 2013b) from greywacke of the Bidou assemblage at the lowest stratigraphic levels in the core area of the Beresford Lake Anticlinorium (Fig. 4.1b, 4.2). The highest stratigraphic levels on the southern limb of the Beresford Lake Anticlinorium are occupied by the Gem and Edmunds assemblages (Fig. 4.1b). The age of the Gem assemblage is constrained by two igneous zircon crystallization ages from dacitic lapilli tuff ( $2727 \pm 2$  Ma; Anderson, 2013b) and rhyolite breccia ( $2722 \pm 2$  Ma; Davis, 1994). The maximum depositional age of the Edmunds assemblage is constrained by the youngest detrital zircon age of  $2705 \pm 2$  Ma (Davis, 1994). Earlier geochronological work in the Ogama-Rockland area was carried out by Turek et al. (1989), who obtained a U-Pb zircon age of  $2728 \pm 8$  Ma from a marginal tonalite phase near the southeastern margin of the Ross River pluton close to the Ogama shaft. Anderson (2008) obtained a U-Pb zircon age of  $2724 \pm 1$  Ma from granodiorite in the central portion of the Ross River pluton.

The host rocks of the Ogama-Rockland deposit include various felsic intrusive phases, of which foliated ( $S_1'$ ) tonalite is the most common (Fig. 4.4, 4.5 4.6, 4.7a). Based on the work in Chapter 3, the Ogama-Rockland gold deposit consists of auriferous quartz-(carbonate) veins associated with  $G_2'$  conjugate sets of steep, west-southwest– to north-northwest-trending, dextral shear zones and steep, north to northeast-trending, sinistral shear zones (Fig. 4.4). Gold mineralization occurs in various stages ( $V_1'$ ,  $V_2'$ ,  $V_5'$ ) in the veins. Folded ( $F_1'$ ) gold-bearing  $V_1'$  veins apparently show no spatial relationships with any aplite dike. However, sheeted planar auriferous  $V_2'$  veins cut across an early set of north-trending aplite dikes and are crosscut by a late set of aplite dikes.  $V_2'$  veins and associated aplite dikes are displaced by a  $G_2'$  ductile shear zone, indicating they were emplaced before  $G_2'$  shearing (Fig. 4.5). High grade mineralized  $V_5'$

veins are interpreted to have been emplaced late during  $G_2'$  shearing, postdating the aplite dikes.

### **4.3 Hydrothermal alteration, vein mineralogy and paragenesis**

#### **4.3.1 Hydrothermal alteration**

There are typically no discernible zoned hydrothermal haloes associated with  $V_1'$ ,  $V_2'$ ,  $V_3'$ ,  $V_4'$  veins. However, hydrothermal alteration halos are often but not always well-developed on both sides of the  $V_5'$  auriferous veins in the Ogama-Rockland area. The geometry of the alteration can be symmetric or asymmetric with respect to the associated vein, and appears to be controlled by lithologic setting and fracture or strain intensity (Fig. 4.8a, b). Mesoscopic alteration zones typically look greenish (Fig. 4.8a) or dark brownish (Fig. 4.8b), or exhibit these two varieties in different portions attached to the vein (Fig. 4.8c). The alteration zones are typically less than 1 m thick. Alteration intensity increases toward the vein and can be roughly divided into (greenish) weak and (brownish) strong zones (Fig. 4.9a, b). Weak alteration is characterized by the presence of sericite along quartz and feldspar grain boundaries and in transgranular fractures (Fig. 4.9c). Individual feldspar grains remain largely unaltered (Fig. 4.9c), whereas biotite grains are typically replaced by chlorite along grain boundaries or cleavage planes. In contrast, the strong alteration zone is marked by complete replacement of most feldspar grains by aggregates of sericite, carbonate, epidote, albite, quartz and clay minerals (Fig. 4.9d, e, f), and by complete replacement of biotite and chlorite grains by sericite and clay minerals (Fig. 4.9d). More detailed descriptions of deformation features in shear zones are given in Chapter 3.

#### **4.3.2 Vein mineralogy**

Textural and relative chronological relationships of vein minerals were studied in approximately 150 hand specimens and 90 polished thin sections. Mineral identification was carried out by conventional transmitted and reflected light microscopy, and aided by scanning electron microscope (SEM) and X-ray microanalysis.

$V_1'$  and  $V_2'$  veins contain over 90% quartz and minor amounts of sericite, carbonate, pyrite, chalcopyrite, molybdenite and low grade gold (at levels of hundreds of ppb).  $V_3'$  veins contain over 95% quartz and minor amounts of carbonate, sericite, and chalcopyrite.  $V_4'$  veins consist of over 95% quartz and small amounts of sericite, carbonate, chalcopyrite, pyrite and molybdenite. The paragenetic sequence of auriferous  $V_1'$  and  $V_2'$  vein minerals is not well understood due to

limited numbers of polished thin sections and lack of key textural evidence.

The following descriptions are concerned specifically with V<sub>5</sub>' fault-fill veins, which are the dominant vein type and contain high grade gold at the Ogama-Rockland area (Fig. 3.26, Chapter 3). Although vein mineralogy and modal proportions are different from one vein to another, a typical mineralized vein consists of more than 90% quartz and minor amounts of other minerals (mainly sericite, carbonates, tourmaline, sulfides). They are mostly mesoscopically massive, but a few show ribbon or laminated texture incorporating microlithons of altered tonalite (Chapter 3), which reflect episodes of vein opening and filling.

#### *4.3.2.1 Quartz*

Quartz is the dominant mineral in every vein, but displays a variety of primary textures and deformation characteristics in thin sections. Grain size varies from approximately 3 mm to less than 5 µm. Large quartz grains (1–3 mm) are typically euhedral to subhedral, elongate and blocky, which is a texture indicative of primary open space filling (Fig. 4.10a, b). Inclusion bands are not uncommon within these grains, and they may show a preferred alignment (Fig. 4.10a, b). Large grains typically exhibit patchy undulose extinction (Fig. 4.10a, b). Quartz subgrains or new grains (< 20 µm), probably formed during “bulging recrystallization” (Stipp et al., 2002; Passchier and Trouw, 2005) of primary large grains, and usually exist at the planar contacts between large crystals (Fig. 4.10a). Small quartz grains (ranging from 50 µm to 200 µm) typically show undulose extinction (Fig. 4.10b, c). Intragranular cracking is quite common. Orthogonal transgranular fracture sets are common in recrystallized quartz grains associated with gold (Chapter 3). Quartz grains are in contact with all other minerals and may contain sericite inclusions.

#### *4.3.2.2 Plagioclase*

This rare vein mineral typically forms millimetric phenocrysts in vein margins. Plagioclase often displays wedge-shaped deformation twinning (Fig. 4.10e). It is usually in contact with quartz, sericite and chalcopyrite crystals and sometimes contains tiny inclusions of sericite (Fig. 4.10e, f).

#### *4.3.2.3 Tourmaline*

This hexahedral prismatic or elongate mineral (mostly around 100–200 µm in diameter) is exclusively abundant at vein margins or in tonalitic slivers within veins (Fig. 4.11a). Elongate mineral aggregates sometimes define a preferred orientation (Fig. 4.11b). Individual grains

display plenty of microcracks and enclose tiny inclusions of sericite and chalcopyrite (Fig. 4.11a, b). Tourmaline is often in contact with sericite, chalcopyrite (Fig. 4.11a, b).

#### *4.3.2.4 Carbonate*

Carbonate minerals (ankerite and calcite) are commonly present in the studied V<sub>5'</sub> fault-fill veins. They typically constitute less than 5% of the vein volume but they are the dominant mineral in some veins. There are three carbonate depositional stages. Early stage 1 carbonates form small individual grains or grain aggregates surrounded by sericite, chlorite, plagioclase and quartz at vein margins. Relatively later stage 2 carbonates occur as small euhedral grains (ca. 1mm) interstitial to coarse-grained euhedral quartz crystals in the center of the vein (Fig. 4.10a), or as elongate grain aggregates (ca. 1mm) surrounded by dynamically recrystallized quartz grains (Fig. 4.10b; See also Chapter 3). A few grains exhibit bent wedge-shaped deformation twinning. Latest stage 3 carbonates form coarse-grained aggregates or carbonate-sericite microveinlets that crosscut quartz microveinlets (Fig. 4.9f).

#### *4.3.2.5 Sericite*

This mineral exists in every V<sub>5'</sub> fault-fill vein and is intimately associated with different sulfide mineral assemblages (Fig. 4.10c, d). Its grain size ranges from less than 10 µm to approximately 150 µm. Sericite generally occurs as radial grain aggregates in contact with tourmaline, chlorite, quartz, plagioclase, chalcopyrite and molybdenite (Fig. 4.10e, f, 4.11a, b). Minor sericite occurs as small inclusions in quartz, plagioclase, tourmaline and chalcopyrite (Fig. 4.10e, 4.11a, f).

#### *4.3.2.6 Chlorite*

This mineral generally replaces biotite in altered tonalitic wall rocks (Chapter 3) and rarely occurs as isolated plates or grain aggregates in shear veins. Chlorite is consistently associated with sericite, tourmaline and sulfides (Fig. 4.10e).

#### *4.3.2.7 Molybdenite*

This mineral is commonly present in V<sub>5'</sub> fault-fill veins. Its grain size varies from 10 µm to 3 mm. Molybdenite is typically blade-shaped, and exhibits straight, bent or kinked cleavages (Fig. 4.11c). Molybdenite aggregates display a preferred orientation defined by aligned elongate grains (Fig. 4.11c). Molybdenite has a close spatial association with tourmaline, chlorite, quartz, sericite, chalcopyrite and pyrite. Isolated molybdenite grains are typically surrounded by sericite and quartz (Fig. 4.11a, b). Molybdenite that is in contact with pyrite and chalcopyrite may show

various textural relationships. It crosscuts pyrite (Fig. 4.11c) and chalcopyrite (Fig. 4.10d, 4.11e), but also occurs as tiny inclusions in pyrite (Fig. 4.11d) and chalcopyrite (Fig. 4.11f), which indicates contemporaneous molybdenite-pyrite and molybdenite-chalcopyrite precipitation. No direct contact or textural relationships are observed between gold and molybdenite, indicating gold and molybdenite were likely deposited at separate stages during veining.

#### 4.3.2.8 Pyrite

This mineral is quite common in V<sub>5</sub>' fault-fill veins. It is typically euhedral to subhedral, ranging from 20 µm to 1 mm. Pyrite is spatially associated with quartz, sericite, chlorite, carbonates, molybdenite, chalcopyrite and gold. In a few cases, individual pyrite grains encompass small inclusions of chalcopyrite, molybdenite, sericite and quartz (Fig. 4.11c, d). These pyrite grains are in contact with quartz, sericite, molybdenite, and chalcopyrite (Fig. 4.10c, d, 4.11c), and are often crosscut by molybdenite (Fig. 4.11c). This occurrence of pyrite sometimes exhibits intragranular microcracking (Fig. 4.11d).

Pyrite also occurs as small (typically 100–300 µm), mostly subrounded inclusions in contact with each other within a single chalcopyrite grain (Fig. 4.12b), the appearance of which is identical to the classic clast-supported texture of conglomerate. The pyrite grains sometimes display clean rims, and enclose a linear alignment of 10–50 µm chalcopyrite inclusions (Fig. 4.12b). These pyrite grains also occur as isolated, angular to subrounded inclusions within individual chalcopyrite grains (Fig. 4.12a, c), and locally are spatially associated with bismuth-bearing minerals (Fig. 4.12a).

In some instances, pyrite is spatially associated with visible native gold in fault-fill veins. In this case, pyrite and the surrounding quartz crystals are typically orthogonally fractured (Fig. 4.12d, e; see also Chapter 3). The pyrite contains ~ 5–20 µm gold inclusions, but is also discontinuously coated or partially corroded by native gold along grain boundaries or fractures (Fig. 4.12d, e).

#### 4.3.2.9 Chalcopyrite

This mineral is the most common and abundant sulfide in V<sub>5</sub>' fault-fill veins. In vein margins or tonalitic slivers within veins, chalcopyrite occurs as anhedral angular or irregular-shaped grains in contact with sericite, quartz, plagioclase, chlorite, carbonates, tourmaline and molybdenite (Fig. 4.10e, f, 4.11a, b). Chalcopyrite is interstitial to quartz and sericite in most cases, and therefore its crystal shape (straight boundary and corroded appearance) is significantly

influenced by surrounding sericite and quartz (Fig. 4.10e, f). Chalcopyrite also occurs as small inclusions in tourmaline (Fig. 4.11b).

Chalcopyrite is intimately associated with sericite, quartz and all other sulfide minerals in the fault-fill veins, where it attaches to sericite, quartz, pyrite, molybdenite, a bismuth-bearing mineral (Fig. 4.10c, d, 4.11c, e, 4.12a), and is sometimes crosscut by molybdenite (Fig. 4.10d, 4.11e). Chalcopyrite may enclose sparsely distributed inclusions of sericite, quartz, molybdenite and pyrite (Fig. 4.11f, 4.12c), and sometimes a stack of pyrite inclusions in contact with each other (Fig. 4.12b). This occurrence of chalcopyrite typically displays intragranular microcracking (Fig. 4.11e, f, 4.12a, b, c). Chalcopyrite may also occur as tiny inclusions in pyrite (Fig. 4.11c).

Chalcopyrite is closely associated with native gold. In this setting, chalcopyrite attaches to quartz, gold, and pyrite (and its oxidized counterpart). Chalcopyrite often exhibits intergrowth with bornite or partial replacement by bornite (Fig. 4.12f).

#### 4.3.2.10 Bornite

This mineral is consistently associated with chalcopyrite. Bornite either slightly or completely replaces chalcopyrite (Fig. 4.12f), or is intergrown with chalcopyrite.

#### 4.3.2.11 Bismuth-bearing minerals

The bismuth-bearing minerals include native bismuth and tellurobismuthite. They are spatially associated with chalcopyrite, bornite and pyrite. The bismuth-bearing minerals are often observed to be partially or completely replaced by related oxidation products due to weathering or supergene oxidizing processes (Fig. 4.12a).

#### 4.3.2.12 Gold

Gold is mostly electrum in composition, with gold to silver ratios ranging from 23:1 to 0.44:1 (Xue, 2011). The size of single grains ranges from 10 µm to 0.5 mm. As summarized in Chapter 3, most gold occurs as visible native gold in fractured quartz and pyrite (Fig. 4.12d, e), or as irregular patches in grain boundaries interstitial to quartz, chalcopyrite-bornite, pyrite and associated oxidized products (Fig. 4.12d, e, f). The interconnection and continuum among these various textural styles of gold indicate synchronicity of these gold occurrences. It is interpreted that these textural styles of gold result from precipitation/remobilization induced by brittle fracturing of quartz and pyrite during late G<sub>2'</sub> deformation (Chapter 3). Such occurrences of gold and associated deformational features are also common in several lode gold deposits in the Archean Abitibi greenstone belt (e.g., Gorman et al., 1981).

Minor gold occurs as < 20 µm globular inclusions in fractured pyrite (Fig. 4.12d, e), which may be a primary feature that is older than the other gold textural styles (e.g., Oberthür et al., 1997). Alternatively, the globular inclusions represent remobilization of “invisible gold” (submicroscopic particles or solid solution; Cabri et al., 1989; Cook and Chryssoulis, 1990) in pyrite (e.g., Mumin, et al., 1994; Velásquez et al., 2014).

#### *4.3.2.13 Goethite and other oxide minerals*

It is commonly observed that oxide minerals marginally or completely replace their counterpart sulfides or metals. For instance, pyrite is usually replaced along grain boundaries by goethite (Fig. 4.12a, f), and bismuth-bearing minerals are replaced by bismite (Fig. 4.12a). These secondary oxidized products are likely due to post-ore supergene weathering processes.

#### *4.3.3 Paragenesis*

V<sub>5</sub>' fault-fill veins are generally considered to develop through multiple fillings of hydrothermal minerals in dilational jogs opening at a small angle to a fault plane (Passchier and Trouw, 2005; Bons et al., 2012). Quartz crystals from shear veins at the Ogama-Rockland deposit typically lack a “fibrous texture” (Durney and Ramsay, 1973), therefore the opening direction of shear veins is not fully tracked. Preserved euhedral quartz grains suggest open space filling might be the most common filling mechanism. Intense deformation features like dynamic recrystallization have obscured textures formed during the primary filling process.

Although the modal proportion of minerals varies from one vein to another, and from one ribbon of a vein to another, the spatial and temporal relationships of vein minerals are roughly consistent throughout the deposit. Based on the textural relationships described above, a generalized depositional sequence of vein minerals in an idealized vein ribbon, including all primary vein minerals, is summarized in Fig. 4.13. Most vein minerals, excluding quartz, are distributed in or close to ribbon walls or vein margins. Plagioclase, carbonates, chlorite, and radiated sericite aggregates were among the first minerals to precipitate in ribbon walls or vein margins. The next stage is the deposition of interstitial angular and irregular-shaped chalcopyrite grains and minor molybdenite needles. Hexahedral or tabular poikilitic tourmaline grains grew during this vein wall filling stage or afterwards since they contain several inclusions of sericite and chalcopyrite. Aggregates of sericite and associated molybdenite, pyrite and chalcopyrite precipitated penecontemporaneously during the initial deposition of quartz crystals close to vein walls, based on inclusions, crosscutting relationships, and contact relationships among sericite,

molybdenite, pyrite and chalcopyrite. Gold inclusions in pyrite may be synchronous with the host pyrite grains, although these inclusions may also represent remobilization of invisible gold in pyrite. Pyrite with gold inclusions and gold coatings is not observed to be spatially associated with molybdenite, suggesting precipitation of auriferous pyrite could well be a separate depositional stage different from that of molybdenite-chalcopyrite-pyrite-sericite aggregates. Some gold is in contact with intergrown chalcopyrite-bornite and pyrite, and has a close spatial association with bismuth-bearing minerals, indicating contemporaneous deposition of gold, pyrite, chalcopyrite-bornite and bismuth-bearing minerals. Minor coarse-grained carbonate aggregates and carbonate-sericite microveinlets are interpreted to have precipitated late in the depositional sequence. Gold in the fractures of pyrite and quartz grains formed latest during brittle fracturing that postdated dynamic recrystallization.

It should be noted that intense deformation processes have modified mineral appearance and gold occurrence during the post-filling stage. As described above, intragranular microcracking, deformational twinning, kinking, dynamic recrystallization and transgranular microfracturing are common in shear veins (see also Chapter 3). These deformational features are responsible for the diversity of interpretations regarding the origin of various gold textures in lode gold deposits. Numerous previous workers have conducted related research on gold-bearing pyrite or arsenic-rich pyrite textures in other gold deposits (e.g., Velásquez et al., 2014, and references therein). One prevailing interpretation is that gold inclusions in pyrite, gold in fractures, and gold coatings around pyrite are all secondary features that originated from microscale remobilization of primary invisible gold in pyrite during deformation (Velásquez et al., 2014). Various gold textures reflect different evolving stages of the gold system (e.g., Mumin et al., 1994). An alternative interpretation is that the various occurrences of native visible gold represent different primary paragenetic stages during filling and subsequent fracturing (e.g., Robert and Brown, 1986). At the Ogama-Rockland deposit, it is still uncertain whether gold is initially present in solid solution or as submicroscopic particles in pyrite due to the lack of systematic geochemical work. Therefore, the origin of visible gold inclusions in pyrite or gold coatings around pyrite could either be a primary feature or secondary remobilization of invisible gold in pyrite. Native gold patches occur interstitial to quartz when pyrite is absent or distant, indicating this occurrence of gold is probably a primary feature. Large irregular-shaped patches of gold in contact with quartz, chalcopyrite-bornite and relatively small pyrite grains cannot have formed

exclusively through microscale remobilization of invisible gold in small neighboring pyrite. Therefore, it is interpreted that native gold interstitial to quartz, or to quartz, chalcopyrite-bornite and pyrite assemblages precipitated later than the neighboring quartz and sulfide aggregates. Gold in fractures within pyrite or quartz typically displays a continuum with gold in interstitial mineralogical sites, indicating gold in interstitial sites was remobilized and re-precipitated in fractures.

#### 4.4 Geochronological methods and results

##### 4.4.1 U-Pb zircon/monazite chronometer

To precisely constrain the timing of early gold mineralization associated with V<sub>2</sub>' veins, we dated the host plutonic rocks (sample 102-13-225A and D; zircon) and an aplite dike (sample 102-13-505; zircon and monazite) that crosscuts V<sub>2</sub>' veins, using the U-Pb system. Isotopes were measured on individual crystals by laser ablation-inductively coupled plasma mass spectrometry (LA-ICPMS) and isotope dilution – thermal ionization mass spectrometry (ID-TIMS) at the Jack Satterly Geochronology Laboratory, University of Toronto. Sample locations are indicated on Fig. 4.4 and 4.5.

###### 4.4.1.1 Mineral separation and analytical methods

Sample processing and U-Pb geochronology followed standard procedures practiced at the Jack Satterly Geochronology Laboratory (Krogh, 1973; Corfu and Muir, 1989a, b; Davis and Lin, 2003; Zhang et al., 2014b). Rock samples weighed about 10 kg and were crushed using a jaw crusher followed by a disc mill. Zircon was extracted by initial heavy liquid and subsequent paramagnetic separation. Final sample selection was by hand-picking under a microscope, choosing the freshest, cleanest and least cracked zircon grains. Monazite was also extracted from the aplite dike and handpicked. Both tonalite samples yielded abundant zircon whereas the aplite dike sample yielded only a small amount of zircon. Optical images of selected zircon and monazite populations are given in Fig. 4.14.

Transparent, uncracked grains were mounted onto double sided tape and targeted on natural surfaces. Selected sample spots were ablated using a 213 nm New Wave laser at 5 Hz and about 5 J/cm<sup>2</sup> with beam diameter of 20 microns. Mass spectrometry was carried out on a Plasmaquad quadrupole ICPMS equipped an S-option 75 l/sec rotary pump to increase sensitivity. Data were collected on <sup>88</sup>Sr (10 ms), <sup>206</sup>Pb (30 ms), <sup>207</sup>Pb (70 ms), <sup>232</sup>Th (10 ms) and <sup>238</sup>U (20 ms). Prior to

analyses spots were pre-ablated using a raster pattern to clean the surface. Following a 10 sec period of baseline accumulation the laser sampling beam was turned on and data were collected for 25 seconds followed by a 50 sec washout period. About 140 measurement cycles per sample were produced and ablation pits are about 15 microns deep.

Data were edited and reduced using custom VBA software written by the author (D.W. Davis).  $^{206}\text{Pb}/^{238}\text{U}$  ratios show increasing fractionation caused by penetration depth through the run while the  $^{207}\text{Pb}/^{206}\text{Pb}$  profile is usually flat. No corrections were made for common Pb, since the  $^{204}\text{Pb}$  peak is too small to be measured precisely and common Pb should be insignificant for unaltered Precambrian zircon and monazite. If present, common Pb, would have the effect of pushing data to the right away from the concordia curve along a mixing line intersecting concordia at approximately 5000 Ma.  $^{88}\text{Sr}$  was monitored from zircon in order to detect intersection of the beam with zones of alteration or inclusions and data showing high Sr or irregular time resolved profiles were either averaged over restricted time windows or rejected. The Th/U ratio of zircon can be a useful petrogenetic indicator and was also measured, although it is only a rough estimate because the ratio is not constant in the standard. Low Th/U (< 0.1) is characteristic of metamorphic and hydrothermal zircon (Rubatto, 2002) whereas most zircon crystallized from felsic melts has Th/U in the range 0.1-1.0. The zircon standard was DD85-17, from a quartz diorite from the Marmion batholith in northwest Ontario previously dated at  $3002 \pm 2$  Ma (Tomlinson et al., 2003). The monazite standard was from DD90-26A, a sample of the Lac LaCroix granite in the western Superior province of Minnesota previously dated at  $2671 \pm 2$  Ma (D.W. Davis, unpublished data). Sets of 3 sample measurements are bracketed by measurements on standards. Differences between standards are time interpolated to correct sample measurements.

For ID-TIMS analysis, partially ablated grains were taken off the mount, annealed at  $1000^\circ\text{C}$  and leached overnight in 30% HF to dissolve any alteration (chemical abrasion method of Mattinson, 2005). Weights of zircon grains selected for ID-TIMS analyses were estimated from photomicrographs (Fig. 4.14). Washed zircon was dissolved using concentrated hydrofluoric acid (HF) in teflon bombs at  $200^\circ\text{C}$  for 5 days (Krogh, 1973). Samples were subsequently redissolved in 3N HCl along with  $^{202}\text{Pb}$ - $^{205}\text{Pb}$ - $^{233}\text{U}$ - $^{235}\text{U}$  spike (Earth time ET2535). U and Pb were separated from the solutions using 50 microliter anion exchange columns (Krogh, 1973). Mixed purified U and Pb solutions were loaded together onto Re filaments using silica gel and

analyzed with a VG354 mass spectrometer in either single collector or multi-dynamic mode. Measurements of small samples were made using a Daly collector in pulse counting mode. Dead time of the measuring system was 14.5 nsec for Pb masses and 13.0 nsec for UO<sub>2</sub> masses. The mass discrimination correction for the Daly detector is constant at 0.07%/Atomic Mass Unit. Enough spike was added to assure precise measurements of <sup>202</sup>Pb-<sup>205</sup>Pb-<sup>233</sup>U-<sup>235</sup>U, as well as sample isotopes, in Faraday collectors. Static measurements of the ratio of intensities at mass 202 and mass 203 (BaPO<sub>16</sub>O<sub>18</sub><sup>+</sup>) were made before and after each static sample Pb measurement in order to correct for isobaric interference on mass 202 from BaPO<sub>16</sub>O<sub>17</sub><sup>+</sup>. Early measurements of <sup>207</sup>Pb/<sup>204</sup>Pb are affected by organic isobars. These are monitored on mass 210 (209 has bismuth interference) and go down slowly during the course of a run. They are not seen to affect <sup>206</sup>Pb/<sup>205</sup>Pb or even <sup>207</sup>Pb/<sup>205</sup>Pb ratios after the first few blocks of data but the <sup>207</sup>Pb/<sup>204</sup>Pb ratios invariably increase over the course of the run, consistent with the signal observed at mass 210, which usually starts at about 200 c/s and is reduced to baseline over several hours. <sup>207</sup>Pb/<sup>204</sup>Pb ratios collected when the mass 210 signal is at baseline are used, by which time the Pb sample is depleted in lighter isotopes and usually shows a fractionation near zero. U is analyzed at a higher temperature than Pb, which can be measured to near exhaustion without compromising U measurements. Faraday amplifiers were calibrated daily. Daly gains were calibrated at the beginning of each sample. <sup>207</sup>Pb and <sup>204</sup>Pb were measured in peak jumping mode on the Daly at near the end of Pb emission to confirm static values.

#### 4.4.1.2 Results

Results of LA-ICPMS measurements are given in Table 4.1.1–4.1.4 (errors are at  $1\sigma$ ), and are plotted on Fig. 4.15. Results of ID-TIMS measurements are given in Table 4.2 (errors are at  $2\sigma$ ) and plotted on Fig. 4.16. All error ellipses are given at two sigma. U decay constants are from Jaffey et al. (1971). All age uncertainties below are reported at two sigma with [without] decay constant uncertainty. <sup>207</sup>Pb/<sup>206</sup>Pb ratios give the most robust age estimates for Archean zircon since they are least susceptible to bias from Pb loss. Results of a first round of ID-TIMS analyses on zircon tend to be discordant, probably because of insufficient leaching. Re-leaching of grains using conc. HF for several hours resulted in concordant data (dwd6038 and higher, Table 4.2).

##### 4.4.1.2.1 Tonalite type-I (Sample 102-13-225A)

This sample was taken from a foliated medium-grained tonalite phase (shown in Fig. 4.4)

that is one dominant phase of the Ross River pluton, hosting various dikes and vein systems. The sample yielded a large amount of zircon, generally as brown or colorless euhedral grains or fragments (Fig. 4.14a).

LA-ICPMS data from 30 grains produced overlapping, generally concordant data with an average  $^{207}\text{Pb}/^{206}\text{Pb}$  age of  $2726.2 \pm 4.7$  [ $\pm 8.2$ ] Ma (MSWD = 0.6, Table 4.1.1, Fig. 4.15a). Six fractions of zircon were analyzed by ID-TIMS (Table 4.2, Fig. 4.16a), and define a Pb loss line with an upper intercept age of  $2727.4 \pm 0.8$  [ $\pm 7.0$ ] Ma but with a high MSWD of 13, partly because one discordant datum has a significantly younger  $^{207}\text{Pb}/^{206}\text{Pb}$  age than the others. Since Pb loss can only reduce the  $^{207}\text{Pb}/^{206}\text{Pb}$  age, this datum is omitted and the remaining five regressed, giving an upper intercept age of  $2728.7 \pm 0.7$  [ $\pm 7.0$ ] Ma (MSWD = 3.8) and a lower intercept age within error of zero. Three fractions that were leached more strongly produced concordant or near-concordant data which give an average  $^{207}\text{Pb}/^{206}\text{Pb}$  age of  $2728.7 \pm 1.1$  [ $\pm 6.9$ ] Ma but with an MSWD of 4.5, which indicates that scatter is not due to different ages of Pb loss (see below). The regression based on 5 data is taken as the best estimate for the age of igneous crystallization of the tonalite type-I phase.

#### *4.4.1.2.2 Tonalite type-II (Sample 102-13-225D)*

This sample was taken from a foliated coarse-grained tonalite phase shown in Fig. 4.4. It is also one of the dominant intrusive phases of the Ross River pluton, hosting various generations of dikes and veins. A large amount of zircon was recovered from this sample as mostly brown or colorless euhedral grains or fragments (Fig. 4.14b).

LA-ICPMS data from 30 grains produced mostly concordant data whose  $^{207}\text{Pb}/^{206}\text{Pb}$  ages overlap within error, giving an average of  $2723.7 \pm 5.8$  [ $\pm 9.0$ ] Ma (MSWD = 1.15, Table 4.1.2, Fig. 4.15b). Five fractions of zircon were analyzed by ID-TIMS, yielding an upper intercept age of  $2727.2 \pm 5.9$  [ $\pm 9.1$ ] Ma (Fig. 4.16b). The very high MSWD of 655 is due to the high precision of the discordant analyses which scatter well outside of error. Two data are concordant within error but one is of relatively low precision. Since Pb loss can only reduce the age, the average of the two concordant data plus the oldest discordant datum is taken as the best estimate for the age of igneous crystallization of the tonalite type-II phase. This is  $2728.2 \pm 0.6$  [ $\pm 6.8$ ] Ma (MSWD = 2.5).

#### *4.4.1.2.3 Aplite dike (Sample 102-13-505)*

Sample 102-13-505 was obtained from steep, west-trending, aplite dikes that crosscut early

sheeted planar V<sub>2</sub>' veins (Fig. 4.5, 4.7c). However, minor steep, north-trending, narrow aplite dikes are cut by V<sub>2</sub>' veins (Fig. 4.5, 4.7b). Hence, it is interpreted that aplite dikes must have been emplaced broadly coevally with V<sub>2</sub>' veins. V<sub>2</sub>' veins contain low grades of gold, as well as molybdenum and copper. Therefore, U-Pb dating of the west-trending aplite dike samples should constrain the minimum age of related gold mineralization associated with the V<sub>2</sub>' veins.

A small amount of zircon was extracted from this sample and generally consists of tiny highly cracked brown or colorless euhedral long prismatic or equant grains or fragments (Fig. 4.14c). LA-ICPMS data from 25 grains again produced mostly concordant or near-concordant overlapping data whose <sup>207</sup>Pb/<sup>206</sup>Pb ages give an average of  $2728.2 \pm 7.2 [\pm 9.9]$  Ma (MSWD = 1.1, Table 4.1.3, Fig. 4.15c).

Five data were obtained by ID-TIMS but of the three strongly leached grains only one is concordant within error (Table 4.2, Fig 4.16c). Regressing all five data gives an upper intercept age of  $2728.5 \pm 2.3 [\pm 7.3]$  Ma, with a lower intercept near zero and a high MSWD of 11.3. Averaging the <sup>207</sup>Pb/<sup>206</sup>Pb ages of the three most concordant data gives  $2727.9 \pm 1.6 [\pm 7.0]$  Ma, which we consider the most reliable estimate for the age of the zircon although the MSWD of 4 is still somewhat high.

This sample also yielded a small amount of monazite generally as tiny equant grains (Fig. 4.14d), which were extracted after decanting most of the magnetic at 1 Amp/10° fraction on the Frantz separator leaving only the finest fraction. LA-ICPMS analyses on 15 grains produced data that scatter widely above and below concordia (Fig. 4.15d). A cluster of near-concordant data defines an average <sup>207</sup>Pb/<sup>206</sup>Pb age of  $2764 \pm 22$  Ma (MSWD = 2.1) but another near-concordant datum appears to be significantly younger ( $2606 \pm 38$  Ma, Table 4.1.4).

Three single monazite grains were analyzed by ID-TIMS and again produced scattered data, only one of which is concordant (Fig. 4.16d, Table 4.2). Regressing combinations of data gives ages of about 2730 Ma but with large errors due to the high MSWDs. The best estimate for the age of the monazite is the <sup>207</sup>Pb/<sup>206</sup>Pb age of the concordant datum, which is  $2732 \pm 5$  Ma. The ID-TIMS analyses show significant amounts of common Pb, which is not corrected in the LA-ICPMS analyses. Hence ages based on LA-ICPMS are probably maximum estimates. High U concentrations of ca. 1000 ppm and Th/U ratios of ca. 40 are typical of magmatic monazite.

#### **4.4.2 Re-Os molybdenite chronometer**

Sample 102-13-257 was acquired from a molybdenite-rich V<sub>4</sub>' vein hosted in foliated

tonalite (Fig. 4.6, 4.7d). The V<sub>4'</sub> vein crosscuts both steep, west-trending, aplite dikes and sheeted laminated V<sub>3'</sub> veins (Fig. 4.6, 4.7d), indicating that this V<sub>4'</sub> vein postdates the aplite dikes and V<sub>3'</sub> veins. Apparent horizontal displacement along the V<sub>4'</sub> vein, as suggested by aplite dikes on both sides of the V<sub>4'</sub> vein, is approximately 2.5 m in a sinistral manner. Since no discernible ductile or brittle-ductile shear zones bound the V<sub>4'</sub> vein, it is interpreted that this V<sub>4'</sub> vein is an oblique-extension vein formed under dilation of a brittle fracture with a boundary-parallel sinistral shear component and a boundary-normal extension component. However, this V<sub>4'</sub> vein is offset by a northwest-trending steep G<sub>2'</sub> ductile shear zone in a dextral manner, indicating this V<sub>4'</sub> vein predates the main G<sub>2'</sub> shearing.

Hand specimens from the V<sub>4'</sub> vein reveal a mesoscopically massive quartz vein that has been sheared and annealed, and contain sub-mm to mm disseminated to congregated molybdenite that is spatially associated with pyrite and chalcopyrite (Fig. 4.17a). Sulfide is sparse and often forms a linear feature in the vein (Fig. 4.17a). However, individual molybdenite blades and grains appear as euhedral platelets. In thin section, molybdenite is typically kinked and bent, and is in contact with sericite, chlorite, quartz, chalcopyrite and pyrite. The dated molybdenite crystals appear only in contact with massive quartz (Fig. 4.17b, c).

#### 4.4.2.1 Analytical methods

Full descriptions on Re-Os analytical methodology are given in Zimmerman et al. (2008). More information on Re-Os analysis and interpretation can be found in recent overviews by Stein et al. (2001) and Stein (2014). Re-Os molybdenite analysis was carried out used the analytical procedures of the AIRIE Program, Colorado State University (Markey et al., 1998, 2003; Stein et al., 2001, 2003). Between 25 and 42 mg of molybdenite mineral separate from multiple crystals was created using a diamond-tipped drillbit, with no other sulfides being discernable in the mineral separate (Fig. 4.17b, c). Dilution by quartz (the mineral separate was estimated to comprise ~80% molybdenite, see footnotes of Table 4.3) does not affect the resultant age because of the extremely high Re and <sup>187</sup>Os concentrations in molybdenite compared to quartz (Stein, 2014). The molybdenite powder, mixed-double <sup>185</sup>Re-<sup>188</sup>Os-<sup>190</sup>Os spikes, and inverse *aqua regia* were added to a Carius tube (Shirey and Walker, 1995). The sealed tube was heated for ~12 h at 275°C to achieve sample-spike equilibration. Osmium solvent extraction from the digested solution used an organic solvent, and was followed by back-extraction of Os into HBr. The Os was isolated by distillation and further purified by

microdistillation. Rhenium was isolated by anion exchange chromatography using cleaned Biorad AG 1-X8, 200–400 mesh, Cl<sup>-</sup> form resin. The Re and Os isotopic compositions were measured using isotope dilution – negative thermal ionization mass spectrometry (ID-NTIMS) after the procedure of Creaser et al. (1991) and Völkening et al. (1991). Approximately 1–2 ng of dissolved Re or Os is loaded and dried on outgassed Pt filaments. Measurements were carried out using a single Faraday cup collector in peak jumping mode with background and interfering isotopes monitored. The Re and Os concentrations were determined by isotope dilution analysis (Heumann 1988). The Re–Os age was determined by the age equation,  $^{187}\text{Os} = ^{187}\text{Re} (e^{\lambda t} - 1)$  with  $\lambda = 1.666 \times 10^{-11} \text{ year}^{-1} \pm 0.31\%$  (Smoliar et al., 1996), since no measurable common Os was taken up into the analyzed molybdenite at the time of its crystallization (see the results below). Errors are fully propagated using standard techniques including isotope dilution error magnification (Crouch and Webster, 1963). Uncertainties of the Re–Os ages are reported at the  $2\sigma$  level, in the form of “ $\pm$  without [with]” the  $^{187}\text{Re}$  decay constant uncertainty. Comparisons with U–Pb ages can be made when the decay constant uncertainties for both the Re–Os and U–Pb systems are included in the calculation of molybdenite and zircon age uncertainties.

#### 4.4.2.2 Results

The Re–Os results of sample 102-13-257 are shown in Table 4.3. This vein sample yielded a model Re–Os molybdenite age of  $2727.4 \pm 4.8 [\pm 10.0]$  Ma. The Re concentration (94.35 ppm) of the molybdenite is characteristic of magmatic vein systems (Stein, 2014). In contrast, molybdenite of metamorphic origin typically has Re concentrations at levels of several ppm or sub-ppm levels (Re concentration < 20 ppm; Stein, 2006). The concentration of common (non-radiogenic) Os is zero within uncertainty.

### 4.5 Discussions

#### 4.5.1 Relative timing of alteration and vein infill

It is suggested that mineral deposition proceeded progressively from the margins to the center in an ideal homogenous massive vein, assuming open-space filling was the principal precipitation mechanism. Continuous mineral coatings on vein walls formed during the filling of the vein, which would separate the fluid in the vein from wallrock. Therefore, fluid-wallrock interaction would be minimal and continued development of alteration envelopes would eventually cease. Hence, the progressive wallrock alteration was likely completed before the

filling of the massive vein. Some veins contain several vein ribbons separated by wallrock laminae or slivers. The laminae or slivers of altered wallrock within the veins suggest repeated fracturing and mineral precipitation along the interface between the vein and wallrock. In some cases, weak alteration halos along subvertical fractures extend beyond the location where the vein ends, indicating that hydrothermal alteration must have taken place as the hydrothermal fluid circulated through the fractures and before deposition of any vein minerals.

In other instances, observations suggest contemporaneous development of hydrothermal alteration and filling of the vein. Hydrothermal pyrite cubes and anhedral chalcopyrite aggregates occurring across vein margins or wallrock microlithons show identical textural features in both the vein and the adjacent deformed wallrock alteration halos (see also Chapter 3). Similar occurrences of molybdenite have also been observed. In addition, the intimate mineral association of sericite, chlorite, carbonates, pyrite, chalcopyrite and molybdenite in the vein is also observed in intensely altered rocks along vein margins. Continuity of hydrothermal minerals across the vein-wallrock contact and similar mineral associations are interpreted as evidence for concomitant precipitation of these minerals in veins and formation of intense alteration envelopes.

Based on this interpretation and previously described observations, it is possible to link progressive alteration processes to the vein paragenetic sequence. Tonalitic wallrock suffered weak alteration as hydrothermal fluids circulated through fractures, as evidenced by sericite replacing plagioclase along grain boundaries and transgranular cracks, and by chlorite replacing biotite along grain boundaries and cleavage planes. Further fluid-wallrock interaction caused progressively intense alteration of the wallrock, with pervasive textural destruction and complete replacement of plagioclase and biotite by sericite and chlorite, respectively. This alteration was accompanied by deposition of carbonates, tourmaline, sericite, and chlorite, as well as precipitation of early-generation sulfides like molybdenite, chalcopyrite and pyrite across the vein-wallrock contact. Gold-associated pyrite and chalcopyrite-bornite, and their spatially associated bismuth-bearing minerals appear to have deposited late in the paragenetic sequence. Small gold inclusions in pyrite and irregular-shaped native gold in interstitial mineralogical sites could have been a primary feature, whereas gold in the fractures of pyrite and quartz more likely represents a separate remobilization event associated with fracturing that postdated dynamic recrystallization of quartz during late stage G<sub>2</sub>' deformation.

#### **4.5.2 Age constraints on magmatism, vein formation, deformation and gold mineralization**

Age relationships are summarized in Fig. 4.18. To tightly constrain the timing of early gold mineralization, zircon was analyzed from two phases of the tonalite host rocks and one aplite dike that cuts auriferous V<sub>2</sub>' veins. The use of the ET2535 spike allowed Pb ages to be determined to a sub-Ma level of precision, in some cases down to 0.2 Ma (2 sigma), far better than with conventional TIMS using only a <sup>205</sup>Pb spike. MSWD values will be enhanced relative to conventional analyses with larger errors in cases where there is non-analytical (geological) scatter. Because Isoplot increases the error estimation of an average by the Student's T factor times the square root of MSWD to determine 95% confidence limits, errors on the mean are much larger than those of individual measurements in cases where the MSWD is large and the number of data (degrees of freedom) is small. The most likely source of geological scatter for discordant data is secondary Pb loss over a range of ages. At some level of precision, even concordant data will scatter outside of error due to the time scale of zircon crystallization within a large magmatic system, which may exceed 1 Ma (e.g., Mungall et al., 2016).

An additional complication is that ages based on U-Pb and Re-Os involve two different decay systems. Hence, errors in the decay constants must be included when these ages are compared. U-Pb age errors that include U decay constant uncertainties are quoted in square brackets below while the Re-Os age error includes the <sup>187</sup>Re decay constant error.

U-Pb zircon analyses from the tonalite type-I phase (sample 102-13-225A) define an age of  $2728.7 \pm 0.7$  Ma [ $\pm 7.0$ ] Ma. Zircon from the tonalite type-II phase (sample 102-13-225D) yields an age of  $2728.2 \pm 0.6$  Ma [ $\pm 6.8$ ] Ma, which overlaps within uncertainty with the age from the tonalite type-I sample. Zircon from the aplite dike (sample 102-13-505) cutting gold-bearing V<sub>2</sub>' veins yields a similar age of  $2727.9 \pm 1.6$  [ $\pm 7.0$ ] Ma, which overlaps the ages from both tonalite samples within uncertainty. Since the Th/U ratios of the zircon from the tonalite and aplite dike samples exhibit a range characteristic of magmatic zircon, the zircon is probably not metamorphic or hydrothermal in origin. Monazite from the aplite dyke also yields an indistinguishable age of  $2732 \pm 5$  Ma, which is less precise than the zircon ages but important since it cannot be ruled out that zircon from the dyke was derived from the host tonalite. Based on U-Pb dating, it is likely that emplacement of the aplite dike took place within at most a few Ma of crystallization of the host tonalite and emplacement of V<sub>2</sub>' veins. These tight age constraints also suggest that early low grade gold mineralization associated with V<sub>2</sub>' veins

occurred at approximately at the same time, since maximum age constraints from the tonalite phases and the minimum age constraint from the aplite dike overlap within uncertainties.

The Re-Os date for molybdenite from one V<sub>4'</sub> vein gives a model age of 2727.4 ± 4.8 [± 10.0] Ma, which is in excellent agreement with the U-Pb zircon ages from the two tonalite phases and one aplite dike, although the V<sub>4'</sub> vein should have been deposited relatively late based on field relationships. Mesoscopically, no discernible pyrite or chalcopyrite is associated with the dated molybdenite crystals (Fig. 4.16b, c). Hence, disturbance from other Re- and Os-bearing sulfides was minimal. Even if minor amounts of pyrite or chalcopyrite were adjacent to the molybdenite, the effect on the Re-Os molybdenite age would be minimal because molybdenite contains Re and Os concentrations that are typically several orders of magnitude higher than other sulfide minerals (Stein, 2014). Molybdenite crystals are typically homogeneous. Overgrowths have not been microscopically observed in individual molybdenite crystals. The molybdenites analyzed in this study appear kinked or bent under the microscope. However, recent research suggests that intense deformation does not affect the Re-Os age of molybdenite (e.g., Stein et al., 2001; Stein, 2014). A high Re concentration also suggests a magmatic origin rather than a metamorphic origin (Stein, 2006, 2014). Considering these factors, this Re-Os date is interpreted as the primary crystallization age of molybdenite in the V<sub>4'</sub> vein.

Combined with the crosscutting and structural relationships established in Chapter 3, it is possible to constrain the timing of deformation in the Ogama-Rockland area. Both dated tonalite phases exhibit S<sub>1'</sub> foliation and local L<sub>1'</sub> mineral lineation, indicating emplacement of tonalite phases of the Ross River pluton (~2728 Ma, this study) must have occurred before or early during G<sub>1'</sub> deformation. It is observed that steep, northwest-striking, dextral ductile shear zones occur along the contact between the aplite dike and tonalite or offset aplite dikes at a high angle, indicating emplacement of the aplite dike must have taken place before G<sub>2'</sub> or early during G<sub>2'</sub> deformation (Chapter 3). It is also noted that some aplite dikes cut across F<sub>1'</sub> folds (“F<sub>2</sub>” folds in Chapter 2, see Fig. 2.6a) near the Walton pluton (Fig. 2.3, Chapter 2), suggesting they postdate F<sub>1'</sub> folding. However, all aplite dikes have been observed to be crosscut by auriferous V<sub>5'</sub> veins and associated G<sub>2'</sub> shear zones where they coexist in outcrop. Therefore, it appears that multiple generations of aplite dike emplacement must have occurred after ca. 2728 Ma (age for emplacement of tonalite), but before formation of auriferous V<sub>5'</sub> shear veins. Aplite dikes may have formed post-G<sub>1'</sub> and pre-G<sub>2'</sub> or early during G<sub>2'</sub>.

#### ***4.5.3 Implications of ore texture and geochronology for the origin and setting of the Ogama-Rockland area***

Regional mapping and geochronological research reveal that volcanism and sedimentation (Bidou assemblage) around the Ogama-Rockland area are constrained to a short time span of ca. 2745–2731 Ma, whereas regional plutonism mostly occurred later at 2733–2715 Ma (Fig. 4.18; Turek et al., 1989; Anderson, 2008, 2013a, b). The new geochronological data presented in this study demonstrate synchronous development of plutonism, dike emplacement, vein formation, and early gold mineralization at ca. 2728 Ma for the Ogama-Rockland gold deposit (Fig. 4.18). The close time association, alteration and ore mineral assemblages, as well as the high Re concentration in the dated molybdenite suggest that granitoid magmas were the source of mineralizing fluids for early gold mineralization. This interpretation may also explain mutual crosscutting relationships between auriferous V<sub>2</sub>' veins and aplite dikes in the field. Regional peak metamorphism is interpreted to have occurred at ca. 2690–2684 Ma during tectonic regime transformation from sinistral transpression to dextral shearing (Krogh et al., 1974; Corfu et al., 1995; Anderson, 2013a), which clearly postdates the age of plutonism and mineralization obtained in this study. Therefore, if precursor research on regional peak metamorphism is correct, then regional metamorphism does not appear to have contributed to early gold mineralization in the Ogama-Rockland area.

Auriferous V<sub>5</sub>' fault-fill veins represent the youngest stage in the vein sequence of the Ogama-Rockland deposit (Chapter 3). These late gold-bearing veins are structurally controlled by G<sub>2</sub>' conjugate shear zones, and were probably emplaced during G<sub>2</sub>' deformation (Chapter 3), which is typical of an orogenic gold model (Groves et al., 1998; Robert et al., 2007). The paragenetic analysis reveals that this late gold mineralization process probably involved primary gold precipitation associated with pyrite, chalcopyrite-bornite, and bismuth-bearing minerals during the late filling stage of the V<sub>5</sub>' veins, as well as secondary gold remobilization related to late fracturing that postdated dynamic recrystallization. Therefore, a further Re-Os geochronological study on pyrite with gold inclusions would be a suitable approach to constrain the timing of late primary gold mineralization, whereas gold filling in fractures of pyrite and quartz may represent a younger metallogenic event that can't be dated directly. Recent studies suggest that superposition of two contrasting ore deposit styles is common in ancient terranes (Groves et al., 2003; Mercier-Langevin et al., 2012). This is probably the case at the Ogama-

Rockland deposit, where early gold mineralization derived from magmatic fluids was overprinted by a later orogenic gold event associated with G<sub>2</sub>' deformation.

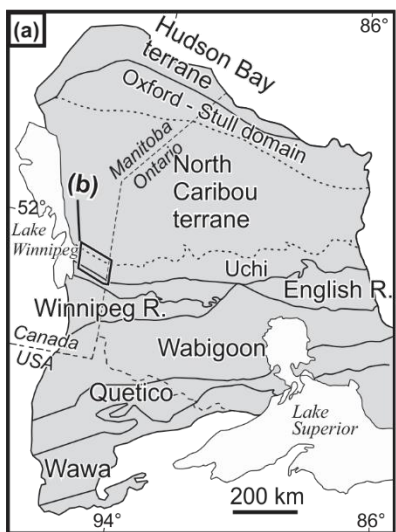
#### 4.6 Conclusions

Paragenetic analysis of alteration and vein minerals was performed to elucidate the relative timing of gold precipitation compared to sulfides and silicate minerals at the Ogama-Rockland gold deposit. U-Pb geochronology on zircon and monazite from the host tonalite phases and an aplite dike that cuts auriferous V<sub>2</sub>' veins, as well as Re-Os geochronology on molybdenite from a late V<sub>4</sub>' vein, were conducted to constrain the absolute age for early gold mineralization. The current study of ore textures and U-Pb and Re-Os geochronology has revealed the following major points:

1. V<sub>5</sub>' fault-fill veins represent a late orogenic gold mineralization event. The paragenetic sequence of V<sub>5</sub>' fault-fill vein minerals is generally characterized by successive deposition of chlorite-sericite, carbonate, tourmaline, molybdenite-pyrite-chalcopyrite-sericite, pyrite-chalcopyrite-bornite-gold with bismuth-bearing minerals, and quartz. Gold in interstitial mineralogical sites or as inclusions in pyrite could be a primary feature, whereas gold in fractures represents a remobilized event during late stage of post-vein filling G<sub>2</sub>' deformation.

Hydrothermal alteration produced zoned alteration envelopes that are characterized by progressive sericitization and carbonatization with progressive interaction of wallrock and hydrothermal fluid. Wallrock alteration antedated and accompanied mineral precipitation in veins, and ceased before or synchronously with complete infill of the veins.

2. Granitoid plutonism, V<sub>2</sub>' vein formation and associated early gold mineralization is tightly constrained at ca. 2728 Ma, based on U-Pb ages from the host tonalite phases and an aplite dike that cuts V<sub>2</sub>' veins. The Re-Os molybdenite age of a later V<sub>4</sub>' vein is indistinguishable from the U-Pb zircon ages. The close spatial and temporal associations between plutonic rocks and vein formation established from field relations and geochronology, as well as the high Re concentration of the dated molybdenite suggest that granitoid magmas were the source of mineralizing fluids. This early gold mineralization was overprinted and enhanced by an undated late orogenic gold event during the late stage of G<sub>2</sub>' deformation.



Uchi subprovince (2.75-2.69 Ga)

- Rice Lake belt
- Edmunds assemblage (2.71-2.69 Ga)
- San Antonio assemblage (<2.705 Ga)
- Gem assemblage (2.73-2.72 Ga)
- Ross River plutonic suite (2.73-2.72 Ga)
- Bidou assemblage (2.75-2.73 Ga)

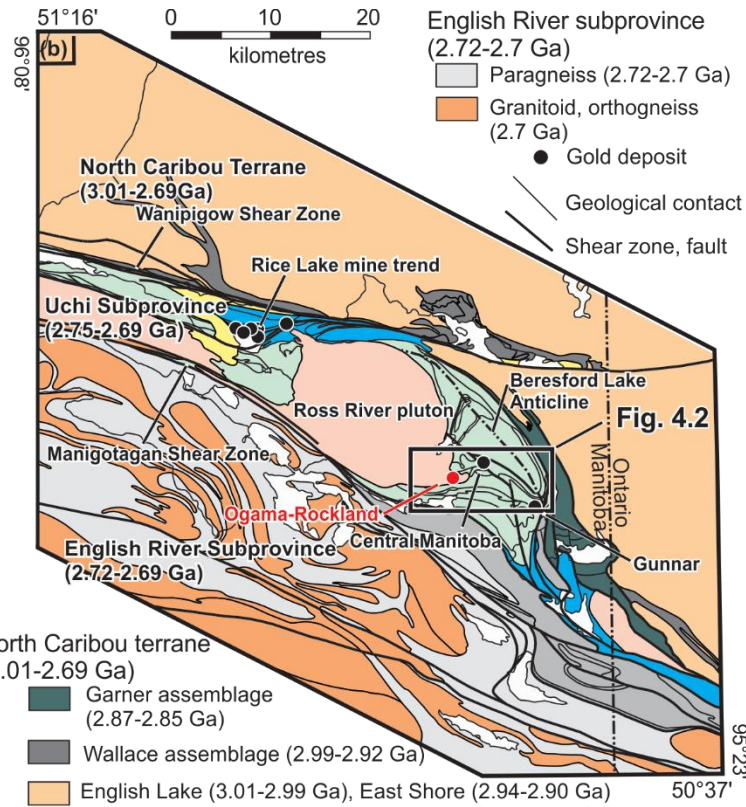


**Fig. 4.2**

Figure 4.1 a) Tectonic framework of the western Superior Province, showing major Subprovinces, domains and terranes; modified from Lin and Beakhouse (2013); b) Regional geologic map of the western Superior Province in southeastern Manitoba, illustrating two major Subprovinces and one terrane, terrane boundaries, significant gold deposits and U-Pb zircon age constraints; modified from Anderson (2013a). See Chapter 1 for age source.

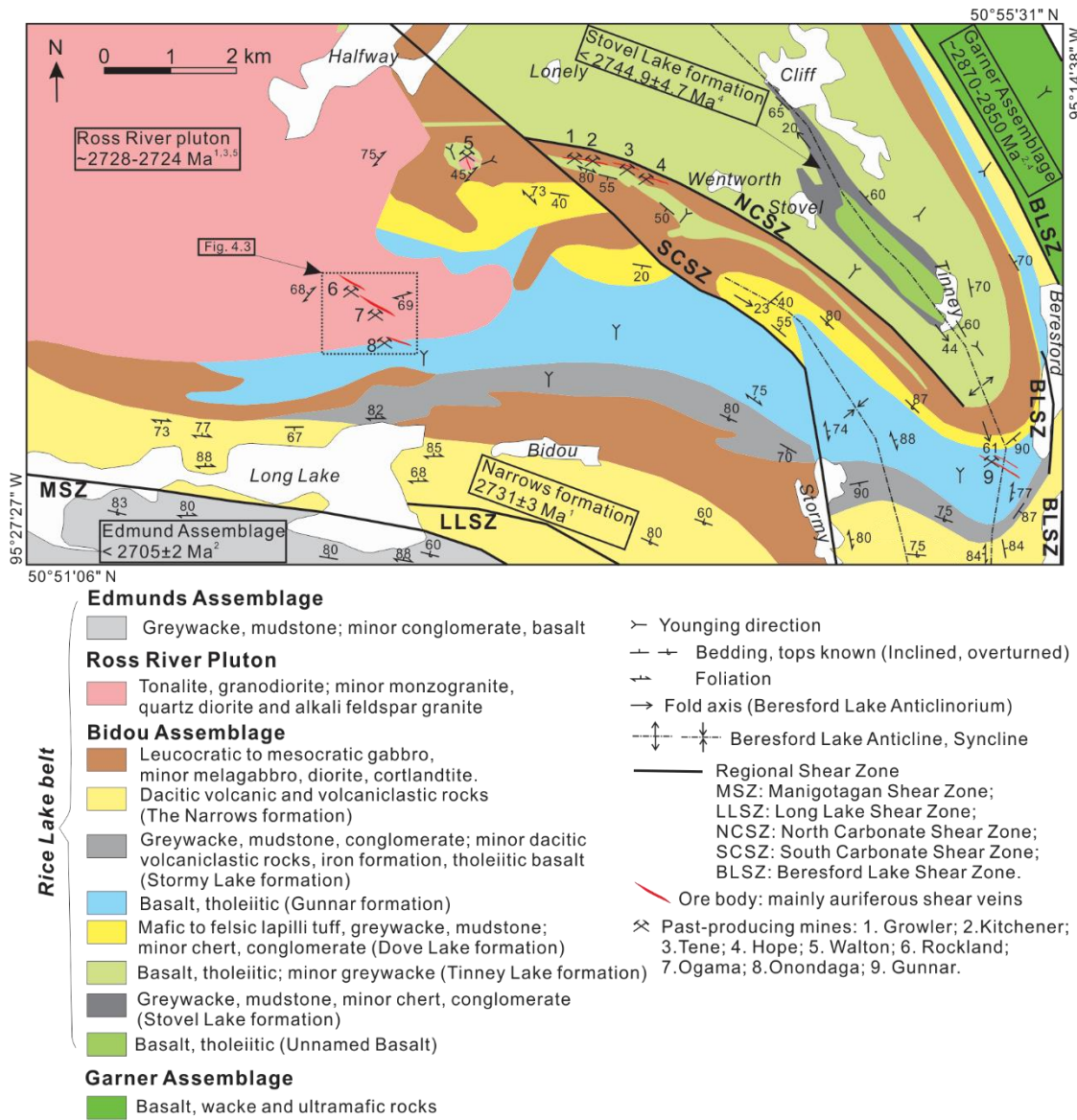


Figure 4.2 Generalized regional geologic map of the Bidou assemblage and Ross River pluton in the southeastern Rice Lake greenstone belt in southeastern Manitoba, showing principal formations, lithologic units, deformation structures, U-Pb zircon ages and gold deposits; modified from Stockwell and Lord (1939), Stockwell (1945), Zwanzig (1971), Brommecker (1996), Anderson (2013b) and Zhou (2014). Age source: <sup>1</sup> Turek et al. (1989), <sup>2</sup> Davis, 1994, <sup>3</sup> Anderson (2008), <sup>4</sup> Anderson (2013b), <sup>5</sup> Chapter 4

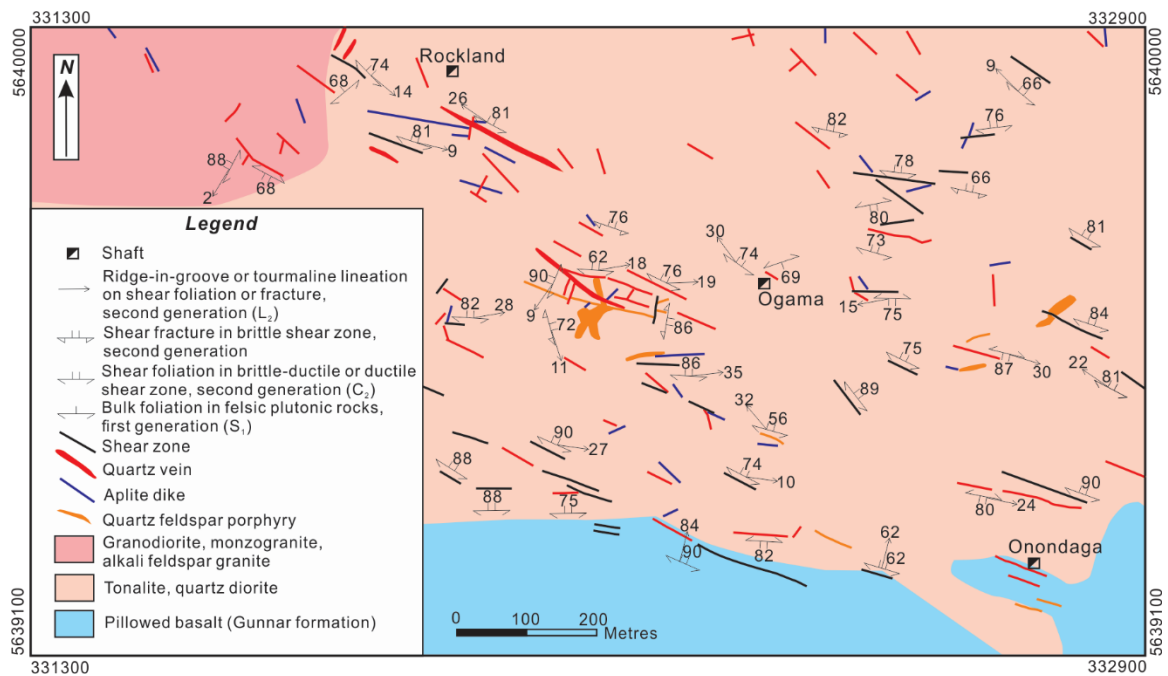


Figure 4.3 Simplified local geologic map around the Ogama-Rockland gold deposit, displaying main lithologic units, deformation structures and past-producing shafts. Modified from Zhou et al. (2012) and Zhou (2014).

Station 197/225/596 (UTM 0332074E, 5639632N; NAD 83) Outcrop mapping

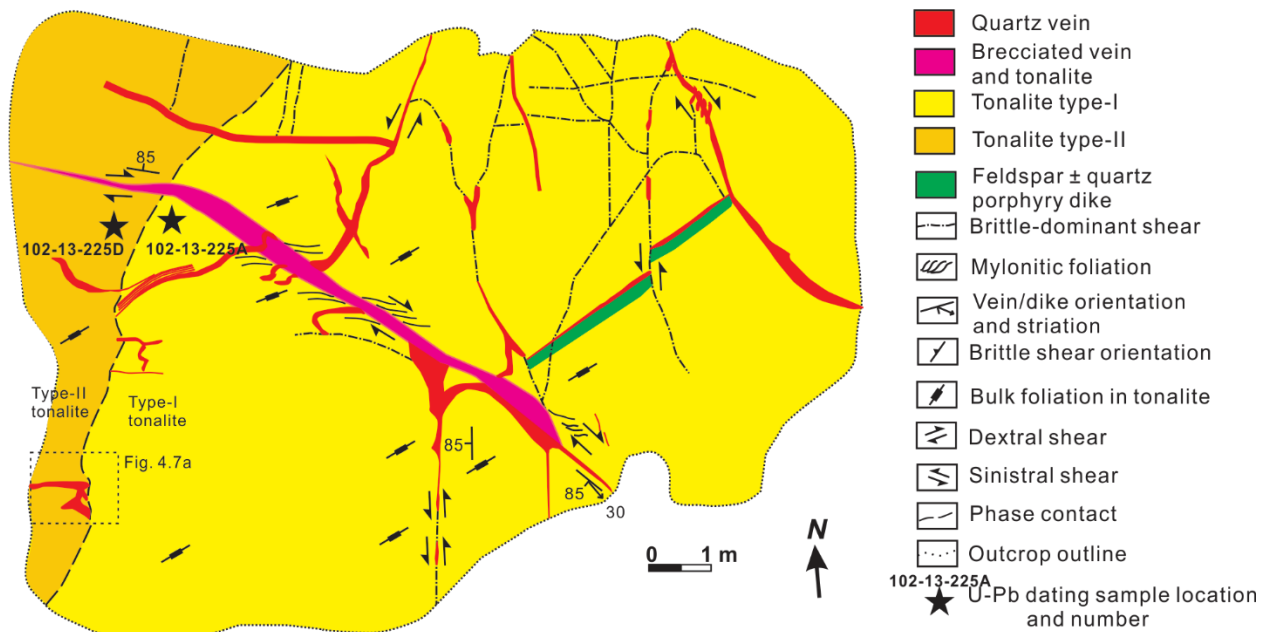


Figure 4.4 Outcrop sketch showing two phases of tonalite, vein system, porphyry dikes and deformation structures. U-Pb geochronological sample locations are indicated.

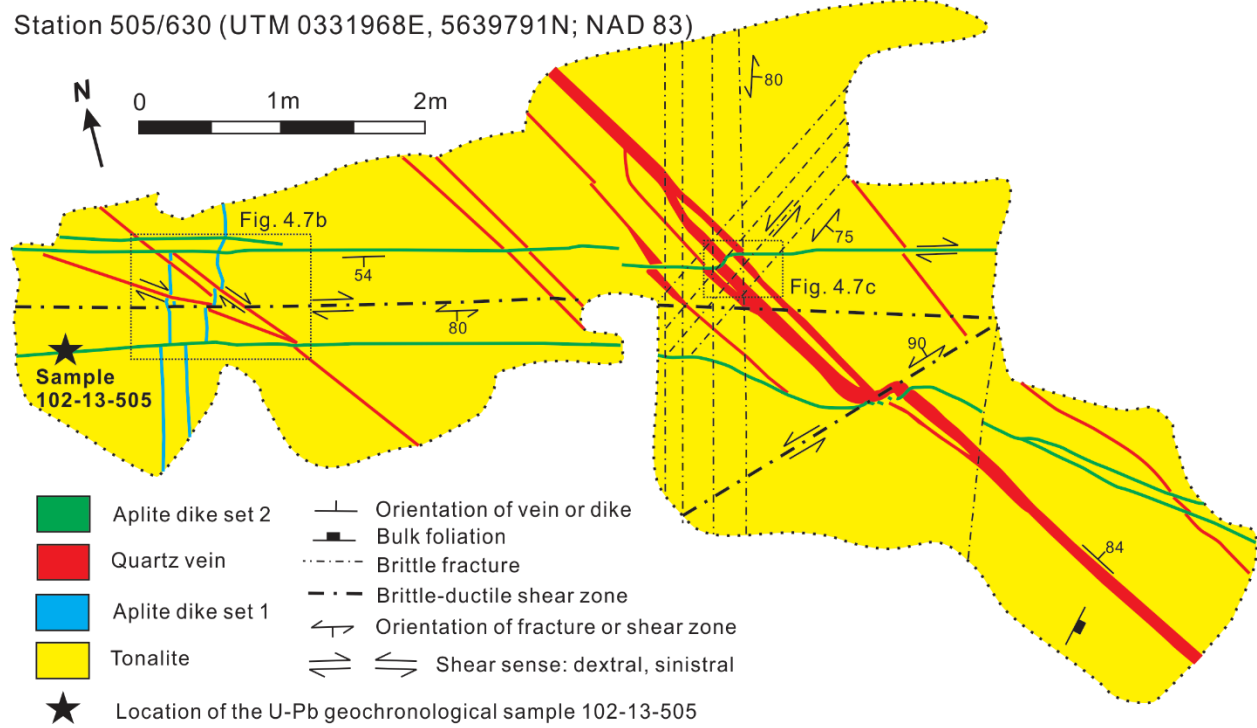


Figure 4.5 Outcrop sketch showing crosscutting relationships between sheeted  $V_2'$  veins and aplite dikes. Location of U-Pb geochronology sample 102-13-505 from one aplite dike that cuts  $V_2'$  veins is indicated.

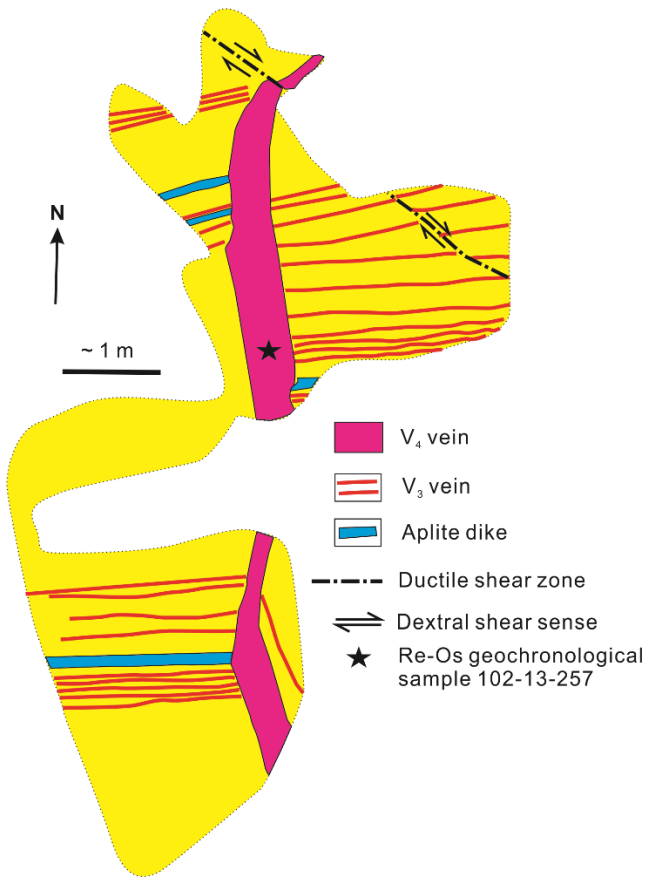


Figure 4.6 Outcrop sketch exhibiting one  $V_4'$  vein cutting across sheeted  $V_3'$  veins. Location of Re-Os sample 102-13-257 is indicated.

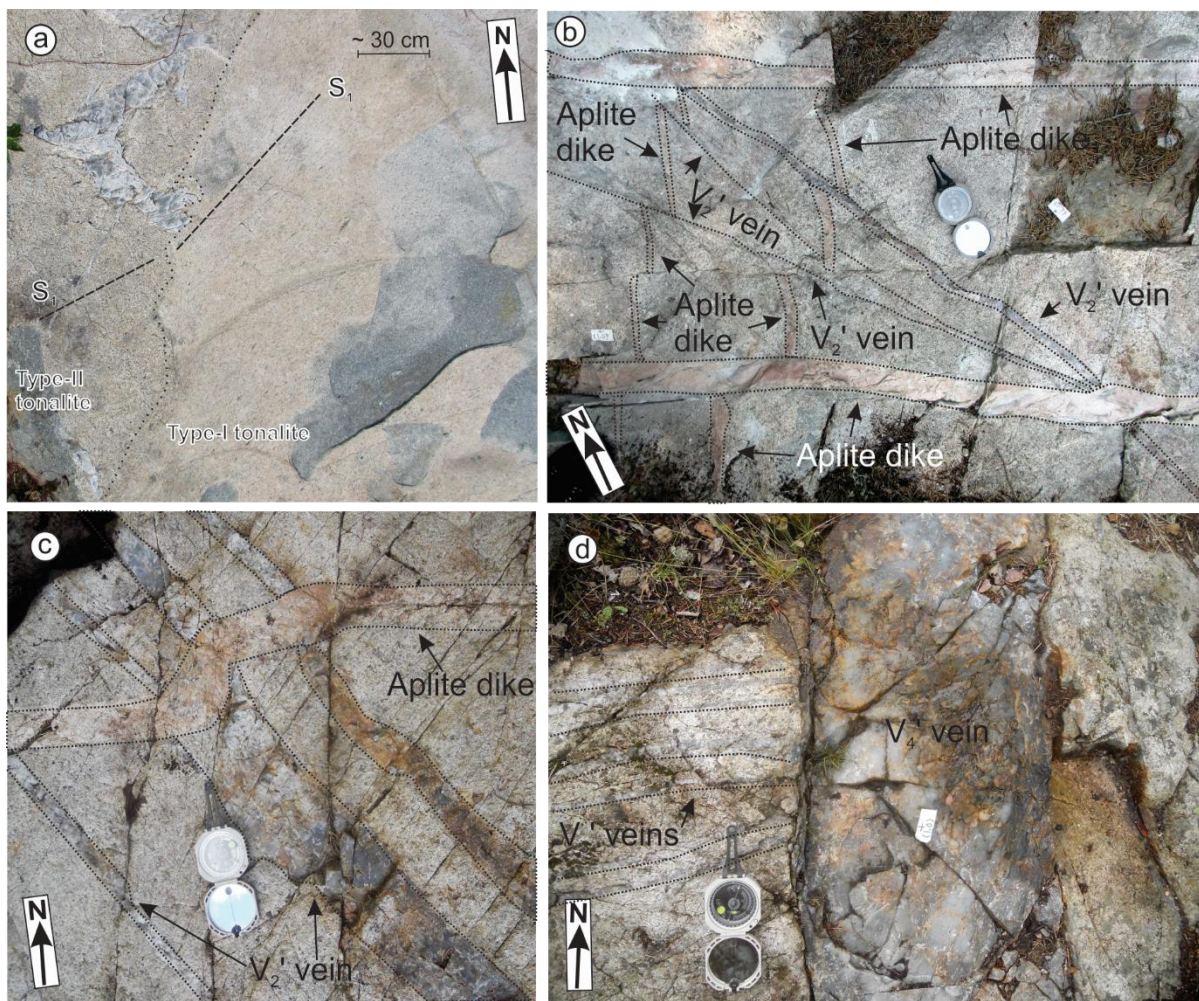


Figure 4.7 Outcrop photographs illustrating major plutonic units and their crosscutting relationships: a) two foliated tonalite phases with a vague curviplanar contact; see location in Fig. 4.4; b) northwest– to north-northwest–trending steep V<sub>2</sub>' veins cut across a north-northeast–trending steep aplite dike set, but are cut by a west-northwest steep aplite dike set; see Fig. 4.5 for location; c) one pinkish west-trending steep aplite dike crosscuts sheeted V<sub>2</sub>' veins; see Fig. 4.5 for location; d) one north-trending steep V<sub>4</sub>' vein crosscuts sheeted V<sub>3</sub>' veins; see Fig. 4.6 for location.

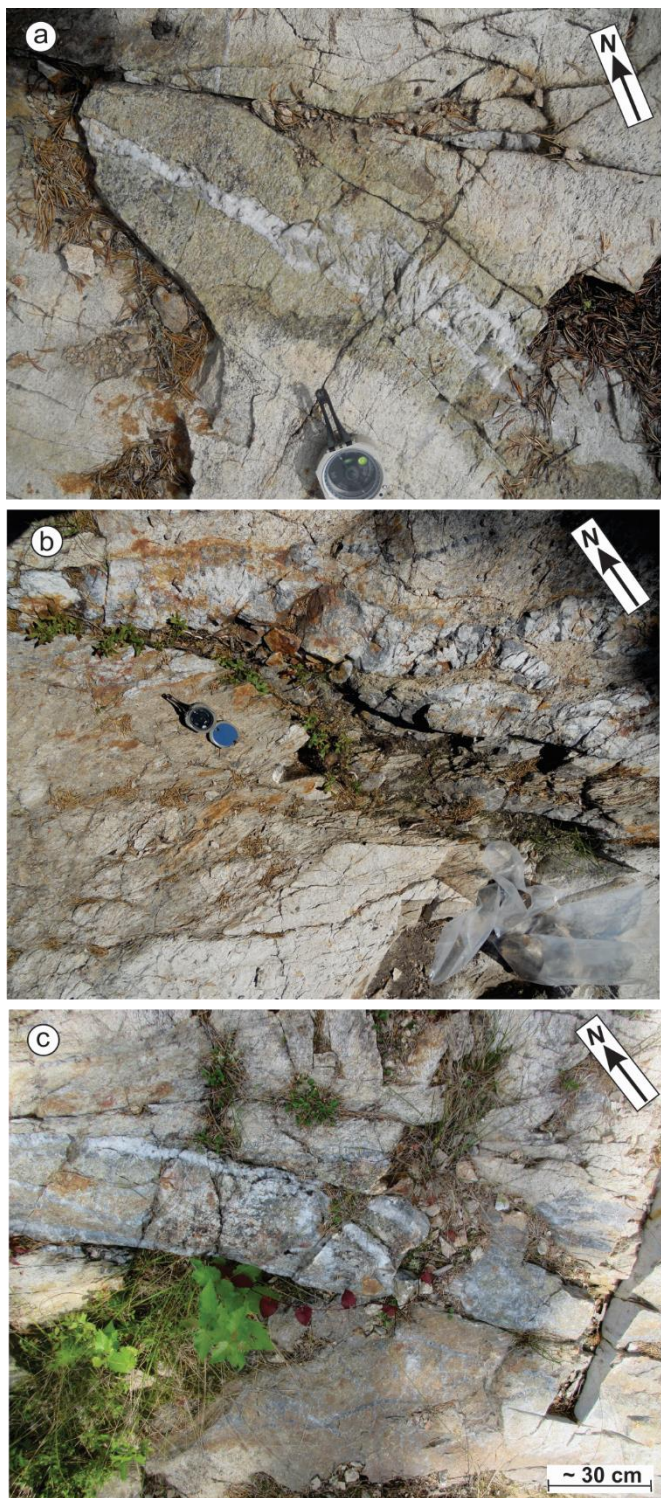


Figure 4.8 Outcrop photographs showing prominent alteration halos along associated veins: a) relatively symmetric greenish sericite alteration halos along a milky white vein; b) ankerite-sericite alteration envelopes adjacent to a west-trending shear vein; note the alteration zone is intensely foliated; c) sericite-ankerite alteration zones along a west-trending steep vein.

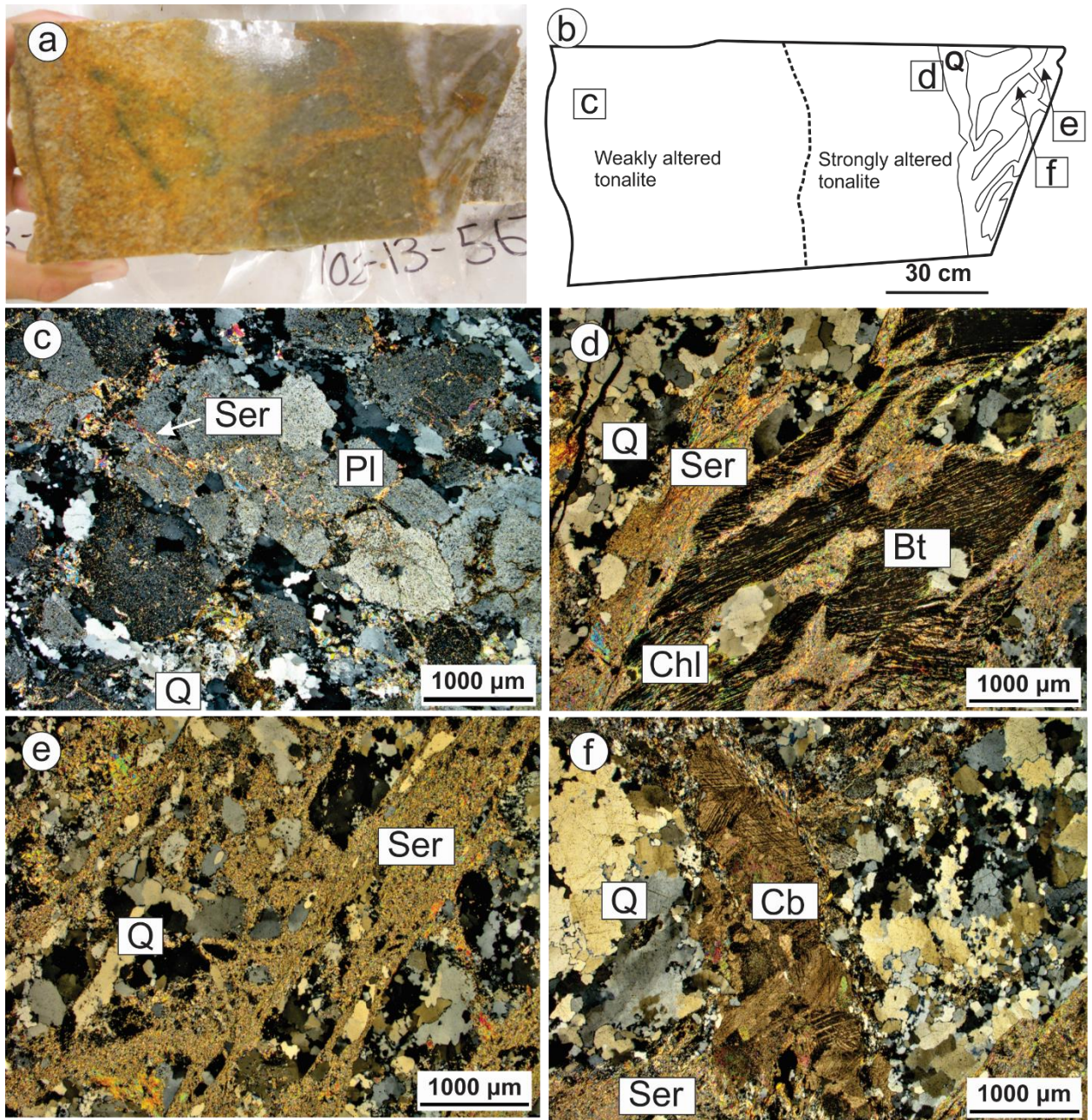


Figure 4.9 Hand specimen photo and sketch as well as photomicrographs of a typical alteration zone: a) hand sample of sericite alteration zones and associated veins from Fig. 4.8a; b) rough division of alteration intensity; alteration progressively increases towards the vein; locations of Fig. 4.9c, d, e are indicated; c) in weakly altered tonalite, sericite alteration occurs along feldspar grain boundaries or transgranular fractures; d) sericite replaces all feldspar grains and partially replaces biotite and chlorite grains in a strong alteration zone; e) complete sericite alteration to wallrock tonalite with no presence of igneous feldspar; f) one carbonate veinlet crosscuts one

quartz veinlet. Q = quartz, Ser = sericite, Pl = plagioclase, Chl = chlorite, Bt = biotite.

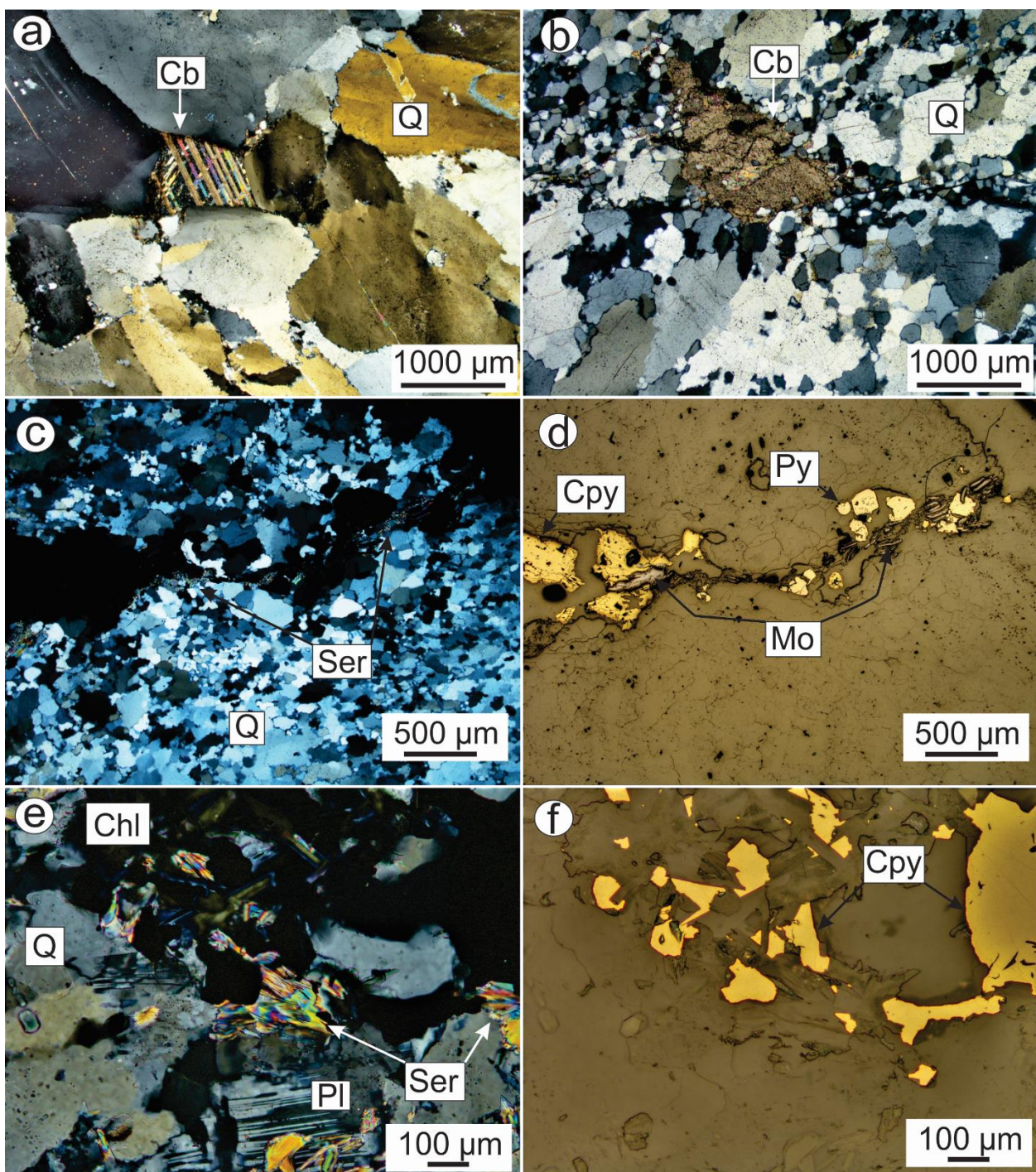


Figure 4.10 Photomicrographs of vein mineral assemblages: a) coarse-grained euhedral to subhedral quartz grains with undulose extinction and carbonate with twinning; note bulging recrystallized grains at quartz grain boundaries; under cross polarized transmitted light; b) irregular-shaped carbonate grain aggregates and recrystallized quartz grains; under cross

polarized transmitted light; c) and d) close spatial association of chalcopyrite, pyrite, molybdenite and sericite in a quartz vein; under cross polarized transmitted light and plane polarized reflected light, respectively; e) and f) close spatial association of plagioclase, sericite, chlorite, quartz and chalcopyrite at vein walls; under cross polarized transmitted light and plane polarized reflected light, respectively. Q = quartz, Cb = carbonate, Ser = sericite, Cpy = chalcopyrite, Py = pyrite, Mo = molybdenite, Chl = chlorite, Pl = plagioclase.

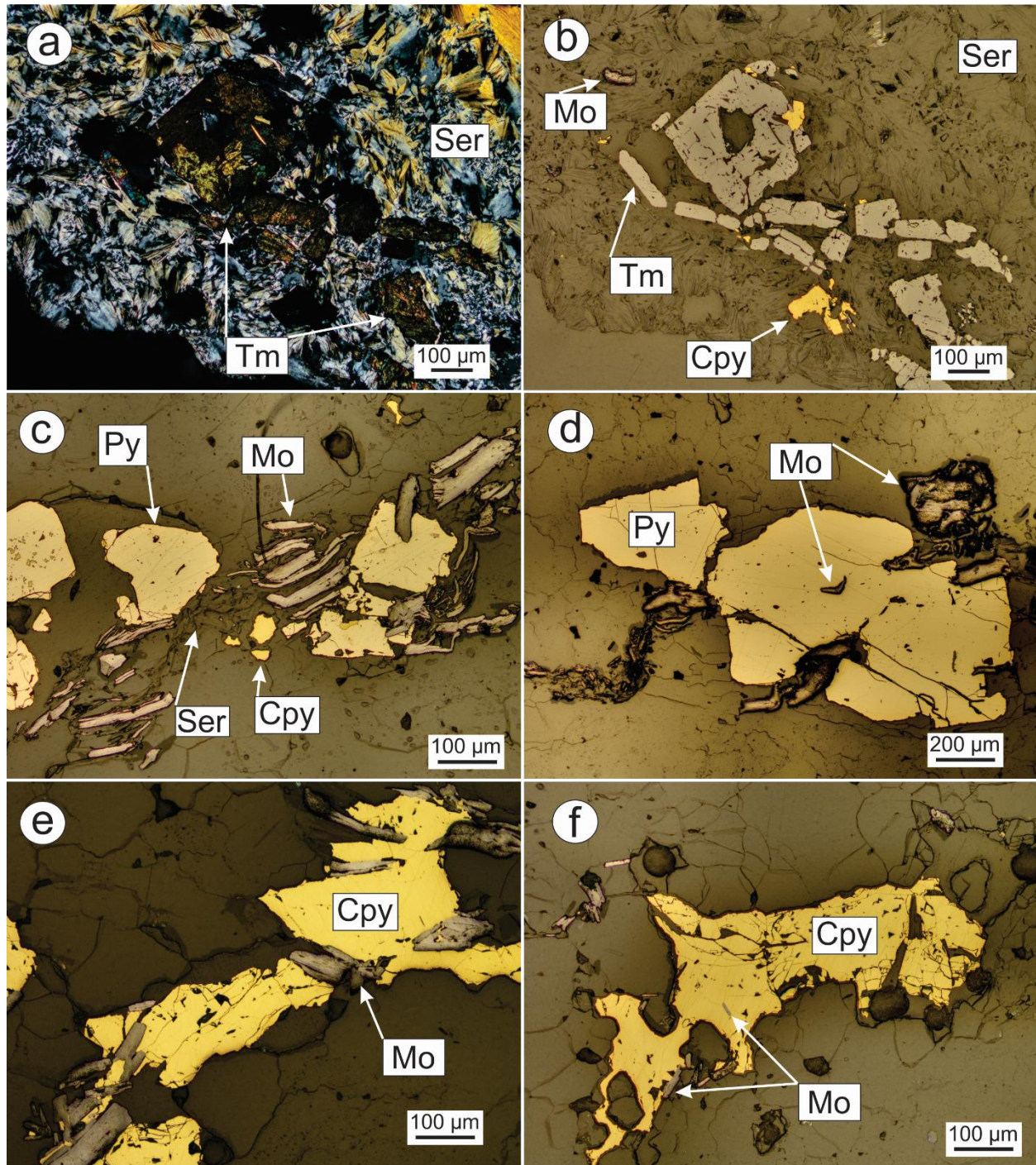


Figure 4.11 Photomicrographs of vein mineral assemblages: a) and b) intimate association of tourmaline, sericite, chalcopyrite and minor molybdenite at vein margins; under cross polarized transmitted light and plane polarized reflected light, respectively; c) close association of pyrite, chalcopyrite, molybdenite and sericite in a quartz vein; d) pyrite in contact to molybdenite and containing molybdenite inclusions; e) molybdenite blades truncating chalcopyrite grains that are

internally fractured; f) chalcopyrite containing molybdenite inclusions and is in contact to molybdenite; c, d, e, f are all under plane polarized reflected light. Q = quartz, Tm = tourmaline, Ser = sericite, Cpy = chalcopyrite, Py = pyrite, Mo = molybdenite.

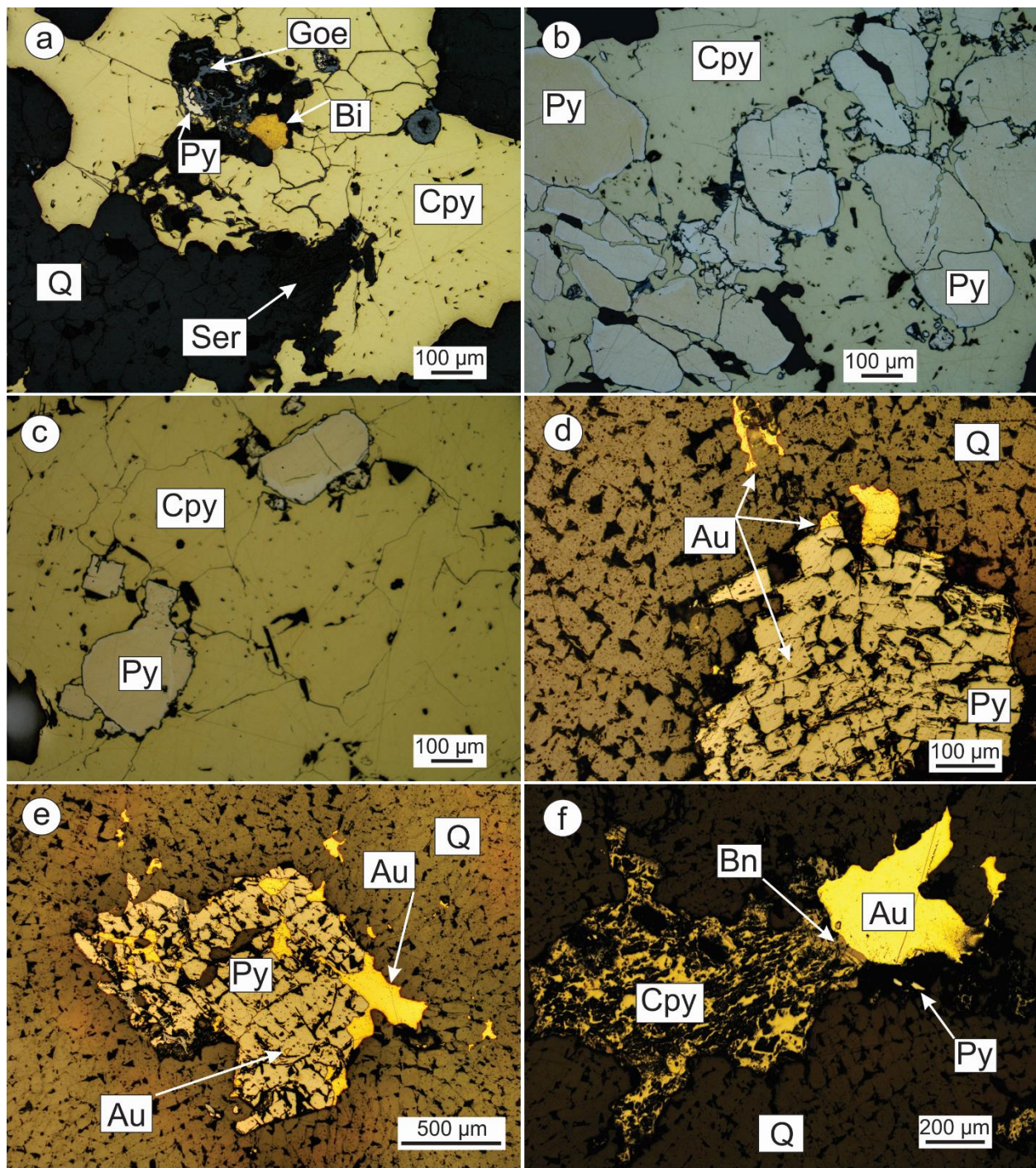


Figure 4.12 Photomicrographs of sulfide mineral assemblages and gold occurrences in veins: a) close association of pyrite, chalcopyrite, bismite, goethite and sericite in quartz veins; note that goethite replaces pyrite and chalcopyrite along grain boundaries; b) subrounded pyrite inclusions are in contact to each other within a single chalcopyrite grain; c) subrounded and angular pyrite inclusions in an individual chalcopyrite crystal; d) gold as inclusions in fractured pyrite, or fills

fractures in quartz, or attaches to pyrite and quartz; e) gold as inclusions in pyrite, or as discontinuous coatings around pyrite; some gold partially replaces pyrite or fills interstitial sites among quartz grains; gold also fills fractures of pyrite and quartz; f) close spatial association of chalcopyrite-bornite, pyrite and gold. All images are under plane polarized reflected light. Q = quartz, Ser = sericite, Cpy = chalcopyrite, Py = pyrite, Bi = bismite, Goe = goethite, Au = gold (electrum), Bn = bornite.

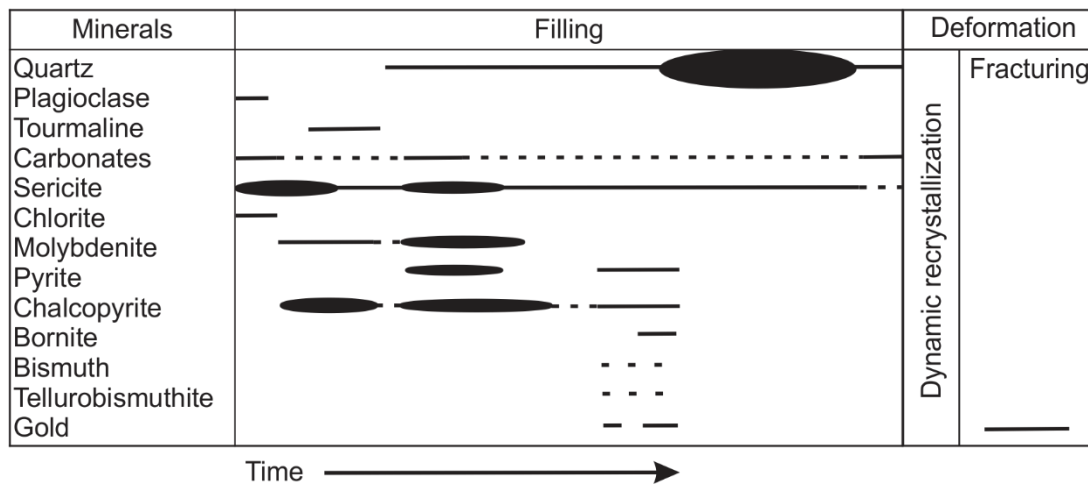


Figure 4.13 Paragenetic sequence of V<sub>5'</sub> fault-fill vein minerals. Line thickness schematically represents quantities of mineral deposited. Dash line represents uncertainties. See text for explanations.

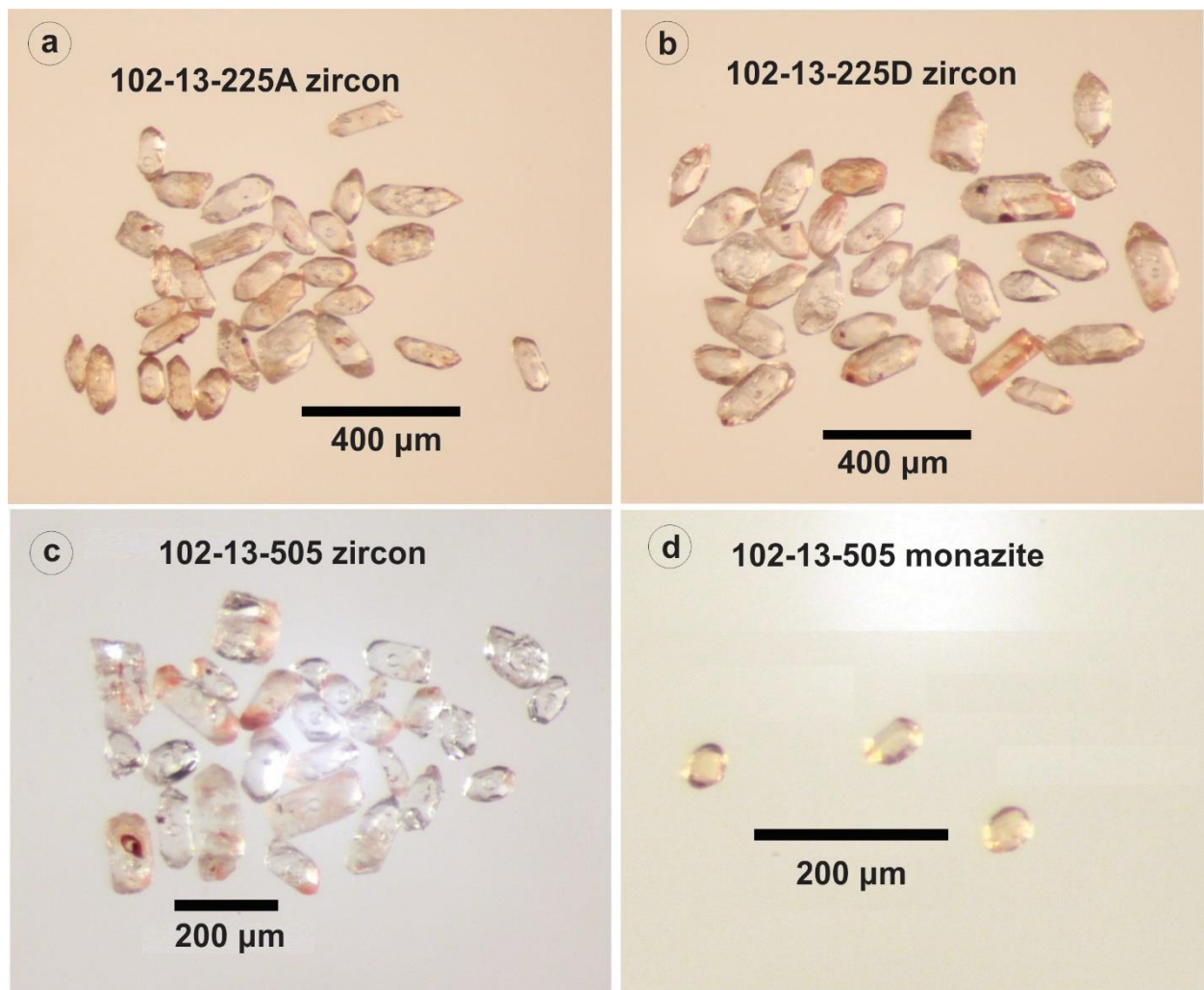


Figure 4.14 Photomicrographs of zircon or monazite picked from a) tonalite type-I, sample 102-13-225A; b) tonalite type-II, sample 102-13-225D; c) and d) aplite dike, sample 102-13-505; a), b), c) are zircon, d) is monazite.

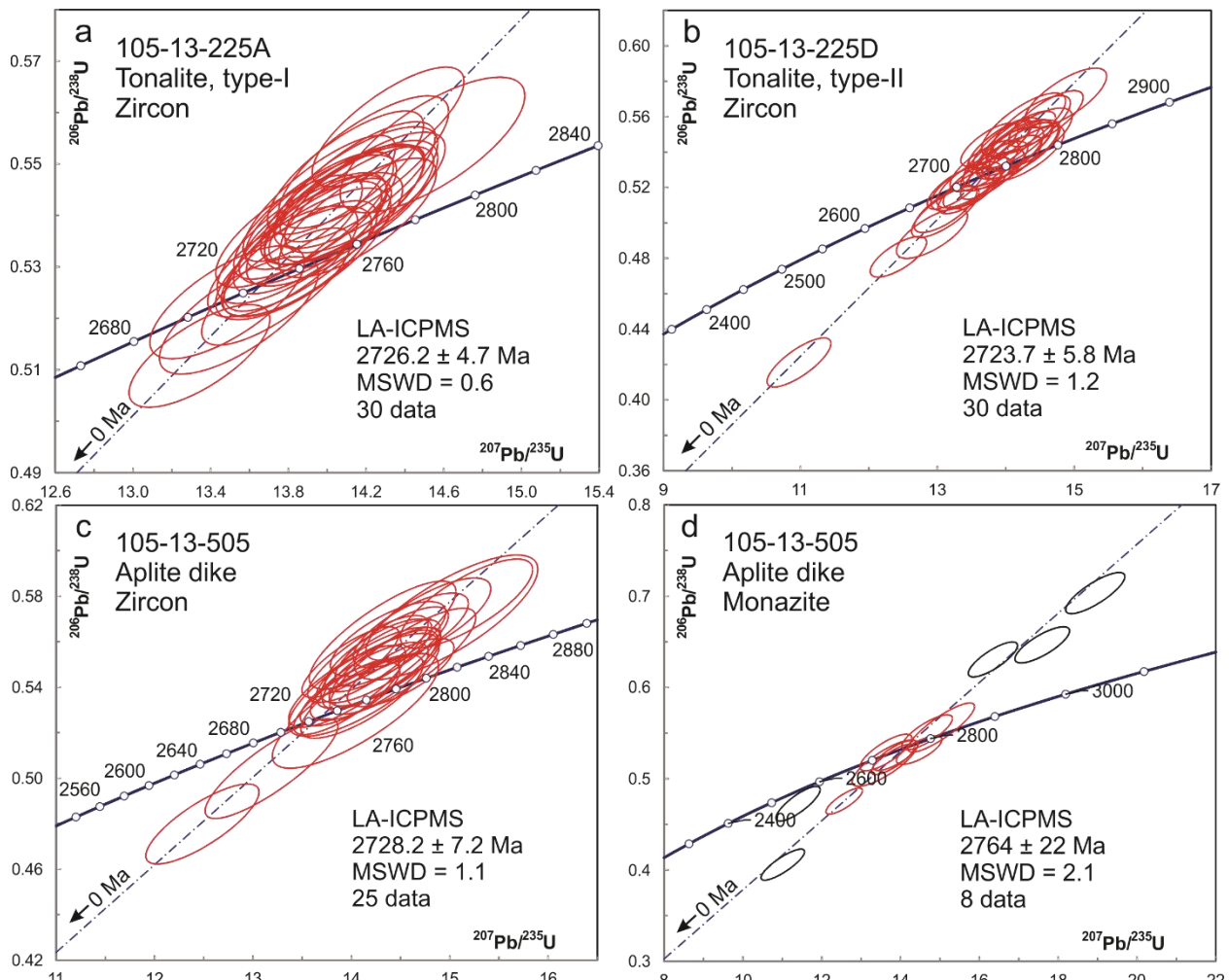


Figure 4.15 U-Pb concordia plots showing LA-ICPMS data on zircon and monazite: a) sample 102-13-225A, zircon from tonalite type-I; b) sample 102-13-225D, zircon from tonalite type-II; c) sample 102-13-505, zircon from aplite dike; d) monazite data from aplite dike 102-13-505. Ellipses in black are omitted from the average age.

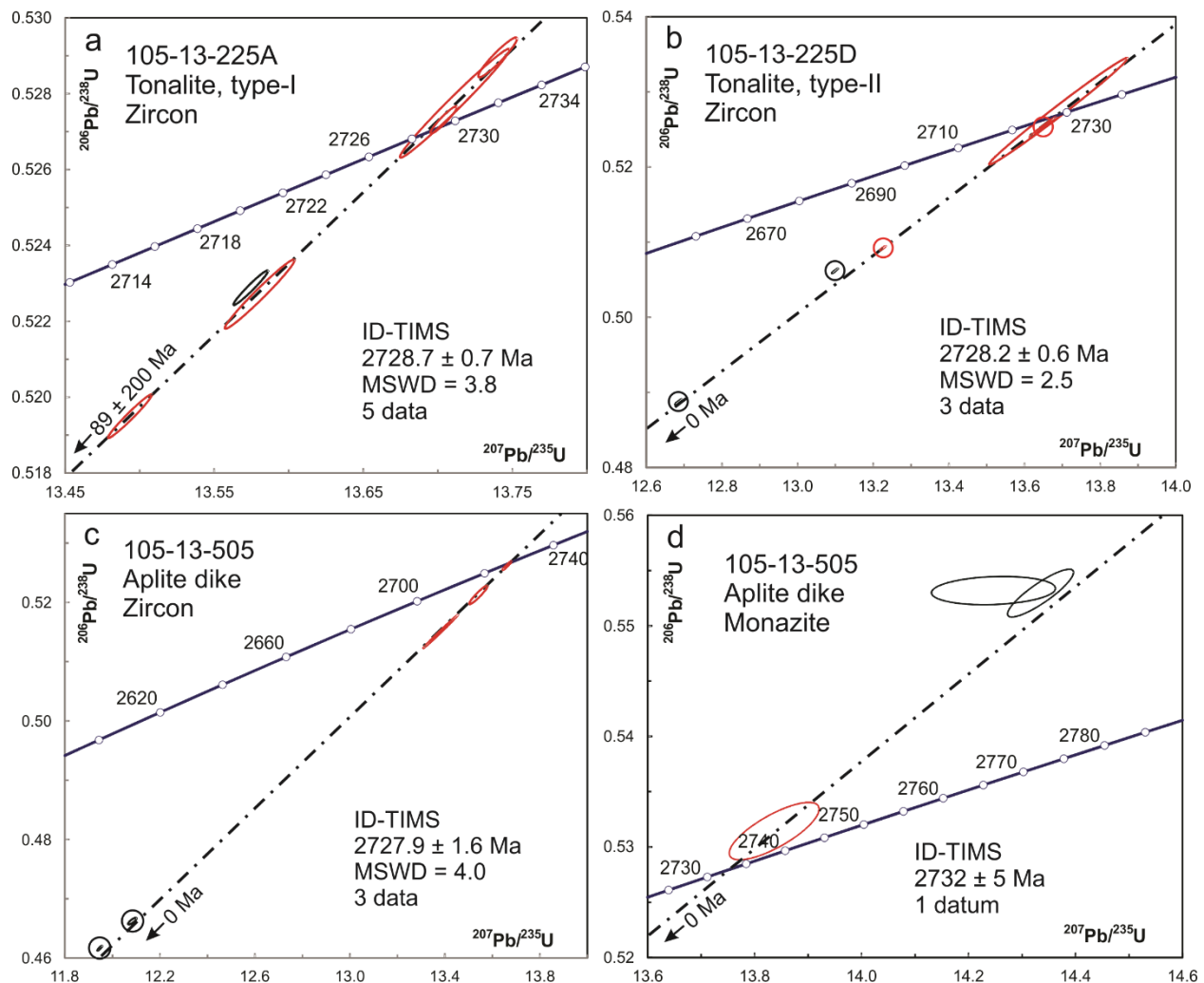


Figure 4.16 U-Pb concordia plots showing ID-TIMS data on zircon and monazite: a) sample 102-13-225A, zircon from tonalite type-I; b) sample 102-13-225D, zircon from tonalite type-II; c) sample 102-13-505, zircon from aplite dike; d) sample 102-13-505, monazite data from aplite dike. Ellipses in black are omitted from the regressions. Some error ellipses are marked by circles.

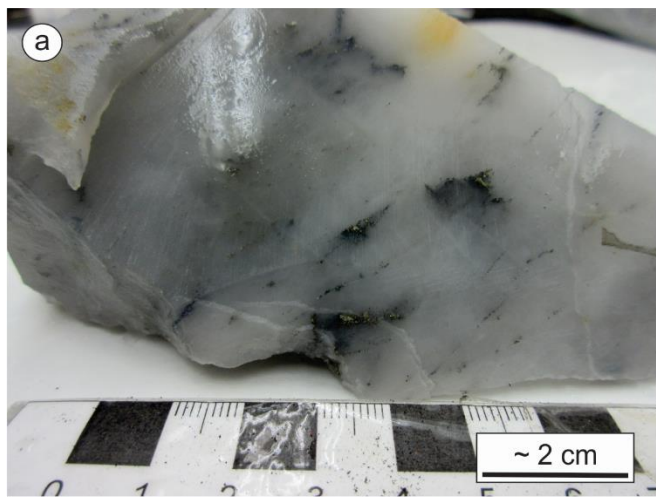


Figure 4.17 a) Linear aggregates of molybdenite-chalcopyrite-pyrite grains in the quartz vein, sample 102-13-257; b) and c) Dated molybdenite aggregates in the quartz vein, sample 102-13-257, before and after diamond drill, respectively.



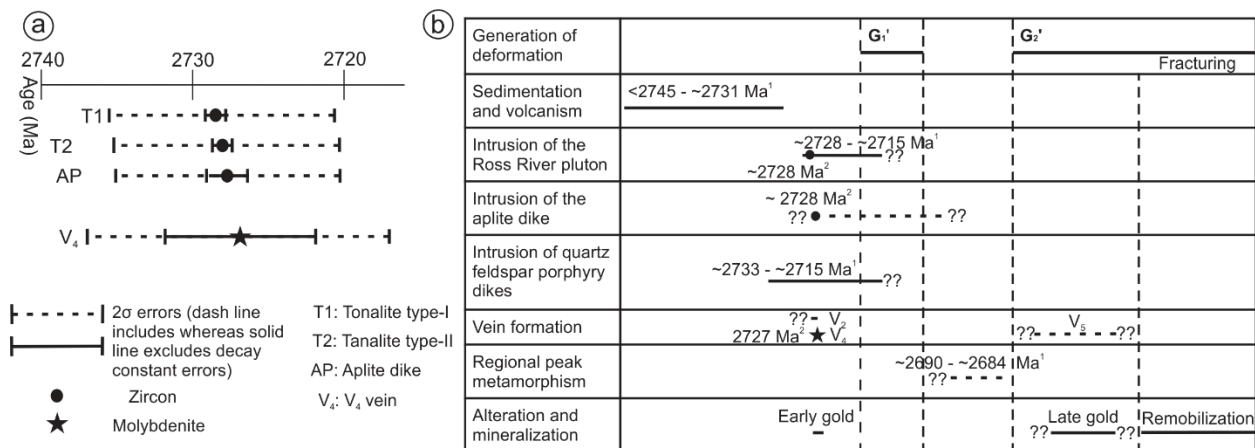


Figure 4.18 a) Age constraints for magmatism and vein formation obtained from this study; ages are reported at the  $2\sigma$  level with (dash line) and without (solid line) decay constant uncertainties; b) Diagram showing major age relationships at the Ogama-Rockland deposit area; Age source: <sup>1</sup> Anderson (2013a); <sup>2</sup> this study. See text for discussion.

Table 4.1.1 LA-ICPMS U-Pb isotope data for single zircons from sample 102-13-225A, tonalite type-I, the Ogama-Rockland area.

Spot	U (ppm)	Pb <sup>206</sup> (ppm)	Th U	<sup>207</sup> Pb <sup>235</sup> U	1 Sig	<sup>206</sup> Pb <sup>238</sup> U	1 Sig	Err. Correl.	<sup>207</sup> Pb <sup>206</sup> Pb Age (Ma)	1 Si g	<sup>207</sup> Pb <sup>235</sup> U Age (Ma)	1 Si g	<sup>206</sup> Pb <sup>238</sup> U Age (Ma)	1 Si g	Disc . (%)
<b>102-13-225A Tonalite, type-I</b>															
<b>Zircon</b>															
1 225A-1 348 179 0.45 13.343 0.14 8 0.5127 1 0.004 0.7159 2731 13 2704 11 2668 17 3															
2 225A-2 201 109 0.30 14.195 0.16 9 0.5445 8 0.005 0.7391 2734 13 2763 11 2802 20 -3															
3 225A-4 133 71 0.25 13.891 0.17 8 0.5329 1 0.004 0.7426 2734 14 2742 12 2754 21 -1															
4 225A-7 107 56 0.37 13.546 0.16 7 0.5206 7 0.004 0.7258 2731 14 2718 12 2702 20 1															
5 225A-8 133 72 0.36 13.987 0.15 4 0.5373 5 0.004 0.7136 2732 14 2749 11 2772 19 -2															
6 225A-9 284 152 0.38 13.928 0.16 6 0.5373 3 0.004 0.7181 2725 13 2745 11 2772 18 -2															
7 225A-10 228 121 0.24 13.771 0.16 8 0.5311 4 0.005 0.7252 2725 13 2734 11 2746 19 -1															
8 225A-13 196 106 0.37 13.931 0.16 8 0.5400 0 0.004 0.7755 2717 13 2745 11 2783 21 -3															
9 225A-14 246 133 0.23 14.086 0.16 7 0.5419 7 0.004 0.7296 2729 13 2756 11 2791 20 -3															
10 225A-15 780 434 0.16 14.314 0.16 0 0.5572 7 0.004 0.7628 2710 12 2771 11 2855 20 -7															
11 225A-16 115 63 0.26 14.157 0.15 3 0.5466 8 0.004 0.7560 2724 12 2760 11 2811 20 -4															
12 225A-17 141 74 0.20 13.739 0.17 7 0.5262 7 0.005 0.7725 2737 12 2732 11 2725 20 1															
13 225A-18 87 48 0.18 14.188 0.16 9 0.5504 3 0.005 0.7568 2716 14 2762 12 2827 22 -5															
14 225A-19 178 97 0.24 13.959 0.17 0 0.5433 0 0.005 0.8017 2710 11 2747 11 2797 21 -4															
15 225A-21 129 69 0.47 13.901 0.18 6 0.5343 3 0.005 0.7811 2731 13 2743 12 2760 22 -1															
16 225A-22 126 68 0.81 14.123 0.15 2 0.5420 2 0.004 0.7363 2734 14 2758 12 2792 22 -3															
17 225A-24 180 98 0.60 13.968 0.16 9 0.5406 5 0.004 0.7380 2719 13 2748 11 2786 19 -3															
18 225A-25 115 60 0.41 13.485 0.17 3 0.5231 5 0.004 0.7117 2716 14 2714 11 2712 19 0															
19 225A-26 124 68 0.31 14.147 0.15 3 0.5454 8 0.004 0.7263 2726 14 2760 12 2806 20 -4															
20 225A-27 143 77 0.13 13.804 0.16 4 0.5369 5 0.004 0.7447 2711 12 2736 11 2771 19 -3															
21 225A-28 71 37 0.19 13.827 0.16 4 0.5307 5 0.004 0.7126 2733 14 2738 11 2745 19 -1															
22 225A-29 88 48 0.19 14.103 0.15 4 0.5421 8 0.004 0.7536 2731 13 2757 11 2792 20 -3															
23 225A-31 110 59 0.21 13.900 0.16 6 0.5357 5 0.004 0.7423 2726 12 2743 11 2765 19 -2															
24 225A-32 166 91 0.30 14.095 0.17 4 0.5483 9 0.004 0.7668 2711 12 2756 11 2818 20 -5															
25 225A-34 205 111 0.23 14.079 0.16 2 0.5422 8 0.004 0.7183 2728 14 2755 12 2793 20 -3															
26 225A-35 176 93 0.19 13.861 0.16 2 0.5316 6 0.004 0.7411 2734 13 2740 11 2748 19 -1															
27 225A-36 115 62 0.11 14.156 0.19 6 0.5395 7 0.005 0.7500 2745 13 2760 11 2781 20 -2															
28 225A-37 36 20 0.17 14.542 0.16 4 0.5537 4 0.004 0.7269 2746 15 2786 13 2841 22 -4															
29 225A-38 189 103 0.24 14.155 0.17 1 0.5422 6 0.005 0.7448 2736 12 2760 11 2793 19 -3															
30 225A-40 97 52 0.17 13.869 0.17 8 0.5356 2 0.005 0.7553 2723 14 2741 12 2765 22 -2															
<b>175 132 0.29 0.15</b>															

Table 4.1.2 LA-ICPMS U-Pb isotope data for single zircons from sample 102-13-225D, tonalite type-II, the Ogama-Rockland area.

Spot	U	Pb <sup>206</sup>	Th	<sup>207</sup> Pb	1	<sup>206</sup> Pb	1	Err.	<sup>207</sup> Pb	1	<sup>207</sup> Pb	1	<sup>206</sup> Pb	1	Disc	
	(ppm)	(ppm)	U	<sup>235</sup> U	Sig	<sup>238</sup> U	Sig	Correl.	<sup>206</sup> Pb	Si g	<sup>235</sup> U	Sig	<sup>238</sup> U	Si g	(%)	
	Age (Ma)	Age (Ma)	Age (Ma)	Age (Ma)	Age (Ma)	Age (Ma)	Age (Ma)		Age (Ma)	Age (Ma)	Age (Ma)	Age (Ma)	Age (Ma)	Age (Ma)	.	
<b>2</b>		<b>102-13-225D Tonalite, type-II</b>														
<b>Zircon</b>																
1	225D-1	115	61	0.52	13.832	0.20	0.5320	0.005	0.7449	2730	16	2738	14	2750	24	-1
2	225D-2	116	63	0.46	14.223	0.18	0.5432	0.005	0.7635	2741	14	2765	13	2797	23	-3
3	225D-3	54	29	0.65	13.805	0.19	0.5273	0.005	0.7840	2741	14	2736	13	2730	24	1
4	225D-4	127	69	0.55	13.955	0.17	0.5446	0.005	0.8108	2706	12	2747	12	2803	23	-4
5	225D-5	341	185	0.55	13.764	0.18	0.5441	0.005	0.7343	2684	14	2734	12	2801	21	-5
6	225D-6	138	75	0.68	13.907	0.16	0.5440	0.004	0.7833	2702	14	2743	12	2800	23	-4
7	225D-7	287	149	0.44	13.262	0.16	0.5196	0.004	0.7441	2699	14	2698	12	2697	21	0
8	225D-8	102	49	0.46	12.432	0.18	0.4808	0.005	0.7192	2721	15	2638	13	2531	20	8
9	225D-9	261	135	0.70	13.471	0.21	0.5182	0.005	0.7413	2729	15	2713	13	2692	23	2
10	225D-10	73	36	0.50	12.922	0.20	0.4940	0.005	0.7099	2740	19	2674	15	2588	25	7
11	225D-11	177	94	0.34	13.689	0.18	0.5322	0.005	0.7419	2712	17	2728	14	2751	25	-2
12	225D-12	302	154	0.69	13.122	0.21	0.5077	0.006	0.7451	2720	16	2688	13	2647	23	3
13	225D-13	268	140	0.71	13.511	0.21	0.5234	0.006	0.7427	2718	17	2716	15	2713	26	0
14	225D-14	300	163	0.73	13.973	0.25	0.5438	0.006	0.7567	2710	17	2748	15	2799	27	-4
15	225D-15	163	88	0.41	14.183	0.25	0.5413	0.007	0.7180	2742	20	2762	17	2789	29	-2
16	225D-16	175	95	0.45	14.341	0.22	0.5471	0.006	0.7386	2743	20	2773	17	2813	30	-3
17	225D-17	170	92	0.52	14.126	0.19	0.5425	0.005	0.7424	2732	18	2758	15	2794	27	-3
18	225D-18	180	76	0.39	10.980	0.21	0.4211	0.005	0.7743	2734	18	2521	16	2266	26	20
19	225D-19	85	44	0.37	13.426	0.20	0.5207	0.005	0.6845	2716	19	2710	15	2702	24	1
20	225D-20	92	48	0.29	13.586	0.20	0.5225	0.005	0.7509	2730	16	2721	14	2710	25	1
21	225D-21	152	77	0.28	13.117	0.22	0.5062	0.006	0.7597	2724	16	2688	14	2640	25	4
22	225D-22	118	66	0.29	14.590	0.22	0.5588	0.006	0.7611	2737	16	2789	14	2862	27	-6
23	225D-23	164	90	0.24	14.186	0.22	0.5471	0.006	0.7634	2725	17	2762	15	2813	27	-4
24	225D-24	416	225	0.59	14.211	0.23	0.5409	0.006	0.7501	2747	17	2764	15	2787	27	-2
25	225D-25	395	219	0.66	14.378	0.22	0.5553	0.006	0.7544	2723	17	2775	15	2847	28	-6
26	225D-26	223	120	0.33	14.302	0.24	0.5391	0.006	0.7416	2763	17	2770	15	2780	26	-1
27	225D-27	269	153	0.42	14.874	0.24	0.5705	0.006	0.7320	2734	19	2807	16	2910	28	-8
28	225D-28	224	120	0.36	13.967	0.21	0.5375	0.006	0.7446	2729	19	2747	16	2773	29	-2
29	225D-29	350	187	0.56	13.993	0.25	0.5344	0.007	0.7373	2741	17	2749	15	2760	26	-1
30	225D-30	216	120	0.75	14.262	0.25	0.5554	0.007	0.7529	2709	19	2767	17	2847	30	-6
	<b>202</b>	<b>98</b>	<b>0.50</b>	<b>0.15</b>												

Table 4.1.3 LA-ICPMS U-Pb isotope data for single zircons from sample 102-13-505, aplite dike, the Ogama-Rockland area.

Spot	U (ppm)	Pb <sup>206</sup> (ppm)	Th U	<sup>207</sup> Pb <sup>235</sup> U	1 Sig	<sup>206</sup> Pb <sup>238</sup> U	1 Sig	Err. Correl.	<sup>207</sup> Pb <sup>206</sup> Pb Age (Ma)	1 Si g	<sup>207</sup> Pb <sup>235</sup> U Age (Ma)	1 Si g	<sup>206</sup> Pb <sup>238</sup> U Age (Ma)	1 Si g	Disc . (%)
<b>3 102-13-505 Aplite Dike</b>															
<b>Zircon</b>															
1 505-1 156 86 0.25 14.277 1 0.5540 5 0.7603 2715 17 2768 15 2842 27 -6															
2 505-2 222 119 0.22 14.109 4 0.5359 5 0.7762 2750 19 2757 17 2766 31 -1															
3 505-5 75 43 0.15 14.964 1 0.5707 2 0.7709 2744 26 2813 24 2911 46 -8															
4 505-6 71 36 0.18 13.190 6 0.5042 0 0.8493 2740 18 2693 20 2632 38 5															
5 505-7 144 78 0.17 14.130 3 0.5410 2 0.7715 2737 23 2758 21 2788 39 -2															
6 505-9 75 40 0.16 14.043 5 0.5296 3 0.7896 2762 25 2753 23 2740 43 1															
7 505-10 90 52 0.30 15.171 5 0.5768 0 0.7650 2749 19 2826 17 2935 33 -8															
8 505-12 135 76 0.24 14.375 0 0.5613 7 0.7148 2705 19 2775 16 2872 28 -8															
9 505-13 104 59 0.29 14.605 9 0.5650 7 0.7216 2720 19 2790 16 2887 27 -8															
10 505-14 110 61 0.28 14.299 8 0.5514 5 0.7804 2725 18 2770 16 2831 31 -5															
11 505-15 173 95 0.36 14.343 1 0.5490 0 0.7961 2738 16 2773 15 2821 29 -4															
12 505-16 111 53 0.41 12.487 5 0.4799 2 0.7964 2731 19 2642 18 2527 31 9															
13 505-17 90 50 0.20 14.168 9 0.5524 8 0.8020 2707 17 2761 17 2835 32 -6															
14 505-18 95 51 0.22 13.959 3 0.5404 3 0.7815 2719 18 2747 16 2785 31 -3															
15 505-19 53 30 0.21 14.319 5 0.5629 7 0.8082 2694 21 2771 20 2879 40 -9															
16 505-20 68 37 0.29 14.523 3 0.5514 5 0.8267 2751 19 2785 20 2831 39 -4															
17 505-22 31 18 0.27 14.784 9 0.5699 4 0.7418 2726 19 2801 17 2907 30 -8															
18 505-23 88 48 0.47 14.184 5 0.5426 0 0.7476 2739 19 2762 16 2794 29 -2															
19 505-24 78 42 0.31 14.502 1 0.5464 1 0.7339 2763 17 2783 14 2810 25 -2															
20 505-25 197 110 0.26 14.411 5 0.5579 1 0.7788 2719 17 2777 15 2858 29 -6															
21 505-26 111 59 0.29 13.989 7 0.5371 8 0.7226 2733 17 2749 14 2771 24 -2															
22 505-28 273 147 0.29 13.953 0 0.5358 8 0.8042 2732 15 2746 15 2766 28 -2															
23 505-29 79 44 0.29 14.275 0 0.5485 3 0.7308 2731 20 2768 17 2819 30 -4															
24 505-30 923 508 0.22 13.991 1 0.5510 3 0.7986 2691 14 2749 14 2829 26 -6															
25 505-31 64 35 0.18 14.292 9 0.5478 1 0.7738 2735 17 2769 16 2816 29 -4															
<b>145 172 0.26 0.08</b>															

Table 4.1.4 LA-ICPMS U-Pb isotope data for single monazites from sample 102-13-505, aplite dike, the Ogama-Rockland area.

Spot	U (ppm)	Pb <sup>206</sup> (ppm)	Th U	<sup>207</sup> Pb <sup>235</sup> U	1 Sig	<sup>206</sup> Pb <sup>238</sup> U	1 Sig	Err. Correl.	<sup>207</sup> Pb <sup>206</sup> Pb	1 Si g	<sup>207</sup> Pb <sup>235</sup> U	1 Si g	<sup>206</sup> Pb <sup>238</sup> U	1 Sig	Disc . (%)
<b>102-13-505 Aplite Dike</b>															
<b>Monazite</b>															
1 505mz-1 2192 1133 --- 13.603 0.33 8 0.5170 3 0.8034 2749 24 2722 23 2687 44 3															
2 505mz-2 4025 2098 --- 13.808 0.22 4 0.5213 8 0.8058 2760 16 2737 15 2705 29 2															
3 505mz-3 621 328 --- 13.630 0.27 0 0.5287 2 0.7830 2716 20 2724 19 2736 34 -1															
4 505mz-4* 1268 515 --- 11.016 0.22 6 0.4059 9 0.8354 2800 18 2524 19 2196 32 25															
5 505mz-5* 518 1385 --- 107.83 3.33 9 4 2.6746 3 0.8139 3431 28 4762 31 8390 7 -281															
6 505mz-6* 781 369 --- 11.401 0.23 0 0.4726 8 0.8173 2606 19 2556 19 2495 34 5															
7 505mz-7 284 149 --- 13.877 0.23 2 0.5255 8 0.7687 2755 18 2741 16 2723 29 1															
8 505mz-8 1867 1029 --- 14.678 0.19 2 0.5509 8 0.7947 2770 18 2795 17 2829 32 -3															
9 505mz-9 1475 702 --- 12.573 0.34 0 0.4755 8 0.8121 2757 14 2648 14 2508 25 11															
10 505mz-10 1642 913 --- 15.035 0.23 6 0.5561 0 0.8582 2794 19 2817 22 2850 45 -3															
11 505mz-11 345 183 --- 14.475 0.28 6 0.5313 4 0.7380 2806 18 2781 15 2747 27 3															
12 505mz-12* 718 464 --- 17.598 0.25 3 0.6466 1 0.7769 2805 17 2968 15 3215 32 -19															
13 505mz-13* 3282 2070 --- 16.346 0.38 5 0.6307 8 0.7959 2724 16 2897 15 3152 31 -20															
14 505mz-14* 43 194 --- 183.25 0.30 1 6 4.5168 4 0.9145 3440 18 5297 29 11009 1 -541															
15 505mz-15* 8871 6240 --- 18.943 0.30 7 0.7034 2 0.8074 2788 16 3039 16 3434 35 -30															

**NOTES:**

mz = monazite

\* omitted from regressions

Err. Correl. = Error correlation coefficient for concordia coordinate

Disc. = Discordance with fixed <sup>207</sup>Pb/<sup>206</sup>Pb age.

Relation between ages and concordia coordinates: Y = 206Pb/238U = EXP(L238\*(206-238Age)) - 1;

X = <sup>207</sup>Pb/<sup>235</sup>U = EXP(L235\*(207-235Age)) - 1

<sup>207</sup>Pb/<sup>206</sup>Pb = 137.88\*X/Y; U decay constants (L238 & L235) from Jaffey et al. (1971).

L238 = 1.55125 X 10<sup>-4</sup> /Ma; L235 = 9.8485 X 10<sup>-4</sup> /Ma

Table 4.2 U-Pb isotope data for zircon fractions and single monazites from the area of the Ogama-Rockland gold deposit

No.	Fraction	Weight (mg)	U (ppm)	Th/U	PbCom (pg)	$^{207}\text{Pb}/^{204}\text{Pb}$	$^{208}\text{Pb}/^{235}\text{U}$	$2\sigma$	$^{206}\text{Pb}/^{238}\text{U}$	$2\sigma$	Rho	$^{207}\text{Pb}/^{206}\text{Pb}$	$2\sigma$	$^{208}\text{Pb}/^{206}\text{Pb}$	$2\sigma$	Age (Ma)	Disc (%)
<b>102-13-225A Tonalite type-I, Ross River pluton: UTM 0332074E, 5639632N, NAD83</b>																	
dwd6013	2 CA zr, 1euh stubby, 1 frag,	0.0067	54.2	0.34	2.8	841	13.581	0.019	0.52272	0.00075	0.97971	0.18843	0.00005	2728.5	0.5	0.8	
dwd6014	2 CA zr, 1 euh, 1 elong frag,	0.0046	118.9	0.49	1.7	2005	13.575	0.009	0.52289	0.00037	0.97020	0.18829	0.00003	2727.2	0.3	0.7	
dwd6015	2 CA zr, crk, 1 euh stubby, 1 elong., melt inclns,	0.0064	95.9	0.31	2.5	1571	13.494	0.012	0.51950	0.00047	0.97713	0.18838	0.00004	2728.1	0.3	1.4	
dwd6038	1 CA zr (x2), spr, sharp term., inclns, clr	0.0024	138.6	0.43	1.5	1438	13.740	0.011	0.52896	0.00043	0.94114	0.18840	0.00005	2728.2	0.5	-0.4	
dwd6039	1 CA zr (x2), frag, strongly etched	0.0108	45.8	0.47	1.3	2420	13.704	0.007	0.52731	0.00029	0.94149	0.18849	0.00004	2729.0	0.3	0.0	
dwd6070	3 euh CA zr (x2), sl etched, triple filament	0.0032	220.0	0.45	2.8	1616	13.711	0.030	0.52775	0.00117	0.98631	0.18843	0.00007	2728.5	0.6	-0.2	
<b>102-13-225D Tonalite type-II, Ross River pluton: UTM 0332074E, 5639632N, NAD83</b>																	
dwd6017	3 euh stubby CA zr,	0.0149	81.2	0.39	1.9	3947	13.226	0.006	0.50920	0.00023	0.96232	0.18838	0.00002	2728.1	0.2	3.3	
dwd6018	2 euh stubby CA zr, sl etched	0.0125	74.1	0.46	1.7	3261	12.685	0.007	0.48874	0.00028	0.95699	0.18824	0.00003	2726.8	0.3	7.2	
dwd6016	1 euh stubby CA zr, sl etched	0.0099	69.6	0.50	1.3	3248	13.099	0.006	0.50617	0.00026	0.96782	0.18769	0.00002	2722.0	0.2	3.7	
dwd6071	1 euh stubby CA zr (x2), sl etched, triple filament	0.0032	68.2	0.45	2.0	695	13.690	0.150	0.52744	0.00581	0.99263	0.18824	0.00025	2726.9	2.2	-0.2	
dwd6072	1 euh CA zr (x2), etched along crk, triple filament	0.0064	243.9	0.45	2.5	4032	13.648	0.028	0.52531	0.00109	0.99417	0.18843	0.00004	2728.5	0.4	0.3	
<b>102-13-505 Aplitic dike, Ross River pluton: 0331968E, 5639791N, NAD83</b>																	
dwd6019	1 CA zr, prism frag, crk, sl etched	0.0045	114.7	0.44	2.5	1126	11.947	0.008	0.46165	0.00034	0.90057	0.18769	0.00006	2722.0	0.5	12.1	
dwd6020	3 CA zr, 1 prism frag, 2 euh frag	0.0053	145.7	0.35	6.3	631	12.084	0.014	0.46622	0.00045	0.97379	0.18798	0.00013	2724.6	1.2	11.4	
dwd6073	1 CA zr, prism frag, sl etched, triple filament	0.0036	157.2	0.31	2.8	1282	13.382	0.060	0.51509	0.00231	0.99691	0.18843	0.00007	2728.5	0.6	2.2	
dwd6074	1 euh CA zr, stubby, minimal etching, triple filament	0.0021	142.3	0.34	2.2	877	13.541	0.032	0.52127	0.00129	0.94410	0.18841	0.00015	2728.3	1.3	1.1	
dwd6075	3 euh CA zr, stubby, moderate etching, triple filament	0.0021	435.7	0.37	2.7	2151	13.662	0.015	0.52620	0.00062	0.96048	0.18830	0.00006	2727.4	0.5	0.1	
dwd6025	1 monazite equ gr	0.0002	694.7	41.94	4.9	173	13.837	0.069	0.53143	0.00212	0.76823	0.18884	0.00060	2732.1	5.2	-0.7	
dwd6026	1 monazite equ gr	0.0002	1151.8	36.31	4.5	310	14.335	0.050	0.55295	0.00177	0.87046	0.18802	0.00033	2724.9	2.9	-5.1	
dwd6027	1 monazite equ gr	0.0002	1249.1	35.46	14.9	100	14.247	0.095	0.55318	0.00104	0.15342	0.18679	0.00124	2714.1	11.0	-5.7	

CA = chemical abraded, zr = zircon grain, euh = euhedral, frag = fragment, elong = elongate, crk = crack, (x2) = chemically abraded two times, incs = inclusions, spr = short prismatic, term = terminal, clr = colorless, sl = slightly, prism = prismatic, equ = equant, gr = grain

U concentrations are based on visual estimates of weight and are probably accurate to about  $\pm 30\%$

Pbcom = Common Pb, assuming all has isotopic composition of blank,  $^{206}\text{Pb}/^{204}\text{Pb} = 18.221$ ,  $^{207}\text{Pb}/^{204}\text{Pb} = 15.612$ ,  $^{208}\text{Pb}/^{204}\text{Pb} = 39.36$  (2% errors)

Th/U calculated from radiogenic  $^{208}\text{Pb}/^{206}\text{Pb}$  ratio and  $^{207}\text{Pb}/^{206}\text{Pb}$  age assuming concordance

Rho concordia = error correlation of  $^{207}\text{Pb}/^{235}\text{U}$  and  $^{206}\text{Pb}/^{238}\text{U}$

Disc = percent discordance for the given  $^{207}\text{Pb}/^{206}\text{Pb}$  age

Decay constants are from Jaffey et al. (1971)

Table 4.3 Re-Os data for one molybdenite from V.<sub>4</sub>' vein at the Ogama-Rockland gold deposit

AIRIE Run #	Sample Name	Re, ppm	Re err, abs (ppm)	<sup>187</sup> Os, ppb	<sup>187</sup> Os err, abs (ppb)	OsC, ppb	OsC err, abs (ppb)	Age and Uncertainty for Text and Comparison to U-Pb Ages	Age, Ma	Age, abs err (Ma), with <sup>187</sup> Re decay	Age, abs err (Ma), analytical constant uncertainty only
MD-1547	102-13-257	94.35	0.15	2756.8	2.1	0.0000	0.0026	2727 ± 10	2727.4	10.0	4.8

Re-Os analyses by Carius tube dissolution with inverse *aqua regia*, equilibrated with a mixed-double Os spike; data are fractionation corrected for Os and blank corrected

Re-Os isotopic ratios were measured by NTIMS (negative thermal ion mass spectrometry) at the AIRIE Program; ages calculated using the <sup>187</sup>Re decay constant of Smoliar et al (1996)

Visual estimate of percent molybdenite in separate: MD-1547 = 80%; sample weights 25–42 milligrams with silicate dilution

Error in Re concentrations is 0.15%, and in Os concentrations 0.077%; all samples are optimally spiked, as indicated in part by this consistency

Reported uncertainties are at the two-sigma level, and based on propagation of all errors; Re and Os blanks are at the low pg to sub-pg level and insignificant to the age calculation

OsC = common Os, err = error, abs = absolute

# **Chapter 5**

## **Summary of conclusions**

## **5.1 Summary of the thesis**

This thesis has elucidated fundamental geological processes that were responsible for gold mineralization in the southeastern Rice Lake greenstone belt. Case studies have been carried out for two Archean lode gold deposits with contrasting host rocks but comparable deformation structure, alteration and mineralization. The greenstone-hosted Central Manitoba mine trend appears to be a typical late orogenic gold deposit based on stratigraphic setting and its structural control by late shear zones, whereas the granitoid-hosted Ogama-Rockland deposit seems to have experienced an early mineralization event (the source was magmatic fluids) that was overprinted and enhanced by a late mineralization event associated with dextral shearing. Sericite, chlorite and carbonate alteration zones occur at both deposits, although their appearances and intensity vary due to contrasting host rock composition. These alteration zones, along with primary lithologic contacts, are favorable places for shear zone development. Those latest dextral shear zones exhibit strong structural control on vein formation and deformation, therefore played an important role on gold deposition and remobilization in veins.

## **5.2 Main conclusions**

### ***5.2.1 Stratigraphy, structure and vein system at the Central Manitoba mine trend***

1. Auriferous quartz veins are concentrated at, and slightly discordant to, sheared contacts between greywacke, basalt and gabbro intrusions, or are entirely hosted by gabbro intrusions adjacent to contacts.
2. Quartz veins are structurally controlled by G<sub>3</sub> and G<sub>4</sub> conjugate sets of brittle-ductile shear zones. West-trending auriferous quartz veins were emplaced before or during G<sub>4</sub> dextral shearing, and then overprinted by late G<sub>4</sub> deformation.
3. Ore bodies plunge shallowly along quartz veins, and are subparallel to vein margin slickenline and ridge-in-groove slickenside striation of G<sub>4</sub> ductile shear zones.
4. Free gold (electrum) is intimately associated with quartz, pyrrhotite, chalcopyrite and bismuth-bearing minerals in high grade veins. Gold was introduced contemporaneously with pyrrhotite and tellurobismuthite relatively early in the paragenetic sequence.

### ***5.2.2 Structural setting and vein system at the Ogama-Rockland deposit***

1. Early gold introduction associated with folded V<sub>1'</sub> veins and low grade planar extension V<sub>2'</sub> veins occurred before G<sub>2'</sub> dextral shearing, and possibly before G<sub>1'</sub> NW-SE bulk shortening

as well.

2. Main gold mineralization/remobilization associated with auriferous northwest-trending steep V<sub>5</sub>' shear veins occurred late during G<sub>2</sub>' shearing.

3. Most native gold occurs in fractures and grain boundaries of quartz, pyrite and chalcopyrite in shear veins, which reflects a strong structural control on the microscopic scale.

4. The steep plunge of ore shoots indicates that interactive development of shear zones and veins played a dominant role in localizing gold mineralization.

### ***5.2.3 Timing of gold mineralization at the Ogama-Rockland deposit***

1. Granitoid plutonism, V<sub>2</sub>' vein formation and associated gold mineralization was tightly constrained at ca. 2728 Ma.

2. The close spatial and temporal associations between plutonic rocks and veins, as well as the high Re concentration of the dated molybdenite suggest granitoid magmas may have been the source of mineralizing fluids.

3. Gold in interstitial mineralogical sites or as inclusions in pyrite could be a primary feature, whereas gold in fractures represents a remobilized event during the late stage of post-vein filling G<sub>2</sub>' deformation.

4. Early gold mineralization was probably overprinted and enhanced by an undated late orogenic gold event during the late stage of G<sub>2</sub>' deformation.

## **6.3 Future work**

Essential geological processes associated with gold mineralization in the Rice Lake belt have been uncovered on the basis of field relations, ore textures, and U-Pb and Re-Os geochronology. However, the following points are still uncertain and requires more work:

1. Genetic relationships among invisible gold, visible gold inclusions, native gold in interstitial mineralogical sites and gold in fractures are still poorly understood. Detailed geochemical work on auriferous pyrite and gold may help explain physico-chemical conditions for primary gold deposition and remobilization.

2. Re-Os analyses on molybdenite from one V<sub>5</sub>' shear vein yield an average model age of  $2782 \pm 4.7$  [ $\pm 10$ ] Ma (sample 102-13-537; see Appendix), which cannot be readily explained since this age is older than the dated tonalite phases and the dated V<sub>4</sub>' vein that was cut by dextral shear zones. Further investigations on the nature of the dated molybdenite and zircon

geochronology of the adjacent wallrock tonalite may help explain this age and its potential geological significance.

# Letter of Copyright Permission

## ELSEVIER LICENSE TERMS AND CONDITIONS

License Number	3994390852227
License date	Nov 22, 2016
Licensed Content Publisher	Elsevier
Licensed Content Publication	Precambrian Research
Licensed Content Title	Stratigraphy, structure and lode gold system at the Central Manitoba mine trend, Rice Lake greenstone belt, Archean Superior Province, Manitoba, Canada
Licensed Content Author	Xiaohui Zhou, Shoufa Lin, Scott D. Anderson
Licensed Content Date	August 2016
Licensed Content Volume Number	281
Licensed Content Issue Number	n/a
Licensed Content Pages	21
Start Page	80
End Page	100
Type of Use	reuse in a thesis/dissertation
Portion	full article
Format	both print and electronic
Are you the author of this Elsevier article?	Yes
Will you be translating?	No
Order reference number	
Title of your thesis/dissertation	Stratigraphy, Structure and Geochronology of Archean Lode Gold Deposits in the Southeastern Rice Lake Greenstone Belt, Southeast Manitoba
Expected completion date	Jan 2017
Estimated size (number of pages)	200
Elsevier VAT number	GB 494 6272 12
Requestor Location	Xiaohui Zhou 200 University Anevue West  Waterloo, ON N2L 3G1 Canada Attn: Xiaohui Zhou

## References

- Acosta-Góngora, P., Gleeson, S.A., Samson, I.M., Ootes, L., Corriveau, L., 2015. Gold refining by bismuth melts in the iron oxide-dominated NICO Au-Co-Bi ( $\pm$ Cu $\pm$ W) Deposit, NWT, Canada. *Economic Geology* 110, 291–314.
- Allmendinger, R.W., Cardozo, N.C., Fisher, D., 2012. *Structural Geology Algorithms: Vectors & Tensors*. Cambridge, England, Cambridge University Press, 289 pp.
- Anderson, E.M., 1951. The dynamics of faulting and dyke formation with applications to Britain: Edinburgh, Oliver and Boyd, 206 p.
- Anderson, S.D., 2008. Geology of the Rice Lake area, Rice Lake greenstone belt, southeastern Manitoba (parts of NTS 52L13, 52M4). Manitoba Science, Technology, Energy and Mines, Manitoba Geological Survey, Geoscientific Report GR2008-1, 97 p.
- Anderson, S.D., 2013a. The Rice Lake mine trend, Manitoba: regional setting, host rock stratigraphy and structural evolution of a classical Archean orogenic gold system. Geological Association of Canada–Mineralogical Association of Canada Joint Annual Meeting, Field Trip Guidebook FT-A1; Manitoba Innovation, Energy and Mines, Manitoba Geological Survey, Open File OF2013-4, 47 p.
- Anderson, S.D., 2013b. Geology of the Garner–Gem lakes area, Rice Lake greenstone belt, southeastern Manitoba (parts of NTS 52L11, 14). Manitoba Innovation, Energy and Mines, Manitoba Geological Survey, Geoscientific Report GR2013-1, 135 p.
- Bailes, A.H., Percival, J.A., Corkery, M.T., McNicoll, V.J., Tomlinson, K.Y., Saserville, C., Rogers, N., Whalen, J.B., Stone, D., 2003. Geology and tectonostratigraphic assemblages, West Uchi map area, Manitoba and Ontario; Manitoba Geological Survey, Open File Report OF2003-1, 1:250 000 scale with marginal notes.
- Barrie, C.D., Boyce, A.J., Boyle, A.P., Williams, P.J., Blake, K., Ogawara, K., Akai, J., Prior, D.J., 2009. Growth controls in colloform pyrite. *American Mineralogist* 94, 415–429.
- Bell, T.H., Rubenach, M.J., 1980. Crenulation cleavage development—evidence for progressive bulk inhomogeneous shortening from "millipede" microstructures in the Robertson River Metamorphics. *Tectonophysics* 68, T9–T15.
- Bell, T.H., 1981. Foliation development: the contribution, geometry and significance of progressive bulk inhomogeneous shortening. *Tectonophysics* 75, 273–296.
- Beach, A., 1975. The geometry of en-echelon vein arrays. *Tectonophysics* 28, 245–263.
- Berthé, D., Choukroune, P., Jegouzo, P., 1979. Orthogneiss, mylonite and noncoaxial deformation of granite: the example of the South Armoric shear zone. *Journal of Structural Geology* 1, 31–42.
- Bhattacharyya, P., Hudleston, P.J., 2001. Strain in ductile shear zones in the Caledonides of northern Sweden; a three-dimensional puzzle. *Journal of Structural Geology* 23, 1549–1565.
- Bons, P.D., Elburg M.A., Gomez-Rivas, E., 2012. A review of the formation of tectonic veins and their microstructures. *Journal of Structural Geology* 43, 33–62.
- Brommecker, R., 1991. The structural setting of gold occurrences in the southeast Rice Lake greenstone belt, southeast Manitoba. M.Sc. thesis, Queen's University, Kingston, Ontario, 267 p.
- Brommecker, R., 1996. Geology of the Beresford Lake area, southeast Manitoba. Geological Survey of Canada, Open File 3318, 127 p.
- Burk, R., Hodgson, C.J., Quartermain, R.A., 1986. The geological setting of the Teck-Korona Au-Mo-Ba deposit, Helmo, Ontario, Canada. In: Macdonald, A.J. (Eds.), *Proceedings of*

- Gold '86, an international symposium on the geology of gold, Konsult International Inc., Toronto, pp. 311–326.
- Cabri, L.J., Chryssoulis, S.L., de Villiers, J.P.R., Laflamme, J.H.G., Buseck, P.R., 1989. The nature of “invisible” gold in arsenopyrite. *Canadian Mineralogist* 27, 353–362.
- Cameron, E.M., Hattori, K. 1987. Archean gold mineralization and oxidized hydrothermal fluids. *Economic Geology* 82, 1177–1191.
- Campbell, F.H.A., 1971. Stratigraphy and sedimentation of part of the Rice Lake Group, Manitoba. In: W.D. McRitchie and W. Weber (Eds.), *Geology and Geophysics of the Rice Lake Region, Southeastern Manitoba (Project Pioneer)*, Manitoba Department of Mines and Natural Resources, Mines Branch, Publication 71-1, pp. 135–188.
- Cardozo, N., Allmendinger, R.W., 2013. Spherical projections with OSXStereonet. *Computers & Geosciences* 51, 193–205, doi:10.1016/j.cageo.2012.07.021.
- Carreras, J., Czeck, D.M., Druguet, E., Hudleston, P.J., 2010. Structure and development of an anastomosing network of ductile shear zones. *Journal of Structural Geology* 32, 656–666, doi:10.1016/j.jsg.2010.03.013.
- Ciobanu, C.L., Birch, W.D., Cook, N.J., Pring, A., Grundler, P.V., 2010. Petrogenetic significance of Au–Bi–Te–S associations: The example of Maldon, Central Victorian gold province, Australia. *Lithos* 116, 1–17.
- Chater, A.M., Lavigne, J., Duke, C.J. 2013. A technical review of the Ogama-Rockland deposit on the Rice Lake property, Manitoba, Canada for Bison Gold Resources Inc., 79p.
- Colvine A.C., 1989. An empirical model for the formation of Archean gold deposits: products of final cratonization of the Superior Province, Canada. In: Keays, R.R., Ramsay, W.R.H., Groves D.I. (Eds.), *The geology of gold deposits: the perspective in 1988*. Economic Geology Monograph 6, pp 37–53.
- Colvine, A.C., Fyon, J.A., Heather, K.B., Marmont, S., Smith, P.M., Troop, D.G., 1988. Archean lode gold deposits in Ontario. Mines and Minerals Division, Ontario Geological Survey, Miscellaneous Paper 139, 136p.
- Cook, N.J., Chryssoulis, S.L., 1990. Concentrations of invisible gold in the common sulfides. *Canadian Mineralogist* 28, 1–16.
- Corfu, F., Davis, D.W., 1991. Comment on the paper Archean hydrothermal zircon in the Abitibi greenstone belt: Constraints on the timing of gold mineralization. *Earth and Planetary Science Letters* 104, 545–552.
- Corfu, F., Muir, T.L., 1989a. The Hemlo-Heron Bay greenstone belt and Hemlo Au-Mo deposit, Superior province, Canada, I: Sequence of igneous activity determined by zircon U-Pb geochronology. *Chemical Geology* 79, 183–200.
- Corfu, F., Muir, T.L. 1989b. The Hemlo-Heron greenstone belt and Hemlo Au-Mo deposit, Superior Province: II. Timing of metamorphism, alteration and Au mineralization from titanite, rutile, and monazite U-Pb geochronology. *Chemical Geology* 79: 201-223.
- Corfu, F., Stone, D., 1998. Age structure and orogenic significance of the Berens River composite batholiths, western Superior Province. *Canadian Journal of Earth Sciences* 35, 1089–1109.
- Corfu, F., Stott, G.M., Breaks, F.W., 1995. U-Pb geochronology and evolution of the English River Subprovince, an Archean low P-high T metasedimentary belt in the Superior Province. *Tectonics* 14, 1220–1233.
- Craig, J.R., Vokes, F.M., Solberg, T.N., 1998. Pyrite: physical and chemical textures. *Mineralium Deposita* 34, 82–101.

- Creaser, R.A., Papanastassiou, D.A., Wasserburg, G.J., 1991. Negative thermal ion mass spectrometry of osmium, rhenium and iridium. *Geochimica et Cosmochimica Acta* 55, 397–401.
- Crouch, E.A.C., Webster, R.K., 1963. Choice of the optimum quantity and constitution of the tracer used for isotopic dilution analysis. *Journal of the Chemical Society* 18, 118–131.
- Davis, D.W., 1982. Optimum linear regression and error estimation applied to U-Pb data. *Canadian Journal of Earth Sciences* 19, 2141–2149.
- Davis, D.W., 1994. Report on the geochronology of rocks from the Rice Lake belt, Manitoba. Royal Ontario Museum, Geology Department, Toronto, Ontario, unpublished report.
- Davis, D.W., 1996: Provenance and depositional age constraints on sedimentation in the Western Superior Transect area from U-Pb ages of zircons. In: LITHOPROBE Western Superior Transect, Second Annual Workshop, R.M. Harrap and H. Helmstaedt (Eds.), LITHOPROBE Secretariat, University of British Columbia, LITHOPROBE Report 53, pp. 18–23.
- Davis, D.W., Lin, S., 2003. Unraveling the geologic history of the Hemlo Archean gold deposit, Superior Province, Canada: A U-Pb geochronological study. *Economic Geology* 98, 51–67.
- Doblas, M., 1998. Slickenside kinematic indicators. *Tectonophysics* 295, 187–197.
- Durney, D.W., Ramsay, J.G., 1973. Incremental strains measured by syntectonic crystal growths. In: De Jong, K.A., Scholten, K. (Eds.), *Gravity and Tectonics*, pp. 67–96. New York: Wiley.
- England, B.M., 1979. Cleavage in pyrite from Tasmania. *Mineralogical Magazine* 43, 183–184.
- Ermanovics, I.F., Wanless, R.K., 1983. Isotopic age studies and tectonic interpretation of Superior Province in Manitoba. *Geological Survey of Canada, Paper 82-12*, 22 p.
- Gapais, D., White, S.H., 1982. Ductile shear bands in a naturally deformed quartzite. *Text Microstruct* 5, 1–17.
- Gapais, D., Bale, P., Choukroune, P., Cobbold, P.R., Mahjoub, Y., Marquer, D., 1987. Bulk kinematics from shear zone patterns: some field examples. *Journal of Structural Geology* 9, 635–646.
- Goldfarb, R.J., Groves, D.I., Gardoll, S., 2001. Orogenic gold and geologic time: A global synthesis. *Ore Geology Reviews* 18, 1–75.
- Gorman, B.E., Kerrich, R., Fyfe, W.S., 1981. Geochemistry and field relations of lode gold deposits in felsic igneous intrusions—porphyries of the Timmins district. *Ontario Geological Survey Miscellaneous Paper 98*, pp.108–123.
- Groves D.I., Goldfarb, R.J., Genre-Mariam, M., Hagemann, S.G., Robert, F., 1998. Orogenic gold deposits: A proposed classification in the context of their crustal distribution and relationships to other gold deposit types. *Ore Geology Reviews* 13, 7–17.
- Groves D.I., Goldfarb R.J., Robert, F., Hart C.J.R., 2003. Gold Deposits in Metamorphic Belts: Overview of current understanding, outstanding problems, future research, and exploration significance. *Economic Geology* 98, 1–29.
- Hagemann S.G., Brown P.E., 2000. Gold in 2000: an introduction, in *Society of Economic Geologists Reviews in Economic Geology* 13, 1–7.
- Heumann, H., 1988. Isotope dilution mass spectrometry. In: Adams, F., Gijbels, R., Van Grieken, R. (Eds.) *Inorganic mass spectrometry*, pp 301–376. New York: Wiley.
- Hodgson, C.J., 1989. The structure of shear-related vein-type gold deposits: a review. *Ore Geology Reviews* 4, 231–273.
- Hood, W., Chater, A., 2009. Report on 2007-2008 diamond drilling and a technical review of the central Manitoba gold property, Bissett/Rice Lake district, southeastern Manitoba, Canada, for Bison Gold Resources Inc., 82p.

- Hronsky, J.M.A., Groves, D.I., Loucks, R.R., Begg, G.C., 2012. A unified model for gold mineralisation in accretionary orogens and implications for regional-scale exploration targeting methods. *Mineralium Deposita* 47: 339–358, doi:10.1007/s00126-012-0402-y
- Hubbert, M.K., Rubey, W.W., 1959. Role of fluid pressure in the mechanics of overthrust faulting. *Geological Society of America Bulletin* 70, 115–205.
- Hull, J., 1988. Thickness-displacement relationships for deformation zones. *Journal of Structural Geology* 10, 431–435.
- Jaffey, A.H., Flynn, K.F., Glendenin, L.E., Bentley, W.C., Essling, A.M., 1971. Precision measurement of half-lives and specific activities of  $^{235}\text{U}$  and  $^{238}\text{U}$ . *Physical Review* 4, 1889–1906.
- Jemielita, R.A., Davis, D.W., Krogh, T.E. 1990. U-Pb evidence for Abitibi gold mineralization postdating greenstone magmatism and metamorphism. *Nature* 346: 831–834.
- Kerswill, J.A., 1986. Gold deposits hosted by iron formation in the Contwoyo Lake area, Northwest Territories [extended abstract]; In: Chater, A.M. (Eds.), *Gold '86 Poster Volume*, Konsult International Inc. Toronto, pp. 82–85.
- Krogh, T.E., 1973. A low contamination method for hydrothermal decomposition of zircon and extraction of U and Pb for isotopic age determinations. *Geochimica et Cosmochimica Acta* 37, 485–494.
- Krogh, T.E., Davis, G.L., 1974. Alteration in zircons with discordant U-Pb ages. *Carnegie Institution of Washington Yearbook* 73, 560–567.
- Krogh, T.E., Davis, G.L., 1975. Alteration in zircons and differential dissolution of altered and metamict zircon. *Carnegie Institution of Washington Yearbook* 74, 619–623.
- Krogh, T.E., Ermanovics, I.F. and Davis, G.L., 1974. Two episodes of metamorphism and deformation in the Archean rocks of the Canadian Shield. *Carnegie Institution of Washington, Geophysical Laboratory Yearbook* 73, pp. 573–575.
- Lafrance, B., DeWolfe, J.C., Stott, G.M., 2004. A structural reappraisal of the Beardmore-Geraldton Belt at the southern boundary of the Wabigoon Subprovince, Ontario, and implications for gold mineralization. *Canadian Journal of Earth Sciences* 41, 217–235.
- Lamouroux, C., Ingles, J., Debat, P., 1991. Conjugate ductile shear zones. *Tectonophysics* 185, 309–323.
- Lemkow, D.R., Sanborn-Barrie, M., Bailes, A.H., Percival, J.A., Rogers, N., Skulski, T., Anderson, S.D., Tomlinson, K.Y., McNicoll, V., Parker, J.R., Whalen, J.B., Hollings, P., Young, M., 2006. GIS compilation of geology and tectonostratigraphic assemblages, western Uchi Subprovince, western Superior Province, Ontario and Manitoba; Manitoba Geological Survey, Open File OF2006-30, CD-ROM.
- Lin, S., 2001. Stratigraphic and structural setting of the Hemlo gold deposit, Ontario, Canada. *Economic Geology* 96, 477–507.
- Lin, S., 2005. Synchronous vertical and horizontal tectonism in the Neo-Archean: kinematic evidence from a synclinal keel in the northwestern Superior craton, Canada. *Precambrian Research* 139, 181–194, doi:10.1016/j.precamres.2005.07.001.
- Lin, S., Corfu, F., 2002. Structural setting and geochronology of auriferous quartz veins at the High Rock Island gold deposit, northwestern Superior Province, Manitoba, Canada. *Economic Geology* 97, 43–57.
- Lin, S., Williams, P.F., 1992. The origin of ridge-in-groove slickenside striae and associated steps in an S-C mylonite. *Journal of Structural Geology* 14, 315–321.
- Lin, S., Jiang, D., Williams, P.F., 2007. Importance of differentiating ductile slickenside

- striations from stretching lineations and variation of shear direction across a high-strain zone. *Journal of Structural Geology* 29, 850–862.
- Lisle, R.J., 2013. Shear zone deformation determined from sigmoidal tension gashes. *Journal of Structural Geology* 50, 35–43.
- Ludwig, K.R., 1998. Using ISOPLOT/Ex version 1.00b — a geochronological toolkit for Microsoft Excel: Berkeley Geochronology Center Special Publication 1, 43 p.
- Macdonald, A.J., 1983. The iron formation – gold association: evidence from the Geraldton area. In: Colvine, A.C. (Eds.), *The geology of gold in Ontario*, Ontario Geological Survey, Miscellaneous Paper 110, pp. 75–83.
- Mancktelow, N.S., 2002. Finite-element modelling of shear zone development in viscoelastic materials and its implications for localisation of partial melting. *Journal of Structural Geology* 24, 1045–1053.
- Mancktelow, N.S., Pennacchioni, G., 2005. The control of precursor brittle fracture and fluid-rock interaction on the development of single and paired ductile shear zones. *Journal of Structural Geology* 27, 645–661.
- Markey, R.J., Stein, H.J., Morgan, J.W., 1998. Highly precise Re–Os age for molybdenite using alkali fusion and NTIMS. *Talanta* 45, 935–946.
- Markey, R.J., Hannah, J.L., Morgan, J.W., Stein, H.J., 2003. A double spike for osmium analysis of highly radiogenic samples. *Chemical Geology* 200, 395–406.
- Marquer, D., Challandes, N., Baudin, T., 1996. Shear zone patterns and strain distribution at the scale of a Penninic nappe: the Suretta nappe (Eastern Swiss Alps). *Journal of Structural Geology* 18, 753–764.
- Means, W.D., 1981. The concept of steady state foliation. *Tectonophysics* 78, 179–199.
- Means, W.D., 1987. A newly recognized type of slickenside striation. *Journal of Structural Geology* 9, 585–590.
- Means, W.D., 1995. Shear zones and rock history. *Tectonophysics* 247, 157–160.
- Mercier-Langevin, P., Daigneault, R., Goutier, J., Dion, C., Archer, P., 2012a. Geology of the Archean Intrusion-Hosted La-Grande-Sud Au-Cu Prospect, La Grande Subprovince, James Bay Region, Québec. *Economic Geology* 107, 935–962.
- Mercier-Langevin, P., Houlé, M.G., Dubé, B., Monecke, T., Hannington, M.D., Gibson, H.L., Goutier, J., 2012b. A special issue on Archean magmatism, Volcanism, and ore deposits: Part 1. Komatiite-Associated Ni-Cu-(PGE) Sulfide and Greenstone-hosted Au deposits: Preface. *Economic Geology* 107, 745–753.
- Mitra, G., 1979. Ductile deformation zones in Blue Ridge basement rocks and estimation of finite strain. *Geological Society of America Bulletin* 90, 935–951.
- Muir, T.L., 1983. Geology of the Hemlo-Heron Bay area. In: Colvine, A.C. (Eds.), *The geology of gold in Ontario*, Ontario Geological Survey, Miscellaneous Paper 110, pp. 230–239.
- Mumin, A.H., Fleet, M.E., Chryssoulis, S.L., 1994. Gold mineralization in As-rich mesothermal gold ores of the Bogosu-Prestea mining district of the Ashanti gold belt, Ghana: Remobilization of “invisible” gold. *Mineralium Deposita* 29, 445–460.
- Mungall, J.E., Kamo, S.L., McQuade, S., 2016. U–Pb geochronology documents out-of-sequence emplacement of ultramafic layers in the Bushveld Igneous Complex of South Africa. *Nature Communications* 7, 13385, doi: 10.1038/ncomms13385 (2016).
- Oberthür, T., Weiser, T., Amanor, J.A., Chryssoulis, S.L., 1997. Mineralogical sitting and distribution of gold in quartz veins and sulfide ores of the Ashanti mine and other deposits in the Ashanti belt of Ghana: Genetic implications. *Mineralium Deposita* 32, 2–15.

- Olson, J.E., Pollard, D.D., 1991. The initiation and growth of en échelon veins. *Journal of Structural Geology* 13, 595–608.
- Passchier, C.W., Trouw, R.A.J., 2005. *Microtectonics*, 2nd ed., Springer, 366p.
- Pennacchioni, G., 2005. Control of the geometry of precursor brittle structures on the type of ductile shear zone in the Adamello tonalites, Southern Alps (Italy). *Journal of Structural Geology* 27, 627–644.
- Pennacchioni, G., Mancktelow, N.S., 2007. Nucleation and initial growth of a shear zone network within compositionally and structurally heterogeneous granitoids under amphibolite facies conditions. *Journal of Structural Geology* 29, 1757–1780.
- Pennacchioni, G., Zucchi, E., 2013. High temperature fracturing and ductile deformation during cooling of a pluton: the Lake Edison granodiorite (Sierra Nevada batholith, California). *Journal of Structural Geology* 50, 54–81.
- Percival, J.A., McNicoll, V., Bailes, A.H., 2006. Strike-slip juxtaposition of ca. 2.72 Ga juvenile arc and >2.98 Ga continent margin sequences and its implications for Archean terrane accretion, western Superior Province, Canada. *Canadian Journal of Earth Sciences* 43, 895–927.
- Platt J.P., Vissers R.L.M., 1980. Extensional structures in anisotropic rocks. *Journal of Structural Geology* 2, 397–410.
- Ponce, C., Druguet, E., Carreras, J., 2013. Development of shear zone-related lozenges in foliated rocks. *Journal of Structural Geology* 50, 176–186.
- Poulsen, K.H., Robert, F., Dubé, B., 2000. Geological classification of Canadian gold deposits: Geological Survey of Canada Bulletin 540.
- Poulsen, K.H., Robert, F., 1989. Chapter 8: Shear zones and gold: Practical examples from the southern Canadian Shield. In: Burswall, J.T. (Eds.), *Mineralization and Shear Zones*; Geological Association of Canada, Short Course Notes 6, pp. 239–266.
- Poulsen, K.H., Weber, W., Brommecker, R., Seneshen, D.N., 1996. Lithostratigraphic assembly and structural setting of gold mineralization in the eastern Rice Lake greenstone belt, Manitoba. Geological Association of Canada–Mineralogical Association of Canada, Joint Annual Meeting, May 27–29, 1996, Winnipeg, Manitoba, Field Trip A4 Guidebook, 106 p.
- Ramsay, J.G., 1980. The crack-seal mechanism of rock deformation. *Nature* 284, 135–139.
- Riedel, W., 1929: Zur Mechanik Geologischer Brucherscheinungen. *Zentral-blatt fur Mineralogie, Geologie und Paleontologie* B, 354–368.
- Robert, F., 2001. Syenite-associated disseminated gold deposits in the Abitibi greenstone belt, Canada. *Mineralium Deposita* 36, 503–516.
- Robert, F., Brown, A.C., 1986. Archean gold-bearing quartz veins at the Sigma mine, Abitibi greenstone belt, Quebec: Part II. vein paragenesis and hydrothermal alteration. *Economic Geology* 81, 593–616.
- Robert, F., Poulsen K.H., 2001. Vein formation and deformation in greenstone gold deposits. In: Richards, J.P. and Tosdal, R.M. (Eds.), *Structural controls on ore genesis: Reviews in Economic Geology* 14, pp. 111–155.
- Robert, F., Poulsen, K.H., Dubé, B., 1994. Structural analysis of lode gold deposits in deformed terranes. *Geological Survey of Canada Open File* 2850, 140p.
- Robert, F., Brommecker, R., Bourne, B.T., Dobak, P.J., McEwan, C.J., Rowe, R.R., Zhou, X., 2007. Models and exploration methods for major gold deposit types. In: Milkereit, B. (Eds.), *Proceedings of Exploration 07: Fifth Decennial International Conference on Mineral Exploration*, pp. 691–711.

- Robert, F., Poulsen, K.H., Cassidy, K.F., Hodgson, C.J., 2005. Gold metallogeny of the Superior and Yilgarn cratons. In: Hedenquist, J.W., Thompson, F.H., Goldfarb, R.J. and Richards, J.P. (Eds.), *Economic Geology* 100th Anniversary Volume, pp. 1001–1033.
- Roper, P.J., 1972. Structural significance of “button” or “fish scale” texture in the phyllonitic schist of the Brevard zone. *Geological Society of America Bulletin* 83, 853 – 860.
- Rubatto, D., 2002. Zircon trace element geochemistry: partitioning with garnet and the link between U-Pb ages and metamorphism. *Chemical Geology* 184, 123–138.
- Sanborn-Barrie, M., 1987. A volcanic-hosted lode gold deposit in a shear zone at the Cochenour Willans Mine, Red Lake, Ontario [abstract]; In: Programs with Abstracts, Geological Association of Canada, Summer Field Meeting, Yellowknife.
- Sasseville, C., Tomlinson, K.Y., Hynes, A., McNicoll, V., 2006. Stratigraphy, structure, and geochronology of the 3.0–2.7 Ga Wallace Lake greenstone belt, western Superior Province, southeast Manitoba, Canada. *Canadian Journal of Earth Sciences* 43, 929–945.
- Schwarz, H.U., Kilfitt, F.W., 2008. Confluence and intersection of interacting conjugate faults: a new concept based on analogue experiments. *Journal of Structural Geology* 30, 1126–1137.
- Scoates, R.F.J., 1971. Ultramafic rocks of the Rice Lake greenstone belt. In: W.D. McRitchie and W. Weber, (Eds.), *Geology and Geophysics of the Rice Lake Region, Southeastern Manitoba (Project Pioneer)*, Manitoba Department of Mines and Natural Resources, Mines Branch, Publication 71-1, pp. 189–201.
- Selby, D., Creaser, R.A., Hart, C.J.R., Rombach, C.S., Thompson, J.F.H., Smith, F.T., Bakke, A.A., Goldfarb, R.J., 2002. Absolute timing of sulfide and gold mineralization: A comparison of Re–Os molybdenite and Ar–Ar mica methods from the Tintina Gold Belt, Alaska. *Geology* 30, 791–794.
- Shirey, S.B., Walker, R.J., 1995. Carius tube digestion for low-blank rhenium–osmium analysis. *Analytical Chemistry* 67, 2136–2141.
- Sillitoe, R.H., Thompson, J.F.H., 1998. Intrusion-related vein gold deposits: types, tectono-magmatic settings and difficulties of distinction from orogenic gold deposits. *Resource Geology* 48, No. 2, 237–250.
- Smart, K.A., Tappe, S., Stern, R.A., Webb, S.J., Ashwal, L.D., 2016. Early Archaean tectonics and mantle redox recorded in Witwatersrand diamonds. *Nature Geoscience* 9, 255–259.
- Smoliar, M.I., Walker, R.J., Morgan, J.W., 1996. Re–Os isotope constraints on the age of Group IIA, IIIA, IVA and IVB iron meteorites. *Science* 271, 1099–1102.
- Stein, H.J., 2006. Low-rhenium molybdenite by metamorphism in northern Sweden: Recognition, genesis, and global implications. *Lithos* 87, 300–327.
- Stein, H.J., 2014. Dating and Tracing the History of Ore Formation. In: Holland H.D. and Turekian K.K. (Eds.) *Treatise on Geochemistry*, Second Edition, vol. 13, pp. 87–118. Oxford: Elsevier.
- Stein, H.J., Markey, R.J., Morgan, J.W., Hannah, J.L., Scherstén, A., 2001. The remarkable Re–Os chronometer in molybdenite: How and why it works. *Terra Nova* 13, 479–486.
- Stein, H.J., Scherstén, A., Hannah, J.H., Markey, R.J., 2003. Subgrain-scale decoupling of Re and  $^{187}\text{Os}$  and assessment of laser ablation ICP-MS spot dating in molybdenite. *Geochimica et Cosmochimica Acta* 67, 3673–3686.
- Stipp, M., Stünitz, H., Heilbronner, R., Schmid, S.M., 2002. The eastern Tonale fault zone: a “natural laboratory” for crystal plastic deformation of quartz over a temperature range from 250 °C to 700 °C. *Journal of Structural Geology* 24, 1861–1884.

- Stockwell, C.H., 1938. Rice Lake – Gold Lake area, southern Manitoba. Canada Department of Mines and Resources, Geological Survey, Memoir 210, 79 p.
- Stockwell, C.H., Lord, C.S., 1939. Halfway Lake–Beresford Lake area, Manitoba. Geological Survey of Canada, Memoir 219, 67 p., and accompanying Maps 535A, 536A and 537A, scale 1:12 000.
- Stott, G.M., Corkery, M.T., Percival, J.A., Simard, M., Goutier, J., 2010. Project units 98-006 and 98-007: a revised terrane subdivision of the Superior Province. In: Summary of Field Work and Other Activities 2010, Ontario Geological Survey, Open File Report 6260, pp. 20-1 – 20-10.
- Sun, S.-S., McDonough, W.F., 1989. Chemical and isotopic systematics of oceanic basalts: implications for mantle composition and processes. In: Magmatism in the Ocean Basins, A.D. Saunders and M.J. Norry, (Eds.), Geological Society of London, Special Publication 42, pp. 313 – 345.
- Tang, M., Chen, K., Rudnick, R.L., 2016. Archean upper crust transition from mafic to felsic marks the onset of plate tectonics. *Science* 351, 372–375.
- Tchalenko, J.S., 1968. The evolution of kink bands and the development of compression textures in sheared clays. *Tectonophysics* 6, 159–174.
- Tomlinson, K.Y., Davis, D.W., Stone, D., Hart, T., 2003. U–Pb age and Nd isotopic evidence for Archean terrane development and crustal recycling in the south-central Wabigoon Subprovince, Canada. *Contributions to Mineralogy and Petrology* 144, 684–702.
- Törmänen, T.O., Koski R.A., 2005. Gold enrichment and the Bi–Au association in pyrrhotite-rich massive sulfide deposits, Escanaba Trough, Southern Gorda Ridge; *Economic Geology* 100, 1135–1150.
- Turek, A., Weber, W., 1991. New U–Pb zircon ages from the Rice Lake area: evidence for 3 Ga crust. In: Report of Activities 1991, Manitoba Energy and Mines, Minerals Division, pp. 53–55.
- Turek, A., Keller, R., Van Schmus, W.R., Weber, W., 1989. U–Pb zircon ages for the Rice Lake area, southeastern Manitoba. *Canadian Journal of Earth Sciences* 26, 23–30.
- Vearncombe, J.R., Barley, M.E., Eisenlohr, B.N., Groves, D.I., Houstoun, S.M., Skwarnecki, M.S., 1989. Structural controls on mesothermal gold mineralization: examples from the Archean terranes of southern Africa and Western Australia. *Economic Geology Monograph* 6, 124–134.
- Velásquez, G., Béziat, D., Salvi, S., Siebenaller, L., Borisova, A.Y., Pokrovski, G.S., de Parseval, P., 2014. Formation and deformation of pyrite and implications for gold mineralization in the El Callao District, Venezuela. *Economic Geology* 109, 457–486.
- Völkening, J., Walczyk, T., Heumann, K.G., 1991. Osmium isotope ratio determinations by negative thermal ion mass spectrometry. *International Journal of Mass Spectrometry and Ion Processes* 105, 147–159.
- Walsh, J.F., Kesler, S.E., Cloke, P.L., Duff, D., 1986. Geology and geochemistry of the Pamour #1 Mine, Timmins, Ontario [extended abstract]. In: Chater, A.M. (Eds.), *Gold '86 Poster Volume*, Konsult International Inc., Toronto, pp. 165–167.
- Whalen, J.B., Percival, J.A., McNicoll, V.J., Longstaffe, F.J., 2003. Intra-oceanic production of continental crust in a Th-depleted ca. 3.0 Ga arc complex, western Superior Province, Canada. *Contributions to Mineralogy and Petrology* 146, 78–99.
- White, S.H., 1979. Large strain deformation: report on a tectonic studies group discussion meeting held at Imperial College, London; introduction. *Journal of Structural Geology* 4,

- 333–339.
- Will, T.M., Wilson, C.J. L., 1989. Experimentally produced slickenside lineations in pyrophyllitic clay. *Journal of Structural Geology* 11, 657–667.
- Xue, L., 2011. Characterization of gold mineralization and distribution in the Rice Lake greenstone belts on Bison Gold's Northern Manitoba exploration properties. B. Sc. thesis, Brandon University, Brandon, Manitoba, 59p.
- Xue, Y., Campbell, I.H., Ireland, T.R., Holden, P., Armstrong, R., 2013. No mass-independent sulfur isotope fractionation in auriferous fluids supports a magmatic origin for Archean gold deposits. *Geology* 41, 791–794, doi:10.1130/G34186.1.
- Zhang, J., Lin, S., Linnen, R., Martin, R., 2014a. Structural setting of the Young-Davidson syenite-hosted gold deposit in the Western Cadillac-Larder Lake Deformation Zone, Abitibi Greenstone Belt, Superior Province, Ontario. *Precambrian Research* 248, 39–59.
- Zhang, J., Linnen, R., Lin, S., Davis, D., Martin, R., 2014b. Paleoproterozoic hydrothermal reactivation in a Neoarchean orogenic lode-gold deposit of the southern Abitibi Subprovince: U-Pb monazite geochronological evidence from the Young-Davidson mine, Ontario. *Precambrian Research* 249, 263–272.
- Zhou, X., Lin, S., Anderson, S.D., 2012. Structural study of the Ogama-Rockland gold deposit, southeastern margin of the Ross River pluton, Rice Lake greenstone belt, southeastern Manitoba (NTS 52L14). In: Report of Activities 2012, Manitoba Innovation, Energy and Mines, Manitoba Geological Survey, pp. 59–67.
- Zhou, X., Lin, S., Anderson, S.D., 2013. Stratigraphic and structural setting of gold deposits in the vicinity of the Central Manitoba mine, Rice Lake greenstone belt, southeastern Manitoba (part of NTS 52L14). In: Report of Activities 2013, Manitoba Mineral Resources, Manitoba Geological Survey, pp. 60–69.
- Zhou, X., 2014. Geology of the Bidou assemblage in the vicinity of the southeastern margin of the Ross River pluton, Rice Lake belt, southeastern Manitoba (part of NTS 52L14). Manitoba Mineral Resources, Preliminary Map PMAP2014-4, scale 1:10 000.
- Zhou, X., Lin, S., Anderson, S.D., 2014. Stratigraphic and structural reappraisal of the Bidou assemblage in the vicinity of the southeastern margin of the Ross River pluton, Rice Lake belt, southeastern Manitoba, and implications for gold mineralization (part of NTS 52L14). In: Report of Activities 2014, Manitoba Mineral Resources, Manitoba Geological Survey, pp. 64–76.
- Zhou, X., Lin, S., Anderson, S.D., 2016. Stratigraphy, structure and lode gold system at the Central Manitoba mine trend, Rice Lake greenstone belt, Archean Superior Province, Manitoba, Canada. *Precambrian Research* 281, 80–100.
- Zimmerman, A., Stein, H.J., Hannah, J.L., Kozelj, D., Bogdanov, K., Berza, T., 2008. Tectonic configuration of the Apusini–Banat–Timok–Srednogorie belt, Balkans–South Carpathians, constrained by high precision Re–Os molybdenite ages. *Mineralium Deposita* 43, 1–21.
- Zwanzig, H.V., 1971. Structural geology at Long Lake, Manitoba. In: W.D. McRitchie and W. Weber (Eds.), *Geology and Geophysics of the Rice Lake Region, Southeastern Manitoba (Project Pioneer)*, Manitoba Department of Mines and Natural Resources, Mines Branch, Publication 71-1, pp. 285–298.

## Appendix

### Enigmatic Re-Os molybdenite dates from a V<sub>5'</sub> fault-fill vein at the Ogama-Rockland deposit

In this Appendix, the author reports two enigmatic Re-Os molybdenite dates from a shear vein at the Ogama-Rockland gold deposit. The author briefly summarizes field and age relations, and then looks into microscopic features of the dated molybdenite. This is followed by discussion of analytical results.

As described in Chapter 3, V<sub>5'</sub> shear veins are mainly hosted by G<sub>2'</sub> dextral ductile shear zones in tonalite phases of the Ross River pluton ( $2728.5 \pm 0.5$  Ma,  $2727.2 \pm 5.9$  Ma, both zircon igneous ages; Chapter 4; Fig. A1) and were likely emplaced during G<sub>2'</sub> dextral shearing. Dextral shearing is the latest deformation generation in the Rice Lake greenstone belt since dextral shear zones cut most lithological units and overprinted all early structural fabrics. This dextral shearing was interpreted to postdate peak metamorphism ( $2684 \pm 3$  Ma, monazite metamorphic age; Corfu et al., 1995) related to the Uchi-English River Subprovince collision and to predate rare post-tectonic intrusions ( $2663 \pm 7$  Ma, zircon igneous age; Turek et al., 1989;  $2664.6 \pm 15.5$  Ma, rutile crystallization age; Anderson, 2013b).

The sample (102-13-537) was chosen from a typical smoky V<sub>5'</sub> shear vein about 100 metres southeast of the Rockland mine shaft (Fig. A1). This vein is bounded by sericite alteration envelopes, hosted in a northwest-trending, subvertical dextral shear zone in the undated tonalite phase (Fig. A2). This vein is along the strike of, and possibly is the western extension of, the high gold grade shear veins at the Ogama mine. The vein may be homogeneously smoky or contain smoky and white ribbons (Fig. A2c, A3a). Vein minerals are predominantly quartz, with minor tourmaline, chlorite, carbonates, sericite and sulfide minerals like pyrite, chalcopyrite, molybdenite and gold (Fig. A3; see also chapter 4). No direct contact relationships were observed between molybdenite and gold.

Molybdenite in thin section occurs as euhedral blade-shaped grains and may exhibit exsolution texture or twinning (Fig. A4a). It often occurs as linear grain aggregates and some of them are bent or kinked (Fig. A4b). No overgrowths have been found.

Analytical methods of Re-Os molybdenite geochronology are described in Chapter 4.

Results are reported in Table A1. Original and second mineral separate locations of the dated vein sample are indicated in Fig. A5. Uncertainties are reported at the  $2\sigma$  level without [with]  $^{187}\text{Re}$  decay constant uncertainties. This sample yields two overlapping dates of  $2782.2 \pm 4.6$  [ $\pm 10.0$ ] Ma and  $2786.7 \pm 4.7$  [ $\pm 10.1$ ] Ma. The Re concentrations of dated molybdenite in the V<sub>5'</sub> vein are ca. 11 and 17 ppm, both of which are significantly lower than that (94 ppm) of the dated V<sub>4'</sub> vein. These values are within the common range for Re concentrations of molybdenite in lode gold system (e.g., Selby et al., 2002).

There is difficulty in interpreting these two dates of the shear vein based on current geochronological data in the Rice Lake belt. These two dates are approximately 50 Ma older than the U-Pb zircon ages of the dated tonalite phases (ca. 2728 Ma, Chapter 4; 1 km southeast of the dated V<sub>5'</sub> vein) of the Ross River pluton described in Chapter 4, which hosts the vein. It is also ~50 Ma older than the dated V<sub>4'</sub> vein (ca. 2727 Ma, Re-Os molybdenite age, Chapter 4), but field relationships suggest V<sub>5'</sub> shear veins are younger than the dated V<sub>4'</sub> vein (Chapter 3). In addition, it is older than any available ages of the supracrustal and plutonic rocks in the entire Rice Lake belt (Fig. 1A; see also Anderson 2013a). However, the immediate wallrock tonalite of this V<sub>5'</sub> vein is not dated. U-Pb geochronology samples of the adjacent wallrock tonalite have recently been collected. The interpretation of these two enigmatic Re-Os dates from the shear vein won't be attempted until the U-Pb zircon age of this wallrock tonalite is determined.

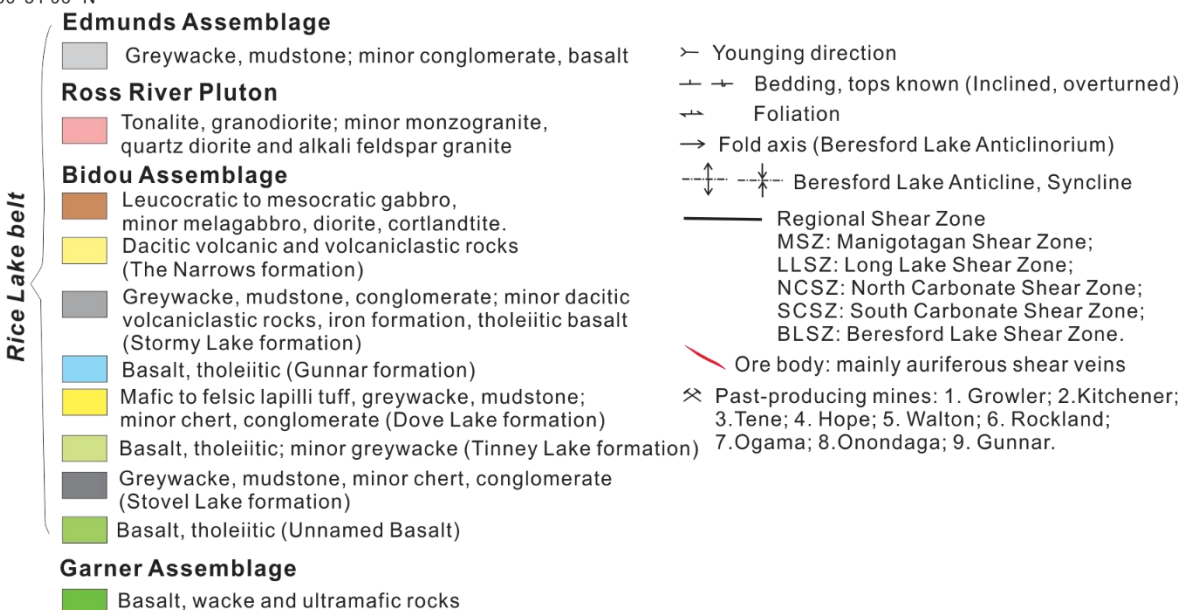
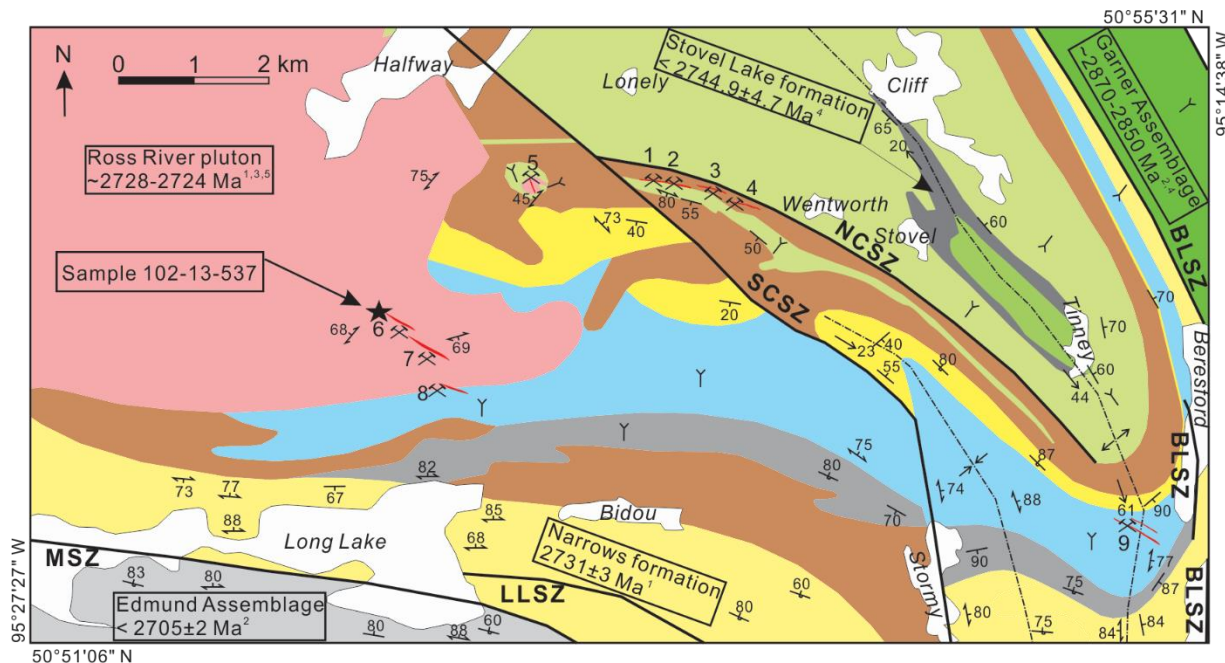


Figure A1 Generalized regional geologic map of the Bidou assemblage and Ross River pluton in the southeastern Rice Lake greenstone belt in southeastern Manitoba, showing principal formations, lithologic units, deformation structures, U-Pb zircon ages and gold deposits. Location of the Re-Os molybdenite sample 102-13-537 is indicated. Modified from Stockwell and Lord (1939), Stockwell (1945), Zwanzig (1971), Brommecker (1996), Anderson (2013b) and Zhou (2014). Age source: <sup>1</sup> Turek et al. (1989), <sup>2</sup> Davis, 1994, <sup>3</sup> Anderson (2008), <sup>4</sup> Anderson (2013b), <sup>5</sup> Chapter 4.

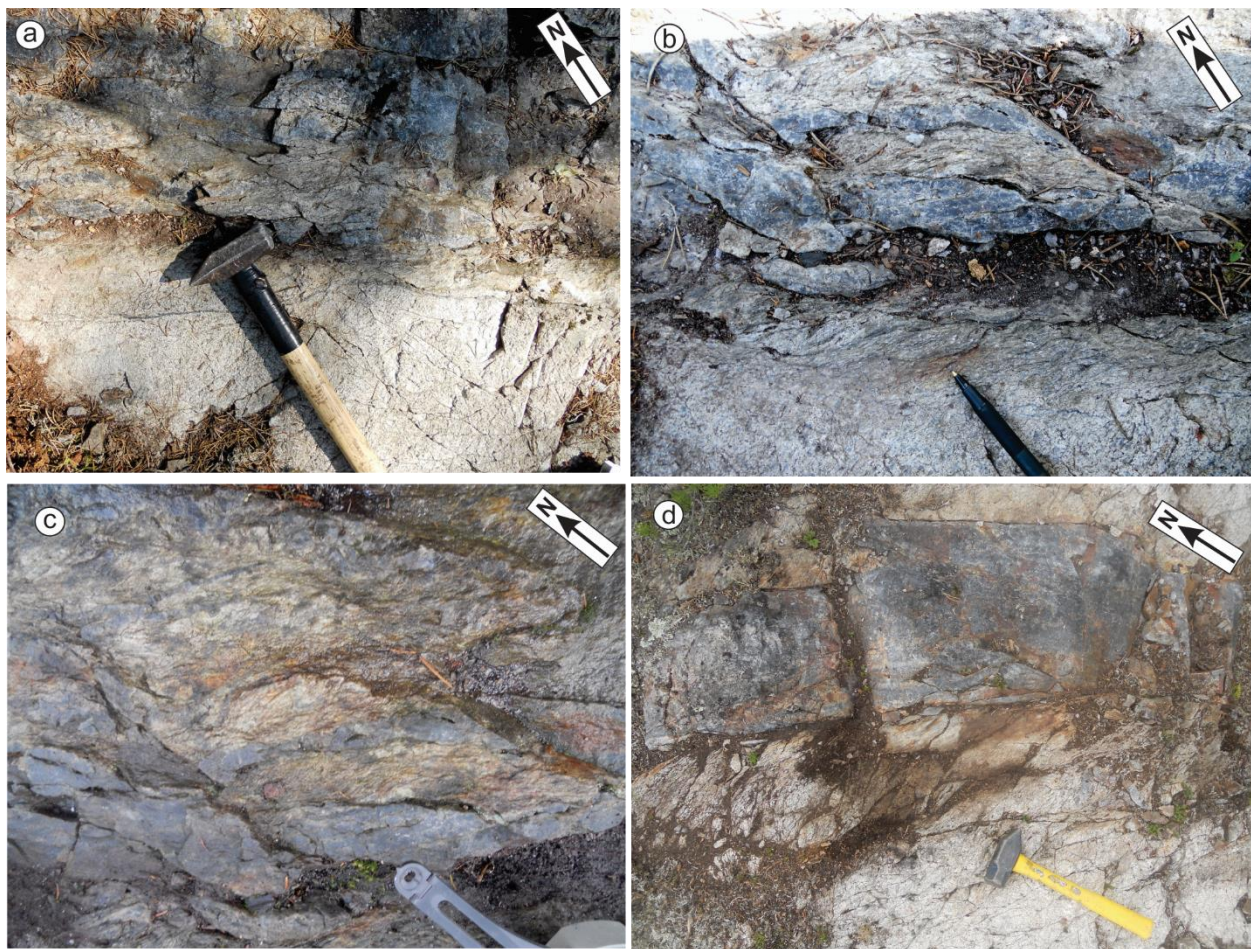


Figure A2 Outcrop photographs of the dated  $V_5'$  shear vein: a) smoky veinlets and S-C mylonite hosted in a northwest-trending subvertical dextral ductile shear zone; b) close up of S-C mylonite and smoky veinlets; S-C fabric indicating dextral shearing; c) close up of sericite-altered wallrock tonalite microlithons and veinlets; d) Mesoscopically massive smoky shear vein and associated dextral ductile shear zone.

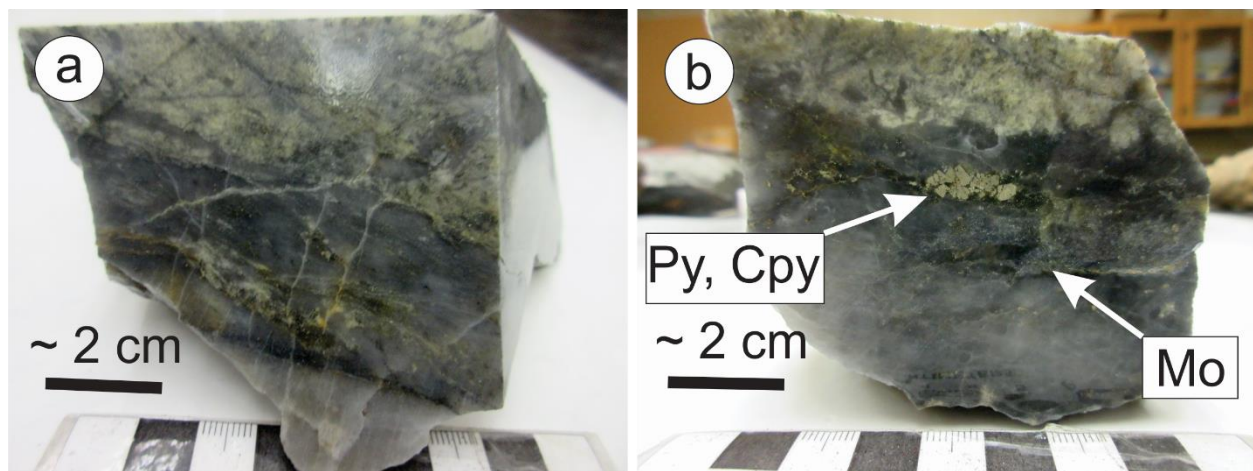


Figure A3 Hand sample photographs of dated V<sub>5'</sub> vein: a) sericite-altered wallrock and associated composite vein including smoky and white ribbons; b) smoky vein ribbon containing pyrite, chalcopyrite and molybdenite. Py = pyrite, Cpy = chalcopyrite, Mo = molybdenite.

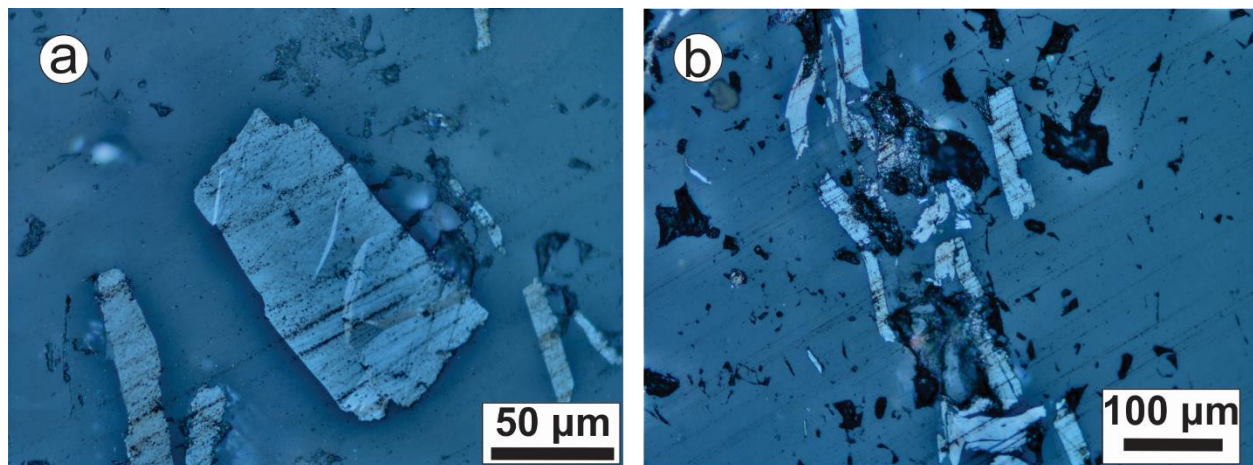


Figure A4 Photomicrographs of molybdenite in the dated V<sub>5'</sub> vein: exsolution texture in molybdenite; b) bent and kinked molybdenite grains form a linear feature.

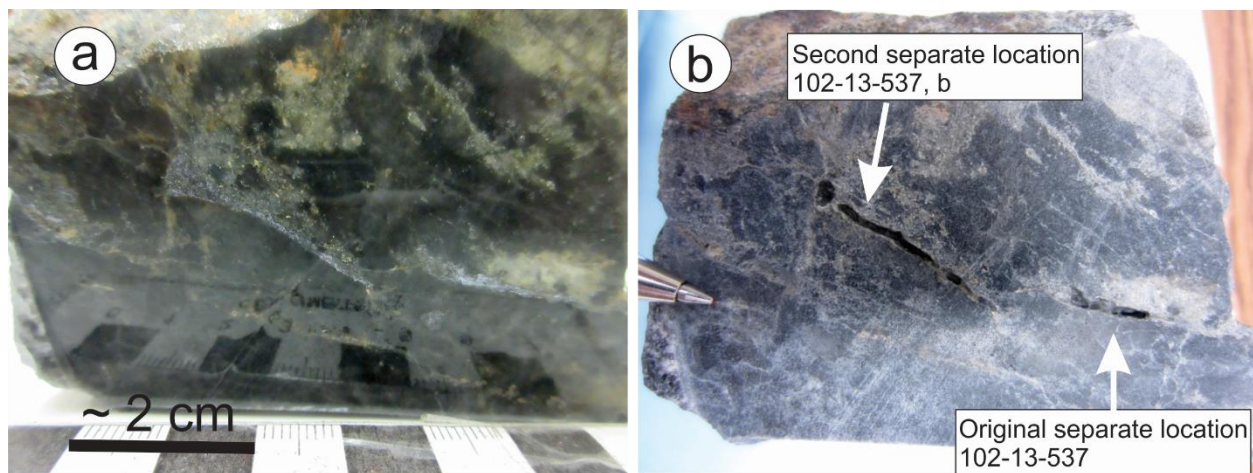


Figure A5 Hand sample photographs of dated V<sub>5</sub>' shear vein a) before and b) after mineral separation. Original and second separate locations are indicated in b).

Table A1 Re-Os data for one molybdenite from V<sub>5</sub>' vein at the Ogama-Rockland gold deposit

AIRIE Run #	Sample Name	Re, ppm	Re err, abs (ppm)	<sup>187</sup> Os, ppb	<sup>187</sup> Os err, abs (ppb)	OsC, ppb	OsC err, abs (ppb)	Age and Uncertainty for Text and Comparison to U-Pb Ages	Age, Ma	Age, abs err (Ma), with <sup>187</sup> Re decay	Age, abs err (Ma), analytical constant uncertainty only
MD-1546	102-13-537	17.390	0.026	518.56	0.40	0.0034	0.0016	2782 ±10	2782.2	10.0	4.6
MD-1596	102-13-537, b	11.837	0.018	353.57	0.27	0.0000	0.0022	2787 ±10	2786.7	10.1	4.7

Re-Os isotopic ratios were measured by NTIMS (negative thermal ion mass spectrometry) at the AIRIE Program; ages calculated using the <sup>187</sup>Re decay constant of Smoliar et al (1996)

Visual estimate of percent molybdenite in separate: MD-1546 = 75%, MD-1596 = 70%; sample weights 25-42 milligrams with silicate dilution

Error in Re concentrations is 0.15%, and in Os concentrations 0.077%; all samples are optimally spiked, as indicated in part by this consistency

Reported uncertainties are at the two-sigma level, and based on propagation of all errors; Re and Os blanks are at the low pg to sub-pg level and insignificant to the age calculation

OsC = common Os, err = error, abs = absolute

Run # MD-1596 is based on a new mineral separate derived from the rock sample;

Re-Os ages for MD-1546 and MD-1596 overlap within their two-sigma uncertainties using only analytical errors for comparison